Numerical Methods for Anisotropic Diffusion

B. van Es (2015)

A catalogue record is available from the Eindhoven University of Technology Library.
On the front cover you see an impression of the Yin-yang fusion reactor MFTF, see Conn [23].
ISBN: 978-90-386-3818-8

This work, supported by NWO and the European Communities under the contract of the Association EURATOM/FOM, was carried out within the framework of the European Fusion Program. The views and opinions expressed herein do not necessarily reflect those of the European Commission.

Numerical Methods for Anisotropic Diffusion

PROEFSCHRIFT

ter verkrijging van de graad van doctor aan de Technische Universiteit Eindhoven,
op gezag van de rector magnificus, prof.dr.ir. C.J. van Duijn,
voor een commissie aangewezen door het College voor Promoties,
in het openbaar te verdedigen op
22 april 2015 om 16:00 uur

door

Bram van Es

geboren te IJmuiden

Dit proefschrift is goedgekeurd door de promotor en co-promotor en de samenstelling van de promotiecommissie is als volgt:

voorzitter: prof.dr. E.H.L. Aarts
promotor: prof.dr.ir. B. Koren
co-promotor: dr. H.J. de Blank (FOM-DIFFER)
leden: prof.dr.ir. E.H. van Brummelen
dr.ir. M.I. Gerritsma (TU Delft)
prof.dr. P.W. Hemker (CWI)
prof.dr. A.E.P. Veldman (Rijksuniversiteit Groningen)
adviseur: dr.ir. J.H.M. ten Thije Boonkkamp

CONTENTS

Page

1 Introduction 1

1.1 Fusion plasma simulations . . . 1

1.2 Relevant cases . . . 1

1.2.1 Edge Localised Modes . . . 2

1.2.2 Neoclassical Tearing Modes . . . 3

1.3 Anisotropic diffusion . . . 4

1.3.1 Issues . . . 5

1.3.2 Model selection and coordinates . . . 6

1.4 Numerical approximation . . . 9

1.5 Objective and thesis outline . . . 10

2 Finite-difference schemes for anisotropic diffusion 11

2.1 Introduction . . . 11

2.2 Finite-difference schemes . . . 16

2.2.1 Asymmetric finite differences . . . 17

2.2.2 Symmetric finite differences . . . 18

2.2.3 Treatment of fluxes . . . 20

2.2.4 Aligned finite differences . . . 20

2.2.5 Interpolation scheme . . . 21

2.2.6 Curvature terms . . . 25

2.2.7 Exact differentiation after interpolation . . . 26

2.3 Linear stability . . . 27

2.4 Numerical results . . . 31

2.4.1 Constant angle of misalignment . . . 31

2.4.2 Varying angle of misalignment . . . 32

2.4.3 Perpendicular numerical diffusion . . . 34

2.4.4 Tilted elliptic temperature distributions . . . 38

2.4.5 Temperature-dependent diffusion coefficients . . . 40

2.4.6 Tilted closed perpendicular test case . . . 41

2.5 Conservation error . . . 41

2.5.1 Aligned gradient operator . . . 44

2.5.2 Aligned divergence operator . . . 46

2.5.3 Aligned conservative formulation . . . 49

2.6 Conclusion . . . 52

3 Finite-volume scheme for anisotropic diffusion 55
3.1 Introduction . . . 55
3.2 Finite-Volume schemes . . . 56
3.2.1 Asymmetric finite volume . . . 57
3.2.2 Symmetric finite volume . . . 57
3.2.3 Eight point flux scheme . . . 58
3.3 Interpolation for fluxes . . . 61
3.3.1 Multi-point flux approximation for eight point flux scheme . . . 61
3.3.2 Non-local flux approximation . . . 62
3.4 Numerical results and methodological adaptations . . . 63
3.4.1 Closed field-line test cases . . . 63
3.4.2 e-dependency . . . 65
3.4.3 Adaptations for closed field lines . . . 66
3.5 Conclusion . . . 73

4 Tensor adapted approximation methods for anisotropic diffusion 75
4.1 Introduction . . . 75
4.2 Relevance of sign transition . . . 78
4.3 Normalisation . . . 82
4.3.1 Cell-centered symmetric finite-difference method . . . 82
4.3.2 Normalized averaging of unit direction vectors . . . 83
4.3.3 Application to symmetric finite-difference method . . . 85
4.4 Nonnegative tensor values . . . 88
4.5 Regularisation . . . 93
4.5.1 Regularisation of the direction vector . . . 93
4.5.2 Locally avoiding non-regular diffusion tensor differencing . . . 94
4.6 Conclusion . . . 100

5 Model adaptation methods 103
5.1 Regions of interest in nuclear fusion plasma . . . 103
5.2 Importance of closed field lines . . . 104
5.3 Zero parallel diffusion coefficient continued . . . 105
5.3.1 Zero diffusion bands . . . 106
5.3.2 Closed field line detection . . . 109
5.4 Adding small perturbations . . . 109
5.4.1 Alteration of parallel temperature gradient . . . 110
5.4.2 Alteration of unit direction vector . . . 112
5.4.3 Added ϵ-sized diffusion terms . . . 114
5.5 Shifting the unit circle . . . 115
5.6 Regularisation of the diffusion tensor . . . 117

5.7 Conclusion 119

6 Conclusion 121

A Importance of symmetry for energy conservation 125

B Interpolation coefficients 127

C Linear operator 129

D Taylor expansions 133

E Von Neumann stability analyis 135

F Regarding consistency of the normalised averaging 139

Bibliography 143

Acknowledgements 153

Summary 157

Samenvatting 159

Curriculum Vitae 161

1

INTRODUCTION

The current work was performed in the context of nuclear fusion research. In this introductory chapter we elaborate on the background of the work, the motivation and the goals.

The objective of this thesis can be summarised as: *improve existing and develop new computational methods to numerically approximate anisotropic diffusion.*

1.1 Fusion plasma simulations

In order to design the experimental fusion reactor ITER, detailed simulations need to be performed to iterate on the values for the design parameters and to predict and understand physical phenomena that occur inside the reactor. The models used for the simulation of the plasma physics of nuclear fusion reactors is mostly in the form of systems of partial differential equations. These equations can not be solved exactly and need to be solved using numerical methods, these numerical methods form the subject of this thesis.
Because the plasma is prone to instabilities and because the future of ITER depends to a large extent on methods to control these instabilities it is crucial that the physical models are correctly captured by these numerical methods.
As the length scales and time scales in a nuclear fusion plasma show extreme variations, the numerical methods not only have to be accurate but also robust throughout the relevant parameter range. The parameter range in fusion plasmas is extremely wide: length and time scales of plasma phenomena can be separated by many orders of magnitude. One of the manifestations of this large separation of scales is anisotropy of diffusive processes. There are four general anisotropies, namely: viscous effects, heat conductivity, pressure and electromagnetic resistivity. In this work we focus on the heat conductivity.

Approximating the perpendicular heat diffusion correctly is important for instance for determining the confinement properties of a fusion plasma or to model instabilities which rely on perpendicular temperature gradients.

1.2 Relevant cases

The simulation of fusion plasmas usually starts with plasma configurations that are close to an instability. Then, either an instability is triggered, or the plasma will become unstable by itself. These unstable scenarios are particularly interesting because one of the key design drivers for ITER is the active control of unstable modes. Many different

types of instabilities have been found in fusion plasma experiments. Two types of instabilities are of particular concern for the design and operation of a fusion power plant, the Edge Localised Mode (ELM) and the Neoclassical Tearing Mode (NTM). For the simulation of both types of instabilities, accurate approximation of perpendicular diffusion is very important.

1.2.1 *Edge Localised Modes*

The operating regime chosen for ITER relies on a particular characteristic of the plasma called the high-confinement mode, or H-mode. The H-mode is a state of the plasma which spontaneously emerges if enough current is driven through the plasma. The H-mode features a sharp gradient in pressure, temperature and density at the edge of the plasma, representing a highly efficient isolation of the generated heat compared to the preceding low-confinement mode. The discovery of the so-called H-mode by Wagner and others [119] in 1982 was received with great enthusiasm, particularly when it appeared that the H-mode was rather easy to generate.

There was a catch; somehow the large gradient in pressure, density and temperature at the plasma edge makes the plasma prone to a nonlinear instability called the Edge Localized Mode. Until now the physical mechanism triggering the Edge Localised Mode is not fully understood, and neither is the transition from low-confinement to high-confinement. To predict the size of the ELMs in ITER, simulations are performed using initial equilibrium data plus some random perturbation, triggering a so-called peeling-ballooning mode that evolves into a fully nonlinear ELM. A typical result for the MHD code JOREK is shown in figure 1.1. Large sized ELMs can cause huge heat

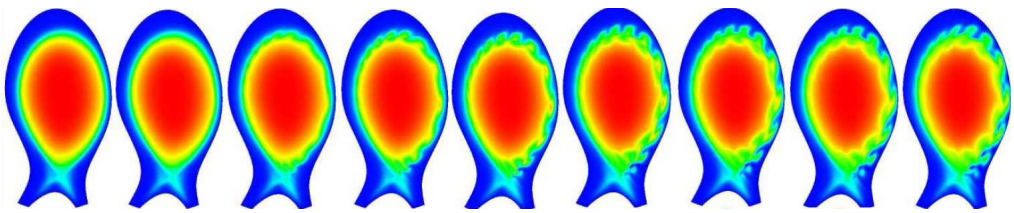

Figure 1.1: Nonlinear simulation of ballooning mode with JOREK, see Pamela and Huysmans [101]. Shown, going to the right, is the evolution of density during a ballooning mode that turns into an ELM in 600 Alfvén times ($\sim 600\,\mu s$).

fluxes on the walls and on the divertor plates. Heat fluxes in the order of a hundred MegaWatt per square meter are predicted for ITER. That is in the order of at least a thousand times more than the heat flux experienced by a spacecraft that re-enters the earth's atmosphere. Although these bursts of energy are in the order of milliseconds only, ITER is predicted to have more than a thousand ELMs per discharge (see e.g. Leonard et al. [81]). The thermal strain on the divertor plates and the reactor walls may cause ablation of the wall material and severe damage to the components facing the heat flux.

ITER and any large size reactor of similar design must be able to deal with these ELMs to enable long term operations. One of the possible methods for mitigating wall/di-

vertor damage due to large sized ELMs is to induce these in a controlled fashion. The periodic induction of ELMs is called pacing. Pacing the ELMs at a high-enough frequency can significantly reduce the energy that is released for each ELM, thus reducing the subsequent wall damage and preventing ablation of wall material (see e.g. Leonard et al. [81]).

A prime candidate for pacing the ELMs is so-called pellet injection of neutral particles. Basically small pellets of deuterium are shot into the plasma. This creates a disturbance triggering the ELM. Exactly how large the pellets must be, how dense and with what velocity they must be injected into the plasma, as well as the injection location and the injection frequency, are questions that require detailed simulations. One of the aspects of pellet injection is the diffusion of the pellet particles along the field lines. The pellet can be modelled as a local increase in density which is instantaneously diffused parallel to the magnetic field line. This requires an accurate approximation of the particle and temperature diffusion both perpendicular and parallel to the field lines.

1.2.2 *Neoclassical Tearing Modes*

In nuclear fusion plasmas there are operating regimes in which so-called magnetic islands can occur. In magnetic islands the magnetic flux surfaces are closed (see figure 1.2) and because of this the projection of the magnetic field line direction on the flux surfaces changes discontinuously through the center point of the magnetic island. As a consequence, the diffusion tensor is discontinuous there. Also, the occurrence of closed field lines may result in extremely large matrix condition numbers which can affect the accuracy of the numerical approximation.

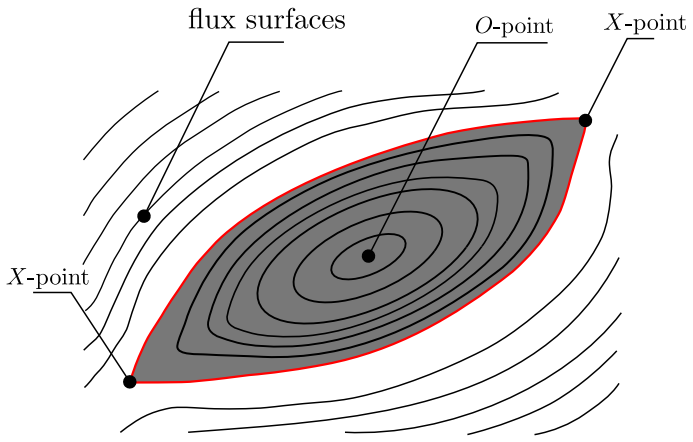

Figure 1.2: Magnetic island.

These magnetic islands, caused by different MHD modes can trigger a self-reinforcing mechanism that will enable the growth of these initial islands. This mechanism is called the Neoclassical Tearing Mode (NTM) and can induce unstable growth of these magnetic islands. Magnetic islands are relevant for the operation of the fusion reactor because the ergodicity of the field lines going through the island prevents effective transport of heat. Basically the temperature and pressure profile is almost flat throughout this island, see 1.3. If an island grows large enough it may lead to a disruption of

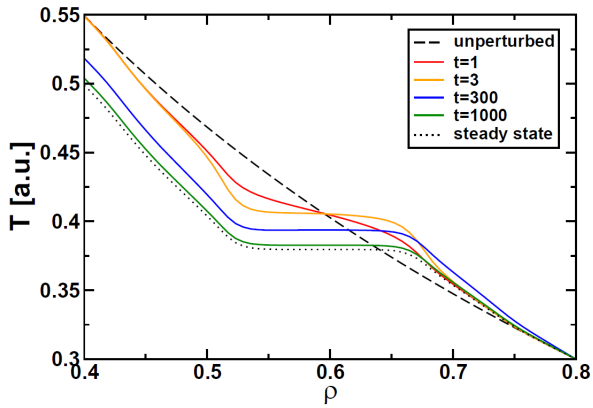

Figure 1.3: Temperature flattening due to magnetic island, see Hölzl [62].

the plasma. To get rid of these magnetic islands the plasma is locally heated by exciting the electrons with Electron Cyclotron Resonance Heating (ECRH). The modelling of both the local heating and the diffusion of heat through the island requires a numerical method that is able to resolve the effect of the local heat source on the perpendicular diffusion of the temperature. This is challenging because the diffusion coefficients are extremely anisotropic.

Summarising, the simulation of fusion plasmas with the inclusion of ELMs and NTMs requires a numerical approximation that accurately captures the perpendicular temperature gradient despite the fact that the parallel diffusion coefficient is many orders of magnitude larger than the perpendicular diffusion coefficient(s). See the thesis by Hölzl [62] for more information, and references therein.

1.3 Anisotropic diffusion

We have explained the importance of anisotropic diffusion, but what is it and what causes it? In fusion plasmas there is extreme anisotropy because the magnetic effects dominate the kinetic effects. This allows diffusive processes, heat diffusion, energy/momentum loss due to viscous friction and to a much lesser extent the magnetic resistivity, to effectively be aligned with the magnetic field lines. This alignment leads to different values for the respective diffusive coefficients in the magnetic field direction and in the perpendicular direction, to the extent that heat diffusion coefficients can be up to 10^{12} times larger in the parallel direction than in the perpendicular direction. To give a simplified sketch of the physical process we start with the idea of charged particles

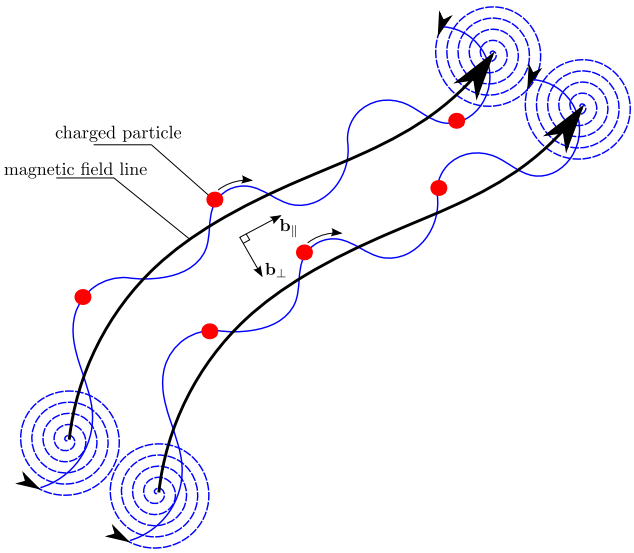

Figure 1.4: Charged particles gyrating around magnetic field lines.

gyrating around the magnetic field lines, see figure 1.4. A basic understanding of the anisotropy can be formed by imagining (with the aid of figure 1.4) that the gyration of the particles, specifically the collisions with gyrating particles around neigbouring field lines, results in a diffusive process perpendicular to the field lines. Because these collisions are in random directions perpendicular to the field line, the diffusion in the plane perpendicular to the field line is isotropic. Imagine then that during the gyration the charged particles travel many orders of magnitude further along the field line than perpendicular to it before colliding with other charged particles. Also consider the fact that the particles travel practically homogeneously in the same direction along the field line. This results in extremely efficient transport of particles in directions parallel to the field lines, compared to directions perpendicular to the field lines, explaining the extreme anisotropy of the diffusion coefficients.

We distinguish two types of anisotropy: anisotropy in the diffusion coefficients, the parallel diffusion coefficient being much larger than the perpendicular diffusion coefficient ($D_\parallel \gg D_\perp$), and an anisotropy in the temperature distribution, the perpendicular temperature gradient being much larger than the parallel temperature gradient ($\nabla_\perp T \gg \nabla_\parallel T$). We note the following caveats; in reality there is no toroidal symmetry and the magnetic field lines impinge the poloidal plane ergodically and do not form closed magnetic flux surfaces.

1.3.1 *Issues*

This anisotropy puts stringent requirements on the numerical methods used to approximate the MHD-equations since any misalignment of the grid may cause the perpen-

dicular diffusion to be polluted by the numerical error in approximating the parallel diffusion. Non-dimensionalising the diffusion terms in the MHD-equations will leave a factor which is either much bigger or much smaller than unity.
So, numerically, large anisotropy may lead to the situation where the errors in the direction in which the coefficient value is largest may influence the coefficients in the perpendicular directions. This necessitates either a high order approximation in the direction of the largest coefficient value and/or a limitation of the degree of anisotropy.

Currently the common approach is to apply magnetic field aligned coordinates which automatically takes care of the directionality of the diffusive coefficients. Complicating factors are the curvature of the magnetic field lines, magnetic reconnection due to magnetic islands and x-points (see figure 1.2). Added difficulty is the time dependency of these points. So any fix (e.g. regridding) must be applied at each time level and will introduce local non-alignment.

Possible resolutions for this problem are:

- anisotropic mesh refinement,
- anisotropic order refinement,
- anisotropy in discretisation method,
- anisotropy in model.

The anisotropy in a fusion plasma is based on the variable direction of the magnetic field, which varies both spatially and temporally. In the case of fusion plasmas, anisotropy in coefficients can range anywhere between 10^6 and 10^{12}. Problems that may arise with highly anisotropic diffusion problems are:

- pollution of physical diffusion perpendicular to the magnetic field lines by numerical diffusion due to grid misalignment,
- non-positivity near large temperature gradients and discontinuous diffusion coefficients,
- mesh locking, stagnation of convergence dependent on anisotropy due to grid misalignment and diffusion tensor variability.

A numerical procedure that is not described in field aligned coordinates may introduce large errors if the magnetic field direction is misaligned with the grid. This will likely affect the accuracy with which plasma instabilities can be predicted.

1.3.2 *Model selection and coordinates*

In this thesis we solely rely on two-dimensional computations. Nuclear fusion plasma simulations are mostly three-dimensional and feature very different length and time scales. The high temperature in a fusion plasma leads to extremely good electrical conductivity. Therefore plasma motion (instabilities, waves, or turbulence) not only leads to advective transport of particles, momentum and heat, but also to an almost exact motion of the magnetic field lines with the plasma velocity. Hence, even vigorous

plasma motion tends to cause hardly any gradients of density and temperature along field lines.
In tokamaks the equilibrium state of the plasma has a high degree of toroidal (rotational) symmetry, which is important for good energy confinement. Also, the magnetic field component in the toroidal direction is largest. Therefore, the magnetic energy in the toroidal field component is much larger than the magnetic energy of the poloidal field component, of the thermal energy, and of the kinetic energy of any plasma instability. This fact implies that any spontaneous plasma motion such as turbulence or instability tends to avoid changes of the toroidal field, because such changes would always increase the magnetic energy more than the available free energy that causes the motion. Therefore the magnetic configuration and temperature always remain rather close to toroidal symmetry.
So, the toroidal magnetic field is much larger than the poloidal field or the magnetic field induced by the plasma and the variations in toroidal direction due to instabilities and turbulence are negligible, and they work on a very small time scale. As a consequence of all this, the toroidal direction is treated in a different manner than the directions perpendicular to it, for instance using Fourier harmonics (see e.g. Günter et al. [54], Sovinec et al. [109]) or using the assumption that toroidal components of the magnetic field and the velocity are constant, leading to the reduced MHD equations (see e.g. Huysmans et al. [64], Pamela et al. [102]).

Throughout the thesis we will refer to *parallel* and *perpendicular directions*, and phenomena *tangential* or *perpendicular to the field lines*. Given that we focus on the cross-section

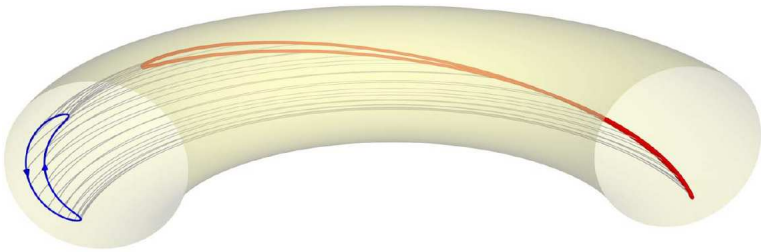

Figure 1.5: Shown here is the projection of a so-called banana orbit, indicated in red, on the poloidal plane, indicated in blue, see Hölzl [62].

of the toroidal direction; the coordinates lie in the poloidal plane, which is a perpendicular cross-section of the toroidal geometry, see figure 1.5. As such we are actually dealing with *projections* of magnetic field lines on a plane and so the extreme anisotropy is slightly mitigated by the fact that the perpendicular lines of the parallel projections have in fact a non-zero parallel component when considered in three dimensions. The lines drawn by the projections of the magnetic field lines represent magnetic flux surfaces. Thus, with parallel/perpendicular and tangential we refer to the magnetic flux surfaces. For the description of our problem in the poloidal plane we simply use a Cartesian coordinate system.

Anisotropic thermal diffusion is described by the following model

$$\mathbf{q} = -\mathbf{D} \cdot \nabla T, \quad \frac{\partial T}{\partial t} = -\nabla \cdot \mathbf{q} + f, \tag{1.1}$$

where T represents temperature, $\mathbf{q}$ the heat flux, f some source term and $\mathbf{D}$ the diffusion tensor. For simplicity we use a rectangular Cartesian grid. The unit direction vector then directly represents the misalignment of the grid. For a two-dimensional problem the diffusion tensor is given by

$$\begin{aligned}
\text{unit direction vector:} \quad & \mathbf{b} = (b_1, b_2)^T = (\cos\alpha, \sin\alpha)^T, \\
\text{Rotation matrix:} \quad & \mathcal{R} = \begin{pmatrix} b_1 & -b_2 \\ b_2 & b_1 \end{pmatrix} \\
& \mathbf{D} = \mathcal{R}\Lambda\mathcal{R}^T, \; \Lambda = diag(D_\parallel, D_\perp), \\
& \mathbf{D} = \begin{pmatrix} D_\parallel b_1^2 + D_\perp b_2^2 & (D_\parallel - D_\perp) b_1 b_2 \\ (D_\parallel - D_\perp) b_1 b_2 & D_\perp b_1^2 + D_\parallel b_2^2 \end{pmatrix},
\end{aligned}$$

which can also be written as

$$\mathbf{D} = (D_\parallel - D_\perp)\mathbf{b}\mathbf{b}^T + D_\perp \mathcal{I},$$

where $D_\parallel$ and $D_\perp$ represent the parallel and the perpendicular diffusion coefficient respectively and where $\mathcal{I}$ is the identity matrix. We define x, y as the non-aligned coordinate system and s, n as the aligned coordinate system, see figure 1.6. The boundary conditions are of Dirichlet type unless mentioned otherwise, they are discussed per test case. The diffusion equation is approximated on a uniform Cartesian grid, with the grid resolution set to $\Delta x = \Delta y = h$.

We define the anisotropy as

$$\varsigma = \frac{D_\parallel}{D_\perp}.$$

In tokamak fusion plasma simulations the diffusion coefficients are often temperature-

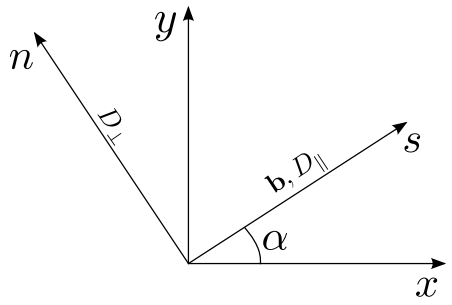

Figure 1.6: Explanation of symbols.

dependent. The parallel and perpendicular diffusion coefficients are assumed to be

proportional to $T^{5/2}$ and $T^{-1/2}$ respectively. I.e. the anisotropy varies strongly with temperature. Throughout the thesis there are two recurring assumptions regarding the test cases. First, for the steady cases, the parallel temperature gradient $\mathbf{b} \cdot \nabla T$ is assumed negligible compared to the perpendicular temperature gradient so we set $\mathbf{b} \cdot \nabla T = 0$. The parallel temperature gradient is assumed to be zero because the temperature along the field lines evolves at a time scale $\sqrt{D_{\parallel}/D_{\perp}}$ times shorter than the perpendicular diffusion time scale, hence for a steady state situation $\mathbf{b} \cdot \nabla T = 0$.

Second, for unsteady cases the perpendicular diffusion coefficient is assumed negligible compared to the parallel diffusion coefficient. Here the reverse holds, *if* the time scale of our simulation is similar to the time scale of the parallel diffusion the perpendicular diffusion takes too long to have any noticeable effect.

In general we state the following

$$\nabla_{\phi} T < \nabla_{\parallel} T \ll \nabla_{\perp} T, \quad \mathbf{b}_{\phi} \cdot \mathbf{B} > \mathbf{b} \cdot \mathbf{B} \gg \mathbf{b}_{\perp} \cdot \mathbf{B}, \quad D_{\phi} \sim D_{\parallel} \gg D_{\perp},$$

where $\mathbf{B}$ represents the equilibrium magnetic field, the subscript $\perp$ indicates the component perpendicular to the magnetic flux surfaces in the poloidal plane and ϕ the component in toroidal direction.

1.4 Numerical approximation

We stated earlier that we can not exactly solve the equations that describe the fusion plasma, and that we rely on numerical methods for this. A core activity of many computational methods revolves around the construction and/or inversion of a matrix called the linear operator. We give a basic example of solving the steady heat diffusion equation to explain what a linear operator actually is. Consider the steady state diffusion equation with a simple boundary condition

$$\begin{aligned} \nabla \cdot (\mathbf{D} \cdot \nabla T) &= Q, \\ T &= f, \mathbf{x} \in \Gamma, \end{aligned} \tag{1.2}$$

where Q is a function that may for instance represent a heat source, T the unknown variable which represents, say temperature, $\mathbf{D}$ the diffusion tensor that relates the temperature gradient ∇T to a heat flux, and where f is a function describing the temperature value on the boundary Γ (a so-called Dirichlet boundary condition).

The solution of this partial differential equation is not known analytically in general and must be approximated by solving the linear system

$$\begin{aligned} \mathcal{L}\mathbf{T}_{\Omega} &= \mathbf{Q}, \\ \mathbf{T}_{\Gamma} &= f, \end{aligned} \tag{1.3}$$

where $\mathcal{L}$ is the aforementioned linear operator, $\mathbf{T}$ a vector with all the temperature unknowns, Q a vector with the source values, and where Ω indicates the problem domain excluding the boundary Γ. Now simply put, the linear operator is a matrix which contains the relationships between all the unknowns such that it represents the analytical

differential operator at a discrete level. Given that we know the result of applying these relationships to the unknown values (the result being the right-hand-side of the equal sign) we can find the approximate values of these unknowns by multiplying the right-hand-side with the inverse of the linear operator.

1.5 Objective and thesis outline

We have explained why the accurate approximation of anisotropic diffusion is important and, in broad terms, why it is challenging. The work in this thesis is focussed on finding methods that improve the accuracy with which extremely anisotropic diffusive processes can be approximated. We do this by proposing new discretisation schemes, by adapting existing schemes, and also by adapting the models.

Chapter 2 describes an aligned finite difference method that we developed for anisotropic diffusion problems. In chapter 2 we also describe several test cases that serve as a benchmark throughout the remainder of the thesis.

In chapter 3 an eight-point finite volume scheme is presented that addresses the aspect of volume connectivity. In chapter 3 we also describe a model-reduction method to improve the accuracy for extreme anisotropy.

In chapter 4 we explain the importance of the diffusion tensor, and give some approaches to improve existing methods.

Lastly, in chapter 5 we describe several model adaptation approaches to improve the accuracy.

2

FINITE-DIFFERENCE SCHEMES FOR ANISOTROPIC DIFFUSION

In fusion plasmas diffusion tensors are extremely anisotropic due to the high temperature and large magnetic field strength. This causes diffusion, heat conduction, and viscous momentum loss, to effectively be aligned with the magnetic field lines. This alignment leads to different values for the respective diffusive coefficients in the magnetic field direction and in the perpendicular direction, to the extent that heat diffusion coefficients can be up to 10^{12} times larger in the parallel direction than in the perpendicular direction. This anisotropy puts stringent requirements on the numerical methods used to approximate the MHD-equations since any misalignment of the grid may cause the perpendicular diffusion to be polluted by the numerical error in approximating the parallel diffusion. One approach is to apply magnetic field-aligned coordinates, an approach that automatically takes care of the directionality of the diffusive coefficients. This approach runs into problems in case of crossing field lines, e.g. at x-points and at points where there is magnetic re-connection, since this makes local non-alignment unavoidable. It is therefore useful to consider numerical schemes that are more tolerant to the misalignment of the grid with the magnetic field lines, both to improve existing methods and to help open the possibility of applying regular non-aligned grids. To investigate this, several discretisation schemes are developed and applied to the unsteady anisotropic heat diffusion equation on a non-aligned grid.

2.1 Introduction

Anisotropic diffusion is a common physical phenomenon that describes processes where the diffusion of some scalar quantity is direction dependent. Anisotropic diffusive processes are for instance transport in porous media, large-scale turbulence where turbulence scales are anisotropic in size, and of interest to us: heat conduction and momentum dissipation in fusion plasmas.

In tokamak fusion plasmas the viscosity and heat conduction coefficient parallel to the magnetic field may be in the order of 10^6 to 10^{12} times larger, respectively, than perpendicular conduction coefficients. This is caused by the fact that, as explained in chapter 1, the heat conductivities parallel and perpendicular to the magnetic field lines are determined by different physical processes; along the field lines particles can travel relatively large distances without collision whereas perpendicular to the field lines the mean free path is in the order of the gyroradius, see e.g. Hölzl [62].

Numerically, high anisotropy may lead to the situation that errors in the direction of the largest diffusion coefficient may significantly influence the diffusion in the perpendicular direction. This necessitates a high-order approximation in the direction of the

This chapter is based on [114].

largest coefficient value (see e.g. Sovinec et al. [109], Meier et al. [94], Chen et al. [20]). Given the high level of anisotropy in tokamak plasmas, a numerical approximation may introduce large perpendicular errors if the magnetic field direction is strongly misaligned with the grid. Problems that may arise with highly anisotropic diffusion problems on non-aligned meshes are in general:

- significant numerical diffusion perpendicular to the magnetic field lines due to grid misalignment, see e.g. Umansky et al. [113],
- non-positivity near high gradients, see e.g. Sharma et al. [107],
- mesh locking, stagnation of convergence dependent on anisotropy, see e.g. Babuška and Suri [11],
- convergence loss in case of variable diffusion tensor, see e.g. Günter et al. [54].

It is possible to use a field-aligned coordinate system. However, this cannot be maintained throughout the plasma; problems arise at x-points and in regions of highly fluctuating magnetic field directions (for instance in case of edge turbulence). To confidently perform simulations of phenomena that rely heavily on the resolution of the perpendicular temperature gradient we must apply a scheme that maintains sufficient accuracy in case of varying anisotropy and misalignment.

The bulk of the present methods are designed with discontinuous diffusion tensors in mind, and often on general and distorted non-uniform grids. We give an (inexhaustive) overview of methods used today, for details the reader is referred to the specific papers.

We start with the Multi-Point Flux Approximation (MPFA), a cell-centered finite volume method commonly used for approximating anisotropic diffusion with discontinuous tensors on distorted meshes, see e.g. Aavatsmarket et al. [2–5], and Edwards and Rogers [43]. The MPFA uses cell-centered unknowns and connects the volumes using shared subcells with a local low-order interpolation of the primary unknowns. The method is robust in terms of diffusion tensor discontinuity as it is locally conservative, but the resulting diffusion operator is often non-symmetric and formal accuracy can not be maintained for higher levels of anisotropy. The MPFA method comes in various flavors, depending on how the fluxes are approximated, for instance the original MPFA-O and MPFA-U methods by Aavatsmark et al. [2, 3] and more recently by Aavatsmark et al. [1] and Agélas et al. [6] respectively, the symmetric MPFA-L and MPFA-G methods.

In the Vertex Approximate Gradient (VAG) scheme devised by Eymard et al. [47, 49] and Costa et al. [24] vertex unknowns are added as degrees of freedom. The cell face unknowns are expressed as a linear combinations of these added vertex unknowns. Placing the cell unknowns in harmonic averaging points (see Agélas [7]) allows for an elimination of the cell center unknowns.

Le Potier [77] devised a cell-centered finite-volume method where the gradients are solved on each vertex by imposing flux continuity conditions, similar to the MPFA approach. Eymard et al. [44] devised a cell-centered finite-volume scheme using a special

discrete gradient operator. Maire and Breil [15, 91] apply an MPFA-like finite-volume method with cell-centered unknowns and a local variational formulation to obtain the fluxes in their Cell-Centered Lagrangian Diffusion (CCLAD) approach, with the requirement that temperature and sub-face normal fluxes are continuous. Maire and Breil [92] also constructed a CCLAD method where the fluxes are constructed using finite differences. Jacq et al. [71] expanded the method to three dimensions.

Le Potier and Ong [80] and Ong [99] devised a cell-centered method which makes use of a dual grid. The dual grid unknowns are chosen to be linear combinations of cell unknowns. This so-called Finite Element Cell-Centered (FECC) method uses less unknowns per cell compared to other dual grid methods which apply both cell-centered unknowns and cell-face or vertex unknowns. Another difference is the use of a third grid which is a sub-grid of the dual grid. The theoretical accuracy convergence of the FECC method seems to be maintained for discontinuous diffusion tensors with large values for the anisotropy [80].

Shashkov and Steinberg [108] constructed the Support Operator Method (SOM), which gives a class of methods known as the Mimetic Finite Difference (MFD) methods. Hyman et al. [65,67] and Brezzi et al. [16,17] apply and categorize the MFD methods. They are applied to the simulation of plasma turbulence by Stegmeir et al. [110]. The MFD methods are mimetic to the extent that they preserve the self-adjointness of the divergence and the flux operator. Key to the MFD methods is the use of a dual grid, where flux values and temperature values are placed on separate grid points, and the application of a variational formulation to find the flux values, such that the self-adjointness between the discrete divergence operator and the discrete gradient operator is guaranteed. Downside of the original MFD schemes is the use of non-local operators. Formal convergence is robust for high levels of anisotropy, grid non-uniformity and discontinous diffusion tensors. Further, the diffusion operator is symmetric positive definite. Günter et al. [54] apply the MFD method to fusion plasma relevant test cases and maintain the order of accuracy for non-aligned (regular, rectangular) meshes. Günter et al. [53] apply the support-operator approach from Hyman et al. [67] to a finite-element method. The method is adapted to have a local flux description by Morel et al. [96], which requires both cell-centered and face-centered unknowns. The MFD method is finally made local and cell-centered by Lipnikov et al. [88] and Lipnikov and Shashkov [86].

Hermeline [57, 58] uses a dual grid, solving the diffusion equation on each grid where the temperature and the diffusion tensor values are defined in the same nodes. This is termed the Discrete Duality Finite-Volume (DDFV) method. The DDFV method requires the solution of the diffusion equation on two meshes and as such requires more unknowns. The resulting matrices are positive definite. Formal convergence for highly anisotropic problems (with the ratio between parallel and perpendicular diffusion coefficient 10^{12}) is close to second-order accurate for higher resolutions but not anisotropy-independent for coarser grids, see Le Potier and Ong [80]. The FECC method bares resemblance to the DDFV method where the former uses a third subgrid and cell-centered unknowns.

Other methods involving the use of dual grids are the Hybrid Finite Volume method

(HFV) and the Mixed Finite Volume (MFV) method, see Eymard et al. [46] and Droniou and Eymard [39] respectively. Droniou et al. [40] formally proved the similarity of the MFD scheme, the HFV scheme and the MFV scheme. The MFD, MFV, HFV and the DDFV methods can be placed within the concept of Compatible Discrete Operators (CDO) where the mathematical operators are treated exactly and the constitutive relations are approximated. Recent examples are the mimetic spectral element method developed by Kreeft et al. [74], applied to approximate Darcy flow with arbitrary order by Rebelo et al. [106]. Bochev and Gerritsma [13] use a mimetic least squares minimiser in combination with a spectral element discretisation to approximate the anisotropic reaction-diffusion equations. Another example of a CDO method applied to anistropic diffusion, similar to the work by Kreeft et al. is given by Bonelle and Ern [14]. Another approach has been developed by Hirani [60], Desbrun et al. [35] and is called Discrete Exterior Calculus, it is applied to scalar Darcy flow by Hirani et al. [61].

Discontinuous Galerkin (DG) methods for elliptic problems have been developed that treat the diffusion equation as a system of first order equations, see Cockburn and Shu [22], Oden et al [98], and Peraire and Persson [104]. Discontinuous Galerkin applied to the original diffusion equation is performed using an interior penalty function by Douglas et al. [37] and through a mixed formulation of the diffusion terms by Bassi and Rebay [12]. A recovery based DG method for diffusion was developed by Van Leer and Nomura [117] and Van Leer et al. [116]. Gassner et al. [52] approximate the numerical fluxes by solving a generalized Riemann problem.
Vincent et al. [118] developed a framework unifying Spectral Differences, Spectral Volumes and Discontinuous Galerkin methods for linear problems using a Flux Reconstruction (FR) approach. Williams et al. [121] extended the FR approach to advection diffusion.

Jardin [72] applies a finite element method with reduced quintic triangular finite elements where the quintic basis functions are constrained to enforce C_1 continuity across element boundaries. Although it shows high order accuracy for an anisotropic diffusion problem, it is not anisotropy independent, it requires 21 basis functions per element and the test case considered is completely symmetric.

Pasdunkorale and Turner [103] devised a Control Volume Finite Element method (CVFEM), which maintains the local flux continuity at the control volume faces for extreme anisotropy. Here the cross diffusion fluxes are resolved partly implicitly using least squares. This is not demonstrated for a full diffusion tensor with extreme anisotropy. The Vandermonde matrices for the least squares solution are based on the grid geometry, with no guarantee for well-posedness.

MPFA, MFD, CVFEM and other methods are somehow related, through flux-continuity requirement and a weak continuity requirement of the temperature over the edges, see Klausen and Russell [73]. Reference results for a variety of test cases can be found in Herbin and Hubert [56] and Eymard et al. [48]. For a more detailed overview of finite-volume methods the reader is referred to the review paper by Droniou [38].

All the methods discussed above leave the analytic formulation untouched and focus

on the numerical procedure. In Degond et al. [30–32] and Mentrelli and Negulescu [95], the steady diffusion equation itself is split in two parts, a limit problem for infinite anisotropy and the original singular perturbation problem. Degond et al. [31] also provide a means for continuous transition between the two problems. Degond et al. [31] perform this splitting to prevent ill-posedness which arises for Neumann boundary conditions and periodic boundary conditions. The two formulations are obtained by discriminating between a mean part and a fluctuating part of the singular perturbation problem. These Asymptotic Preserving (AP) schemes have difficulties preserving accuracy and stability in case of closed field lines. Narski and Ottaviani [97] introduce a penalty stabilization term in the weak formulation of the AP-scheme to conserve accuracy in case of closed field lines. The downsides of this approach are that the penalty stabilization has a tuning parameter, it requires an L-stable time integration scheme and it requires the solution of two systems instead of one. An important benefit of AP-schemes is that the condition number does not scale with the anisotropy, without the use of a preconditioner. A basic characteristic of the AP scheme for the parabolic equation is that for $D_\perp / D_\parallel$ going to zero the parallel temperature gradient $\mathbf{b} \cdot \nabla T$ also goes to zero.

Del Castillo-Negrete and Chacón [33,34] apply a Lagrangian Green's function approach that does not require any algorithmic inversion and thus prevents issues with ill-conditioning. Chacón et al. [19] apply a more generic semi-Lagrangian approach to unsteady anisotropic diffusion. Chacón et al. treat the perpendicular diffusion as a source, allowing to rewrite the diffusion equation with a Green's function. However, this method is limited to a spatially constant value for the parallel diffusion coefficient. The field lines are assumed to be time-invariant and it assumes a particular scaling for the variation of the magnetic field line strength. In particular, the variation of the magnetic field strength along the field line is considered to be negligible.

None of the schemes is monotonous without special treatment of the linear operator or the mesh. Sharma et al. [107] apply a flux limiter to enforce the monotonicity locally but this is only applicable to relatively small levels of anisotropy not relevant for fusion plasma and it increases the perpendicular numerical diffusion and lowers the global accuracy. Methods that rely on changing the mesh basically change the elements based on the local values of the anisotropic diffusion to enforce that the local mass-matrices are $M-$matrices, see for instance Li and Huang [82], Aricò and Tucciarelli [9]. These methods are limited to low anisotropy. Monotonicity preserving methods that maintain the accuracy have been devised. These methods put restraints on the diffusion tensor and often require a nonlinear approach, see for instance Le Potier et al. [78], Lipnikov et al. [85,87,89].

In the present chapter the focus is on applying a co-located finite-difference discretisation in the direction of the strongest diffusion by means of interpolation. This can be applied to the flux operator only or to the entire operator. In this chapter we try to live up to the accuracy properties of Günter et al.'s symmetric scheme by applying an interpolation scheme based on the direction of diffusion while still using a Cartesian grid. Furthermore we introduce a test case with elliptic closed field lines and we interpret the large difference in accuracy. We do not put any requirement on the diffusion tensor

other than that it is symmetric positive definite. As we treat the singularly perturbed diffusion problem the scheme is not asymptotic preserving. For comparison we apply the asymmetric and symmetric finite-difference schemes given in Günter et al. [54].

For $\varsigma \to \infty$, the anisotropic diffusion problem reduces to

$$\frac{\partial T}{\partial t} = \nabla \cdot \Big(D_{\parallel} (\mathbf{b} \cdot \nabla T) \mathbf{b} \Big) = 0.$$

This limit problem has infinitely many solutions if $\mathbf{b} \cdot \nabla T = 0$ and no temperature boundary conditions are prescribed for the field lines. So in the limit of the anisotropy going to infinity the diffusion equation may be ill-posed. This may occur when there are closed magnetic field lines. This is noticeable in the discretisation through a higher condition number of the linear operator for increasing anisotropy, see Degond et al. [30,31].

Regarding the steady state solution of the extremely anisotropic diffusion problems; on the one hand closed field line topologies are relatively easy in the sense that there is only non-zero perpendicular diffusion and on the other hand this is exactly the challenge since any error in the perpendicular diffusion working in the tangential direction is multiplied by a very large number. For the unsteady problem we have the opposite issue; any error in the non-zero parallel diffusion will pollute the perpendicular diffusion, where often the perpendicular diffusion coefficient is set to zero.

In this chapter we look at the order of convergence and the perpendicular numerical diffusion for extremely high levels of anisotropy.

2.2 Finite-difference schemes

We limit the discussion to finite-difference schemes. Given a uniform grid this can be directly translated to a finite-volume approach for the asymmetric and symmetric schemes discussed in sections 2.2.1 and 2.2.2 respectively. We consider several second-order accurate finite-difference schemes for the approximation of model equation (1.1). The first two schemes are described in Günter et al. [54]. The difference between these schemes lies in the treatment of the flux, particularly the location of the flux. The term co-located is used to indicate that the variables $T, \mathbf{b}$ are defined in coinciding points. The asymmetric and symmetric schemes, discussed in the following sections, have the field direction $\mathbf{b}$ defined in the flux points and may be referred to as staggered schemes. The new schemes, to be presented here, aim to improve the accuracy of co-located schemes by applying a stencil that lies on an approximation of the field line. We use sub-indices x, y, s, n to denote the respective derivatives.

2.2.1 *Asymmetric finite differences*

The first finite-difference scheme for heat diffusion we discuss is depicted in figure 2.1. For a spatially constant diffusion tensor this scheme reduces to the standard second-order accurate scheme for diffusion. The label asymmetry is coined because of the

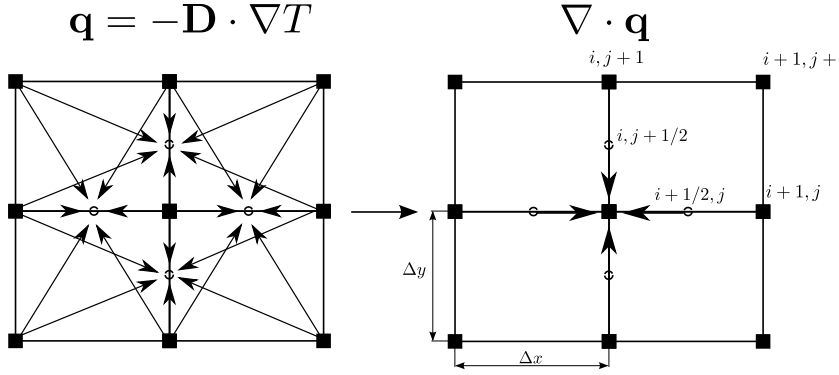

Figure 2.1: Asymmetric scheme, temperature T is defined on the full indices and the diffusion tensor $\mathbf{D}$ on the half-indices.

different treatment of the x- and y-differential in each point. The different treatment is a direct result of taking the flux values in $i \pm \frac{1}{2}, j$ and $i, j \pm \frac{1}{2}$,

$$\begin{aligned}
\left.\frac{\partial T}{\partial x}\right|_{i+\frac{1}{2},j} &= \frac{T_{i+1,j} - T_{i,j}}{\Delta x}, \\
\left.\frac{\partial T}{\partial y}\right|_{i+\frac{1}{2},j} &= \frac{T_{i+1,j+1} + T_{i,j+1} - T_{i,j-1} - T_{i+1,j-1}}{4\Delta y}, \\
\left.\frac{\partial T}{\partial x}\right|_{i,j+\frac{1}{2}} &= \frac{T_{i+1,j+1} + T_{i+1,j} - T_{i-1,j+1} - T_{i-1,j}}{4\Delta x}, \\
\left.\frac{\partial T}{\partial y}\right|_{i,j+\frac{1}{2}} &= \frac{T_{i,j+1} - T_{i,j}}{\Delta y},
\end{aligned}$$

and similar formulas for $\left.\frac{\partial T}{\partial x}\right|_{i-\frac{1}{2},j}$, $\left.\frac{\partial T}{\partial y}\right|_{i-\frac{1}{2},j}$, $\left.\frac{\partial T}{\partial x}\right|_{i,j-\frac{1}{2}}$, $\left.\frac{\partial T}{\partial y}\right|_{i,j-\frac{1}{2}}$. For the heat conduction term we have

$$\mathbf{q}_{i+\frac{1}{2},j} = -\mathbf{D}_{i+\frac{1}{2},j} \cdot \left(\left.\frac{\partial T}{\partial x}\right|_{i+\frac{1}{2},j}, \left.\frac{\partial T}{\partial y}\right|_{i+\frac{1}{2},j} \right)^T.$$

Finally, the diffusion follows from

$$\nabla \cdot \mathbf{q} = \frac{(q_1)_{i+\frac{1}{2},j} - (q_1)_{i-\frac{1}{2},j}}{\Delta x} + \frac{(q_2)_{i,j+\frac{1}{2}} - (q_2)_{i,j-\frac{1}{2}}}{\Delta y}.$$

The scheme is denoted as *asymmetric scheme, G. et al.*[1].

[1] G. et al. is a reference to Günter et al. [54]

2.2.2 *Symmetric finite differences*

Still another approach is taken by Günter et al. [54]. They use a symmetric scheme (with a symmetric linear operator) that is mimetic by maintaining the self-adjointness of the differential operator. The approach goes as follows. First, the gradients are determined at the center points, see figure 2.2:

$$\left.\frac{\partial T}{\partial x}\right|_{i+\frac{1}{2},j+\frac{1}{2}} = \frac{T_{i+1,j+1} + T_{i+1,j} - T_{i,j+1} - T_{i,j}}{2\Delta x},$$
$$\left.\frac{\partial T}{\partial y}\right|_{i+\frac{1}{2},j+\frac{1}{2}} = \frac{T_{i,j+1} + T_{i+1,j+1} - T_{i+1,j} - T_{i,j}}{2\Delta y}.$$

Next, the diffusion tensor is applied to the gradient to obtain the heat flux

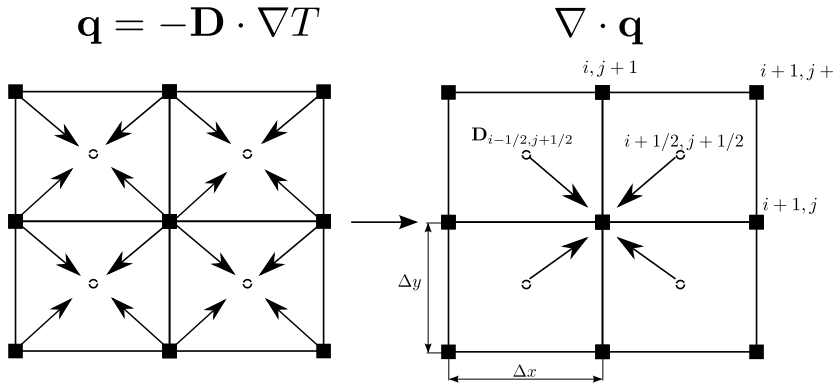

Figure 2.2: Symmetric scheme, temperature T is defined on the full indices and the diffusion tensor $\mathbf{D}$ on the half-indices.

$$\mathbf{q} = -\mathbf{D} \cdot \nabla T, \quad \mathbf{q}_{i+\frac{1}{2},j+\frac{1}{2}} = -\mathbf{D}_{i+\frac{1}{2},j+\frac{1}{2}} \cdot \left(\left.\frac{\partial T}{\partial x}\right|_{i+\frac{1}{2},j+\frac{1}{2}}, \left.\frac{\partial T}{\partial y}\right|_{i+\frac{1}{2},j+\frac{1}{2}} \right)^T.$$

Finally, the divergence is taken over the heat flux to obtain the diffusion operator

$$\nabla \cdot \mathbf{q} = \frac{(q_1)_{i+\frac{1}{2},j+\frac{1}{2}} + (q_1)_{i+\frac{1}{2},j-\frac{1}{2}} - (q_1)_{i-\frac{1}{2},j+\frac{1}{2}} - (q_1)_{i-\frac{1}{2},j-\frac{1}{2}}}{2\Delta x} + \frac{(q_2)_{i+\frac{1}{2},j+\frac{1}{2}} + (q_2)_{i-\frac{1}{2},j+\frac{1}{2}} - (q_2)_{i-\frac{1}{2},j-\frac{1}{2}} - (q_2)_{i+\frac{1}{2},j-\frac{1}{2}}}{2\Delta y}.$$

Here we note an important aspect which is seemingly overlooked in literature. The flux vectors are averaged, but simply averaging the flux vectors is not correct since $|\sum \mathbf{b}| < \sum |\mathbf{b}|$ for every set of vectors that is not in the same quadrant. So instead we have to use normalized averaging $\overline{\mathbf{b}} = \sum \mathbf{b} / |\sum \mathbf{b}|$ to average the unit direction vectors. This requires an explicit formulation of the averaging procedure so that we can specifically apply a normalized average of the unit direction vector. This is discussed in more detail in chapter 4. The scheme is denoted as *symmetric scheme, G. et al*.

Importance of self-adjointness

The symmetric scheme preserves the self-adjointness between the divergence and the gradient operator. By maintaining the self-adjointness discretely the following integral identity is fulfilled exactly

$$\int_V \phi \nabla \cdot \mathbf{q} dV + \int_V \mathbf{q} \cdot \nabla \phi dV = \oint_{\partial S} \phi (\mathbf{q} \cdot \mathbf{n}) dS,$$

where ϕ is an arbitrary real-valued function in x, y. The total energy of a system described by the diffusion equation is given by $E = c_v \int_V T dV$ where c_v is a volumetric constant. In absence of any surface and source terms this should be constant. This means that $\frac{\partial E}{\partial t} = 0$ or $\int_V \nabla \cdot (\mathbf{D} \cdot \nabla T) dV = 0$. If we take a constant value for ϕ we find that

$$\phi \int_V \nabla \cdot \mathbf{q} dV = \frac{\partial E}{\partial t} = 0,$$

and so energy is preserved exactly in absence of surface and source terms, see appendix A. The integral identity can be written as

$$\int_V \phi \nabla \cdot \mathbf{q} dV + \int_V \mathbf{D}^{-1} \mathbf{q} \cdot \mathbf{D} \nabla \phi dV = \oint_{\partial S} \phi (\mathbf{q} \cdot \mathbf{n}) dS. \tag{2.1}$$

Now assuming that ϕ or $\mathbf{q} \cdot \mathbf{n}$ are zero on the domain boundary, the right-hand side vanishes. With inner products defined as

$$(\phi, \psi)_H = \int_V \phi \psi dV, \quad (\overrightarrow{A}, \overrightarrow{B})_{\mathcal{H}} = \int_V \left(\mathbf{D}^{-1} \overrightarrow{A}, \overrightarrow{B} \right) dV,$$

where ψ is an arbitrary real-valued scalar function and $\overrightarrow{A}, \overrightarrow{B}$ are arbitrary real-valued vectors. The integral identity can now be written as

$$(\phi, \nabla \cdot \mathbf{q})_H - (\mathbf{q}, \mathbf{D} \nabla \phi) = 0, \tag{2.2}$$

stating that the divergence and the flux operator are adjoint to each other. First, either the divergence operator or the flux operator is defined as the prime operator, for instance through the integral identity

$$\int_V \nabla \cdot \mathbf{q} dV = \oint_{\partial S} \mathbf{q} \cdot \mathbf{n} dS$$

the divergence operator can be determined. Then, using the integral identity (2.1) the other derived operator can be constructed. This procedure leads to the so-called Mimetic Finite Difference (MFD) methods, see for instance Shashkov and Steinberg [108], Hyman et al. [65] and Lipnikov et al. [84,88]. Note that, in general, on the boundaries of the domain the right-hand side of integral identity (2.1) does not go to zero and the construction of the linear operator changes, see e.g. Hyman and Shashkov [66]. For MFD methods on general grids local inner products are needed to construct divergence and flux operators that are adjoint. The symmetric finite-difference scheme from Günter et al. preserves the self-adjointness for general anisotropic diffusion tensors on a uniform, rectangular Cartesian grid and for this specific case it is similar to the global Support Operator Method (SOM) described in Shashkov and Steinberg [108] and the global MFD method described in Hyman et al. [65].

2.2.3 *Treatment of fluxes*

For the values of the diffusion coefficients $D_\parallel, D_\perp$ in the flux points we have to apply averaging since they are dependent on the temperature which is known only in the surrounding points.

We use either arithmetic averaging or harmonic averaging. Harmonic averaging is relevant for plasma physics simulations if the density varies strongly and is part of the heat flux. If, in a neighboring cell the density goes to zero, harmonic averaging ensures that the averaged value becomes equal to the minimum of the cell values. This ensures that the heat flowing in the direction of a cell goes to zero if the density in that cell goes to zero. This may be the case if we consider turbulence at the edge for instance, see Sharma and Hammett [107]. For the asymmetric scheme by Günter et al. we have, for flux point $i + \frac{1}{2}, j$:

$$\text{Arithmetic:} \quad \mathbf{T}_{i+\frac{1}{2},j} = \frac{\mathbf{T}_{i+1,j} + \mathbf{T}_{i,j}}{2}, \quad \text{Harmonic:} \frac{2}{\mathbf{T}_{i+\frac{1}{2},j}} = \frac{1}{\mathbf{T}_{i+1,j}} + \frac{1}{\mathbf{T}_{i,j}}.$$

Analogous to the asymmetric scheme by Günter et al, for the symmetric scheme the diffusion tensor is either taken as the arithmetic mean or as the harmonic mean of the four surrounding points, e.g. for point $i + \frac{1}{2}, j + \frac{1}{2}$:

$$\begin{aligned}
&\text{Arithmetic:} \quad \mathbf{T}_{i+\frac{1}{2},j+\frac{1}{2}} = \frac{\mathbf{T}_{i+1,j+1} + \mathbf{T}_{i+1,j} + \mathbf{T}_{i,j+1} + \mathbf{T}_{i,j}}{4}, \\
&\text{Harmonic:} \quad \frac{4}{\mathbf{T}_{i+\frac{1}{2},j+\frac{1}{2}}} = \frac{1}{\mathbf{T}_{i+1,j+1}} + \frac{1}{\mathbf{T}_{i+1,j}} + \frac{1}{\mathbf{T}_{i,j+1}} + \frac{1}{\mathbf{T}_{i,j}}.
\end{aligned}$$

2.2.4 *Aligned finite differences*

The idea is that differencing along the field line yields an approximation less prone to large false perpendicular diffusion. To do this we have to use interpolation to find the values of T and $\mathbf{D}$ on the field line. The field line trajectory itself is approximated by tracing. In the current implementation, T, $\mathbf{b}$ and $\mathbf{D}$ are assumed to be co-located. Using the definition for the diffusion tensor we can write the diffusion operator as

$$\text{diffusion operator:} \quad \nabla \cdot (\mathbf{D} \cdot \nabla T) = \nabla \cdot \left[\left(D_\parallel - D_\perp \right) \mathbf{b} \cdot \nabla T \mathbf{b} \right] + \nabla \cdot D_\perp \nabla T.$$

By now applying the product rule and some vector identities we can write the diffusion operator in parts:

$$\nabla \cdot (\mathbf{D} \cdot \nabla T) = \mathcal{A}_1 + \mathcal{A}_2 + \mathcal{A}_3 + \mathcal{A}_4, \tag{2.3}$$

where the parts are given by

$$\begin{aligned}
\text{field line curvature:} \quad & \mathcal{A}_1 = \left(D_\parallel - D_\perp \right) (\mathbf{b} \cdot \nabla \mathbf{b}) \cdot \nabla T, \\
\text{field strength gradient:} \quad & \mathcal{A}_2 = \left(D_\parallel - D_\perp \right) (\nabla \cdot \mathbf{b}) \, (\mathbf{b} \cdot \nabla T), \\
\text{standard diffusion:} \quad & \mathcal{A}_3 = \left(D_\parallel - D_\perp \right) \mathbf{b}\mathbf{b}^T : \nabla \nabla T + D_\perp \nabla^2 T, \\
\text{diffusion gradient:} \quad & \mathcal{A}_4 = \mathbf{b} \cdot \nabla \left(D_\parallel - D_\perp \right) (\mathbf{b} \cdot \nabla T) + \nabla T \cdot \nabla D_\perp.
\end{aligned}$$

The *field line curvature* term results from field line curvature in the presence of a temperature gradient and does not require a variation in the strength of the magnetic field. The *field strength variation* comes from the fact that we impose the constraint $\nabla \cdot \mathbf{B} = 0$ on the MHD-equations so that

$$|\mathbf{B}|\nabla \cdot \mathbf{b} = -\mathbf{b} \cdot \nabla |\mathbf{B}|,$$

and thus $\nabla \cdot \mathbf{b} \neq 0$ if $\nabla |\mathbf{B}| \neq 0$. Note that $\nabla \cdot \mathbf{b}$ has no particular physical meaning. The *standard diffusion* is caused by the second-order derivative of the temperature and is the only diffusion in case the field lines are non-curved, the magnetic field is constant and the diffusion coefficients are constant. The *diffusion variation* term corresponds to the diffusion resulting from a gradient of the diffusion coefficients in the presence of a temperature gradient.
Rewriting the above formulation in s, n coordinates yields

$$\begin{aligned}
\mathcal{A}_1 =& -(D_\parallel - D_\perp)\mathcal{F}_1 T_n, \\
\mathcal{A}_2 =& (D_\parallel - D_\perp)\mathcal{F}_2 T_s, \\
\mathcal{A}_3 =& D_\parallel T_{ss} + D_\perp T_{nn}, \\
\mathcal{A}_4 =& D_{\parallel_s} T_s + D_{\perp_n} T_n.
\end{aligned} \tag{2.4}$$

Applying the chain rule with $x = b_1 s - b_2 n, \quad y = b_1 n + b_2 s$ we get for $\mathcal{F}_1, \mathcal{F}_2$:

$$\mathcal{F}_1 = -b_1 b_{2_s} + b_2 b_{1_s}, \quad \mathcal{F}_2 = -b_2 b_{1_n} + b_1 b_{2_n}. \tag{2.5}$$

Here the subscripts s, n indicate derivatives. Now we can write

$$\begin{aligned}
\nabla \cdot (\mathbf{D} \cdot \nabla T) = &-(D_\parallel - D_\perp)\mathcal{F}_1 T_n + (D_\parallel - D_\perp)\mathcal{F}_2 T_s \\
&+ D_\parallel T_{ss} + D_\perp T_{nn} + D_{\parallel_s} T_s + D_{\perp_n} T_n.
\end{aligned}$$

When applying the equations of magnetohydrodynamics to nuclear fusion plasmas, an assumption often made is that the temperature is diffused instantaneously along the field line, i.e. $D_\parallel = 0$. This means that the variation of the temperature in the direction of the field line is zero, i.e. $\mathbf{b} \cdot \nabla T = 0$, $T_s = 0$. The terms $\mathcal{F}_1$,$\mathcal{F}_2$ in parts $\mathcal{A}_1, \mathcal{A}_2$ can be approximated in three different ways: (1) use an aligned stencil to approximate $b_{1_s}, b_{1_n}, b_{2_s}, b_{2_n}$, (2) estimate $x_{ss}, x_{nn}, y_{ss}, y_{nn}$ by following the field line track, (3) apply interpolation of b_1, b_2 to obtain $b_{1_s}, b_{1_n}, b_{2_s}, b_{2_n}$ directly. We will describe these approaches in sections 2.2.5, 2.2.6 and 2.2.7 respectively.

2.2.5 *Interpolation scheme*

We continue by applying a stencil aligned with the principal axes of the diffusion tensor to approximate equation (2.4) using field-aligned stencil points. The stencil points r, l, u, d, c are given in figure 2.3, these points lie somewhere on the field lines going through the central stencil point. We consider x, y as local coordinates, where the origin is located in the stencil point i, j. The values at the locations r, l, u, d are determined by bi-quadratic interpolation:

$$\begin{aligned}
v(x, y) = &c_1 x^2 y^2 + c_2 x^2 y + c_3 y^2 x + c_4 x^2 \\
&+ c_5 y^2 + c_6 xy + c_7 x + c_8 y + c_9, \quad x, y \in [-h, h],
\end{aligned} \tag{2.6}$$

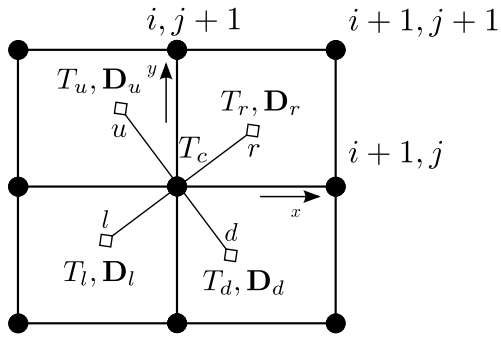

Figure 2.3: Locally transformed grid, 5-point stencil.

where v can represent $T, b_1, b_2, D_\parallel$ or $D_\perp$. For convenience we assume that we have a uniform Cartesian grid with $\Delta x = \Delta y = h$. Then, for T, the coefficients $c_1, \dots c_9$ follow from

$$\mathbf{c} = \mathbf{V}^{-1}\mathbf{T}, \tag{2.7}$$

where $\mathbf{c}$ contains the coefficients $c_1, \dots c_9$, $\mathbf{T}$ the temperature unknowns and where $\mathbf{V}$ is the Vandermonde matrix containing the polynomial terms for each node, also see appendix B. The identical relations hold for the coefficients $c_1, \dots c_9$ for $b_1, b_2, D_\parallel$ and $D_\perp$. The coefficients $c_1, \cdots c_9$ that follow from (2.7) are given by

$$\begin{aligned}
c_1^V &= \frac{1}{h^4}\left(T_{i,j} - \frac{T_{i,j-1}}{2} - \frac{T_{i-1,j}}{2} - \frac{T_{i+1,j}}{2} - \frac{T_{i,j+1}}{2}\right. \\
&\qquad \left. + \frac{T_{i-1,j-1}}{4} + \frac{T_{i+1,j-1}}{4} + \frac{T_{i+1,j+1}}{4} + \frac{T_{i-1,j+1}}{4}\right), \\
c_2^V &= \frac{1}{4h^3}\left(2T_{i,j-1} - 2T_{i,j+1} + T_{i-1,j+1} + T_{i+1,j+1} - T_{i-1,j-1} - T_{i+1,j-1}\right), \\
c_3^V &= \frac{1}{4h^3}\left(2T_{i-1,j} - 2T_{i+1,j} + T_{i+1,j-1} + T_{i+1,j+1} - T_{i-1,j-1} - T_{i-1,j+1}\right), \\
c_4^V &= \frac{1}{2h^2}\left(T_{i-1,j} - 2T_{i,j} + T_{i+1,j}\right), \quad c_5^V = \frac{1}{2h^2}\left(T_{i,j-1} - 2T_{i,j} + T_{i,j+1}\right), \\
c_6^V &= \frac{1}{4h^2}\left(T_{i-1,j-1} + T_{i+1,j+1} - T_{i+1,j-1} - T_{i-1,j+1}\right), \\
c_7^V &= \frac{T_{i+1,j} - T_{i-1,j}}{2h}, \quad c_8^V = \frac{T_{i,j+1} - T_{i,j-1}}{2h}, \\
c_9^V &= T_{i,j},
\end{aligned} \tag{2.8}$$

where the superscript V denotes *Vandermonde*. Note that the coefficients $c_1, \dots c_8$ are all approximations of differential terms in point i, j,

$$\begin{aligned}
&c_1 = \tfrac{1}{4}T_{xxyy} + \mathcal{O}(h^2), \quad c_2 = \tfrac{1}{2}T_{xxy} + \mathcal{O}(h^2), \quad c_3 = \tfrac{1}{2}T_{yyx} + \mathcal{O}(h^2), \\
&c_4 = \tfrac{1}{2}T_{xx} + \mathcal{O}(h^2), \quad c_5 = \tfrac{1}{2}T_{yy} + \mathcal{O}(h^2), \quad c_6 = T_{xy} + \mathcal{O}(h^2), \\
&c_7 = T_x + \mathcal{O}(h^2), \quad c_8 = T_y + \mathcal{O}(h^2).
\end{aligned} \tag{2.9}$$

For a spatially constant diffusion tensor the Vandermonde coefficients are similar to the approximation of the respective differential terms for the asymmetric scheme by Günter et al. For comparison purposes we change the coefficients so that they have similar approximation as the symmetric scheme by Günter et al. in case of constant diffusion coefficients. Effectively we change the approximations for T_x, T_y, T_{xx} and T_{yy} to involve more nodes to approximate the respective differentials,

$$\begin{aligned}
c_4^S &= \frac{1}{8h^2}\left(T_{i-1,j+1} + T_{i-1,j-1} - 2T_{i,j-1} + 2T_{i-1,j} - 4T_{i,j}\right.\\
&\qquad \left. +2T_{i+1,j} - 2T_{i,j+1} + T_{i+1,j+1} + T_{i+1,j-1}\right),\\
c_5^S &= \frac{1}{8h^2}\left(T_{i-1,j+1} + T_{i-1,j-1} - 2T_{i-1,j} + 2T_{i,j-1} - 4T_{i,j}\right.\\
&\qquad \left. +2T_{i,j+1} - 2T_{i+1,j} + T_{i+1,j+1} + T_{i+1,j-1}\right),\\
c_7^S &= \frac{1}{8h}\left(2T_{i+1,j} + T_{i+1,j+1} + T_{i+1,j-1} - 2T_{i-1,j} - T_{i-1,j+1} - T_{i-1,j-1}\right),\\
c_8^S &= \frac{1}{8h}\left(2T_{i,j+1} + T_{i-1,j+1} + T_{i+1,j+1} - 2T_{i,j-1} - T_{i-1,j-1} - T_{i+1,j-1}\right).
\end{aligned} \tag{2.10}$$

These are second-order accurate approximations of T_{xx}, T_{yy}, T_x, T_y respectively. This is equivalent to

$$\begin{aligned}
c_4^S &= c_4^V + c_1^V\frac{1}{2}h^2, \qquad c_5^S = c_5^V + c_1^V\frac{1}{2}h^2,\\
c_7^S &= c_7^V + c_3^V\frac{1}{2}h^2, \qquad c_8^S = c_8^V + c_2^V\frac{1}{2}h^2,
\end{aligned}$$

where the superscript S denotes symmetric. When using these coefficients in the bi-quadratic interpolation they do not exactly yield all nodal values for the given locations. The locations of r, l, u, d are based on the field line going through the point i, j, a first estimate is to apply a single step in the direction of the field line. With s the coordinate in field line direction, n the coordinate normal to it and with Δs and Δn the steps in both directions, and defining $\mathbf{b} = (b_1, b_2)^T$, $\mathbf{b}_\perp = (-b_2, b_1)^T$, the locations are given by

$$\begin{aligned}
(x_r, y_r) &= \mathbf{b}^T\Delta s, \qquad (x_l, y_l) = -\mathbf{b}^T\Delta s,\\
(x_u, y_u) &= \mathbf{b}_\perp\Delta n, \qquad (x_d, y_d) = -\mathbf{b}_\perp\Delta n.
\end{aligned} \tag{2.11}$$

Now we apply these coordinates (2.11) to construct discrete schemes in s, n-coordinates for the individual parts $\mathcal{A}_1$,$\mathcal{A}_2$,$\mathcal{A}_3$ and $\mathcal{A}_4$.

Accuracy analysis

In the previous section we established two sets of coefficients for a bi-quadratic interpolation scheme. The following analysis holds for a general set of these coefficients, provided the coefficients are at least second-order accurate approximations of the differential terms given by (2.9). The superscripts of the coefficients denote the respective variables that are interpolated. We remark that although the accuracy requirement holds for the sum $\mathcal{A}_1 + \mathcal{A}_2 + \mathcal{A}_3 + \mathcal{A}_4$, we choose to impose it on $\mathcal{A}_1$,$\mathcal{A}_2$,$\mathcal{A}_3$ and $\mathcal{A}_4$ individually because we wish to identify the specific terms that cause numerical issues. For the approximation of $\mathcal{A}_4$ we have the following expression:

$$\mathcal{A}_4 \approx \frac{D_{\parallel_r} - D_{\parallel_l}}{2\Delta s}\frac{T_r - T_l}{2\Delta s} + \frac{D_{\perp_u} - D_{\perp_d}}{2\Delta n}\frac{T_u - T_d}{2\Delta n}. \tag{2.12}$$

To verify that this scheme approximates part $\mathcal{A}_4$ second-order accurately we substitute the interpolation functions into equation (2.12) and we collect the coefficients for zeroth and first-order terms of h. Noting that $x_{r,l,u,d}, y_{r,l,u,d}, s, n$ are of order h we get

$$0^{th}\text{-order: } \frac{1}{4\Delta s^2}\left(c_7^{D_\parallel}(x_r - x_l) + c_8^{D_\parallel}(y_r - y_l)\right)\left(c_7^{T}(x_r - x_l) + c_8^{T}(y_r - y_l)\right),$$
$$\frac{1}{4\Delta n^2}\left(c_7^{D_\perp}(x_u - x_d) + c_8^{D_\perp}(y_u - y_d)\right)\left(c_7^{T}(x_u - x_d) + c_8^{T}(y_u - y_d)\right),$$

1^{st}-order:

$$\frac{1}{4\Delta s^2}\left(c_7^{D_\parallel}(x_r - x_l) + c_8^{D_\parallel}(y_r - y_l)\right)$$
$$\left(c_4^T\left(x_r^2 - x_l^2\right) + c_5^T\left(y_r^2 - y_l^2\right) + c_6^T\left(x_r y_r - x_l y_l\right)\right),$$
$$\frac{1}{4\Delta n^2}\left(c_7^{D_\perp}(x_u - x_d) + c_8^{D_\perp}(y_u - y_d)\right)$$
$$\left(c_4^T\left(x_u^2 - x_d^2\right) + c_5^T\left(y_u^2 - y_d^2\right) + c_6^T\left(x_u y_d - x_u y_d\right)\right).$$

Now the zeroth-order expression must be equal to $\mathcal{A}_4$ and the first-order expression must be zero. The requirements that can be distilled from this are

$$(x_r - x_l)^2 = 4b_1^2\Delta s^2, \quad (y_r - y_l)^2 = 4b_2^2\Delta s^2,$$
$$(x_r - x_l)(y_r - y_l) = 4b_1 b_2 \Delta s^2,$$
$$(x_u - x_d)^2 = 4b_2^2\Delta n^2, \quad (y_u - y_d)^2 = 4b_1^2\Delta n^2,$$
$$(x_u - x_d)(y_u - y_d) = -4b_1 b_2 \Delta n^2,$$
$$x_{r,u}^2 - x_{l,d}^2 = 0, \quad y_{r,u}^2 - y_{l,d}^2 = 0, \quad x_{r,u}y_{r,u} - x_{l,d}y_{l,d} = 0.$$

This holds for the locations given by equation (2.11). From this it appears that the term $\mathcal{A}_4$ can be approximated with second-order accuracy.
For the terms $\mathcal{A}_3, \mathcal{A}_2, \mathcal{A}_1$ we apply the following finite-difference formulae

$$\mathcal{A}_3 \approx D_\parallel \frac{T_r - 2T_c + T_l}{\Delta s^2} + D_\perp \frac{T_u - 2T_c + T_d}{\Delta n^2}, \tag{2.13}$$
$$\mathcal{A}_2 \approx \left(D_\parallel - D_\perp\right)\left(-b_2\frac{b_{1_u} - b_{1_d}}{2\Delta n} + b_1\frac{b_{2_u} - b_{2_d}}{2\Delta n}\right)\frac{T_r - T_l}{2\Delta s}, \tag{2.14}$$
$$\mathcal{A}_1 \approx -\left(D_\parallel - D_\perp\right)\left(-b_1\frac{b_{2_r} - b_{2_l}}{2\Delta s} + b_2\frac{b_{1_r} - b_{1_l}}{2\Delta s}\right)\frac{T_u - T_d}{2\Delta n}. \tag{2.15}$$

Following a similar logic as for $\mathcal{A}_4$, substituting the interpolation values in equations (2.13), (2.14), (2.15) and collecting terms of equal order in h gives second-order accuracy for all terms. We call this method *aligned Vandermonde* or *aligned symmetric* depending on the coefficients. In practice we decrease Δs and Δn with increasing anisotropy, and we may simply and safely take $\Delta s = \Delta n$. The construction of the linear operator is described in appendix C.

2.2.6 *Curvature terms*

The aligned schemes presented above assume that the direction does not change from the interpolation point l up to the interpolation point r, and likewise from interpolation point u to point d. Now we consider a numerical treatment of the terms $b_{1_s}, b_{1_n}, b_{2_s}, b_{2_n}$ in equation (2.5) based on field line curvature, so we explicitly allow for curvature to approximate these terms. Given an interpolation function for b_1 and b_2 within the stencil area we can apply tracing to find the points r, l, u, d, depicted in figure 2.3. We go from the center point to the interpolation points r, l, u, d by applying the (second-order accurate) modified Euler scheme (Heun):

$$
\begin{aligned}
&\text{tangential direction:}\\
&\mathbf{x}_k^* = \mathbf{x}_{k-1} \pm \Delta s^* \mathbf{b}(x_{k-1}, y_{k-1}),\\
&\mathbf{x}_k = \mathbf{x}_{k-1} \pm \frac{1}{2}\Delta s^* \left(\mathbf{b}(x_{k-1}, y_{k-1}) + \mathbf{b}(x_k^*, y_k^*)\right), \quad k = 1, \cdots K,\\
&\text{normal direction:}\\
&\mathbf{x}_k^* = \mathbf{x}_{k-1} \pm \Delta n^* \mathbf{b}_\perp(x_{k-1}, y_{k-1}),\\
&\mathbf{x}_k = \mathbf{x}_{k-1} \pm \frac{1}{2}\Delta n^* \left(\mathbf{b}_\perp(x_{k-1}, y_{k-1}) + \mathbf{b}_\perp(x_k^*, y_k^*)\right), \quad k = 1, \cdots K,
\end{aligned}
$$

where K is the number of sub-steps $\Delta s^*, \Delta n^*$, and where $x_0 = y_0 = 0$ (see figure 2.4). The values $\Delta s = K\,\Delta s^*$ and $\Delta n = K\,\Delta n^*$ are used to approximate the derivatives in the curvature terms with

$$
\frac{\partial b_1}{\partial s} \approx \frac{b_{1_r} - b_{1_l}}{\Delta s},
$$

and similarly for the other derivatives. Repeatedly stepping in s, n-direction and apply-

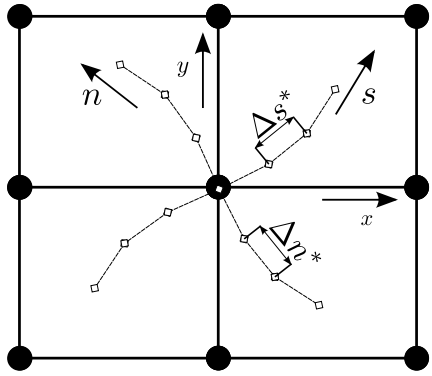

Figure 2.4: Approximate track of field line and perpendicular curve.

ing the interpolation of $\mathbf{b}$ increases the computational cost. The benefit is that we can easily control the accuracy with which we follow the field line, simply by changing the number of tracing steps.

Bi-linear interpolation per quadrant

For the aligned method we use a bi-quadratic interpolation scheme where we apply all nine stencil points for the determination of the values in aligned stencil points. Here we briefly consider a quadrant-wise bi-linear interpolation with the location of the central node set to the center point (i, j). This gives

$$
\begin{aligned}
&T_{l,r,u,d} = a x_{r,l,u,d} y_{r,l,u,d} + b x_{r,l,u,d} + c y_{r,l,u,d} + d,\\
T_r: \quad & d = T_{i,j},\ c = \frac{T_{i,j+1} - T_{i,j}}{y_{i,j+1} - y_{i,j}},\ b = \frac{T_{i+1,j} - T_{i,j}}{x_{i+1,j} - x_{i,j}},\\
&\qquad a = \frac{T_{i+1,j+1} - b(x_{i+1,j} - x_{i,j}) - c(y_{i,j+1} - y_{i,j}) - d}{(x_{i+1,j} - x_{i,j})(y_{i,j+1} - y_{i,j})},\\
T_l: \quad & d = T_{i,j},\ c = \frac{T_{i,j} - T_{i,j-1}}{y_{i,j} - y_{i,j-1}},\ b = \frac{T_{i,j} - T_{i-1,j}}{x_{i,j} - x_{i-1,j}},\\
&\qquad a = \frac{T_{i-1,j-1} - b(x_{i,j} - x_{i-1,j}) - c(y_{i,j} - y_{i,j-1}) - d}{(x_{i,j} - x_{i-1,j})(y_{i,j} - y_{i,j-1})},\\
T_u: \quad & d = T_{i,j},\ c = \frac{T_{i,j+1} - T_{i,j}}{y_{i,j+1} - y_{i,j}},\ b = \frac{T_{i,j} - T_{i-1,j}}{x_{i,j} - x_{i-1,j}},\\
&\qquad a = -\frac{T_{i-1,j+1} - b(x_{i,j} - x_{i-1,j}) - c(y_{i,j+1} - y_{i,j}) - d}{(x_{i,j} - x_{i-1,j})(y_{i,j+1} - y_{i,j})},\\
T_d: \quad & d = T_{i,j},\ c = \frac{T_{i,j} - T_{i,j-1}}{y_{i,j} - y_{i,j-1}},\ b = \frac{T_{i+1,j} - T_{i,j}}{x_{i+1,j} - x_{i,j}},\\
&\qquad a = -\frac{T_{i+1,j-1} - b(x_{i+1,j} - x_{i,j}) - c(y_{i,j} - y_{i,j-1}) - d}{(x_{i+1,j} - x_{i,j})(y_{i,j} - y_{i,j-1})}.
\end{aligned}
$$

Just considering the differentiation of the second-order terms in parallel direction we get

$$
\begin{aligned}
T_{ss} \approx \frac{1}{h^2} \big[& -2T_{i,j}(b_1 + b_2 - b_1 b_2) + T_{i+1,j}(b_1 - b_1 b_2) + T_{i-1,j}(b_1 - b_1 b_2)\\
& + T_{i,j+1}(b_2 - b_1 b_2) + T_{i,j-1}(b_2 - b_1 b_2) + (T_{i+1,j+1} + T_{i-1,j-1}) b_1 b_2 \big].
\end{aligned}
$$

Writing out the fourth-order Taylor expansion of the term T_{ss}, assuming constant diffusion coefficients, gives

$$
T_{ss} = b_1 T_{xx} + b_2 T_{yy} + 2 b_1 b_2 T_{xy} + \mathcal{O}\left(h^2\right).
$$

This is not consistent with the analytic form; we have b_1 and b_2 instead of b_1^2 and b_2^2 respectively. This inconsistency is due to the fact that bi-linear interpolation is used and so the directions are only approximated with first-order accuracy. The downside of quadrant-wise bi-linear interpolation is that one has to track in which quadrant the stencil point is to apply the appropriate interpolation.

2.2.7 *Exact differentiation after interpolation*

We can also find a direct approximation of the various spatial derivatives involved in the anisotropic diffusion operator, by writing the interpolation function (2.6) in terms

of s, n and by taking the appropriate derivatives of this rewritten function. Then, the interpolation functions for b_1 and b_2 need to be applied to find the final form of the approximation. We use the non-conservative form

$$T_t = D_{\parallel} v_{ss}^T + D_{\perp} v_{nn}^T + v_s^{D_{\parallel}} v_s^T + v_n^{D_{\perp}} v_n^T + \left(D_{\parallel} - D_{\perp}\right)\left(S v_s^T - N v_n^T\right),$$

where the terms with v represent the bi-quadratic interpolation functions of the quantities denoted with the superscript, the derivatives are denoted with the subscript i.e. v_s^T is the $s-$derivative of the interpolation function for the temperature. The first-order differentials are written as

$$v_s^{D_{\parallel}} v_s^T + v_n^{D_{\perp}} v_n^T = (c_7^T b_1 + c_8^T b_2)(c_7^{D_{\parallel}} b_1 + c_8^{D_{\parallel}} b_2) + (-c_7^T b_2 + c_8^T b_1)(-c_7^{D_{\perp}} b_2 + c_8^{D_{\perp}} b_1).$$

The diffusive terms are given by

$$D_{\parallel} v_{ss}^T + D_{\perp} v_{nn}^T = 2D_{\parallel}\left(c_4 b_1^2 + c_5 b_2^2 + c_6 b_1 b_2\right) + 2D_{\perp}\left(c_4 b_2^2 + c_5 b_1^2 - c_6 b_1 b_2\right),$$

and the curvature-dependent terms by

$$\begin{aligned}
&\left(D_{\parallel} - D_{\perp}\right)\left(S v_s^T - N v_n^T\right) = \\
&2D_{\parallel}\left[c_7\left(b_1 c_7^{b_1} + \frac{1}{2} b_1 c_8^{b_2} + \frac{1}{2} b_2 c_8^{b_1}\right) + c_8\left(b_2 c_8^{b_2} + \frac{1}{2} b_2 c_7^{b_1} + \frac{1}{2} b_1 c_7^{b_2}\right)\right] + \\
&2D_{\perp}\left[c_7\left(b_2 c_7^{b_2} - \frac{1}{2} b_1 c_8^{b_2} - \frac{1}{2} b_2 c_8^{b_1}\right) + c_8\left(b_1 c_8^{b_1} - \frac{1}{2} b_2 c_7^{b_1} - \frac{1}{2} b_1 c_7^{b_2}\right)\right].
\end{aligned}$$

The aligned finite-difference scheme is identical to the interpolation scheme for $\Delta s, \Delta n \rightarrow 0$, see appendix D.

We call these methods *interp. Vandermonde* or *interp. symmetric*, depending on the coefficients that are used. Summarizing, we apply the following methods

- *asymmetric scheme, Günter et al.*,
- *symmetric scheme, Günter et al.*,
- *current work, aligned Vandermonde/symmetric scheme*,
- *current work, interpolated Vandermonde/symmetric scheme*.

2.3 Linear stability

The Lax equivalence theorem states that *for a consistent finite difference method for a well-posed linear initial value problem, the method is convergent if and only if it is stable.* Hence, an important aspect of numerical analysis is the study of numerical stability.

It is important for the application of the different schemes to know how the numerical stability depends on both the anisotropy and the angle of rotation. The diffusion equation is absolutely stable which means that *for any two initial conditions, the difference*

between the two solutions dissappears for $t \to \infty$, see e.g. van Kan et al. [115]. This property imposes a requirement on the linear operator, namely that the real parts of the eigenvalues are negative. The stability referred to in the Lax equivalence theorem is the Lax-Richtmyer stability, which says that a norm of the matrix used in the iteration is smaller than or equal to unity. The matrix, which we call G is defined by

$$T^{n+1} = G(\Delta t \mathcal{L})T^n + f,$$

where G depends on the time integration method that is used. Now the solution is stable if all eigenvalues of G are smaller than one in absolute sense, see e.g. van Kan et al. [115]. Clearly, we only need to look at the eigenvalue with the largest absolute value, which is the spectral radius of the matrix. So a suitable matrix norm of G is the spectral radius ρ. For the θ time-integration scheme the amplification matrix is given by

$$G = (\mathcal{I} - \theta\Delta t\mathcal{L})^{-1}(\mathcal{I} + (1-\theta)\Delta t\mathcal{L}), \quad \theta \in [0,1]. \tag{2.16}$$

Inserting eigenvalues of $\mathcal{L}$ in equation 2.16 leads to the eigenvalues of the amplification matrix G. Since the resulting function for G monotonously decreases starting from the marginally stable value $G = 1$ we insert the largest eigenvalue in absolute sense to find the stability requirement. The stability requirement is then written as

$$\Delta t < \frac{K}{\rho}, \tag{2.17}$$

where K is specific for the time integration scheme and in this case depends on the value for θ. The K-dependency on θ is found by substituting the spectral radius into equation (2.16) for the amplification matrix, and by requiring stability:

$$|G| = \left| \frac{1 \pm (1-\theta)\Delta t\rho}{1 \pm \theta\Delta t\rho} \right| \leq 1.$$

For $1 \geq \theta \geq 0.5$ the time integration is unconditionally stable. For K we find

$$K = \frac{2}{(1-2\theta)}, \quad 0 \leq \theta < 0.5. \tag{2.18}$$

This yields the following stability requirement for $0 \leq \theta < 0.5$:

$$\Delta t \leq \frac{2}{\rho(1-2\theta)}.$$

Now we need a description for the spectral radius. An upper bound for the spectral radius of the amplification matrix is given by

$$\rho(\mathbf{G}) = \lim_{k\to\infty} \|\mathbf{G}^k\|^{1/k}, \tag{2.19}$$

i.e. taking a large value of k will give an approximation of the spectral radius. In our case we would like to formulate some stability requirements which depend on problem parameters such as angle of rotation and level of anisotropy and so the spectral radius needs to be formulated generically, preferably in analytical form. To obtain this for general angle of misalignment and for a general set of parameters of the time integration

scheme is intractable. A less accurate but very fast approach is the application of the Gershgorin circle theorem. For each matrix row i we have

$$|\lambda - g_{ii}| \leq \sum_{j \neq i} |g_{ij}| = R_i,$$

where g_{ij} is a matrix element of G, i.e. for each row the bounds of the corresponding eigenvalues can be found and subsequently an upper bound for the in absolute value largest eigenvalue can be determined. With this theorem, the bound for the spectral radius can be found quickly for different parameters. Doing so we can find an estimate for the stability requirement for a given range of grid resolutions and subsequently we can relate the maximum time step to the grid resolution and the values of the diffusion coefficients for a given value of θ.

To get a rough estimate of the spectral value we consider the two-dimensional anisotropic diffusion equation with constant anisotropic coefficients and zero misalignment, given by

$$T_t = D_{\parallel} T_{xx} + D_{\perp} T_{yy} + f.$$

Assuming that the linear operators for T_{xx}, T_{yy} are symmetric and commutative and that we have uniform rectangular grids, we can add the eigenvalues. Using the Gershgorin circle theorem as the most conservative estimate for the spectral radius, the time step restriction for the symmetric and the asymmetric scheme is given by

$$\rho = \frac{1}{h^2}\left[4(D_{\parallel} + D_{\perp})\right], \quad \Delta t \leq \frac{h^2 K}{4(D_{\parallel} + D_{\perp})}, \tag{2.20}$$

where K depends on the time integration method, and is given by equation (2.18) for the θ-method. This implies that for extremely anisotropic problems, explicit methods are completely unsuitable if both the parallel and the perpendicular diffusion have to be resolved.

To get an idea of the effect of grid misalignment we consider the anisotropic diffusion equation with the misalignment angle α represented by $\cos\alpha = b_1, \sin\alpha = b_2$,

$$T_t = (D_{\parallel} b_1^2 + D_{\perp} b_2^2) T_{xx} + (D_{\parallel} b_2^2 + D_{\perp} b_1^2) T_{yy} + 2(D_{\parallel} - D_{\perp}) b_1 b_2 T_{xy} + f.$$

We assume symmetry and commutation for the linear operators $\mathcal{L}_{xx}, \mathcal{L}_{yy}, \mathcal{L}_{xy}$. This is only true if $\mathcal{L}_{xy}$ can be written as a linear combination of powers of $\mathcal{L}_{xx}$ and as a linear combination of powers of $\mathcal{L}_{yy}$, which is the case for instance for the symmetric scheme. Since $\mathcal{L}_{xy}$ is symmetric with zero valued diagonals we know that its trace is zero, and so the eigenvalues also sum to zero. Now since $\mathcal{L}_{xy}$ is symmetric there is a full set of real eigenvalues, which implies that all negative eigenvalues have a positive counterpart. Assuming we can use the same formulation for the spectral radius of $\mathcal{L}_{xy}$ as for $\mathcal{L}_{xx}$ and $\mathcal{L}_{yy}$ and using the Gershgorin circle theorem we have the following time step restriction for $0 \leq \theta < \frac{1}{2}$ for the symmetric and the asymmetric scheme

$$\rho = \frac{1}{h^2}\left[4(D_{\parallel} + D_{\perp}) + 2(D_{\parallel} - D_{\perp}) b_1 b_2\right], \quad \Delta t \leq \frac{h^2 K}{4(D_{\parallel} + D_{\perp}) + 2(D_{\parallel} - D_{\perp}) b_1 b_2},$$

with $K = \frac{2}{(1-2\theta)}$, $0 \leq \theta < \frac{1}{2}$.

Finally we apply the Von Neumann stability analysis for the θ method, see appendix E for details, yielding

$$\Delta t \leq \frac{h^2 K}{4(D_{\parallel} + D_{\perp})}, \quad \text{for} \quad 0 \leq \theta < \frac{1}{2}.$$

This is slightly less stringent than the criteria resulting from the Gershgorin circle theorem, and it is independent of the angle of misalignment. Concluding, we can say that for constant anisotropy and constant angle of misalignment the symmetric and asymmetric method remain unconditionally stable for $\theta \geq \frac{1}{2}$, regardless of the level of anisotropy. For $0 \leq \theta < \frac{1}{2}$ the time step is inversely proportional to the diffusion coefficients.

Closely related to the analysis above is the determination of the condition number κ of the linear operator. The condition number is a measure for the sensitivity of the system $Ax = b$ to variations in b, or in terms of perturbations δ and ϵ for x and b respectively,

$$\frac{||\delta||/||x||}{||\epsilon||/||b||} \leq \kappa$$

For normal matrices it holds

$$\kappa = \frac{|\lambda|_{max}}{|\lambda|_{min}}.$$

If there are closed field lines and $\mathbf{b} \cdot \nabla T \rightarrow 0$ only the perpendicular part plays a role for the minimal eigenvalue and so

$$\kappa \approx \frac{\rho}{\pi^2 D_{\perp}}, \tag{2.21}$$

where we take $\pi^2 D_{\perp}$ as the minimum eigenvalue of the elliptic operator, assuming periodic boundary conditions, see Haberman [55].

In case of the above example with constant diffusion coefficients and constant angle of misalignment the condition number is estimated by

$$\kappa \approx \frac{1}{h^2} \frac{4(D_{\parallel} + D_{\perp}) + (D_{\parallel} - D_{\perp}) b_1 b_2}{|\lambda|_{min}}.$$

An estimate of the condition number and the stability requirement for the more general case of varying field lines is not tractable since the unit direction vector $[b_1, b_2]^T$ is problem dependent. Instead we take $|\lambda|_{min} = \pi^2(D_{\parallel} + D_{\perp})$, see Haberman [55]. This shows that the condition number and the numerical stability depend on the specific problem. The condition number for linear operators approximating anisotropic diffusion is scaled with the ratio between diffusion coefficients *only if* there are closed field lines present in the domain. This makes iterative solution procedures intractable for closed field line problems with high levels of anisotropy.

2.4 Numerical results

In this section we show the results for several steady test cases. For all the test cases, we have $\frac{\partial T}{\partial t} = 0$ and the source function f is such that it produces the exact solution which is given for each test case. We use Dirichlet boundary conditions with the boundary value determined by the assumed solution. As we assume that the time derivative is zero, in all the test cases we may take $\mathbf{b} \cdot \nabla T = 0$. In the test case descriptions, the angle of misalignment α refers to the angle of the principal axes of diffusion with respect to the coordinate axes. The number of grid points is given by $N \times N$.

2.4.1 *Constant angle of misalignment*

As an initial test we consider a simple steady anisotropic diffusion problem. The imposed exact solution reads:

$$T(x,y) = xy\left[\sin(\pi x)\sin(\pi y)\right]^{\gamma}, \quad x,y \in [0,1],$$

where γ is large and where the angle of misalignment α $\left(\mathbf{b} = [\cos\alpha, \sin\alpha]^T\right)$ is set to a constant value, i.e. $\mathbf{D} = (D_{\parallel} - D_{\perp})\mathbf{b}\mathbf{b}^T + D_{\perp}\mathcal{I} =$ constant. The solution simulates a temperature peak. Computational results for this test case are given in figure 2.5. The

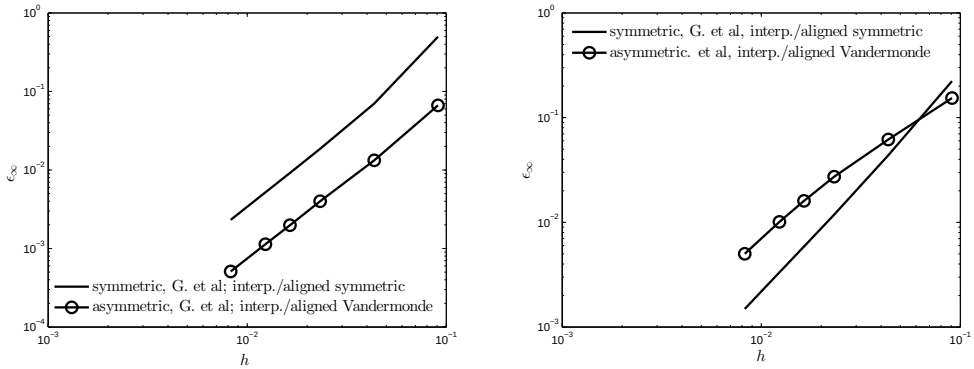

(a) (b)

Figure 2.5: Error ϵ_∞ for test cases with spatially constant angles of misalignment, $\gamma = 10$, the level of anisotropy $\varsigma = 10^9$, at varying mesh width, (a) $\alpha = 5°$, (b) $\alpha = 30°$. In the plots all symmetric schemes overlap and likewise do all asymmetric schemes.

error norm is defined by

$$\epsilon_\infty = \frac{|\tilde{T} - T|_{max}}{T_{max}},$$

where $\tilde{T}$ is the approximate temperature. It is clear from the figure that the symmetric schemes conserve the order of accuracy independent of the anisotropy and angle of misalignment. The co-located schemes are only slightly less accurate than the staggered schemes. For larger values of the anisotropy ς, the asymmetric schemes are less than second-order convergent on coarse grids, but they regain second-order convergence on finer grids.

2.4.2 *Varying angle of misalignment*

Again the problem is considered on a square domain, this time described by $-0.5 \leq x, y \leq 0.5$. The following steady-state solution is assumed on the domain

$$T(x,y) = 1 - \left[(x-x_c)^2 + (y-y_c)^2\right]^{3/2},$$

with $x_c = y_c = 0$ for the closed field line case and $x_c = y_c = 0.5$ for the open field line case. The direction of parallel diffusion, and the diffusion tensor are given by

$$\mathbf{b} = \frac{1}{\sqrt{(x-x_c)^2 + (y-y_c)^2}} \begin{pmatrix} -(y-y_c) \\ x - x_c \end{pmatrix}, \quad \mathbf{D} = (D_\parallel - D_\perp)\mathbf{b}\mathbf{b}^T + D_\perp \mathcal{I}, \tag{2.22}$$

where $D_\parallel$ and $D_\perp$ are spatially constant. Note that both $\nabla \cdot \mathbf{b}$ and $\mathbf{b} \cdot \nabla T$ are zero, this means that the term $\mathcal{A}_2$ comes into play only due to numerical errors, term $\mathcal{A}_4$ is exactly zero since $\nabla D_\parallel$, $\nabla D_\perp$ are zero. Test case 2 stresses terms $\mathcal{A}_1$ and $\mathcal{A}_3$, with added contribution due to numerical errors in term $\mathcal{A}_2$.

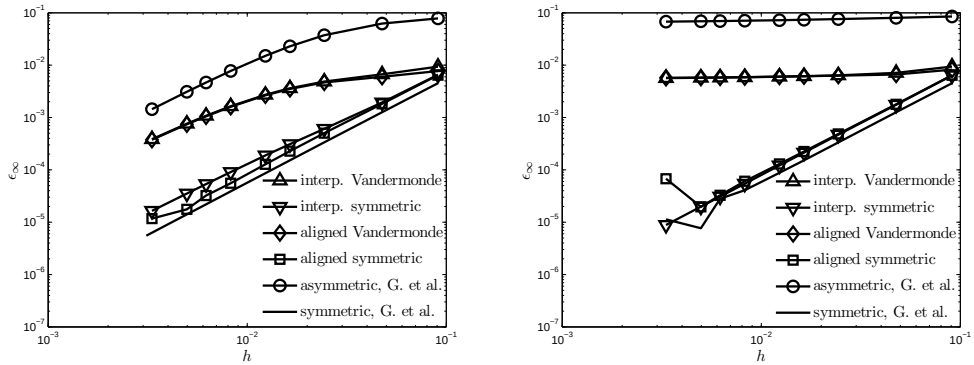

Figure 2.6: Error ϵ_∞ for test cases with varying misalignment, (a) $\varsigma = 10^3$, (b) $\varsigma = 10^9$.

We study the accuracy of the various schemes for two anisotropic cases, one being extremely anisotropic, $\varsigma = 10^9$, both with $x_c = y_c = 0$. We observe from figure 2.6 that for the extremely anisotropic case our aligned symmetric scheme and our interpolated symmetric scheme preserve their second-order of accuracy. All other schemes fail completely; they are all inconsistent for the $\varsigma = 10^9$ test case.
A detail to be observed from figure 2.6 is that for extremely high levels of anisotropy the symmetric scheme of Günter et al. and the current symmetric schemes show a wiggle in the error convergence. This is partly caused by the fact that the linear operator becomes ill-conditioned for $h \to 0$ with a condition number of order 10^{13} and partly by the fact that at the origin $\mathbf{b}$ is undefined for this particular test problem. Shifting the origin by a small value ϵ of order 10^{-16} removes the wiggle. Günter et al. [53] had problems with number representation for a fourth-order mimetic finite-difference scheme. They resolved this by increasing the number representation accuracy. Further,

it can be shown that the analytic problem becomes ill-posed for $\varsigma \to \infty$ (see Degond et al. [30]). The asymmetric scheme does not suffer from number representation errors here. However, this is probably due to the solution not being close enough to the limit solution.

Finally, in figure 2.7 we make a more extensive study of the behavior of the different schemes at varying anisotropy. Here the interpolated symmetric scheme and aligned symmetric scheme perform better than the symmetric scheme by Günter et al.; their errors do not increase with increasing anisotropy above $\varsigma = 10^9$.

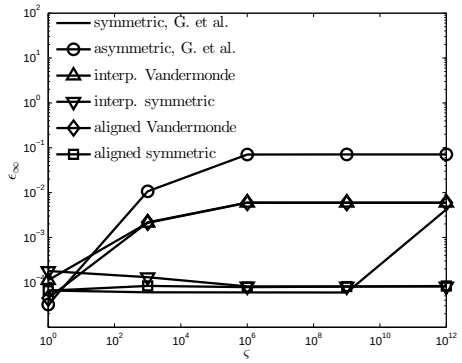

Figure 2.7: ϵ_∞-error norm versus the anisotropy ς for $N = 100$.

The aligned scheme and the interpolation scheme perform equally well as the symmetric scheme by Günter et al. in terms of anisotropy independence of the error, see figure 2.7. Starting from an anisotropy ratio of $\varsigma = 10^9$ the symmetric scheme by Günter et al. begins to deteriorate. This is most likely due to ill-conditioning of the linear operator. The fact that the symmetric scheme by Günter et al. suffers from ill-conditioning for extreme values of the level of anisotropy is an indication that the parallel and perpendicular components are numerically strictly separated. For $\varsigma \to \infty$ equation (1.1) in combination with Dirichlet and Neumann boundary conditions becomes ill-posed due to the fact that $\nabla \cdot (D_\parallel \mathbf{b} \cdot \nabla T \mathbf{b}) = 0$ has infinitely many solutions. The fact that the asymmetric scheme by Günter et al. does not suffer from ill-conditioning of the linear operator is an indication that for $\varsigma \to \infty$ the approximation does not approach the limit solution of (1.1).
Setting $D_\parallel$ to zero enforces that $\mathbf{q}_\parallel = 0$ in the $t \to \infty$ limit, this restores the accuracy of the aligned methods. The aligned Vandermonde and the interpolated Vandermonde method are now close to second-order accuracy. The order of accuracy for the aligned symmetric method and the interpolated symmetric method are slightly decreased below second order.

Running the test case with $x_c = y_c = 0.5$ gives second-order convergence for all schemes. The qualitative difference between $x_c = y_c = 0$ and $x_c = y_c = 0.5$ is the presence of a singular point in the former case, a point where the direction vector $\mathbf{b}$ is undefined and over which the vector changes discontinuously.

We suspect that the accuracy of the symmetric scheme by Günter et al. has some

dependency on the symmetry of the problem, this will be investigated in section 2.4.4. For the following four test cases we dismiss the asymmetric scheme by Günter et al. and the aligned and interpolated schemes with Vandermonde coefficients, since for this particular test case they show near zeroth-order convergence for high values of anisotropy.

2.4.3 *Perpendicular numerical diffusion*

Sovinec et al. [109] devised a test to directly compare the perpendicular numerical diffusion to the actual numerical diffusion. This test case is also considered by Günter et al. [54] and Sharma et al. [107]. The exact solution and the forcing function are given by

$$T = \psi, \quad f = 2\pi^2\psi, \quad \psi = \cos(\pi x)\cos(\pi y), \quad x, y \in [-0.5, 0.5]. \tag{2.23}$$

The error in the perpendicular diffusion is indicated by $|T(0,0)^{-1} - 1|$. We use homogeneous Dirichlet boundary conditions. The field lines are tangential to the contours of constant temperature, i.e.

$$\mathbf{b} = \frac{1}{\sqrt{\psi_x^2 + \psi_y^2}} \begin{pmatrix} -\psi_y \\ \psi_x \end{pmatrix}.$$

In figures 2.8a and 2.8b we see a huge difference between the symmetric scheme by

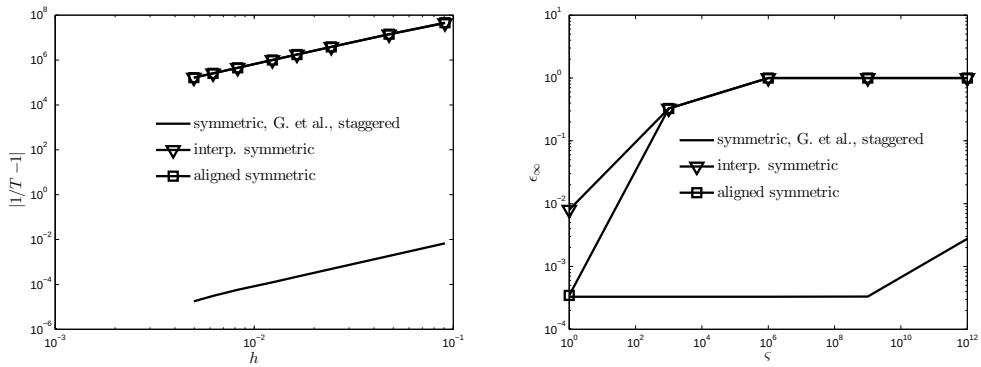

(a) (b)

Figure 2.8: (a) Error in perpendicular diffusion $|T^{-1} - 1|$ with $\varsigma = 10^9$, (b) ϵ_∞-error norm versus the anisotropy ς for $N = 100$.

Günter et al. and our schemes. The error difference is approximately equal to the level of anisotropy ς. Because the numerical approximation goes to zero for higher values of the anisotropy the error growth in figure 2.8b stagnates, i.e. $|\tilde{T} - T|_{max}/T_{max} \to 1$.
To find out which term is causing this difference we replace the approximations for the different terms $\mathcal{A}_{1,2,3,4}$ by the exact values. We find that replacing the approximation for $\mathcal{A}_1$ by the exact value gives the accuracy we also see for the symmetric scheme of Günter et al. For this test case, specifically using the exact value for $\mathcal{F}_1$ in $\mathcal{A}_1$ does

not change the accuracy significantly. This means that the main source of error is the approximation of $T_n = \mathbf{b}_\perp \cdot \nabla T$. Any numerical error in approximating $\mathbf{b}_\perp \cdot \nabla T$ is multiplied by $D_\parallel$. Only the symmetric scheme by Günter et al. with the diffusion tensor values defined exactly on the flux points is able to capture the perpendicular diffusion accurately and practically independent of the level of anisotropy. In realistic scenarios the diffusion tensor itself is an approximation and the diffusion coefficients are dependent on the temperature and so the symmetric scheme will likely deteriorate in accuracy. Note that this affects only the approximation of the diffusion tensor, the gradient of the temperature and the divergence of the flux are still self-adjoint at the discrete level. The effect of temperature dependence of the diffusion coefficients on the accuracy and convergence is shown in section 2.4.5. In the previous test case described in section 2.4.2, we see that the aligned symmetric methods perform similar to the symmetric scheme by Günter et al. An important question is, what causes the difference between these results. First we establish the importance of the singular point. Since we do not have an exact solution in the singular point, we notice that shifting the singular point towards the sides or corners has significant impact on the error magnitude and the error magnitude is less dependent on the level of anisotropy.

Change of domain size

If we decrease the size of the domain and keep the singular point in the center of the domain, the error in approximating the perpendicular diffusion is strongly reduced, see figure 2.9. This indicates that the singular point itself is not the culprit for the

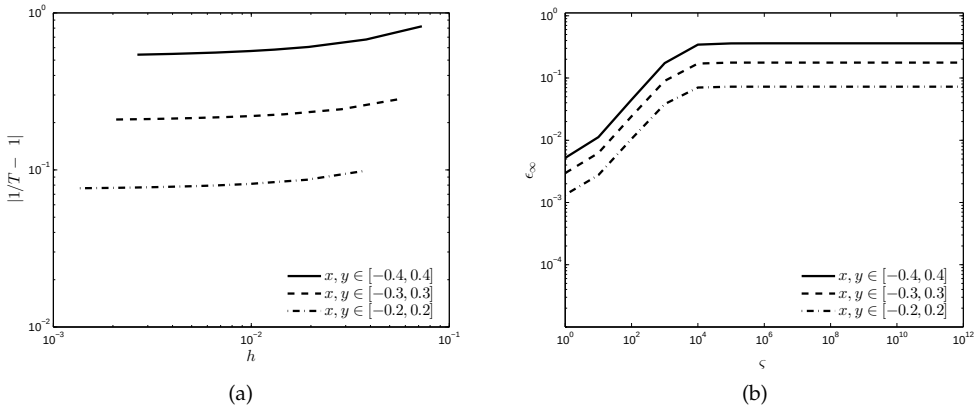

Figure 2.9: (a) Error in perpendicular diffusion,with the aligned symmetric scheme and the interp. symmetric scheme, $\varsigma = 10^9$, (b) ϵ_∞-error norm versus the anisotropy ς for $N = 100$.

anisotropy-dependent error but rather the boundary conditions, or more specifically the behavior of the numerical scheme at exactly the boundary of $x, y \in [-0.5, 0.5]$. If we increase the size of the domain to $x, y \in [-1, 1]$ so it encloses the boundaries of the previous case with $x, y \in [-0.5, 0.5]$, we see that at this inner boundary the temperature does not change smoothly for higher levels of anisotropy, see figure 2.10. For the asymmetric scheme by Günter et al. we also see this non-smooth transition, there is a discontinuous slope at exactly the boundary of $x, y \in [-0.5, 0.5]$.

The loss in order of convergence independent of the domain size does suggest a role for the singular point.

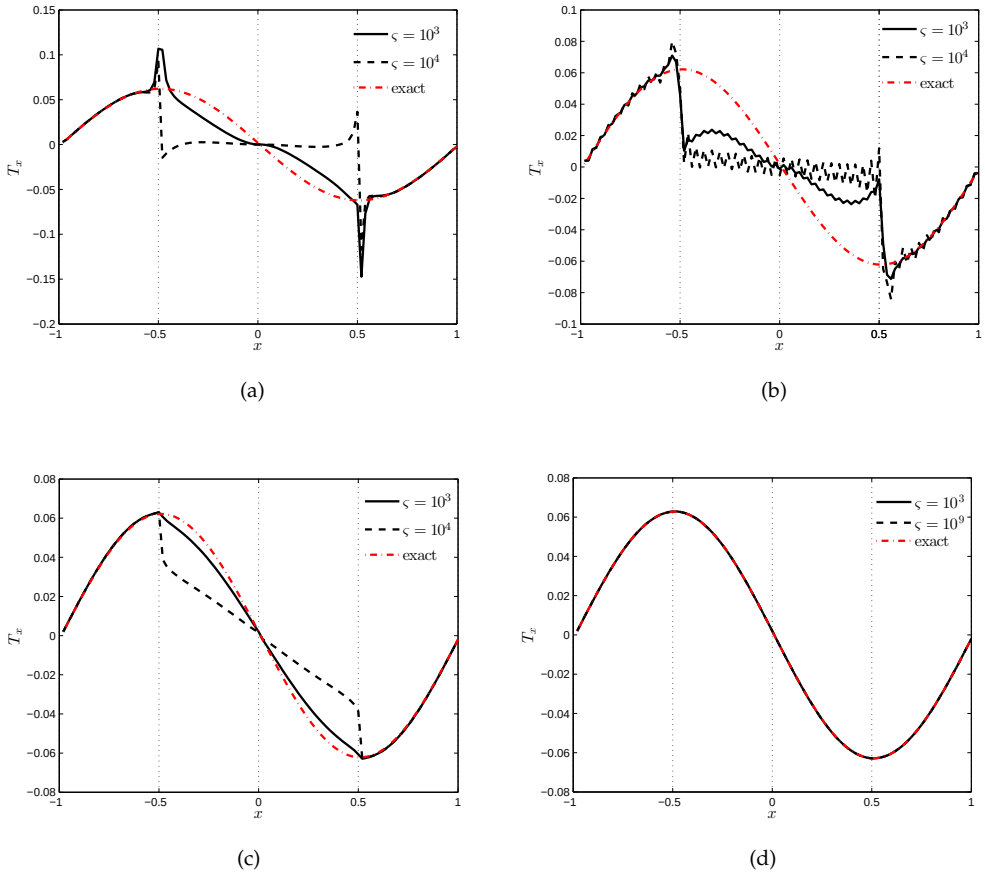

Figure 2.10: Approximate value of $\frac{\partial T}{\partial x}$ over the center line with a 100×100 grid, (a) interp. asymmetric, (b) interp. symmetric, (c) asymmetric Günter et al., (d) symmetric Günter et al.

Change of boundary conditions

We change the boundary conditions from Dirichlet to Neumann to enforce the gradient on the boundary of the domain $x, y \in [-0.5, 0.5]$. We want to implement a Neumann boundary condition for the entire boundary Γ. This requires that the net flux contributions of the boundary must be exactly equal to the source contribution, i.e. $\int_\Gamma \mathbf{q} \cdot \mathbf{n} d\Gamma = \int_\Omega f d\Omega$, where Γ represents the boundary of the surface or volume Ω. The solution is determined up to an additive constant now. Along the boundary we have that the normal direction is perpendicular to the field lines, knowing that $\mathbf{b} \cdot \nabla T = 0$ we have that $\int_\Gamma \mathbf{q} \cdot \mathbf{n} d\Gamma = D_\perp \int_\Gamma \frac{\partial T}{\partial n} d\Gamma$.

We derive the temperature value at the inner point closest to the boundary directly from the flux value and from the values of the adjacent ghost point(s) (found from the exact

temperature distribution (2.23)), see figure 2.11. For the co-located schemes (aligned

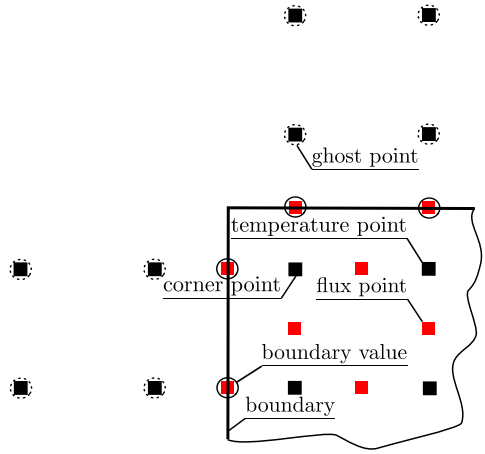

(a)

Figure 2.11: Ghost points for Neumann condition.

symmetric, and interp. symmetric) the flux points are located in the same points as the temperature nodes, and for the semi-staggered schemes midway between the temperature nodes, this slightly affects the approximation of the flux on the edge. We use the following unweighted central differencing scheme to approximate the derivatives at the left and right boundary:

$$\partial_x T = \frac{-T_{i+2,j} + 8T_{i+1,j} - 8T_{i-1,j} + T_{i-2,j}}{12h} + \mathcal{O}(h^4),$$

and similarly for the $y-$derivative applied to the upper and lower boundaries. The Neumann boundary condition is sufficient since the derivatives tangential to the boundaries are zero.

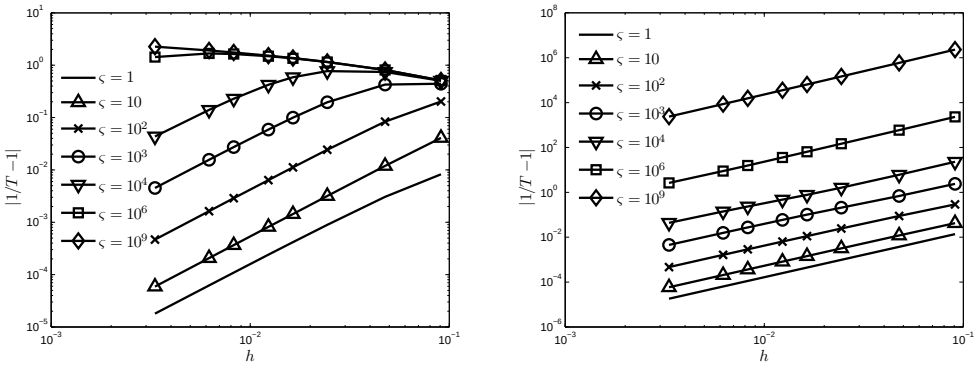

(a) (b)

Figure 2.12: Error in perpendicular diffusion for varying levels of anisotropy for the asymmetric scheme by Günter et al., using (a) Neumann boundary conditions with boundary flux values on primal grid, (b) Dirichlet boundary conditions.

In figure 2.12a we show results for varying levels of anisotropy using Neumann and Dirichlet conditions for the asymmetric scheme. We see that the accuracy of the perpendicular diffusion is significantly improved by using Neumann boundary conditions. We also see that for anisotropy levels starting from $10^3 - 10^4$ there is divergence initially, this is confirmed by a second-order implementation of the Neumann boundary condition. We suspect this is caused by an incorrect implementation of the boundary conditions near the corner points.

2.4.4 *Tilted elliptic temperature distributions*

So far we have used forcing functions that are spatially symmetric. We propose a new test case for extremely anisotropic heterogeneous diffusion that is not symmetric around the coordinate axes and contains mixed open and closed field lines. We apply a forcing function that gives the solution for a tilted elliptic temperature distribution. This distribution has no symmetry axes aligned with the coordinate axes. The first tilted elliptic distribution has no closed field lines. Basically, the field lines go in the same general direction, see figure 2.13a. The exact solution is given by

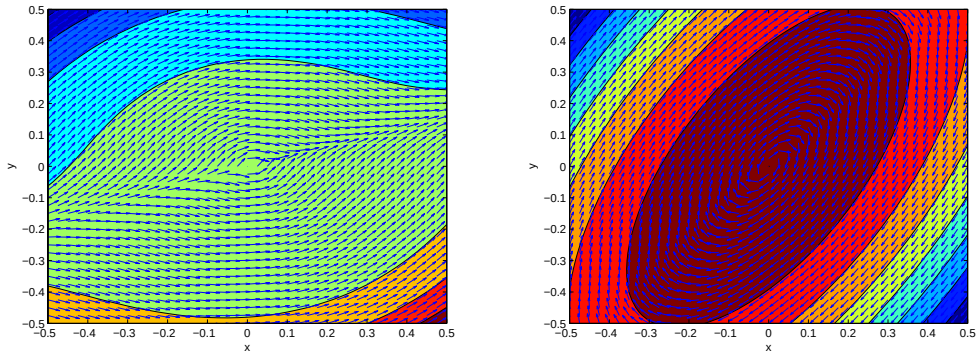

(a) (b)

Figure 2.13: Tilted test cases, field line direction with (a) open field line distribution (2.24), with $a = 25, b = -75$, (b) closed field line distribution (2.25), with $a = 0.15, b = 0.85$.

$$T(x, y) = 1 + (ax + by)(x^2 + y^2)^{3/2}, \qquad x, y \in [-0.5, 0.5], \tag{2.24}$$

with again the field line tangential to the contours;

$$\mathbf{b} = \frac{1}{\sqrt{T_x^2 + T_y^2}} \begin{pmatrix} -T_y \\ T_x \end{pmatrix}.$$

In figure 2.14 we present numerical results. We see that all three schemes considered are very similar in performance, maintaining order of convergence and having similar accuracy. At the origin of the domain both b_1 and b_2 go to zero. So the unit direction vector is undefined there. However, the unit direction vector is continuous in all directions through the origin.

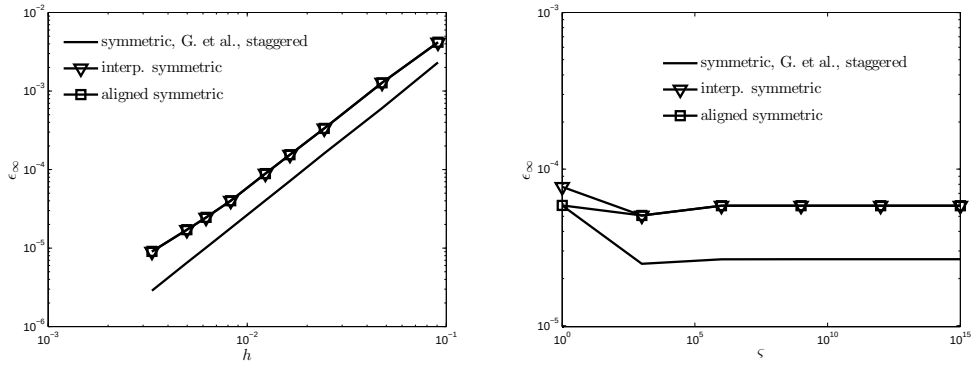

(a) (b)

Figure 2.14: First tilted test case, with $a = 25, b = -75$, (a) ϵ_∞ convergence for $\varsigma = 10^9$, (b) ϵ_∞-error norm versus the anisotropy ς for a 100×100 grid.

The distribution for the second tilted test case is given by

$$T(x,y) = 1 - (a^2(x\cos\theta + y\sin\theta)^2 + b^2(x\sin\theta - y\cos\theta)^2)^{3/2}, \quad x,y \in [-0.5, 0.5], \tag{2.25}$$

with $\mathbf{b}$ as before. Distribution (2.25) is shown in figure 2.13b for $\theta = 1/3\pi$. This test case has closed field lines. From the results shown in figures 2.15 and 2.16 we see that

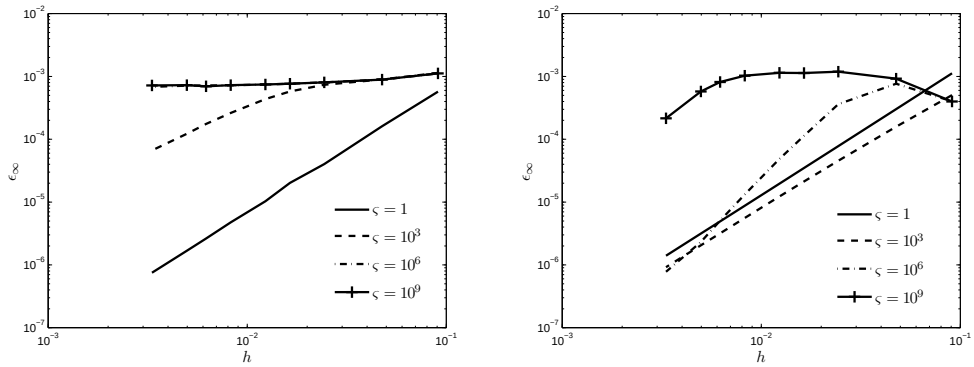

(a) (b)

Figure 2.15: Second tilted test case, convergence plots for several levels of anisotropy with $a = 0.15$, $b = 0.85$, $\theta = \pi/3$, (a) aligned symmetric scheme, (b) symmetric scheme by Günter et al.

for the second tilted test case for both schemes second-order convergence sets in later depending on the level of anisotropy.

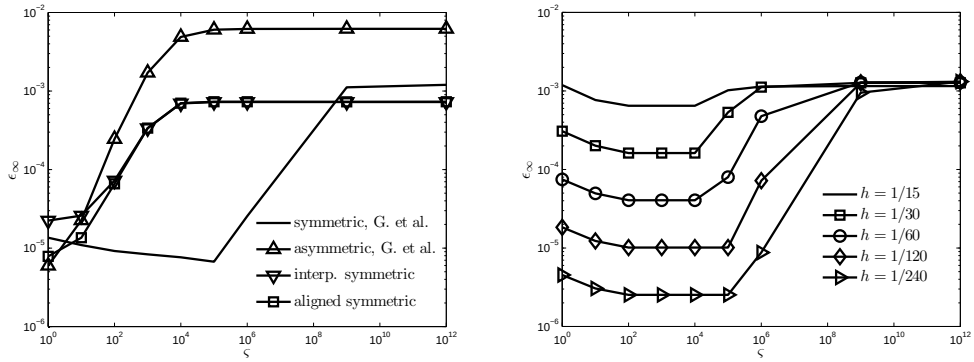

(a) (b)

Figure 2.16: Second tilted test case, accuracy plot for several levels of anisotropy with $a = 0.15$, $b = 0.85$, $\theta = \pi/3$ (a) multiple schemes, grid is 100×100, (b) symmetric scheme by Günter et al.

2.4.5 *Temperature-dependent diffusion coefficients*

Until now we have not yet addressed part $\mathcal{A}_4$ of the diffusion equation. To do this we describe the coefficients by

$$D_\parallel = c_\parallel T^{5/2}, \quad D_\perp = c_\perp T^{-1/2}.$$

These expressions are representative of actual MHD-simulations for fusion plasmas except for the absence of density. We apply temperature dependence of the diffusion coefficients to the test case described in section 2.4.2. From the results shown in figure 2.17a we see that the aligned symmetric method and the interpolated symmetric method maintain second-order convergence independent of the anisotropy whereas the symmetric method by Günter et al. now has reduced convergence. There is no noticeable difference between using a harmonic mean and an arithmetic mean.

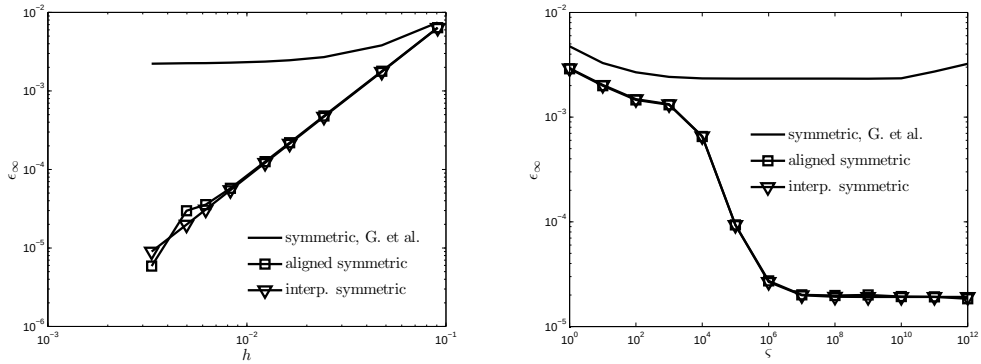

(a) (b)

Figure 2.17: Test case 1 with temperature-dependent diffusion coefficients, ϵ_∞-error, (a) convergence for $\varsigma = 10^9$, (b) dependence on anisotropy for a 100×100 grid.

The reason for the loss of performance for the symmetric scheme of Günter et al. is that instead of having diffusion tensor values exactly on the dual grid we now have to interpolate between the primal grid points.

An obvious way to prevent the need for interpolation is to define the temperature on both the primal and the dual grid, i.e. favoring the DDFV and the FECC methods in case of temperature dependent diffusion coefficients.

2.4.6 *Tilted closed perpendicular test case*

In the previous section we described a tilted elliptic test case for heterogeneous anisotropic diffusion which we believe is more thorough and realistic than what is currently considered as diffusion benchmark test cases for fusion relevant anisotropic diffusion (see e.g. Herbin and Hubert [56] and Eymard et al. [48]). Note that we focus on misaligned extremely anisotropic heterogeneous diffusion on structured grids.

The tilted elliptic distribution has no axis-symmetry in the exact solution which prevents fortuitous cancellation of errors. We further note that one of the basic constraints of MHD is the absense of magnetic monopoles, i.e. $\nabla \cdot \mathbf{B} = 0$. This means that *all* magnetic field lines *must* be closed physically. A diffusion test case that mimicks this property is the Sovinec test case, however it is not tilted. A new non-axis symmetric test case is now formed by combining the idea of the Sovinec test case, containing only closed field lines, with the idea of tilted elliptic distributions. This distribution can be used as a source function for steady test cases with $\mathbf{b} \cdot \nabla T = 0$, with the field lines aligned to the contours of the distribution. We redo the test case described in section 2.4.3, by adding ellipticity:

$$T = \frac{1}{D_\perp}\psi, \quad \psi = \Big[a^2(x\cos\theta + y\sin\theta)^2 + b^2(x\sin\theta - y\cos\theta)^2\Big]\cos(\pi x)\cos(\pi y), x, y \quad \in [-0.5, 0.5].$$

Note that the configurations look similar to the flux surfaces of magnetic islands for different MHD modes, depending on the parameters a and b. For this tilted test case the symmetric scheme by Günter et al. is not able to approximate anisotropic diffusion whilst maintaining formal accuracy globally independent of the level of anisotropy.

2.5 Conservation error

The schemes we present in the current work discretize the non-conservative form of the diffusion equation. To quantify the effect of non-conservation we apply the current interp. symmetric scheme and the symmetric scheme of Günter et al. to an unsteady test problem with zero source terms and Neumann boundary conditions. For the time integration we use the Crank-Nicolson scheme with the time step chosen such that the time integration error is negligible. In this problem we assume that $\mathbf{q}_\perp = 0$, so any

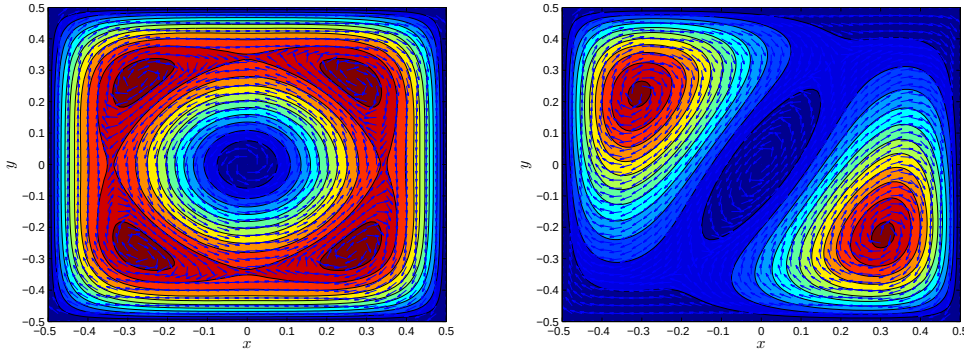

(a) (b)

Figure 2.18: Tilted closed test case, $\theta = \pi/3$ (a) $a = 3, b = 3$, (b) $a = 1, b = 3$.

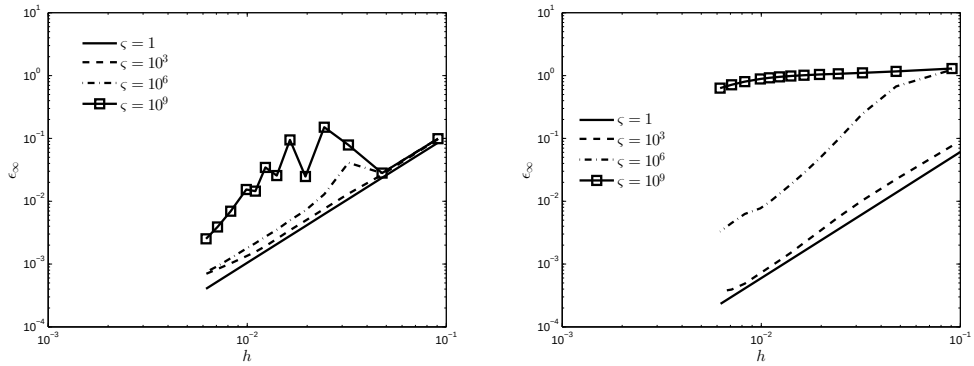

(a) (b)

Figure 2.19: Tilted closed test case with symmetric scheme by Günter et al., $\theta = \pi/3$ (a) $a = 3, b = 3$, (b) $a = 1, b = 3$.

perpendicular diffusion is numerical. We define the global conservation error at time level n as

$$\epsilon_T = 1/N \left| \sum_k^N T_{k,n} - \sum_k^N T_{k,0} \right|,$$

where k refers to the k-th component of the solution vector and where N is the number of unknowns. As a test case we consider the diffusion of a Gaussian initial distribution

$$T(x, y, t = 0) = \exp\left(-r^2/2\sigma^2\right), \quad r^2 = (x - d)^2 + (y - d)^2, \quad x, y \in [-0.5, 0.5],$$

with $\sigma = 0.05$. The direction of diffusion $\mathbf{b}$ is given by

$$\mathbf{b} = \frac{1}{\sqrt{(x - x_0)^2 + (y - y_0)^2}} \begin{pmatrix} -(y - y_0) \\ x - x_0 \end{pmatrix}.$$

The Gaussian distribution is diffused along the circular field lines. We consider a closed field line case, with $x_0 = y_0 = 0$.

Regarding the implementation of the boundary conditions: For the symmetric scheme by Günter et al. the flux points are placed exactly on the boundary. For the current co-located schemes the temperature and the flux quantities are located in the same points. The implementation of the Neumann boundary conditions for the current scheme is done by using ghost points.

As a reference result we apply the symmetric scheme by Günter et al. to a field-aligned grid of size 256×256. The length of the domain is exactly the circumference of the field line along which the peak of the Gaussian is diffused and for the endtime we use the same endtime as the reference result. In the length of the domain we use periodic boundary conditions. From the results shown in figures 2.20a and 2.20b we

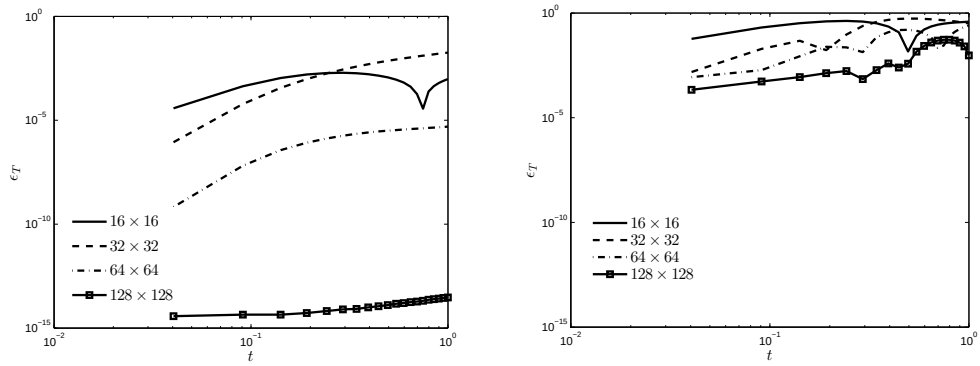

Figure 2.20: ϵ_T error of the symmetric scheme for two-dimensional diffusion test case with a Gaussian initial distribution, $D_\perp = 0, \sigma = 0.05, t_{end} = 1, d = 0.25, x, y \in [-2, 2]$, (a) symmetric, G. et al., (b) interp. symmetric scheme.

see that both schemes are not conservative, the interpolation scheme with symmetric coefficients being most non-conservative.

We see in figure 2.21b that the interpolated symmetric scheme merges the circular distribution into one peak. We run the simulation again, now with the initial distribution displaced by $d = 0.25$. The results shown in figure 2.22 underline that the radially inward numerical diffusion is much more pronounced than outward numerical diffusion. For the interpolated symmetric scheme we also implemented Dirichlet and periodic conditions, leading to very similar results, indicating that the wiggles in the center of the domain as well as the inward movement of the peak are not caused by the use of approximate Neumann boundary conditions.
The poor result of the interpolated symmetric scheme compared to the symmetric scheme by Günter et al. is caused by wiggles. These wiggles show a dip directly adjacent to the Gaussian. The diffusion operator distributes the Gaussian into the direction of the dip. In time, the circular Gaussian creeps towards the center and merges into one hill. As we refine the grid, we see much better behavior of the interpolated

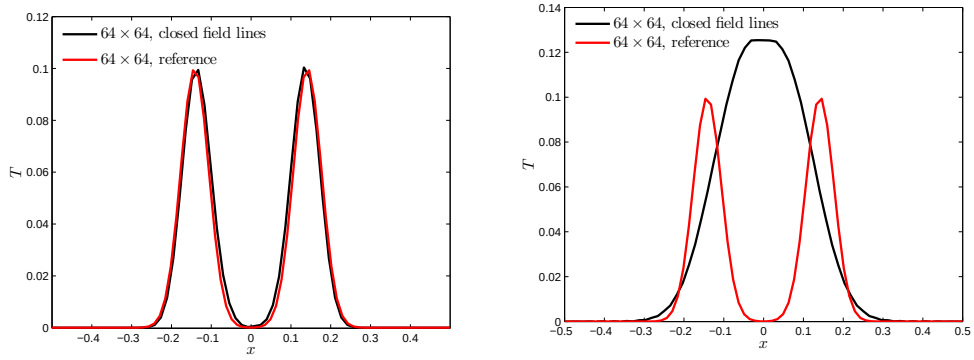

(a) (b)

Figure 2.21: Cross-section at $y = 0$, two-dimensional diffusion test case with a Gaussian initial distribution, $\sigma = 0.05, x_0 = 0, t_{end} = 0.5, D_\perp = 0$, closed field lines, $d = 0.1$, on a 64×64 grid with $\Delta t = t_{end}/40$, (a) symmetric scheme, G. et al., (b) interp. symmetric scheme.

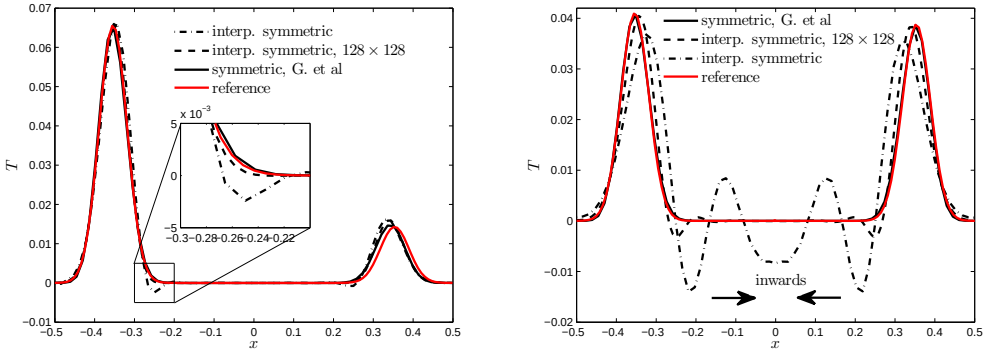

(a) (b)

Figure 2.22: Cross-section at $y = 0$, two-dimensional diffusion test case with a Gaussian initial distribution, $\sigma = 0.05, x_0 = 0, D_\perp = 0, d = 0.25$, on a 64×64 grid with $\Delta t = 1/100$, (a) $t_{end} = 0.1$, (b) $t_{end} = 0.5$.

symmetric scheme as the wiggles are reduced, see figure 2.22.

2.5.1 *Aligned gradient operator*

Starting from the symmetric scheme by Günter et al. we consider an aligned stencil for each gradient. We leave the operator for the divergence untouched. Originally in each flux point $\mathbf{D} \cdot \nabla T$ is approximated by

$$\mathbf{D} \cdot \nabla T|_{i+1/2,j+1/2} \approx \begin{pmatrix} D_{11} \frac{T_{i+1,j+1}+T_{i+1,j}-T_{i,j+1}-T_{i,j}}{2h} + D_{12} \frac{T_{i+1,j+1}+T_{i+1,j}-T_{i,j+1}-T_{i,j}}{2h} \\ D_{21} \frac{T_{i+1,j+1}+T_{i+1,j}-T_{i,j+1}-T_{i,j}}{2h} + D_{22} \frac{T_{i+1,j+1}+T_{i+1,j}-T_{i,j+1}-T_{i,j}}{2h} \end{pmatrix},$$

and likewise for the other flux points. This can be written as

$$\mathbf{D}^* \cdot [\mathbf{b} \cdot \nabla T,\, \mathbf{b}_\perp \cdot \nabla T]^T, \quad \mathbf{D}^* = \begin{pmatrix} b_1 D_{11} + b_2 D_{12} & b_1 D_{12} - b_2 D_{11} \\ b_1 D_{21} + b_2 D_{22} & -b_2 D_{21} + b_1 D_{22} \end{pmatrix}.$$

Now we approximate $\mathbf{b} \cdot \nabla T$ and $\mathbf{b}_\perp \cdot \nabla T$ by applying an aligned stencil in combination with a bilinear interpolation of the four surrounding points. The bilinear interpolation $\tilde{T}(x, y)$ for a flux point $(i + 1/2, j + 1/2)$ is given by

$$\begin{aligned} \tilde{T}(x,y)_{i+1/2,j+1/2} = xy(T_{xy})_{i+1/2,j+1/2} + x(T_x)_{i+1/2,j+1/2} \\ + y(T_y)_{i+1/2,j+1/2} + \overline{T}_{i+1/2,j+1/2}, \end{aligned}$$

and similarly for the other flux points. The coefficients in these bilinear interpolations are given by

$$\begin{aligned} (T_{xy})_{i+1/2,j+1/2} &\approx \frac{T_{i+1,j+1} + T_{i,j} - T_{i+1,j} - T_{i,j+1}}{h^2}, \\ (T_x)_{i+1/2,j+1/2} &\approx \frac{T_{i+1,j+1} + T_{i+1,j} - T_{i,j} - T_{i,j+1}}{h^2}, \\ (T_y)_{i+1/2,j+1/2} &\approx \frac{T_{i+1,j+1} + T_{i,j+1} - T_{i,j} - T_{i+1,j}}{h^2}, \\ \overline{T}_{i+1/2,j+1/2} &= \frac{T_{i+1,j+1} + T_{i+1,j} + T_{i,j+1} + T_{i,j}}{4}, \end{aligned}$$

and similarly for the other flux points. In each flux point we now step in the forward

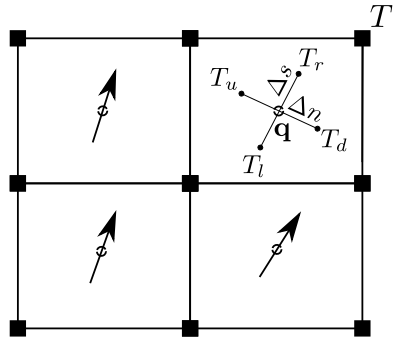

Figure 2.23: Conservative aligned difference.

and backward direction of $\mathbf{b}$ and $\mathbf{b}_\perp$ with some step size Δs and Δn respectively and obtain a central difference approximation for the aligned gradients $\mathbf{b} \cdot \nabla T$, $\mathbf{b}_\perp \cdot \nabla T$, see figure 2.23. The resulting approximations are

$$\begin{aligned} \mathbf{b} \cdot \nabla T|_{i+1/2,j+1/2} &= b_1 (T_x)_{i+1/2,j+1/2} + b_2 (T_y)_{i+1/2,j+1/2}, \\ \mathbf{b}_\perp \cdot \nabla T|_{i+1/2,j+1/2} &= -b_2 (T_x)_{i+1/2,j+1/2} + b_1 (T_y)_{i+1/2,j+1/2}, \end{aligned}$$

which leads to the symmetric scheme by Günter et al. that we started with. So we conclude that the symmetric scheme is aligned by construction.

2.5.2 *Aligned divergence operator*

If we use a nine point interpolation for the temperature we lose conservation. Instead we consider a weighted average of the symmetric gradient approximations. We can obtain a suitable description of the local derivatives by defining the approximations for T_x and T_y as

$$\begin{aligned}
T_x \approx & \alpha_{ru}\frac{T_{i+1,j+1}+T_{i+1,j}-T_{i,j+1}-T_{i,j}}{2h}+\alpha_{lu}\frac{T_{i,j}+T_{i,j+1}-T_{i-1,j+1}-T_{i-1,j}}{2h} \\
& +\alpha_{ld}\frac{T_{i,j}+T_{i,j-1}-T_{i-1,j}-T_{i-1,j-1}}{2h}+\alpha_{rd}\frac{T_{i+1,j}+T_{i+1,j-1}-T_{i,j}-T_{i,j-1}}{2h}, \\
T_y \approx & \alpha_{ru}\frac{T_{i+1,j+1}+T_{i,j+1}-T_{i,j}-T_{i+1,j}}{2h}+\alpha_{lu}\frac{T_{i,j+1}+T_{i-1,j+1}-T_{i-1,j}-T_{i,j}}{2h} \\
& +\alpha_{ld}\frac{T_{i,j}+T_{i-1,j}-T_{i-1,j-1}-T_{i,j-1}}{2h}+\alpha_{rd}\frac{T_{i+1,j}+T_{i,j}-T_{i,j-1}-T_{i+1,j-1}}{2h},
\end{aligned} \tag{2.26}$$

with a bilinear description for each α, and with the conditions

$$\begin{aligned}
&\alpha_{ru}(\tfrac{h}{2},\tfrac{h}{2})=1, \quad \alpha_{ru}(-\tfrac{h}{2},\tfrac{h}{2})=0, \quad \alpha_{ru}(\tfrac{h}{2},-\tfrac{h}{2})=0, \quad \alpha_{ru}(-\tfrac{h}{2},-\tfrac{h}{2})=0, \\
&\alpha_{lu}(\tfrac{h}{2},\tfrac{h}{2})=0, \quad \alpha_{lu}(-\tfrac{h}{2},\tfrac{h}{2})=1, \quad \alpha_{lu}(\tfrac{h}{2},-\tfrac{h}{2})=0, \quad \alpha_{lu}(-\tfrac{h}{2},-\tfrac{h}{2})=0, \\
&\alpha_{rd}(\tfrac{h}{2},\tfrac{h}{2})=0, \quad \alpha_{rd}(-\tfrac{h}{2},\tfrac{h}{2})=0, \quad \alpha_{rd}(\tfrac{h}{2},-\tfrac{h}{2})=1, \quad \alpha_{rd}(-\tfrac{h}{2},-\tfrac{h}{2})=0, \\
&\alpha_{ld}(\tfrac{h}{2},\tfrac{h}{2})=0, \quad \alpha_{ld}(-\tfrac{h}{2},\tfrac{h}{2})=0, \quad \alpha_{ld}(\tfrac{h}{2},-\tfrac{h}{2})=0, \quad \alpha_{ld}(-\tfrac{h}{2},-\tfrac{h}{2})=1.
\end{aligned}$$

We get the following bilinear descriptions

$$\begin{aligned}
\alpha_{ru} &= \left(\frac{1}{2}+\frac{x}{h}\right)\left(\frac{1}{2}+\frac{y}{h}\right), \\
\alpha_{lu} &= \left(\frac{1}{2}-\frac{x}{h}\right)\left(\frac{1}{2}+\frac{y}{h}\right), \\
\alpha_{rd} &= \left(\frac{1}{2}+\frac{x}{h}\right)\left(\frac{1}{2}-\frac{y}{h}\right), \\
\alpha_{ld} &= \left(\frac{1}{2}-\frac{x}{h}\right)\left(\frac{1}{2}-\frac{y}{h}\right),
\end{aligned} \tag{2.27}$$

which also fulfills the consistency requirement that $\sum \alpha = 1$. Note that we also have the following conservation properties for the coefficients

$$\begin{aligned}
&\alpha_{ru}(\tfrac{h}{2},0)=\tfrac{1}{2}, \quad \alpha_{ru}(0,\tfrac{h}{2})=\tfrac{1}{2}, \quad \alpha_{ru}(x,-\tfrac{h}{2})=0, \quad \alpha_{ru}(-\tfrac{h}{2},y)=0, \\
&\alpha_{lu}(\tfrac{h}{2},y)=0, \quad \alpha_{lu}(0,\tfrac{h}{2})=\tfrac{1}{2}, \quad \alpha_{lu}(x,-\tfrac{h}{2})=0, \quad \alpha_{lu}(-\tfrac{h}{2},0)=\tfrac{1}{2}, \\
&\alpha_{rd}(\tfrac{h}{2},0)=\tfrac{1}{2}, \quad \alpha_{rd}(x,\tfrac{h}{2})=0, \quad \alpha_{rd}(0,-\tfrac{h}{2})=\tfrac{1}{2}, \quad \alpha_{rd}(-\tfrac{h}{2},y)=0, \\
&\alpha_{ld}(\tfrac{h}{2},y)=0, \quad \alpha_{ld}(x,\tfrac{h}{2})=0, \quad \alpha_{ld}(0,-\tfrac{h}{2})=\tfrac{1}{2}, \quad \alpha_{ld}(-\tfrac{h}{2},0)=\tfrac{1}{2}.
\end{aligned}$$

We call these coefficients *locally symmetric*. When using these coefficients in the bi-quadratic interpolation they do not exactly yield all nodal values for the given locations since it is not an approximation of the temperature but rather a weighted summation of gradients.
In this manner we approximate the diffusion equation in conservative form with the divergence written in local coordinates

$$\begin{aligned}
T_t &= \left(b_1\frac{\partial}{\partial s} - b_2\frac{\partial}{\partial n}\right)\left(D_{11}T_x + D_{21}T_y\right) + \left(b_2\frac{\partial}{\partial s} + b_1\frac{\partial}{\partial n}\right)\left(D_{21}T_x + D_{22}T_y\right) + f \Rightarrow \\
T_t &\approx b_1\frac{(D_{11}T_x + D_{21}T_y)_r - (D_{11}T_x + D_{21}T_y)_l}{2\Delta s} \\
&\quad - b_2\frac{(D_{11}T_x + D_{21}T_y)_u - (D_{11}T_x + D_{21}T_y)_d}{2\Delta n} \\
&\quad + b_2\frac{(D_{21}T_x + D_{22}T_y)_r - (D_{21}T_x + D_{22}T_y)_l}{2\Delta s} \\
&\quad + b_1\frac{(D_{21}T_x + D_{22}T_y)_u - (D_{21}T_x + D_{22}T_y)_d}{2\Delta n} + f.
\end{aligned}$$

For the diffusion tensor values we use the same weighted averaging procedure as before. The diffusion tensor values are taken both averaged and exact in the dual grid points. The products of the diffusion tensor components and the gradients can be combined. For instance, for $\alpha_{ru}(D_{11}T_x)_r$ we have

$$\alpha_{ru}(D_{11}T_x)_{ru} = \alpha_{ru}(D_{11})_{ru}\frac{T_{i+1,j+1} + T_{i+1,j} - T_{i,j+1} - T_{i,j}}{2h}.$$

Note that due to symmetry we will end up with the original symmetric scheme for any set of coordinates $(x_r, y_r), (x_l, y_l), (x_u, y_u), (x_d, y_d)$. To create a unique scheme, we introduce a weighting factor $\omega \in [0, 1]$ for the perpendicular part of the divergence approximation. This will increase the conservation errors a bit but may improve the behavior near high gradients in n-direction. This weighted scheme is not consistent for $D_\perp \neq 0$ if $\omega \neq 1$.

For the locations of the stencil we take a step Δs forward and backward in the direction of the field line, and a step Δn perpendicular to the field line and construct a stencil using the local coefficients $\alpha_{ru}, \alpha_{lu}, \alpha_{rd}$ and α_{ld}. The unit direction vector we use to align the stencil is obtained by normalized averaging (see section 2.2.2) of the unit direction vectors in the surrounding points $(i \pm 1/2, j \pm 1/2), (i \pm 1/2, j \mp 1/2)$. In figure 2.24 we see that indeed the conservation of the total temperature is not maintained to machine accuracy, but it does converge with second-order accuracy. Note the decrease in conservation error with increasing ω. In figures 2.25 and 2.26 we show results for the same test case but now with averaged values for the diffusion tensor. Both for the locally symmetric and the symmetric scheme by Günter et al. we now apply arithmetic averaging. We consider this to be representative for the case of temperature dependent diffusion coefficients.

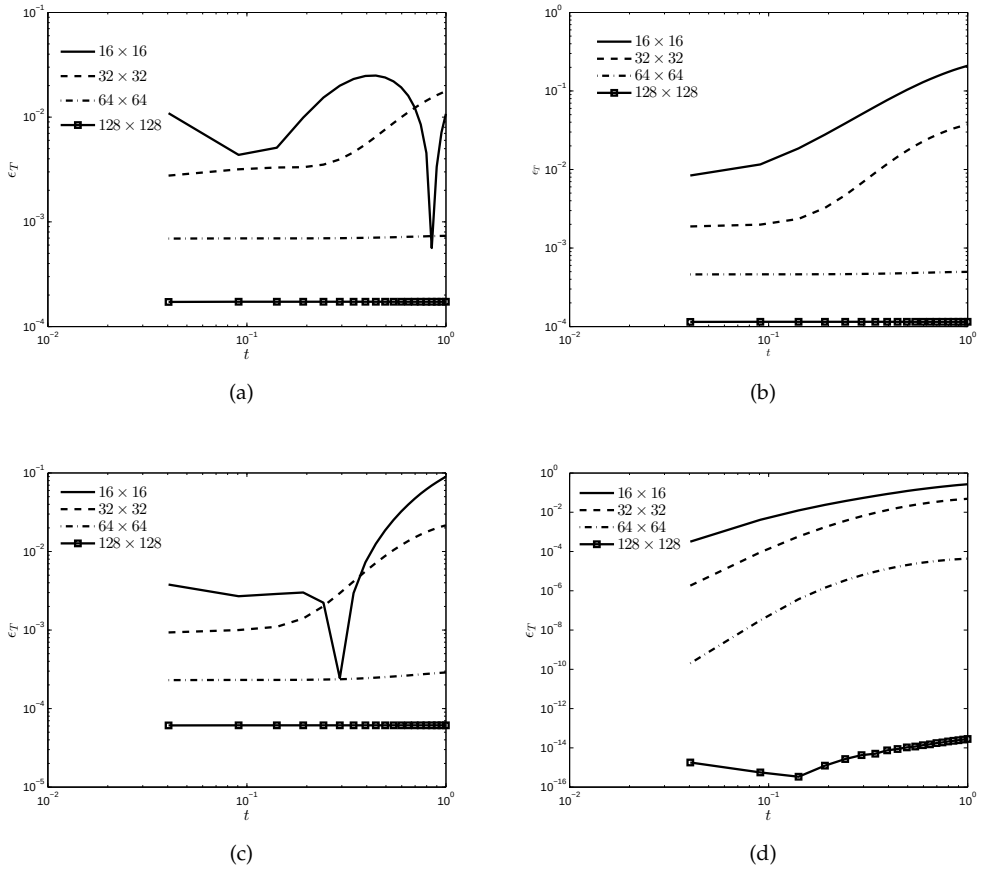

Figure 2.24: ϵ_T error versus time of the locally symmetric scheme for a two-dimensional diffusion test case with a Gaussian initial distribution, $D_\perp = 0, \sigma = 0.05, t_{end} = 1, d = 0.25, x, y \in [-2, 2]$ (a) $\omega = 0.25$, (b) $\omega = 0.5$ (c) $\omega = 0.75$, (d) $\omega = 1$.

We see that the solution of the symmetric scheme by Günter et al. is now smeared out in perpendicular direction. In figure 2.26 we see that for averaged diffusion tensor coefficients the symmetric scheme by Günter et al. has excellent conservation of the total temperature but a poor approximation of the local temperature values and vice versa for the locally symmetric scheme. If we apply *normalized* averaging of the diffusion tensor values we see that the locally symmetric scheme and the symmetric scheme by Günter et al. perform similarly. This is an indication that any averaging of the diffusion tensor must be done with care. For a more detailed discussion on the diffusion tensor we refer the reader to chapter 4.

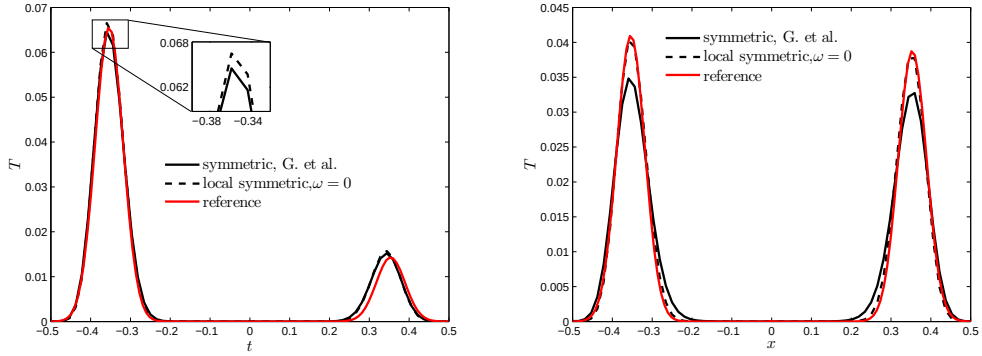

(a) (b)

Figure 2.25: Cross-section at $y = 0$, two-dimensional diffusion test case, with a Gaussian initial distribution, using averaged diffusion tensor values, $\sigma = 0.05, x_0 = 0, D_\perp = 0, d = 0.25$, on a 64×64 grid with $\Delta t = 1/100$, (a) $t_{end} = 0.1$, (b) $t_{end} = 0.5$.

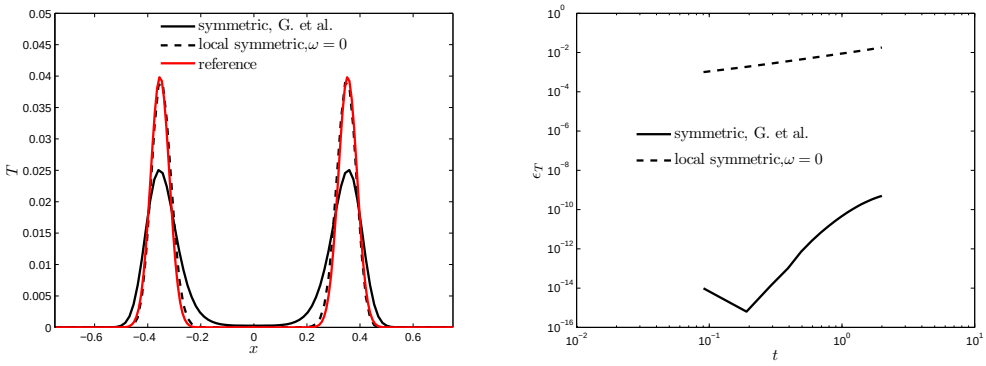

(a) (b)

Figure 2.26: Two-dimensional diffusion test case, with a Gaussian initial distribution, using averaged diffusion tensor values, $\sigma = 0.05, t_{end} = 2, D_\perp = 0, d = 0.25, x, y \in [-1.5, 1.5]$, on a 96×96 grid with $\Delta t = 1/100$, (a) Cross-section at $y = 0$ (b) ϵ_T error.

2.5.3 *Aligned conservative formulation*

Finally, the aligned conservative formulation is found by writing both the divergence and the gradient in local coordinates,

$$\begin{aligned}\nabla \cdot \mathbf{q} = \\ \left(b_1\frac{\partial}{\partial s} - b_2\frac{\partial}{\partial n}\right)\left[D_{11}\left(b_1\frac{\partial}{\partial s} - b_2\frac{\partial}{\partial n}\right)T + D_{21}\left(b_2\frac{\partial}{\partial s} + b_1\frac{\partial}{\partial n}\right)T\right] + \\ \left(b_2\frac{\partial}{\partial s} + b_1\frac{\partial}{\partial n}\right)\left[D_{21}\left(b_1\frac{\partial}{\partial s} - b_2\frac{\partial}{\partial n}\right)T + D_{22}\left(b_2\frac{\partial}{\partial s} + b_1\frac{\partial}{\partial n}\right)T\right].\end{aligned} \tag{2.28}$$

Writing out the diffusion tensor components this simplifies to

$$\begin{aligned}\nabla \cdot \mathbf{q} = &\left(b_1\frac{\partial}{\partial s} - b_2\frac{\partial}{\partial n}\right)\left[b_1 D_{\parallel}\frac{\partial T}{\partial s} - b_2 D_{\perp}\frac{\partial T}{\partial n}\right] \\ &+ \left(b_2\frac{\partial}{\partial s} + b_1\frac{\partial}{\partial n}\right)\left[b_2 D_{\parallel}\frac{\partial T}{\partial s} + b_1 D_{\perp}\frac{\partial T}{\partial n}\right].\end{aligned} \tag{2.29}$$

Splitting the differential terms and re-ordering results in the components $\mathcal{A}_1, \mathcal{A}_2, \mathcal{A}_3, \mathcal{A}_4$ presented in section 2.2.4. The aligned discretisation requires five aligned stencils, see figure 2.27. For the determination of the direction vectors in the points rf, lf, uf, df we

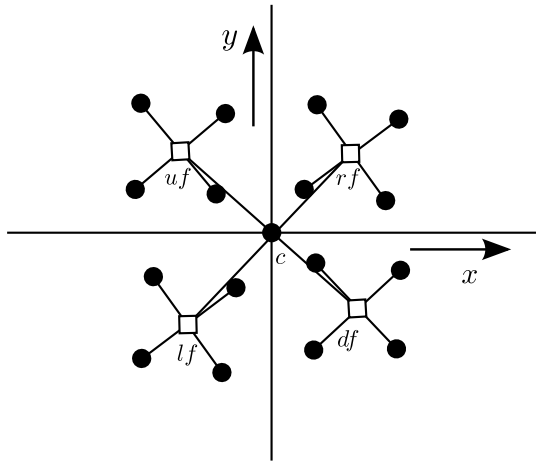

Figure 2.27: Locally transformed grid for the conservative formulation.

apply a normalised version of bilinear interpolation, i.e.

$$\mathbf{b}(x,y) = \frac{\alpha_{ru}\mathbf{b}_{ru} + \alpha_{lu}\mathbf{b}_{lu} + \alpha_{rd}\mathbf{b}_{rd} + \alpha_{ld}\mathbf{b}_{ld}}{|\alpha_{ru}\mathbf{b}_{ru} + \alpha_{lu}\mathbf{b}_{lu} + \alpha_{rd}\mathbf{b}_{rd} + \alpha_{ld}\mathbf{b}_{ld}|}, \tag{2.30}$$

where, in case of a co-located grid the values $\mathbf{b}_{ru}, \mathbf{b}_{lu}, \mathbf{b}_{rd}, \mathbf{b}_{ld}$ are normalised averages of the surrounding vertex values of $\mathbf{b}$, e.g.

$$\mathbf{b}_{ru} = \frac{\mathbf{b}_{i+1,j+1} + \mathbf{b}_{i,j+1} + \mathbf{b}_{i,j} + \mathbf{b}_{i+1,j}}{|\mathbf{b}_{i+1,j+1} + \mathbf{b}_{i,j+1} + \mathbf{b}_{i,j} + \mathbf{b}_{i+1,j}|}, \tag{2.31}$$

and likewise for the other averages. From the viewpoint of conservation: Since in the general case each nodal point has a different unit direction vector it is not possible to create common flux points with all the neighboring control volumes, i.e. it is not possible to create non-overlapping connected control volumes.

The temperature values in the stencil points follow from either a local or a non-local interpolation.

For the non-local interpolation, the temperature values follow from the biquadratic interpolation of all nine temperature unknowns, specifically for the unit direction vectors we use the Vandermonde coefficients. For the step sizes $\Delta s, \Delta n$ we take $\frac{1}{2}h$ for the

divergence approximation and $\frac{1}{4}h$ or $\frac{1}{8}h$ for the gradient approximation. Specifically we ensure that all the aligned stencil points lie in the interpolation region.

This aligned approximation of the conservative formulation does not reduce to any existing scheme. For future research we suggest to vary the step sizes. In figure 2.28

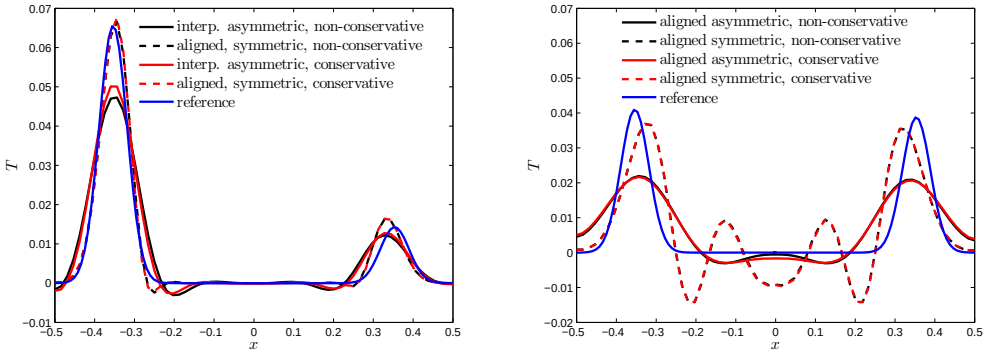

(a) (b)

Figure 2.28: Cross-section at $y = 0$, two-dimensional diffusion test case with a Gaussian initial distribution, $\sigma = 0.05, x_0 = 0, D_\perp = 0, d = 0.25$, on a 64×64 grid with $\Delta t = 1/100$, (a) $t_{end} = 0.1$, (b) $t_{end} = 0.5$.

we see that the results for the aligned approximations of the conservative and non-conservative formulation of the diffusion equation are very similar. We note that the aligned schemes are very sensitive in terms of stability and the step sizes of the aligned stencils. Reducing the step sizes brings the aligned conservative schemes closer to the interpolation schemes. In terms of conservation the approximations are also very similar.

We are seeking for an aligned method with discrete conservation. Discrete conservation in our case requires that assuming we have control volumes surrounding the temperature unknowns, the fluxes through the connecting surfaces are continuous. This gives a necessary condition: the sum of the flux approximations accross the cell faces between the neighboring volumes must be equal from both sides of the cell face. Supporting that condition we need *locality of the flux approximation*; a local interpolation can e.g. be formed by taking the bilinear interpolation in the particular quadrant where the aligned nodes for the gradient stencils are located. For the local interpolation, the lengths $\Delta s, \Delta n$ can be chosen such that the flux points rf, lf, uf, df lie on the cell faces between control volumes. For higher order accuracy we need to increase the number of points. Automatically we will obtain a segmented/curved stencil as shown in figure 2.4. The topic of higher order aligned schemes is left open for further study.

It is clear however that a fully aligned discretely conservative approximation is not possible since the flux points on the cell faces between control volumes are not overlapping. If we only align the gradient approximation and treat the divergence approximation in a conventional manner, as we do in section 2.5.1 we end up with an existing scheme if we use bilinear interpolation for the gradient approximation, namely the symmetric

scheme by Günter et al. As a variation on the approach in section 2.5.1 we can apply a non-local interpolation for the gradient approximation. We can also have a combination; a local interpolation for the perpendicular diffusion and a non-local interpolation for the parallel diffusion and vice-versa.

We see in figures 2.29a and 2.29b that the local interpolation for the gradient ap-

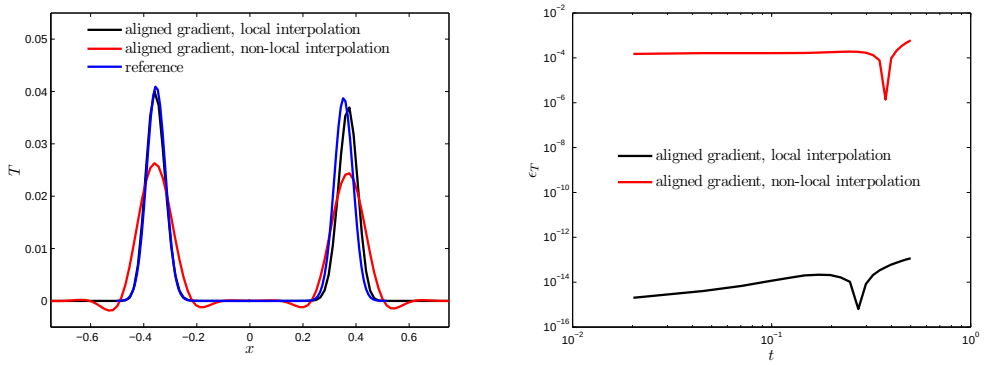

(a) (b)

Figure 2.29: Two-dimensional diffusion test case with a Gaussian initial distribution, $\sigma = 0.05, x_0 = 0, D_\perp = 0, d = 0.25$, on a 64×64 grid with $\Delta t = 1/100, t_{end} = 0.5$, (a) Cross-section at $y = 0$, (b) ϵ_T error.

proximation is superior in terms of conservation and accuracy. We also note that using a non-local interpolation only for the perpendicular gradient gives the same conservation error and accuracy as the fully local gradient approximation. The latter is due to the fact that $D_\perp$ is set to zero.

Summarizing, the symmetric scheme by Günter et al. has a gradient and divergence approximation that is aligned by construction. The locally symmetric scheme introduced in section 2.5.2 was obtained by adding a weighting term to the perpendicular part of the divergence approximation. If the level of anisotropy is moderate the weighting term should be set to one for consistency. We obtained a partially aligned scheme where the gradient approximation was approximated in an aligned fashion with local and non-local interpolation.

2.6 Conclusion

We have developed and applied a new differencing method on a co-located grid that implements the concept of following the field line track within the stencil area to obtain the differencing points that are finally used in the approximation. In terms of accuracy and convergence the aligned methods are similar to exactly differentiating the interpolation schemes. The symmetric variants of our method are more accurate and less anisotropy-dependent than the standard asymmetric scheme by Günter et al. The symmetric scheme by Günter et al. works well in maintaining the order of convergence for

a wide variety of cases and it exhibits very low pollution of the perpendicular diffusion but it also seems to be more susceptible to number representation problems. This is apparent because the linear operator becomes ill-conditioned for large anisotropy ratios (noticeable above $\varsigma = 10^9$).

We find that preserving continuity of the gradient is of key importance for maintaining the accuracy of the perpendicular diffusion. We see that in all cases where the aligned symmetric scheme and the symmetric interpolation scheme do not maintain order of convergence and/or the level of accuracy, the approximation of the perpendicular flux T_n determines this behavior. For all test cases the temperature gradient tangential to the field line is zero. For large gradients in magnetic field strength this term should also be considered. Over almost all the test cases, the symmetric scheme by Günter et al. is better able to maintain the order of accuracy. The symmetric scheme by Günter et al. does however show anisotropy-dependent accuracy for closed elliptic magnetic field line distributions, most likely due to a lack of symmetry in the solution. This anisotropy dependence is increased if we also make the diffusion-tensor components temperature dependent. This is caused by the interpolation required to get the temperature values in the flux points. For the tilted cases with temperature dependent diffusion coefficients our aligned scheme and interpolated symmetric scheme show comparable and even superior results depending on the test case.

The non-conservative nature of the current scheme has an effect on the approximation of initial value problems with a non-aligned anisotropic diffusion tensor due to non-monotonous behavior in the direction perpendicular to the field line. As an improvement we suggest a locally symmetric scheme which is derived from the symmetric scheme by Günter et al. using an aligned divergence operator. We also suggest a method with an aligned approximation for both the divergence and the gradient.

3

FINITE-VOLUME SCHEME FOR ANISOTROPIC DIFFUSION

In this chapter, we propose a special finite-volume scheme to test the importance of connectivity of the finite volumes. We apply the scheme to the anisotropic heat-conduction equation, and compare its results with those of existing finite-volume schemes for anisotropic diffusion.

3.1 Introduction

Most of the techniques to handle diffusion in anisotropic media are based on finite-volume or finite-element methods and revolve around handling the interpolation of the flux over the cell faces. A lot of work has been done on finite-volume schemes for the solution of diffusion problems on unstructured grids with discontinuous and anisotropic diffusion tensors. Here an important assumption in constructing the formulation of the cell-face fluxes is the continuity of the heat flux over the cell-faces, see for instance Edwards and Rogers [43], Maire et al. [91] and Jacq et al. [71]. Vertex values are used in several cell-centered schemes to approximate the flux over the cell face, see e.g. Le Potier [78], Lipnikov et al. [87], Coudière et al. [25]. The vertex values are approximated with for instance continuity and monotonicity in mind. The vertex values may be defined explicitly but this requires some sort of dual grid, see e.g. Hermeline [57], Le Potier [80], Morel et al. [96]. Shashkov and Steinberg [108] put the flux values in the vertices and then average to the centers of the cell-faces. For a more detailed overview of finite-volume methods the reader is referred to the review paper by Droniou [38] and the introduction in chapter 2. What motivated Morel, Maire, Breil, Hymann, Shashkov and others in developing flux(-normal) continuous schemes was grid robustness of finite-volume methods and finite-element methods in case of diffusion-tensor discontinuities. Van Es et al. [114] looked at the importance of alignment for a finite-difference method. In that paper several schemes are compared. The importance of internodal/volume continuity was expected because the formal accuracy for all schemes using series expansions was second order and a decisive effect of lower continuity at the boundaries was not visible in a local error analysis although it clearly mattered in terms of boundary treatment.

In this chapter we propose and apply a finite-volume scheme that can change the connectivity between the volumes by changing the length of the cell faces with a free parameter. We apply both cell-face and vertex-centered flux points.

As before we approximate the anisotropic thermal diffusion, described by

$$\mathbf{q} = -\mathbf{D} \cdot \nabla T, \quad \frac{\partial T}{\partial t} = -\nabla \cdot \mathbf{q} + f, \tag{3.1}$$

where T represents the temperature, $\mathbf{b}$ the unit direction vector of the field line, f some source term and $\mathbf{D}$ the diffusion tensor. The boundary conditions are of Dirichlet type and are discussed per test case.

3.2 Finite-Volume schemes

All the schemes to be discussed formally have local second-order accuracy, which can be shown by carefully expanding the approximations using Taylor series, see appendix D. However, as can be seen in the results of the test cases discussed in section 3.4, the accuracy of these methods may drop below their formal accuracy even though the test cases have $\mathcal{C}_\infty$ solutions and source functions. One important aspect that may be overlooked by the local analysis is the continuity between elements, or some equivalent property for finite differences. The symmetric scheme by Günter et al. [54] shows anisotropy independent results in case the diffusion tensor components are captured exactly by the staggered grid points.
The symmetric scheme has $\mathcal{C}_0$ flux values and $\mathcal{C}_1$ temperature values at the flux points, in all directions, i.e. on the dual grid the solution is $\mathcal{C}_1$. Or speaking in finite-volume terms, the values of the solution on the flux points that connect neighbouring control volumes are $\mathcal{C}_1$. The equivalent control volume of the asymmetric scheme, which shows a loss of accuracy and convergence, is only $\mathcal{C}_1$ connected to the control volumes to the left/right and bottom/top, there is no direct connection with the diagonally neighbouring control volumes. To test the hypothesis that continuity between elements is important for the capturing of anisotropic diffusion we adapt the asymmetric finite-volume scheme so that all control volumes are $\mathcal{C}_1$ connected. Both the symmetric and

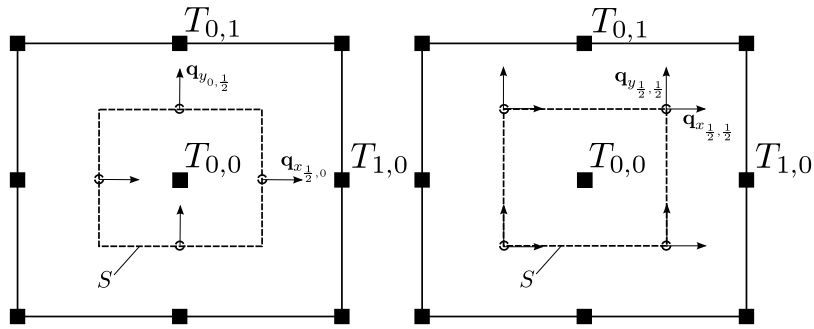

(a) Asymmetric (b) Symmetric

Figure 3.1: Control volumes.

the asymmetric scheme have equivalent finite-volume schemes, the difference now lies

in the position of the fluxes on the surface of the control volume, see figure 3.1. A basic assumption of the finite-volume method is that the solution is spatially constant inside the control volumes. For the diffusion equation this implies

$$T_t = -\frac{1}{V}\oint_S \mathbf{q}\cdot\mathbf{n}dS + \frac{1}{V}\int_V f dV, \quad \mathbf{q} = -\mathbf{D}\cdot\nabla T.$$

We get the same discrete formulation when using finite differences or finite volumes in case of equidistant grids, to be considered here. The mesh sizes are given by $\Delta x = \Delta y = h$. First we discuss the reference methods, namely the asymmetric finite-volume scheme and the symmetric finite-volume scheme.

3.2.1 *Asymmetric finite volume*

The first scheme we discuss has the flux points defined on the cell-face centers, see figure 3.1a. We have the following approximations for the gradients on the axes

$$\begin{aligned}
\left.\frac{\partial T}{\partial x}\right|_{i+\frac{1}{2},j} &= \frac{T_{i+1,j} - T_{i,j}}{h},\\
\left.\frac{\partial T}{\partial y}\right|_{i+\frac{1}{2},j} &= \frac{T_{i+1,j+1} + T_{i,j+1} - T_{i,j-1} - T_{i+1,j-1}}{4h},\\
\left.\frac{\partial T}{\partial x}\right|_{i,j+\frac{1}{2}} &= \frac{T_{i+1,j+1} + T_{i+1,j} - T_{i-1,j+1} - T_{i-1,j}}{4h},\\
\left.\frac{\partial T}{\partial y}\right|_{i,j+\frac{1}{2}} &= \frac{T_{i,j+1} - T_{i,j}}{h},
\end{aligned}$$

and similar formulas for $\left.\frac{\partial T}{\partial x}\right|_{i-\frac{1}{2},j}$, $\left.\frac{\partial T}{\partial y}\right|_{i-\frac{1}{2},j}$, $\left.\frac{\partial T}{\partial x}\right|_{i,j-\frac{1}{2}}$, $\left.\frac{\partial T}{\partial y}\right|_{i,j-\frac{1}{2}}$. For the heat-conduction term we have

$$\mathbf{q}_{i+\frac{1}{2},j} = -\mathbf{D}_{i+\frac{1}{2},j}\cdot\left(\left.\frac{\partial T}{\partial x}\right|_{i+\frac{1}{2},j}, \left.\frac{\partial T}{\partial y}\right|_{i+\frac{1}{2},j}\right)^T,$$

and similarly for other fluxes. Finally, the contour integral of the fluxes is approximated by

$$\oint_S \mathbf{q}\cdot\mathbf{n}dS = \left[\left(\mathbf{q}_{i,j+\frac{1}{2}} - \mathbf{q}_{i,j-\frac{1}{2}}\right)\cdot(0,1) + \left(\mathbf{q}_{i+\frac{1}{2},j} - \mathbf{q}_{i-\frac{1}{2},j}\right)\cdot(1,0)\right]h.$$

3.2.2 *Symmetric finite volume*

Another approach is taken by Günter et al. [54], they use a symmetric scheme (with a symmetric linear operator) that is mimetic by maintaining the self-adjointness of the differential operator. The flux points are placed at the vertices of the control volumes.

The control volume with the location of the fluxes is given in figure 3.1b. The divergence terms are determined at the center points in the following manner

$$\begin{aligned}\left.\frac{\partial T}{\partial x}\right|_{i+\frac{1}{2},j+\frac{1}{2}} &= \frac{T_{i+1,j+1}+T_{i+1,j}-T_{i,j+1}-T_{i,j}}{2h},\\ \left.\frac{\partial T}{\partial y}\right|_{i+\frac{1}{2},j+\frac{1}{2}} &= \frac{T_{i,j+1}+T_{i+1,j+1}-T_{i+1,j}-T_{i,j}}{2h},\end{aligned} \tag{3.2}$$

where all other gradients are determined in a similar manner. Next, the diffusion tensor is applied to obtain the heat flux

$$\mathbf{q}_{i+\frac{1}{2},j+\frac{1}{2}} = -\mathbf{D}_{i+\frac{1}{2},j+\frac{1}{2}} \cdot \left(\left.\frac{\partial T}{\partial x}\right|_{i+\frac{1}{2},j+\frac{1}{2}}, \left.\frac{\partial T}{\partial y}\right|_{i+\frac{1}{2},j+\frac{1}{2}} \right)^T,$$

and similarly for the other fluxes. Finally, the contour integral of the fluxes is approximated by

$$\begin{aligned}\oint_S \mathbf{q}\cdot\mathbf{n}dS = \frac{1}{2}\Big[&\left(\mathbf{q}_{i+\frac{1}{2},j+\frac{1}{2}}+\mathbf{q}_{i+\frac{1}{2},j-\frac{1}{2}}\right)\cdot(1,0) - \left(\mathbf{q}_{i-\frac{1}{2},j-\frac{1}{2}}+\mathbf{q}_{i+\frac{1}{2},j-\frac{1}{2}}\right)\cdot(0,1)\\ &+\left(\mathbf{q}_{i+\frac{1}{2},j+\frac{1}{2}}+\mathbf{q}_{i-\frac{1}{2},j+\frac{1}{2}}\right)\cdot(0,1) - \left(\mathbf{q}_{i-\frac{1}{2},j-\frac{1}{2}}+\mathbf{q}_{i-\frac{1}{2},j+\frac{1}{2}}\right)\cdot(1,0)\Big]h.\end{aligned}$$

3.2.3 *Eight point flux scheme*

To investigate the importance of flux continuity and connectivity we apply a cell-face-centered flux (CF) scheme and a vertex-centered flux (VF) scheme on a grid with varying connectivity. The grid is varied through a parameter e, $e \in [0, \sqrt{2}h]$, where for $e = 0$

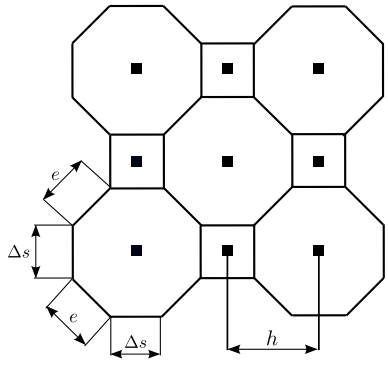

Figure 3.2: Part of hybrid grid ($0 < e < \sqrt{2}h$).

and $e = \sqrt{2}h$ the grid is uniform and rectangular, and for e between 0 and $\sqrt{2}h$ we have a hybrid grid consisting of octogonals with edges of lengths e and Δs and squares with edge length Δs (figure 3.2).

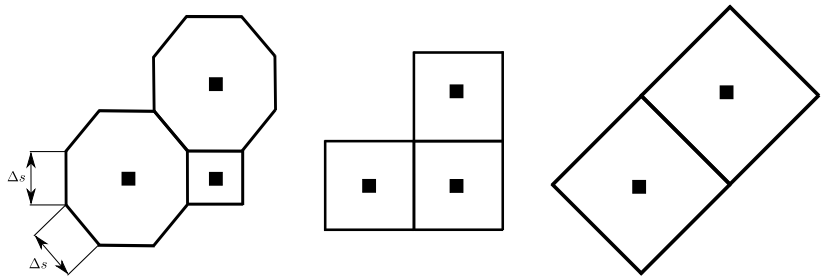

(a) (b) (c)

Figure 3.3: (a) $e = \Delta s$, (b) $e = 0$, (c) $e = \sqrt{2}h$.

Note that it holds $\Delta s = h - e/\sqrt{2}$, and hence, with all edges of the same length, $e = \Delta s$, $\Delta s = (2 - \sqrt{2})h$. The latter situation has been depicted in figure 3.3a. The two extreme cases $e = 0$ and $e = \sqrt{2}h$ are given in figures 3.3b and 3.3c, respectively. Note that in the case of $e = \sqrt{2}h$ the grid may be better aligned to features that are oblique with respect to the coordinate axes, but it will be coarser and have less finite volumes. For each volume we approximate the contour integral of the fluxes as follows

$$\oint_S \mathbf{q} \cdot \mathbf{n} dS \approx \sum_{i=1}^{M} \tilde{\mathbf{q}}_i \cdot \mathbf{n}_i \, l_i,$$

where $\tilde{\mathbf{q}}_i$ is an approximation of the flux across cell face i, and where $M = 4$ and $M = 8$ for the square and octogonal finite volume, respectively. Extending this approach to three dimensions is straightforward for a uniform Cartesian grid.

Vertex-centered fluxes

The VF scheme has the following description of the divergence

$$\begin{aligned} \oint_{octo} \mathbf{q} \cdot \mathbf{n} dS = \frac{1}{2}\sqrt{2} \left[\left(\overline{\mathbf{q}}_{ur,ru} - \overline{\mathbf{q}}_{ld,dl} \right) \cdot (1,1) + \left(\overline{\mathbf{q}}_{rd,dr} - \overline{\mathbf{q}}_{ul,lu} \right) \cdot (1,-1) \right] e \\ + \left[\left(\overline{\mathbf{q}}_{ru,rd} - \overline{\mathbf{q}}_{lu,ld} \right) \cdot (1,0) + \left(\overline{\mathbf{q}}_{ul,ur} - \overline{\mathbf{q}}_{dl,dr} \right) \cdot (0,1) \right] \Delta s, \\ \oint_{square} \mathbf{q} \cdot \mathbf{n} dS = \left[\left(\overline{\mathbf{q}}_{ru,rd} - \overline{\mathbf{q}}_{lu,ld} \right) \cdot (1,0) + \left(\overline{\mathbf{q}}_{ru,lu} - \overline{\mathbf{q}}_{rd,ld} \right) \cdot (0,1) \right] \Delta s, \end{aligned} \tag{3.3}$$

for the octogonal and the square volumes respectively, where we have to retain the normality of the resulting unit direction vector for the averaging of the fluxes.

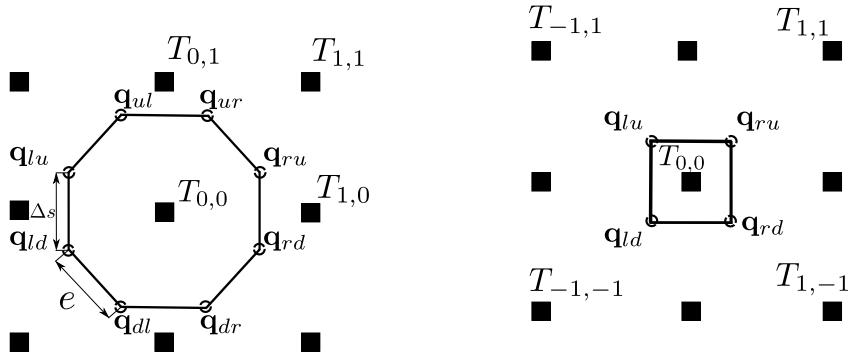

(a) Octogonal volume (b) Square volume

Figure 3.4: Control volumes with vertex centered fluxes.

The averaged flux vectors $\overline{\mathbf{q}}_{ur,ru}, \overline{\mathbf{q}}_{ul,lu}, \cdots$ generally denoted as $\overline{\mathbf{q}}_{A,B}$, are computed as

$$\overline{\mathbf{q}}_{A,B} = \frac{1}{4}\left[\left((D_\parallel)_A + (D_\parallel)_B - (D_\perp)_A - (D_\perp)_B\right)\left(\mathbf{b}\mathbf{b}^T\right)_{A,B} + \left((D_\perp)_A + (D_\perp)_B\right)\mathcal{I}\right]\cdot\left(\nabla T_A + \nabla T_B\right),$$

with $\mathbf{b}_{A,B} = (\mathbf{b}_A + \mathbf{b}_B)/|\mathbf{b}_A + \mathbf{b}_\mathbf{B}|$ and $\mathcal{I}$ the identity matrix. Here the gradient approximations follow from the interpolation, see figure 3.4 for the nomenclature. Note that applying a separate normalized averaging of the unit direction vectors gives a division by zero if the unit direction vectors are opposed. In this case we simply have to pick one of the directions, or, if we know that an opposed direction means there is an *O*-point, we can set the respective parallel flux to zero. Almost directly opposed field lines are numerically not an issue for the normalisation. With *O*-point we refer to the center of rotation of closed field lines (see figure 1.2), exactly at the *O*-point the direction is not defined.
In case of diffusion tensor values not defined exactly in the flux points but rather in the cells, or in case of sharply varying densities, harmonic averaging is preferred for the tensor values on the cell faces (see Edwards and Rogers [43] and Sharma and Hammett [107]). This is generally not the case for MHD simulations of fusion plasmas where the density and the diffusion tensor vary smoothly. For this reason we do not consider piecewise constant diffusion tensors, rather we apply a continuous nine-point interpolation. We define the diffusion tensor values exactly in the flux evaluation points.

Cell-face centered fluxes

With the flux vectors in the corner points of the control volume pointing in a direction of 45° with respect to the coordinate axes, the scheme is written as

$$\oint_{octo} \mathbf{q}\cdot\mathbf{n}dS = \left[\frac{1}{2}\sqrt{2}\left((\mathbf{q}_{c_1} - \mathbf{q}_{c_3})\cdot(1,1) + (\mathbf{q}_{c_2} - \mathbf{q}_{c_4})\cdot(1,-1)\right)e + \left((\mathbf{q}_r - \mathbf{q}_l)\cdot(1,0) + (\mathbf{q}_u - \mathbf{q}_d)\cdot(0,1)\right)\Delta s\right], \tag{3.4}$$

$$\oint_{square} \mathbf{q}\cdot\mathbf{n}dS = \left[(\mathbf{q}_r - \mathbf{q}_l)\cdot(1,0) + (\mathbf{q}_u - \mathbf{q}_d)\cdot(0,1)\right]\Delta s,$$

for the octogonal and the square volumes respectively. The cell-face fluxes $\mathbf{q}_{c_1}, \mathbf{q}_{c_2}, \mathbf{q}_{c_3}, \mathbf{q}_{c_4}$ and $\mathbf{q}_r, \mathbf{q}_l, \mathbf{q}_u, \mathbf{q}_d$ are given in figure 3.5. Using a circle with radius $\frac{1}{2}\sqrt{2}h$ we ensure that the flux points c_1, c_2, c_3, c_4 lie exactly on the average points of the four surrounding nodes (see figure 3.5). For the x- and y-derivatives in the vertical and horizontal flux

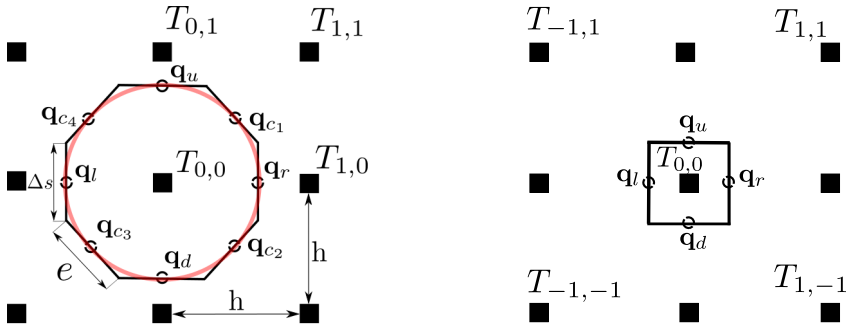

(a) Octogonal volume (b) Square volume

Figure 3.5: Control volumes with cell-face centered fluxes.

points respectively we use a nine-point interpolation scheme for the temperature, see section 3.3. For $e = 0$ the scheme reduces to the asymmetric scheme from section 3.2.1. For $e = \sqrt{2}h$ we end up with a symmetric description for the derivatives. This is equivalent to the symmetric scheme from section 3.2.2 if we use symmetric approximations for the derivatives. For verification we will also show the results for the asymmetric and symmetric schemes from sections 3.2.1 and 3.2.2 respectively.

3.3 Interpolation for fluxes

Given the formulation of the discrete divergence for the VF and CF scheme we need to find the discrete description of the fluxes. We discuss the use of a local and a non-local flux approximation.

3.3.1 *Multi-point flux approximation for eight point flux scheme*

Suppose we apply a local multi-point flux interpolation with the volumes surrounding the flux point, assuming we have cell-centered temperature values. Just like the MPFA method mentioned in section 2.1 the flux through the interfaces is determined using subcell-descriptions of the temperature. Here triangles may be formed by connecting the center points of three neighbouring volumes, see figure 3.6. We need two triangles for the determination of one edge flux, as per triangle we determine half of the flux going through the edge (see figure 3.7). We consider the approach described in e.g. Aavatsmark et al. [3,4] and Edwards and Rogers [43] for two-dimensional problems, i.e. we consider subcells with one temperature value per subcell face. Unlike the MPFA-methods, we do not have cell-centered diffusion tensors, but rather edge-centered or vertex-centered diffusion tensor values. We have already surrounded each vertex with an interaction triangle (see figure 3.7), which connects the surrounding temperature

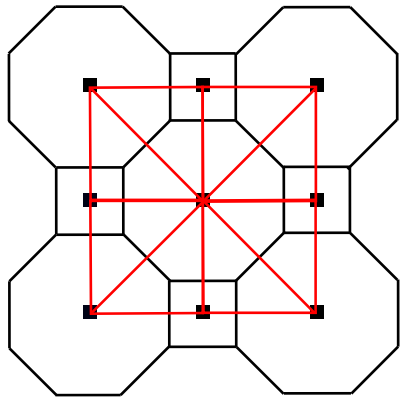

Figure 3.6: Interaction triangles, indicated by red lines

unknowns. The octogonal volume has eight vertices and thus eight interaction triangles, the square volume has four. It is clear that using a mixture of octogonals and squares

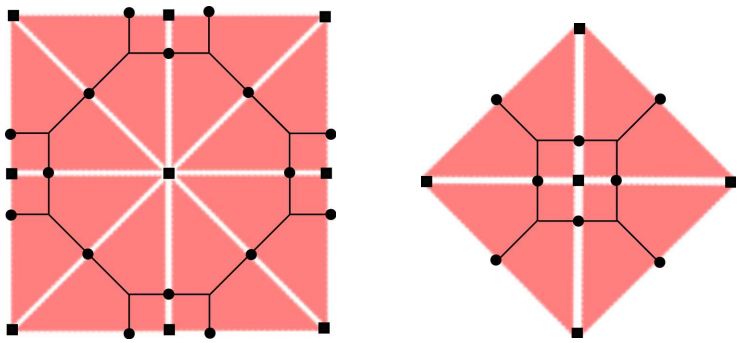

(a) (b)

Figure 3.7: Interaction triangles for (a) octogonal volume, (b) square volume, solid squares (■) indicate temperature unknowns and solid circles (•) indicate added unknowns to solve for the fluxes.

for the finite volumes leads to a mixture of nine-point stencils and five-point stencils when applying a locally conservative method (see figure 3.7). Only for $e = \sqrt{2}h$ and $e = 0$ a nine-point stencil emerges. It is known from literature that to properly resolve non-grid-aligned anisotropic diffusion with a linear scheme at least a nine-point stencil is required (see e.g. Umansky et al. [113]). The five-point stencil for the square volumes, which is unavoidable when using a combination of octogonal and square volumes, does not satisfy this requirement. Hence we will not further consider this multi-point flux approach.

3.3.2 *Non-local flux approximation*

Since the flux points r, l, u, d are off-center with respect to the centered temperature values we are forced to involve more points to obtain second-order accuracy in ap-

proximating the derivatives in these flux points. To have second-order accuracy for general values of e we apply biquadratic interpolation of the surrounding temperature values. When applying a nine-point interpolation we are assuming to have a continuous temperature and flux distribution. In case of a smoothly varying diffusion tensor and temperature value this assumption is realistic. Also see the Center Flux Scheme by Ferziger and Peric [50].

We have the following description for the derivatives:

$$\begin{aligned}\left.\frac{\partial T}{\partial x}\right|_{x,y} &\approx F(x,y) = \frac{\partial}{\partial x}\sum_{i=0}^{2}\sum_{j=0}^{2}\gamma_{ij}x^i y^j,\\ \left.\frac{\partial T}{\partial y}\right|_{x,y} &\approx G(x,y) = \frac{\partial}{\partial y}\sum_{i=0}^{2}\sum_{j=0}^{2}\gamma_{ij}x^i y^j,\end{aligned} \tag{3.5}$$

where the set of coefficients γ_{ij} is found by applying the Vandermonde matrix to the cell-centered temperature unknowns and subsequently differentiating the interpolation function, see appendices B and C. A second option is to weigh the symmetric approximation of the derivatives given by equation (3.2) such that the derivatives are given by equation (2.26). These derivatives are consistently summed in a weighted fashion for the flux points r, l, u, d, where the weights are given by equation (2.27). We call the resulting coefficients *locally symmetric*, see appendix C.

3.4 Numerical results and methodological adaptations

In the following test case we will consider both Vandermonde and locally symmetric coefficients. If results are similar we only show the results for the Vandermonde coefficients.

3.4.1 *Closed field-line test cases*

In this section we show the results for closed field-line test cases with extreme levels of anisotropy. In this test case $\mathbf{b}\cdot\nabla T = 0$. We vary the values of the parameters e and ς. The test cases we consider have continuous distributions for the diffusion tensor and the temperature. The error norm is defined by

$$\epsilon_\infty = \frac{|\tilde{T} - T|_{max}}{|T|_{max}},$$

where $\tilde{T}$ is the approximate temperature. The problem is considered on a square domain, described by $-0.5 \leq x, y \leq 0.5$. The following steady-state solution is assumed on the domain:

$$T(x,y) = 1 - (x^2 + y^2)^{3/2}, \tag{3.6}$$

with the unit direction vector given by

$$\mathbf{b} = \frac{1}{\sqrt{x^2+y^2}}\begin{pmatrix} -y \\ x \end{pmatrix}.$$

In figure 3.8, we study the accuracy of the various schemes for two anisotropic cases,

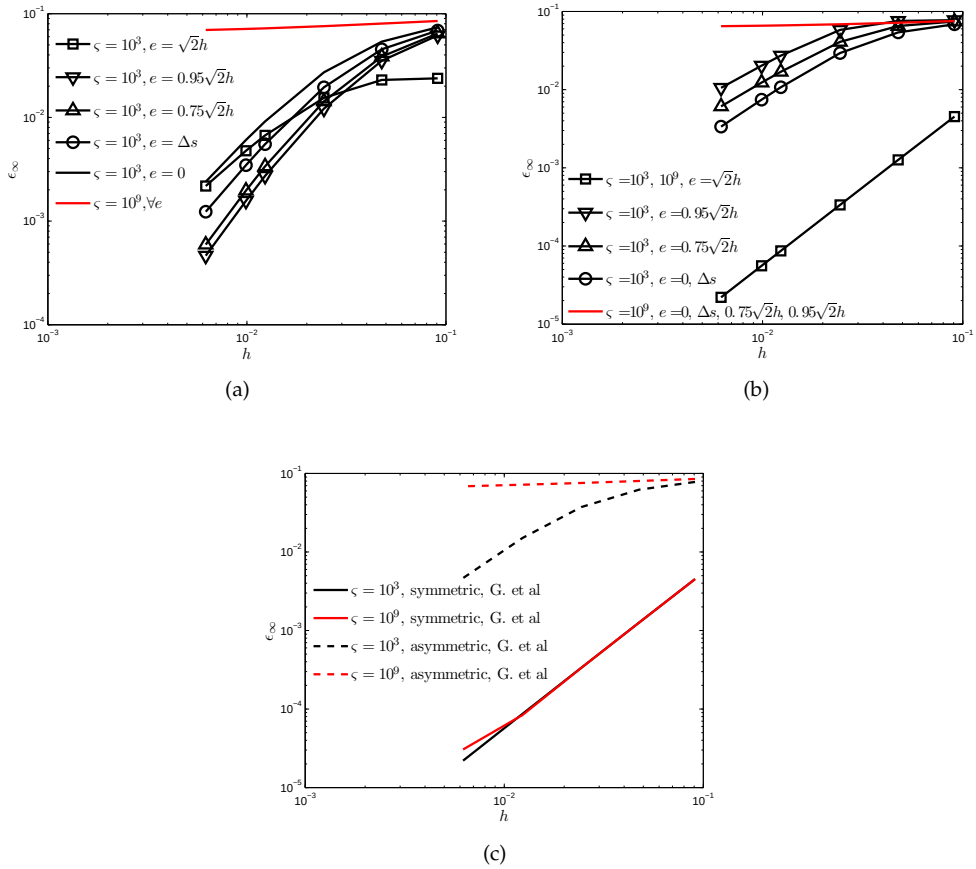

Figure 3.8: Error ϵ_∞ for anisotropy ratios $\varsigma = 10^3$ and $\varsigma = 10^9$, CF scheme with (a) Vandermonde coefficients, (b) locally symmetric coefficients, and (c) the asymmetric and symmetric scheme of Günter et al.

one being extremely anisotropic, $\varsigma = 10^9$. The main observation to be made from figure 3.8 is that for the extremely anisotropic $\varsigma = 10^9$ case only the symmetric scheme by Günter et al. and the CF scheme, with $e = \sqrt{2}h$ and locally symmetric coefficients, are second-order convergent and of low error magnitude. Using the locally symmetric coefficients; for $e \to \sqrt{2}h$ we go from a non-local interpolation involving all the temperature unknowns for each derivative to a local interpolation involving only the volumes surrounding the flux points. This explains the jump in (order of) accuracy going from $e = 0.95\sqrt{2}h$ to $e = \sqrt{2}h$ in figure 3.8b. In figure 3.9 we still present results obtained with the VF scheme for the same test case. Here, as opposed to the CF scheme with locally symmetric coefficients (figure 3.8), the VF scheme with locally symmetric coefficients does not perform well for $\varsigma = 10^9$.

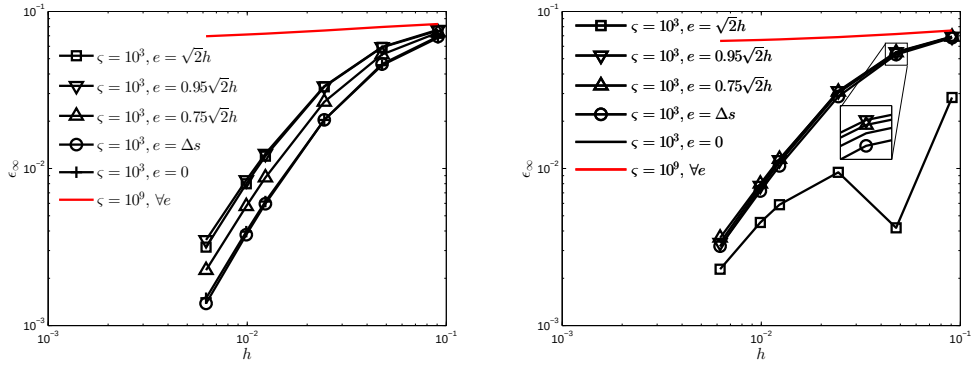

(a) (b)

Figure 3.9: Error ϵ_∞ for anisotropy ratios $\varsigma = 10^3$ and $\varsigma = 10^9$, VF scheme with (a) Vandermonde coefficients, (b) locally symmetric coefficients.

3.4.2 *e-dependency*

We proceed by studying the e-dependency in more detail. We consider a constant angle test case which is described by

$$T(x, y) = xy\left[\sin(\pi x)\sin(\pi y)\right]^{10}, \quad x, y \in [0, 1],$$

where the angle of misalignment α is set to a constant value. The solution simulates a temperature peak. For both the cell face-centered scheme and the vertex-centered

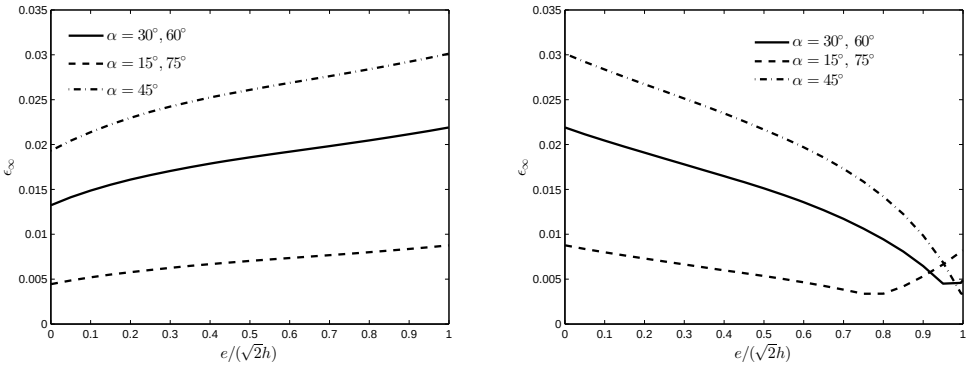

(a) (b)

Figure 3.10: Error ϵ_∞ for constant angle test case, $\varsigma = 10^9$, 50×50 grid and varying values of e, (a) VF scheme, (b) CF scheme.

scheme we observe a noticeable influence of the dominant angle of anisotropy on the e-dependency of the error, see figure 3.10. Concerning the effect of e-variation, notice the opposite behavior of the VF scheme and the CF scheme. Also note that for most values of e the error increases as the dominant angle of anisotropy goes to 45°. At and

near $e = \sqrt{2}h$, for the CF scheme the behavior is opposite though; CF scheme's best results are obtained for $\alpha = 45°$. For the CF scheme, we also clearly observe the best behavior is at or near $e = \sqrt{2}h$.

3.4.3 *Adaptations for closed field lines*

There is a clear distinction between closed and open field-line cases. The closed field-line cases allow for specific adaptations to improve the accuracy.

Topology mimicking

To incorporate the closed field-line topology in the finite-volume discretisation we enforce that the unit direction vectors are tangential to the edges of the finite volume, see figure 3.11. Note that in this way we enforce that $\int \nabla \cdot \mathbf{b} d\Omega = 0$ since $\oint \mathbf{b} \cdot \mathbf{n} d\Gamma = 0$. In general this is not consistent with the diffusion equation because in general $\nabla \cdot \mathbf{b} \neq 0$. Sovinec et al. [109] devised a test containing only closed field lines to directly com-

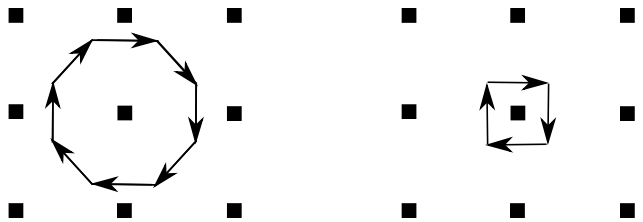

Figure 3.11: Topology local field lines for (a) octogonal volume, (b) quadrilateral volume.

pare the perpendicular numerical diffusion to the actual numerical diffusion. The exact solution and the forcing function are given by

$$T = \psi, \quad f = 2\pi^2\psi, \quad \psi = \cos(\pi x)\cos(\pi y), \quad x, y \in [-0.5, 0.5]. \tag{3.7}$$

The error in the perpendicular diffusion is given by $|T(0,0)^{-1} - 1|$. We use homogeneous Dirichlet boundary conditions. The field lines are tangential to the contours of constant temperature, i.e.

$$\mathbf{b} = \frac{1}{\sqrt{\psi_x^2 + \psi_y^2}} \begin{pmatrix} -\psi_y \\ \psi_x \end{pmatrix}.$$

We obtain *fourth-order* convergence for the Sovinec test case *independent* of the level of anisotropy, using Vandermonde coefficients, with $e = \sqrt{2}h$, with vertex averaged gradients and with the unit direction vectors enforced to be tangent to the cell faces, see figure 3.12a. The Sovinec test case has closed field lines, as such the topology of the entire domain is mimicked by the individual volumes. We believe this is key to the high-order approximation. We see that the accuracy increases monotonously as e goes to $\sqrt{2}h$, and that it jumps to fourth-order for $e = \sqrt{2}h$. Further, we see the inverse for the CF scheme, where we have fourth-order accuracy for $e = 0$ and second order for higher values of e, with a subsequent decrease in accuracy for increasing e, see figure

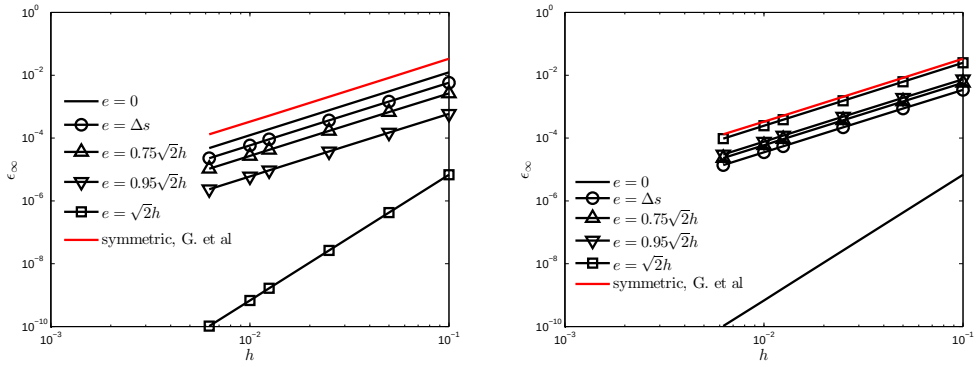

Figure 3.12: Error ϵ_∞ for Sovinec test case, $\varsigma = 10^9$, with varying values of e, using Vandermonde coefficients. Here the symmetric scheme by Günter et al. is used as a reference. (a) VF scheme, (b) CF scheme.

3.12b.
The VF scheme with exact unit direction vectors and the VF scheme with averaged unit direction vectors are identical since the local values for the unit direction vector (and thus also its approximation) do not play a role in the accuracy. We note that using the locally symmetric coefficients the results are almost identical, without the fourth-order convergence for $e = \sqrt{2}h$.

If we force the field lines for the parallel diffusion coefficient to be tangential to the cell faces, letting the field lines for the perpendicular diffusion coefficient untouched, we get the same result as setting $D_\parallel$ to zero everywhere in the domain for any level of anisotropy without the fourth-order accuracy for $e = \sqrt{2}h$.

Importance of O-point

We now apply the VF and CF scheme to the Sovinec test case, without the foregoing enforcement of field line topology. We notice a huge difference between odd and even numbered grids; both the VF and the CF scheme perform much better on odd-numbered grids than on even-numbered grids. On the odd-numbered grids, for both schemes, the error of the perpendicular diffusion remains fairly constant with increasing anisotropy, see figure 3.13, and for the even numbered grids the error scales first order with the level of anisotropy.

The gain in accuracy is caused by the fact that the central volume exactly mimicks the topology of the closed field line with $\mathbf{b} \cdot \nabla T = 0$ leading to a zero contribution of $D_\parallel$. To verify this we enforce $D_\parallel = 0$ for the flux points positioned closest to the O-point for the even-numbered grids. The results, given in figure 3.14, show that enforcing $D_\parallel = 0$ close to the O-point has a similar effect as having a volume exactly on the O-point.

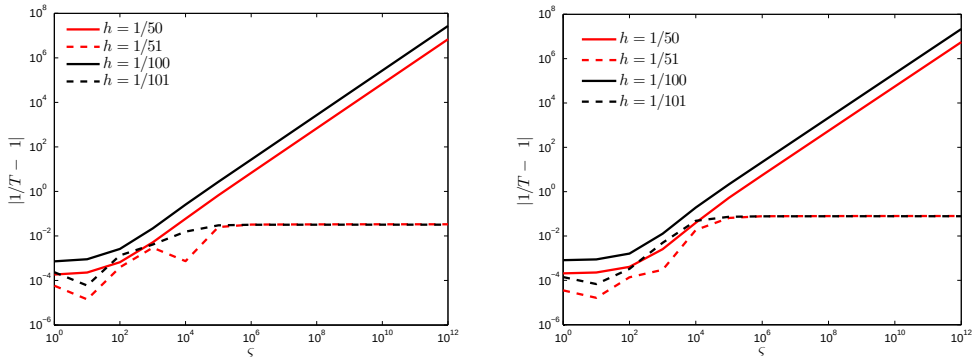

(a) (b)

Figure 3.13: Error $|T^{-1} - 1|$ for Sovinec test case with varying anisotropy, $e = \Delta s$, Vandermonde coefficients, with odd and even number of finite volumes (a) VF scheme, (b) CF scheme.

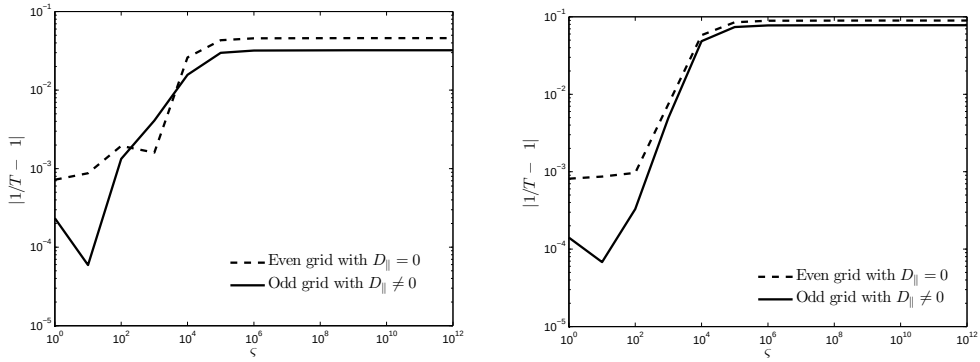

(a) (b)

Figure 3.14: Error $|T^{-1} - 1|$ for Sovinec test case for varying anisotropy for $e = \Delta s$, Vandermonde coefficients, odd and even grid with $D_{\|} \neq 0$ and $D_{\|} = 0$, respectively (a) VF scheme , (b) CF scheme.

For both the VF scheme and the CF scheme we get $\mathcal{O}(h^4)$ convergence for $e \to \sqrt{2}h$ and $e \to 0$ respectively for the isotropic case if we have a finite volume exactly on the O-point, see figure 3.15c. The 4^{th}-order convergence becomes independent of the level of anisotropy if we mimick the topology everywhere in the domain as we saw in section 3.4.3.

Enforcing $D_{\|} = 0$

We see that enforcing $D_{\|} = 0$ around the O-point, as well as placing a volume exactly on the O-point leads to a considerable gain in accuracy for the Sovinec test case. This approach is interesting as a means to improve existing methods because the location of the O-point can be derived from the magnetic field data. The same caveat as for the topology mimicking holds here; validity is limited to situations where the parallel

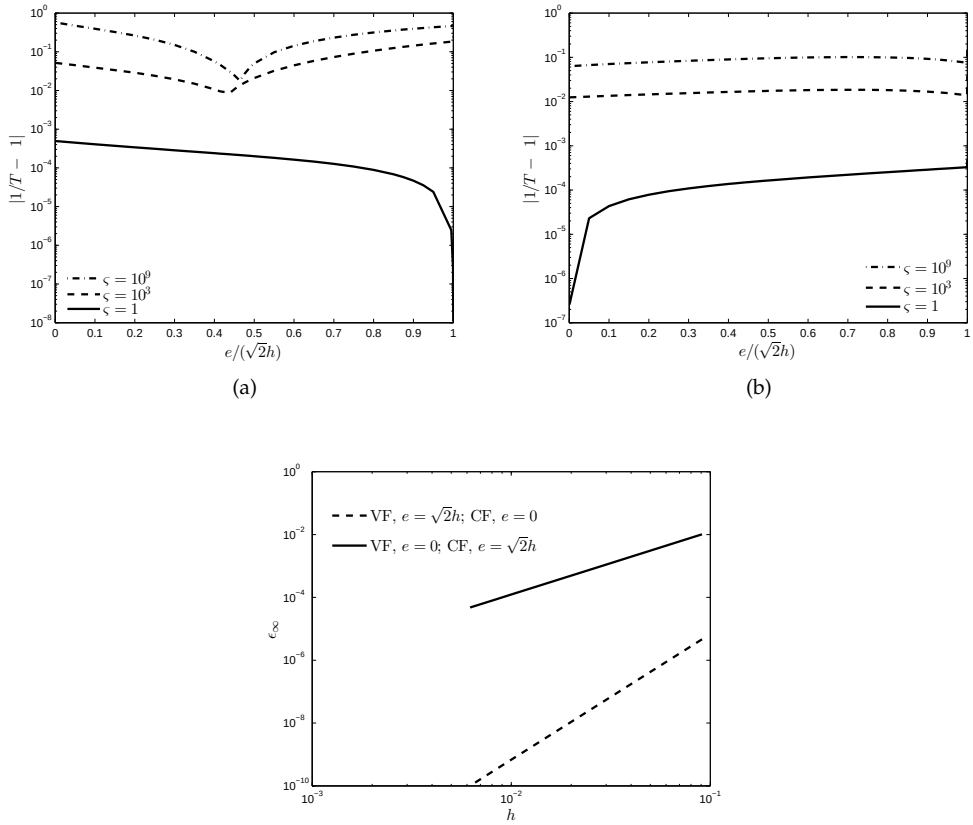

Figure 3.15: Sovinec test case, Error $|T^{-1} - 1|$ for varying e with anisotropy $\varsigma = 1, 10^3, 10^9$, $N = 51$, Vandermonde coefficients (a) VF scheme, (b) CF scheme, (c) convergence of error ϵ_∞ for $\varsigma = 1$.

flux is zero. However, it is not necessarily limited to steady cases. The involvement with the problem parameter $D_{\parallel}$ might be seen as a form of model reduction. If a

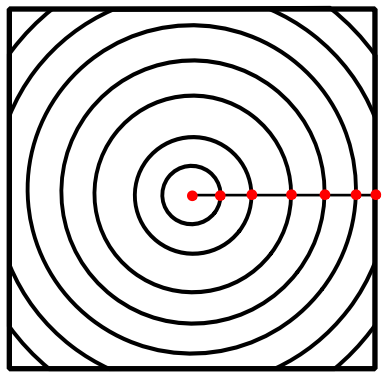

Figure 3.16: Points where we set $D_{\parallel}$ to zero.

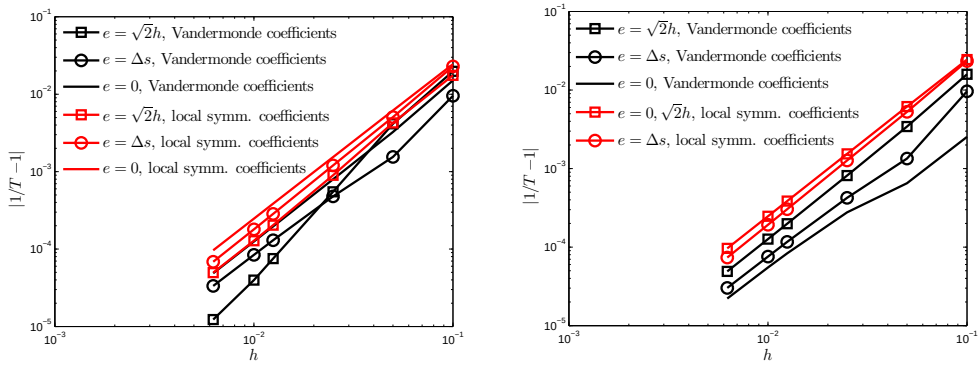

Figure 3.17: Convergence of $|T^{-1} - 1|$ for Sovinec test case with $\varsigma = 10^9$, (a) VF scheme , (b) CF scheme.

point on the last closed field line is found and subsequently $D_{\|}$ is enforced to be zero on the line connecting the outer point and the O-point (see figure 3.16) we have full second-order accuracy for $e = 0, e = \Delta s$ and $e = \sqrt{2}h$, see figure 3.17. We know from chapter 2 that the symmetric scheme by Günter et al. loses anisotropy independence for tilted elliptic temperature distributions. Note that the symmetric scheme is identical to the symmetric finite volume scheme for a uniform rectangular grid. This tilted elliptic distribution has no symmetry axes aligned with the coordinate axes and as such is more general than the previous test case.
The distribution for the tilted test case is given by

$$\begin{aligned} T(x,y) &= 1 - (a^2(x\cos\theta + y\sin\theta)^2 + b^2(x\sin\theta - y\cos\theta)^2)^{3/2}, \\ x,y &\in [-0.5, 0.5], \end{aligned} \tag{3.8}$$

with $\mathbf{b}$ given by

$$\mathbf{b} = \frac{1}{\sqrt{T_x^2 + T_y^2}} \begin{pmatrix} -T_y \\ T_x \end{pmatrix},$$

which ensures that $\mathbf{b} \cdot \nabla T = 0$. First we set $D_{\|} = 0$ on a vertical line through the O-point. Second-order accuracy is obtained for $e = 0$ using the VF scheme, see figure 3.18. Continuing with $e = 0$ we try different enforcements of $D_{\|} = 0$, from enforcement in the O-point only to enforcement along the full vertical. Second-order accuracy convergence for the VF scheme is obtained completely when we set $D_{\|}$ to zero on the line $x = 0, y > -0.5$ through the origin and likewise for $D_{\|}$ set to zero on the line $x = 0, y > 0$, see figure 3.19. For an enforcement along the line $x = 0, 0 < y < 0.2$ stagnation of convergence sets in for a moderate resolution. In general the stagnation of convergence is delayed further for a longer line of $D_{\|} = 0$ enforcement. An explanation for this is that the longer we make this line of enforcement, the more closed field lines we are able to resolve. This explains the fact that we do not see an improvement for $D_{\|} = 0$ on the full vertical line compared to the half vertical line for the VF scheme since for both $x = 0, y > -0.5$ and $x = 0, y > 0$ we treat all the closed field lines. The results for the CF scheme also improve, but there is no full recovery of the second-order accuracy.

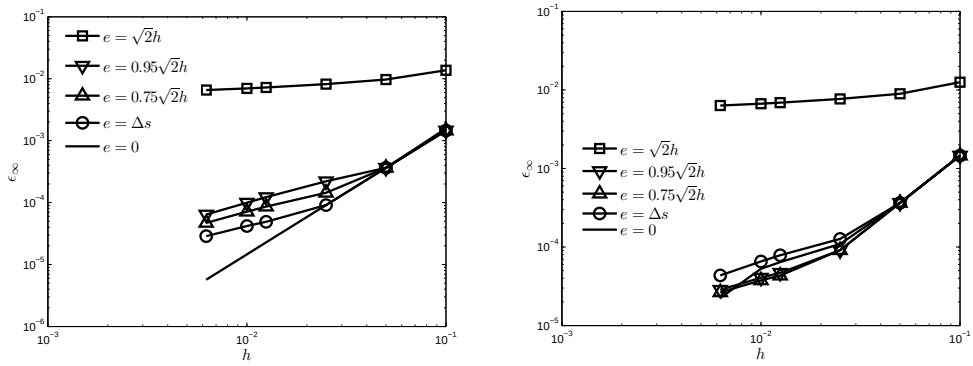

Figure 3.18: Convergence of ϵ_∞ for the tilted elliptic test case with $D_\parallel$ set to zero on vertical line through origin, for varying e, $\varsigma = 10^9, \theta = 1/3\pi, a = 0.15, b = 0.85$, Vandermonde coefficients, (a) VF scheme , (b) CF scheme.

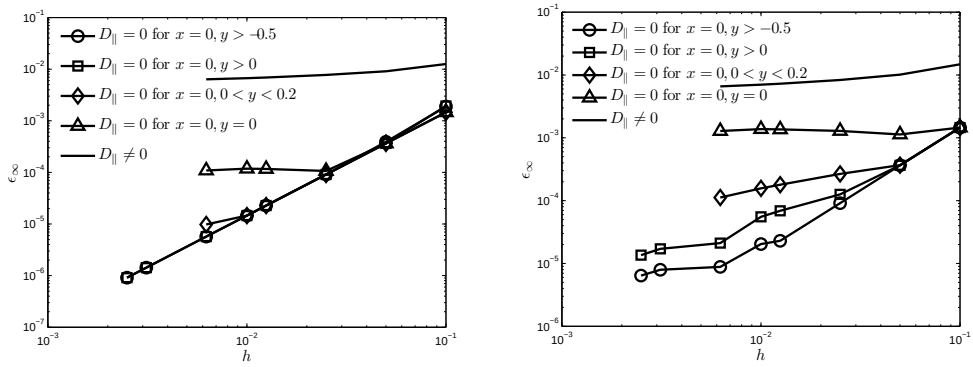

Figure 3.19: Convergence of ϵ_∞ for the tilted elliptic test case for $e = 0$, $\varsigma = 10^9, \theta = 1/3\pi, a = 0.15, b = 0.85$, Vandermonde coefficients, (a) VF scheme , (b) CF scheme.

Here we should note that for $e = 0$ the only difference between the CF scheme and the VF scheme is the treatment of the temperature gradients. Finally we apply the $D_\parallel = 0$ enforcement on the line $x = 0, y > 0$ to the test case given by equation (3.6). Comparing the convergence results shown in figure 3.20 to those in figures 3.8, 3.9 we see a full anisotropy independent recovery of the convergence for $e = 0, \Delta s, \sqrt{2}h$.

Enforcing $D_\parallel = 0$ unsteady

To further test the influence of the closed field line adaptations discussed in section 3.4.3 we approximate the unsteady diffusion equation with a zero initial condition and a source function that produces the Sovinec distribution, i.e. the exact final temperature distribution and source f are given by equation (3.7). We apply $D_\parallel = 0$ on the half

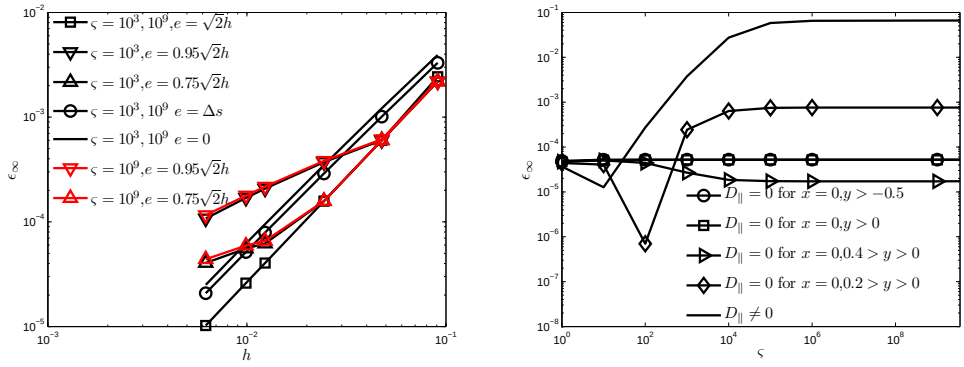

(a) (b)

Figure 3.20: Error ϵ_∞ for test case with solution (3.6) using the VF scheme with Vandermonde coefficients, (a) convergence with $\varsigma = 10^9$ and $D_\parallel = 0$ on $x = 0, y > 0$, (b) anisotropy dependency on 100×100 grid with $e = \Delta s$.

line of the domain for the VF scheme with $e = \Delta s$. For the time-integration we use the Crank-Nicolson scheme. The analytical solution (see Chacón et al. [19]) is given by

$$T(x, y, t) = \frac{1 - \exp\left(-2D_\perp \pi^2 t\right)}{D_\perp} \cos \pi x \cos \pi y. \tag{3.9}$$

In figure 3.21 we show the temporal value of the infinity error norm for an anisotropy

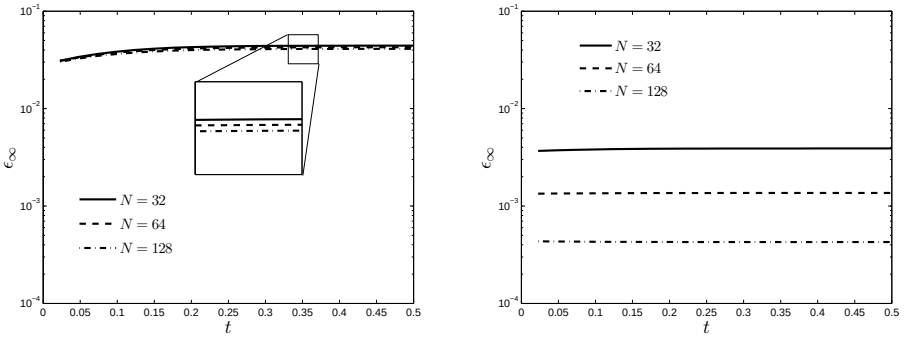

(a) (b)

Figure 3.21: Error ϵ_∞ for unsteady test case (3.9) using the VF scheme with Vandermonde coefficients, $e = \Delta s$, $\Delta t = 1/400$, $\varsigma = 10^6$, (a) without adaptation, (b) with $D_\parallel = 0$ on the half line $x = 0, y > 0$.

level of $\varsigma = 10^6$. It is clear from the figure that setting $D_\parallel$ to zero on the half line greatly improves the accuracy, the accuracy for the 32×32 grid is comparable to the result by Chacón et al. [19].

3.5 Conclusion

The motivation for this research was that $\mathcal{C}_1$ continuous connections of each volume with all of its nine neighbouring volumes would improve the accuracy for large values of the anisotropy. To have varying connectivity we introduced a parameter e. For $0 < e < \sqrt{2}h$ we have octogonal and quadrilateral volumes connected with each other. The results indicate that connectivity plays a role in the accuracy. For all test cases the optimal result in terms of convergence was obtained for either $e = 0$ or $e = \sqrt{2}h$, which is equivalent to the symmetric scheme. The connectivity as such is not of primary importance for maintaining the convergence and accuracy for the extreme anisotropy. Since a variation in e does not require any regridding, it may be beneficial for an unsteady problem to adapt the value of e based on previous timesteps. An extension to three dimensions is possible.

We further conclude that $D_{\|} = 0$ enforcement is a viable approach to improve numerical methods in case of extremely anisotropic problems with closed field lines and zero parallel diffusion. Inserting $D_{\|} = 0$ on a line connecting the O-point with the last closed field line recovers the formal accuracy in all the test problems described in this paper, including the Sovinec test case and the tilted elliptic test case. We also conclude that having a temperature unknown exactly in the O-point can improve the anisotropy independence significantly in case of closed field lines.

4

TENSOR ADAPTED APPROXIMATION METHODS FOR ANISOTROPIC DIFFUSION

In this chapter, we present several locally applied methods to improve existing numerical schemes for general diffusion tensors. We demonstrate the methods with the schemes presented in the previous chapters. The adaptations revolve around special treatments of the diffusion tensor.

4.1 Introduction

Throughout the literature regarding the approximation of anisotropic diffusion the diffusion operator is treated as a tensor, which may be diagonal or full, homogeneously or heterogeneously distributed, symmetric positive definite or not, and continuous or discontinuous, see e.g. the review papers by Droniou [38], Droniou et al. [40, 41].
Arbitrary order mimetic schemes have emerged that allow for distorted grids and (anisotropic) diffusion: a higher order extension of the Hybrid Finite Volume (HFV) scheme by di Pietro et al. [105], the arbitrary order Virtual Element Method (VEM) by Da Veiga et al. [26, 27], the higher order mimetic finite difference methods by Lipnikov and Manzini [83] and Da Veiga et al. [28], the mimetic spectral element method by Kreeft et al. [74] (applied to Darcy flow by Rebelo et al. [106]), the high order mimetic method using B-splines by Hiemstra et al. [59], Discrete Exterior Calculus (DEC) (applied to scalar Darcy flow by Hirani et al. [61]), and earlier, a mixed finite element, finite volume method by Subramanian and Perot [112]. Also, a lot of work has gone into adapting the Discontinous Galerkin method for compatibility with diffusion operators. Arbitrary order DG methods for elliptic and parabolic equations have been presented in literature: Discontinuous Galerkin (DG) methods for elliptic problems have been developed that treat the diffusion equation as a system of first order equations, see Cockburn and Shu [22], Oden et al. [98], and Peraire and Persson [104]. Cockburn et al. [21] devised a unified framework to mixing continuous and discontinous Galerkin methods. For the original diffusion equation, discontinuous Galerkin is applied by Douglas et al. [37], using an interior penalty function, and by Bassi and Rebay [12], using a mixed formulation of the diffusion terms. A recovery based DG method for diffusion was developed by Van Leer and Nomura [117] and Van Leer et al. [116]. Gassner et al. [52] approximate the numerical fluxes by solving the diffusive generalized Riemann problem. An overview is also given by Pietro and Ern [36].

Besides an increase in the order of the basis functions, or the resolution of the grid spacing, one can employ multiple grid levels to enable a multigrid-like solution strategy to improve convergence (see e.g. Antonietti et al. [8]) or the use of flux reconstruction and

post-processing to enhance the accuracy (see e.g. Cangiani and Manzini [18]).

How is the diffusion tensor treated in literature? A common assumption regarding variability is that the diffusion tensor is a cell-wise or edge-wise constant function, and regarding tensor properties that it is SPD. In the above mentioned state-of-the-art mimetic methods the diffusion tensor represents the constitutive relation between the gradient and the divergence operator; it is the only part of the discretisation that constitutes the metric of the problem.

The focus of this chapter is the influence of the diffusion tensor on the accuracy. We suggest three local adaptations: (1) normalisation of the diffusion tensor averages, (2) rotation of the unit direction vectors and (3) regularisation of the diffusion tensor differencing. We emphasize in this chapter that the diffusion tensor is not just an arrayed collection of scalars but rather the result of the coordinate transformation diagonally weighted with the diffusion coefficients.

The symmetric scheme by Günter et al. applied in the previous two chapters shall be denoted as the Symmetric Finite Difference (SFD) scheme. As said in section 2.1 the global MFD scheme is very similar to the Hybrid Finite Volume (HFV) scheme and the Mixed Finite Volume (MFV) scheme (see Droniou [40]), and also very similar to the SFD scheme.

Relation to the Hodge-operator

Consider the following description of the diffusion equation

$$\begin{aligned} \text{Divergence:} \quad & \nabla \cdot \mathbf{q} = f, \\ \text{Constitutive relation:} \quad & \mathbf{q} = \mathbf{D}\nabla T, \\ \text{Gradient:} \quad & \nabla T = \mathbf{g}, \end{aligned} \tag{4.1}$$

which we will solve by applying an approximation for each equation, see e.g. Subramanian and Perot [112]:

$$\begin{aligned} \mathcal{D}\overline{\mathbf{q}} &= \int f dV, \\ \overline{\mathbf{q}} &\approx \mathcal{H}\overline{\mathbf{g}}, \\ \overline{\mathbf{g}} &= \mathcal{G}T, \end{aligned}$$

where

$$\overline{\mathbf{q}} = \begin{pmatrix} \int q_1 dy \\ \int q_2 dx \end{pmatrix}, \quad \overline{\mathbf{g}} = \begin{pmatrix} \int g_1 dx \\ \int g_2 dy \end{pmatrix}. \tag{4.2}$$

We note that the above description of $\mathcal{D}\overline{\mathbf{q}}$ represents the boundary integral $\oint \mathbf{q} \cdot \mathbf{n} ds$ on a rectangular grid. This boundary integral is a result of the Gaussian divergence theorem. In Shashkov and Steinberg [108], Brezzi et al. [17], Hyman et al. [65] and others, a mimetic finite-difference scheme is constructed by defining inner products that allow for the construction of adjoint gradient and divergence operators. Hyman et

al. [68], Liska et al. [90], Brezzi et al. [17] and Lipnikov et al. [84] demonstrate the use of families of inner products. Mimetic discretisation basically implies that the discrete operators mimick certain mathematical properties *exactly*. These mathematical properties are for instance divergence free constraints or conservation of primary quantities (e.g. temperature, density, velocity) and secondary quantities (e.g. energy, enstrophy, helicity).

Assuming T and f are exact, there is a divergence operator $\mathcal{D}$ and a gradient operator $\mathcal{G}$ that allow for an exact solution of the divergence and the gradient part of system (4.1). The symmetric scheme by Günter et al. is very similar to the global Support Operator Method (SOM) for finite-difference schemes (see Shashkov and Steinberg [108]), and the global MFD method (see Hyman et al. [65]) applied for the specific case of a uniform, rectangular Cartesian grid.
The operator for this approximation is contained in the Hodge-operator $\mathcal{H}$. Given that we have the exact descriptions for the divergence operator and the gradient operator, we can state that the Hodge-operator $\mathcal{H}$ contains all the approximations. More specifically, all the approximations are contained in the *interpolation of the flux vector over the cell faces*. The Hodge operator $\mathcal{H}$ contains the relation between local values of the diffusion tensor $\mathbf{D}$ and the flux approximations. The specific treatment of the diffusion tensor is crucial for the characteristics of the final approximation, simply because the only approximation takes place when interpolating the diffusion tensor components on the temperature gradients.

It is not just the importance of the Hodge-operator that explains the focus of this chapter. In the results of chapter 2 we saw that the symmetric finite-difference scheme is not able to maintain formal accuracy for all test problems using Cartesian coordinates, even though the exact solutions are infinitely smooth and the self-adjointness between the flux and the divergence operator is maintained exactly. We know from literature and we saw that the number accuracy (round-off) can play a role in the approximation accuracy due to ill-conditioning of the linear operator. However this ill-conditioning does not explain the anisotropy dependent accuracy for lower resolutions, in particular for the tilted elliptic test problems. The common denominator for all the test problems that posed a challenge for the tested numerical schemes, is the presence of closed field lines. This closedness of field lines is represented in the distribution of the diffusion tensor and thus in the Hodge-operator. The discrete differential operators in a mimetic discretisation are metric free, the Hodge-operator is the only metric-dependent operator. The discrete differential operators only contain the connections between different geometric forms, see e.g. Palha et al. [100]. As said, there is the basic integral identity that leads to arithmetically averaging the flux vector components and this arithmetic operation is reflected in the Hodge operator. We focus exclusively on the diffusion tensor, the averaging of the diffusion tensor and the differencing of the diffusion tensor. First we look at the aspect of normalisation and see if we can find a way to incorporate normalised averages of the unit direction components in the averaged flux values in section 4.3. Second, we locally avoid sign switching in section 4.4. Third, we consider regularisation of the diffusion tensor in section 4.5. Note we still call a method mimetic if we only change the treatment of the constitutive relation between the gradient and the divergence operator, see for instance Rebelo et al. [106], Kreeft et al. [74], Subrama-

nian and Perot [112]. However, to ensure the self-adjointness between the divergence and the flux operator, explicit care needs to be taken with regard to the discrete inner products since that involves the diffusion tensor.

4.2 Relevance of sign transition

There is one important feature present in all presented test cases that gives convergence problems for high levels of anisotropy: *closed field lines*. The presence of closed field lines leads to the existence of a singular point through which the unit direction vector and thus the diffusion tensor changes discontinuously. This discontinuous change in the unit direction vector leads to a local zeroth order error of the **b**-derivatives. More importantly, we know that the following will occur; $|\sum_i \mathbf{b}_i| < \sum_i |\mathbf{b}_i|$, i.e. arithmetic averaging is inappropriate.
As said, methods in literature commonly assume that the diffusion tensor is SPD (see e.g. Jacq et al. [70, 71], Maire and Breil [92], Costa et al. [24], Rebelo et al. [106]). For square symmetric matrices that are SPD all eigenvalues are positive. We have

$$|\mathbf{D} - \lambda\mathcal{I}| = 0 \Longrightarrow \quad \lambda_{\pm} = (D_{11} + D_{22})/2 \pm \sqrt{1/4\,(D_{11} + D_{22})^2 - \left(D_{11}D_{22} - D_{21}^2\right)}.$$

Assuming $\varsigma \to \infty$ this leads to

$$\lambda_{\pm} = D_{\parallel}/2 \left(1 \pm \sqrt{4(b_1 b_2)^2 + (b_1^2 - b_2^2)^2}\right).$$

So $\lambda_+ = D_{\parallel}, \lambda_- = 0$ for $b_1 b_2 \neq 0$. This implies that for $\varsigma \to \infty$ the diffusion tensor is at least symmetric positive semi-definite regardless of the geometry. Thus the linear operator becomes singular for $\varsigma \to \infty$. This result of positive eigenvalues is what one would expect based on physical arguments, a reversal of the largest eigenvalue sign would imply that heat locally flows in the direction of a positive temperature gradient.

The diffusion tensor is elliptic (and thus coercive see e.g. McLean [93]) if there is a $\gamma > 0$ for which it holds that $\mathbf{v} \cdot \mathbf{D}\mathbf{v} > \gamma ||\mathbf{v}||^2, \quad \forall \mathbf{v} \in \mathcal{R}^d$:

$$\mathbf{v} = [a, b]^T, \quad \mathbf{v} \cdot \mathbf{D}\mathbf{v} = a^2 D_{11} + b^2 D_{22} + 2ab D_{21} > \gamma \left(a^2 + b^2\right).$$

This requirement is fulfilled for $\text{sign}(b_1) = \text{sign}(b_2)$, otherwise, ellipticity **cannot** be guaranteed since $(D_{\parallel} - D_{\perp})|b_1 b_2|$ can be larger than $D_{\parallel} b_1^2 + D_{\perp} b_2^2$ and $D_{\parallel} b_2^2 + D_{\perp} b_1^2$ for large enough values of the anisotropy: For $\varsigma \to \infty$, the aforementioned requirement reduces to $(a^2 b_1^2 + b^2 b_2^2) > -2ab b_1 b_2$. Basically, assuming $\varsigma > 1$, whenever $b_1 b_2 < 0$ the diffusion tensor is not coercive. The diffusion tensor is strongly elliptic if there are two positive constants α and β (see e.g. da Veiga et al. [29]) such that

$$\alpha ||\mathbf{v}||^2 \leq \mathbf{v} \cdot \mathbf{D}\mathbf{v} \leq \beta ||\mathbf{v}||^2, \quad \mathbf{v} \in \mathcal{R}^d.$$

This is also not fulfilled in the general case for anisotropic diffusion coefficients. In literature regarding MFD, HFV, MEFD and other methods that build on the weak formulation, the diffusion tensor is assumed strongly elliptic and (strictly) positive definite to enable a proof of existence and uniqueness of the weak solution (see e.g. Droniou [38, 40]).

We further demonstrate the relevance of sign-switching, firstly by considering an open field line case compared to a closed field line case, and secondly, in the following section, by applying normalised averaging to the cell-centered symmetric finite difference method.

Suppose that we have constant diffusion coefficients throughout the domain and the field lines are completely circular. Also suppose that flux points are exactly coinciding with the axes through the O-point of the circular distribution. Now imagine we shift the location of the O-point in x- and y-direction with a value Δh smaller than h. We have three situations:
(1) $\Delta h = 0$, the flux points are exactly coinciding with the circle axes, all the unit direction vectors in each average flux are in the same quadrant.
(2) $\Delta h < \frac{1}{2}h$, the unit direction vectors around the circle axes are in different quadrants. Hence, the local arithmetic averaging is incorrect and introduces an error.
(3) $\Delta h = \frac{1}{2}h$, now the unit direction vectors around the circle axes have the same angle in magnitude but a different sign. When arithmetically averaging the diffusion tensor values the off-diagonal terms drop out. This situation is fortuitous as it requires that the unit direction vectors have exactly the same absolute angle with respect to the nearest circle axis. We see from figure 4.1 that the convergence is fourth-order initially until

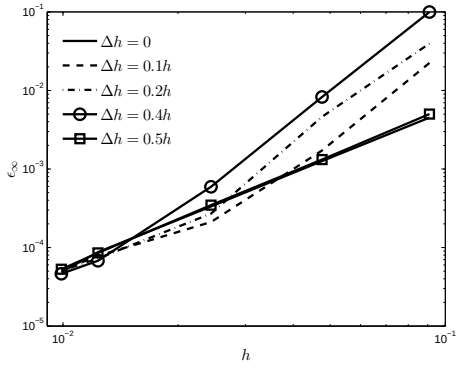

Figure 4.1: Mixed open/closed field line problem using the SFD scheme with $\varsigma = 10^9$, with various offsets of the O-point.

the accuracy is restored at about $N = 100$. This can be explained as follows. Due to shifting the O-point we have induced a geometrical error that is reduced exponentially for a linearly decreasing value of h. Hence the total error is superconvergent until the induced error is much smaller than the other error sources. Also, the temperature gradient perpendicular to the circle-axes approaches the parallel temperature gradient, which for this particular example is zero. This will keep the error contribution small in an absolute sense. It is easy to see that tilted elliptic field line distributions are more challenging. The temperature derivatives belonging to the off-diagonal terms are no longer approaching the parallel temperature gradient and are thus larger than zero for $h \to 0$. Also, it is possible that both averages in x- and y-direction involve unit direction vectors in different quadrants. The quadrant transitions now occur off-axis, see figure

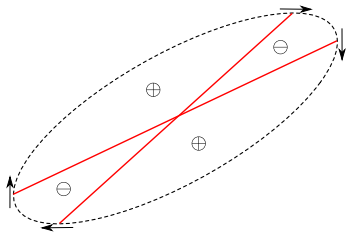

Figure 4.2: Elliptic field lines, off-axis quadrant transitions of unit direction vectors transition lines shown in red, and sign of off-diagonal diffusion tensor components $D_{12} = D_{21}$ is indicated with $\oplus$ and $\ominus$.

4.2. In figure 4.3a we see the results of the SFD scheme for three different angles of rota-

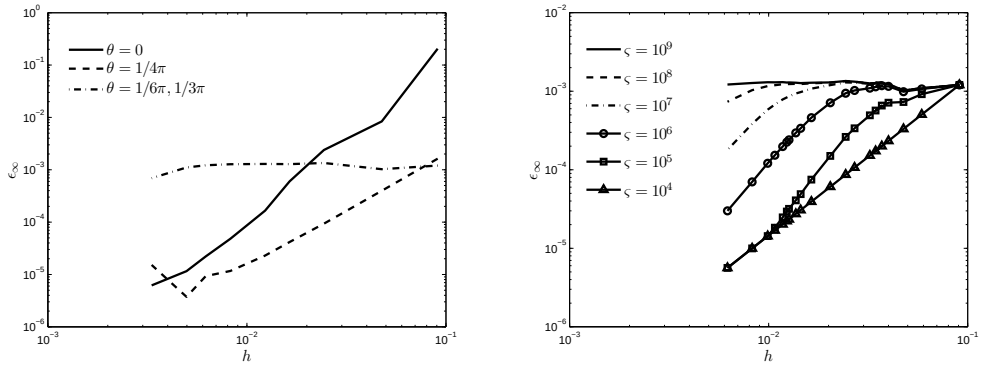

(a) (b)

Figure 4.3: Elliptic field line problem approximated with the SFD scheme, error ϵ_∞ convergence, (a) for different values of θ, $\varsigma = 10^9$, (b) for $\theta = 1/6\pi$ and several values of ς.

tion θ of the elliptic field line distribution with $a = 0.15, b = 0.85$ and $\varsigma = 10^9$. For $\theta = 0$ we see again fourth-order convergence, tending towards the accuracy of the $\theta = 1/4\pi$ result after which it continues with second order. The cause for this behavior is likely the same as for the circular field line case. For all angles $\theta = [\pi(n-1)/4\,, \pi n/4]$ where $n = 1, \ldots 4$ we get zeroth order convergence for moderate resolutions, which means that the error causing the error offset stays dominant for decreasing step size h. In figure 4.3b we show the results for varying levels of anisotropy. For an increasing level of anisotropy the onset of the asymptotic second-order convergence is clearly postponed. In figures 4.4a and 4.4b we show the local error approximations for $\theta = 1/4\pi$ and $\theta = 1/6\pi$ respectively. The only qualitative difference between the results for the two values of θ is the asymmetry of the local error, the magnitude of the local error is similar. Note that the transition lines are clearly visible in both figures 4.4a and 4.4b. The symmetry of the local error does not by itself explain the good convergence for $\theta = 1/4\pi$ because the asymmetric finite-difference scheme has a symmetric distribution of the local error as well.

For the circular problem and for the elliptic problem with $\theta = n/2\pi\,, n = 0, \ldots 4$, the asymmetric scheme by Günter et al. yields areas of positive and negative valued local

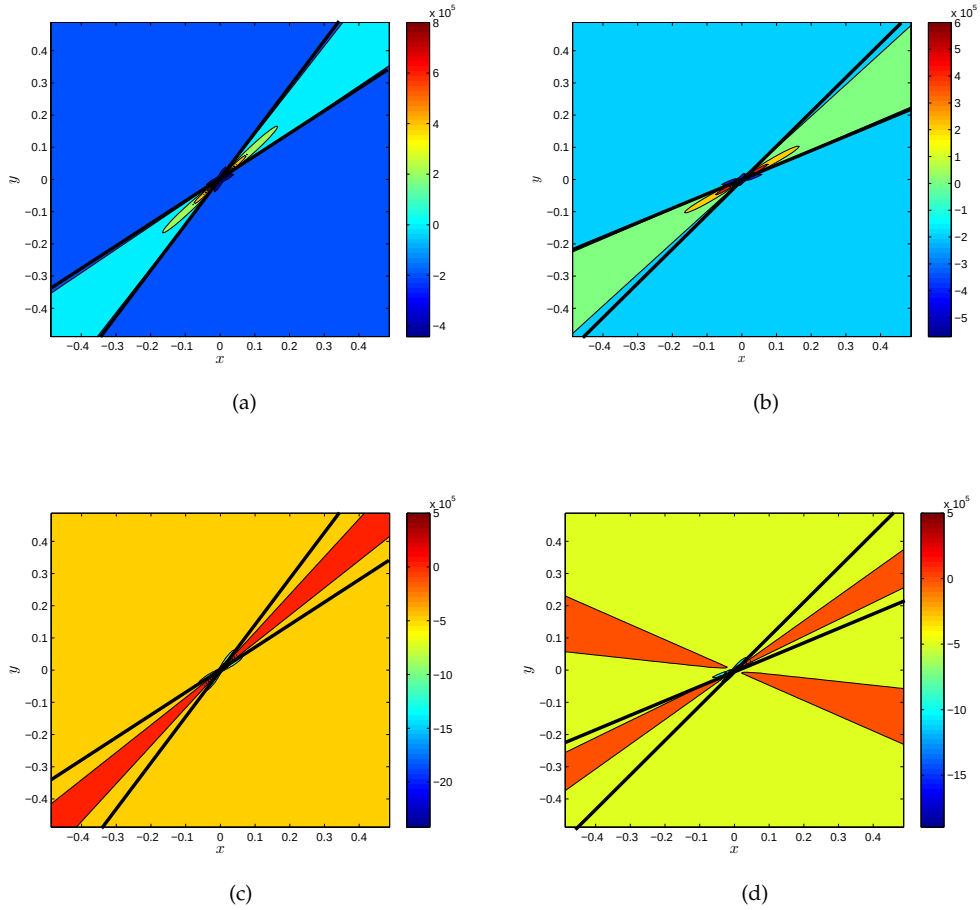

Figure 4.4: Elliptic field line problem with $\varsigma = 10^9$, local approximation error ϵ_{local} where $\epsilon_{local} = \mathcal{L}\left(\overline{T}_{exact} - \overline{T}_{approx}\right)$ with $\mathcal{L}$ being the diffusion operator, the transition line is indicated here by a thick black line, (a) SFD $\theta = 1/4\pi$, (b) SFD $\theta = 1/6\pi$ (c) asymmetric scheme $\theta = 1/4\pi$, (d) asymmetric scheme $\theta = 1/6\pi$.

error that are not of equal size if $\varsigma > 1$. More specifically, the arc lengths along the circle or elliptic lines are not equal. For the symmetric finite-difference scheme these arc lengths seem to be identical in size. Ostensibly this explains the difference in convergence behavior between the symmetric and the asymmetric scheme. Since, if we integrate the local approximation of the diffusion along the field line, we get

$$\text{symmetric finite differences: } \int^{2\pi r} \tilde{\mathbf{q}} \cdot \mathbf{n} ds = 0,$$

$$\text{asymmetric finite differences: } \int^{2\pi r} \tilde{\mathbf{q}} \cdot \mathbf{n} ds \neq 0 \propto \varsigma,$$

where $\tilde{\mathbf{q}}$ is the approximation of the flux. For $\varsigma = 1$ we do not have regions of different sign for the local error. This means that, integrated along the field line we do not have a resultant error that scales with the level of anistropy.

So what explains the difference in accuracy and convergence between the asymmetric scheme and the symmetric finite-difference scheme in this elliptic case? We see in figure 4.2 that the transition lines outline the regions in which the off-diagonal diffusion tensor values are negative or positive. From figure 4.4a it is clear that for $\theta = 1/4\pi$ the sign of the local error is everywhere the reverse of the sign of the off-diagonal diffusion tensor value. Clearly, from figure 4.4b we see that for $\theta = 1/6\pi$ this connection between the sign of the local error and the sign of the off-diagonal diffusion tensor values is not exact. We expect this is the case for all angles $\theta = [\pi(n-1)/4\ , \pi n/4]$ where $n = 1, \ldots 4$. The explanation is now the same as before. For the symmetric scheme, the four regions with positive and negative sign cancel each other when integrated along a field line. The cancellation is only possible because the regions of equal local error sign are directly opposite to each other, in quadrants with the same sign for $b_1 b_2$, as is indicated by the transition lines enclosing the region of different sign of the local error. The moment we rotate the elliptic distribution, there is a small gap between the transition line and the boundaries of the region of different sign for the local error. These gaps, visible between the black transition line and the region of positive sign in figure 4.4a result in a non-zero value of the local approximation integrated along the field line. This value scales with the level of anisotropy ς.

4.3 Normalisation

We start with the aspect of normalisation. In literature the normalisation of the diffusion tensors is done implicitly by using the (norm of the) matrix-vector product $\mathbf{D}\,\mathbf{n}$ to construct the flux approximation, see e.g. Morel et al. [96], Hyman et al. [67], Breil and Maire [15], Eymard et al. [45] and Lipnikov and Shashkov [86]. If the diffusion tensor is viewed as a matrix filled with scalars, in that sense arithmetic or harmonic averaging are correct. However, the diffusion tensor is *not just a collection of scalars*, it is the result of a geometric operation working on the diffusion coefficients. We consider the diffusion tensor as the result of a rotational transformation of the diffusion coefficients: The diffusion coefficients are seen as weighted coordinate elements.

4.3.1 *Cell-centered symmetric finite-difference method*

To demonstrate the importance of normalised versus non-normalised averaging of the diffusion tensor we apply the symmetric scheme on a colocated grid, i.e. the temperature unknowns and the diffusion tensor values are located in the same points. To apply the symmetric scheme we have to average the diffusion tensor values from the temperature nodes to the flux points. We apply both arithmetic averaging and normalised averaging. We see in figure 4.5 that for the Sovinec test case the error in perpendicular diffusion scales directly with the level of anisotropy if we apply arithmetic averaging of the diffusion tensors. In the same figure we see that the normalised averaging dramatically improves the accuracy. This explains the result of section 2.5.2 where a locally symmetric method with weighted averaging of the diffusion tensor values gives better results than the SFD scheme.

For the aligned methods we rely heavily on the interpolation of the unit direction vec-

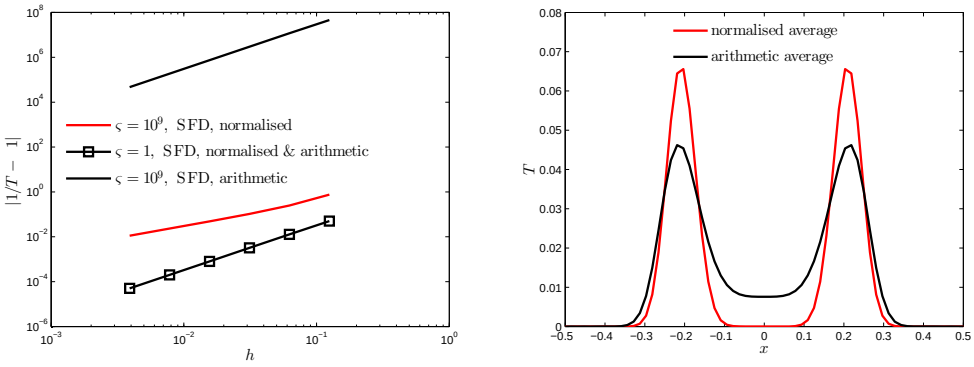

(a) (b)

Figure 4.5: (a) Steady: perpendicular accuracy Sovinec test case (b) Unsteady: Temperature cross section of Gaussian distribution diffused along circular field lines, with $\sigma = 0.05$, radius$= 0.15\sqrt{1/2}$, $t_{end} = 0.5$, $D_{\parallel} = 1, D_{\perp} = 0, 64 \times 64$ grid.

tors and so the question arises whether normalisation can increase the accuracy of these methods.

4.3.2 *Normalized averaging of unit direction vectors*

We look at the aspect of normalised averaging of diffusion tensors. The symmetric scheme by Günter et al. has the following approximation for the divergence

$$\nabla \cdot \mathbf{q} = \frac{(q_1)_{i+\frac{1}{2},j+\frac{1}{2}} + (q_1)_{i+\frac{1}{2},j-\frac{1}{2}} - (q_1)_{i-\frac{1}{2},j+\frac{1}{2}} - (q_1)_{i-\frac{1}{2},j-\frac{1}{2}}}{2\Delta x} + \frac{(q_2)_{i+\frac{1}{2},j+\frac{1}{2}} + (q_2)_{i-\frac{1}{2},j+\frac{1}{2}} - (q_2)_{i-\frac{1}{2},j-\frac{1}{2}} - (q_2)_{i+\frac{1}{2},j-\frac{1}{2}}}{2\Delta y},$$

where the nomenclature is given in figure 2.2. I.e. it requires the weighted averaging of diffusion tensor values, where the weighting terms are given by the gradient components. In a finite-difference sense the discrete divergence is a result of the sum of the differentials of averaged flux values. In the finite-volume and discontinuous Galerkin sense, the discrete divergence is the summation of flux integrals along the boundary of the volume. For the finite-volume approximation on a rectangular domain in x, y-coordinates we have

$$\int_V \nabla \cdot \mathbf{q} dV = \oint_S \mathbf{q} \cdot \mathbf{n} dS = \int_{i+\frac{1}{2},j} q_x dy - \int_{i-\frac{1}{2},j} q_x dy + \int_{i,j+\frac{1}{2}} q_y dx - \int_{i,j-\frac{1}{2}} q_y dx,$$

where the x, y subscripts denote the x, y-components of the flux vector. We know that these line integrals can be represented as an infinite sum of flux values, e.g.

$$\int_{-\frac{h}{2}}^{\frac{h}{2}} q_x dy = \sum_{k=1}^{\infty} q_x(y_k)\Delta y, \quad y_k = -\frac{h}{2} + k\,\Delta y,$$

which is approximated by a numerical quadrature

$$\int_{-\frac{h}{2}}^{\frac{h}{2}} q_x dy \approx \frac{h}{2}\sum_{k=1}^{p}\omega_k q_x(y_k), \quad \frac{1}{2}\sum\omega = 1.$$

The following equivalence holds:

$$\int_{-\frac{h}{2}}^{\frac{h}{2}} q_x dy = \overline{q_x}h, \tag{4.3}$$

i.e. the line integrals can be represented by an averaged flux value times the surface of the boundary. These averaged flux values have the form

$$\overline{q_x} = \overline{D_{11}T_x + D_{21}T_y}, \quad \overline{q_y} = \overline{D_{21}T_x + D_{22}T_y},$$

where the averaging is arithmetic. For this particular problem the arithmetic averaging is a result of the line or surface integration of an interpolation of flux vector components. In general, this interpolation is a linear combination of flux vector components on the line or surface over which the integration takes place. It *must* be a linear combination of the flux vector components for the simple reason that otherwise we cannot construct a linear operator. Furthermore, applying harmonic averaging to the diffusion tensor values gives an unbounded result since all the diffusion tensor components are allowed to be zero-valued. For these reasons weighted harmonic averaging of the diffusion tensor is not considered. Rather, we limit the possible application of harmonic averaging to the diffusion coefficients.

We know that simply arithmetically averaging flux vectors is *not always correct* since $|\sum_i \mathbf{b}_i| < \sum_i |\mathbf{b}_i|$ for every set of vectors that are not in the same quadrant. So for the general case we have to apply a normalised averaging procedure. For arithmetic averaging we have to use $\overline{\mathbf{b}} = \sum_{i=1}^{N}\mathbf{b}_i / |\sum_{i=1}^{N}\mathbf{b}_i|$. This requires an explicit formulation of the averaging procedure so that we can specifically apply a normalized average of the unit direction vector. We readily see that we cannot directly apply normalisation of the unit direction vector value as it is multiplied by the unknown temperature gradient, i.e. normalisation can only be applied by considering a previous solution.

Note that the diffusion tensor has the following origin

$$\mathbf{D} = \mathcal{R}\ \mathrm{diag}(D_{\parallel}, D_{\perp})\mathcal{R}^T, \quad \mathcal{R} = [b_1, -b_2; b_2, b_1]\,,$$

i.e. the result of a local coordinate transformation for a rotation, in this case given for Cartesian coordinates. If we average this diffusion tensor, we also average the rotation matrices. The question is, can we simply use arithmetic averaging, i.e. is it correct that

$$\overline{\mathbf{D}} = 1/N\sum_{i=1}^{N}\mathcal{R}_i\ \mathrm{diag}(D_{\parallel}, D_{\perp})_i\mathcal{R}_i^T\,?$$

We answer this question by stating that the result of this averaging should be such that $\overline{\mathbf{D}}$ can be written as

$$\overline{\mathbf{D}} = \overline{\mathcal{R}}\ \mathrm{diag}(\overline{D_{\parallel}}, \overline{D_{\perp}})\overline{\mathcal{R}}^T, \tag{4.4}$$

where $\overline{\mathcal{R}}$ must fulfill the basic identity $||\overline{\mathcal{R}}|| = 1$. In other words we introduce the notion that the averaged diffusion tensor must fulfill basic identities. This is not fulfilled by arithmetic averaging as we get the diffusion tensor values

$$\overline{\mathbf{D}} = 1/N \begin{bmatrix} \sum_i (D_\parallel b_1^2)_i + (D_\perp b_2^2)_i & \sum_i \left[(D_\parallel - D_\perp) b_1 b_2 \right]_i \\ \sum_i \left[(D_\parallel - D_\perp) b_1 b_2 \right]_i & \sum_i (D_\parallel b_2^2)_i + (D_\perp b_1^2)_i \end{bmatrix},$$

from which we cannot retrieve the form (4.4). This will apply for any transformation matrix $\mathcal{R}$. An averaging procedure which does retrieve the form (4.4) starts with the notion that

$$\mathcal{R} = (\mathbf{b}\, \mathbf{b}_\perp), \quad \mathcal{R}^T = \begin{pmatrix} \mathbf{b}^T \\ \mathbf{b}_\perp^T \end{pmatrix},$$

and together with the following procedure to average vectors

$$\overline{\mathbf{b}} = \sum_i \omega_i \mathbf{b}_i / \left| \sum \omega_i \mathbf{b}_i \right|,$$

we can write

$$\overline{\mathbf{D}} = \overline{\mathcal{R}}\ \mathrm{diag}(\overline{D_\parallel}, \overline{D_\perp}) \overline{\mathcal{R}^T},$$
$$\overline{\mathcal{R}} = \frac{1}{|\sum \mathbf{b}|} \left(\sum \mathbf{b} \sum \mathbf{b}_\perp \right), \overline{\mathcal{R}^T} = \frac{1}{|\sum \mathbf{b}|} \begin{pmatrix} \sum \mathbf{b}^T \\ \sum \mathbf{b}_\perp^T \end{pmatrix},$$

with either arithmetic or harmonic averaging for the diffusion coefficients $D_\parallel$ and $D_\perp$.

In the divergence approximation we have the gradient approximations as weights. So we get

$$\overline{\mathcal{R}} = \frac{1}{|\sum \omega \mathbf{b}|} \left(\sum \omega \mathbf{b} \sum \omega \mathbf{b}_\perp \right), \overline{\mathcal{R}^T} = \frac{1}{|\sum \omega \mathbf{b}|} \begin{pmatrix} \sum \omega \mathbf{b}^T \\ \sum \omega \mathbf{b}_\perp^T \end{pmatrix},$$

where ω represents the gradient approximations T_x, T_y. As the weights are solution dependent, this normalised symmetric finite difference method is inherently non-linear. The application of normalised averaging requires an iterative procedure where the solution of the previous iteration or time step is used to estimate the correct averaged diffusion tensor values. Note that the normalised averaging of the diffusion tensor values that is suggested here is not entirely consistent as $\overline{A}\,\overline{B} \neq \overline{A\,B}$, see appendix F. Hence, normalised averaging should be applied with care.

4.3.3 *Application to symmetric finite-difference method*

We should note that we do not have full diffusion tensor averaging but rather the averaging of diffusion tensor components. I.e. first we have to find the correct averaged diffusion tensor and then we extract the diffusion tensor components. For example,

averaging $(D_{11}T_x)_{ur}$ and $(D_{11}T_x)_{dr}$, where for convenience the subscripts *ur* and *dr* indicate the locations $(i+1/2, j+1/2)$ and $(i+1/2, j-1/2)$ respectively, yields

$$\overline{(T_x\mathbf{D})_{ur}, (T_x\mathbf{D})_{dr}} = \overline{T}_x\overline{\mathcal{R}}\ \mathrm{diag}(\overline{D_\parallel}, \overline{D_\perp})\ \overline{\mathcal{R}}^T,$$
$$\overline{\mathcal{R}} = \frac{1}{|(T_x\mathbf{b})_{ur} + (T_x\mathbf{b})_{dr}|}\left[(T_x\mathbf{b})_{ur} + (T_x\mathbf{b})_{dr},\quad (T_x\mathbf{b}_\perp)_{ur} + (T_x\mathbf{b}_\perp)_{dr}\right],$$

and similarly for all other terms. For the diffusion coefficients we can choose a different averaging, for example weighted arithmetic or harmonic averaging. The SFD scheme is now written as

$$\begin{aligned}\nabla\cdot\mathbf{q} =& \frac{\overline{(D_{11}T_x)_{ur}, D_{11}T_x)_{dr}} + \overline{(D_{21}T_y)_{ur}, D_{21}T_y)_{dr}}}{\Delta x}\\ &- \frac{\overline{(D_{11}T_x)_{ul}, D_{11}T_x)_{dl}} + \overline{(D_{21}T_y)_{ul}, D_{21}T_y)_{dl}}}{\Delta x}\\ &+ \frac{\overline{(D_{21}T_x)_{ur}, D_{21}T_x)_{ul}} + \overline{(D_{22}T_y)_{ur}, D_{22}T_y)_{ul}}}{\Delta y}\\ &- \frac{\overline{(D_{21}T_x)_{dr}, D_{21}T_x)_{dl}} + \overline{(D_{22}T_y)_{dr}, D_{22}T_y)_{dl}}}{\Delta y},\end{aligned}$$

and we denote this as the *normalised symmetric finite difference* (NSFD) method. The apparent downside is the possibility of a division by zero when either T_x or T_y is zero. In the original SFD scheme the derivative approximations are weighted with the specific diffusion tensor values, however we want to retrieve the form given by equation (4.4). To approximate the original weighting we take the L_2 norm of the diffusion tensors,

$$\overline{(T_x)_{ur}, (T_x)_{dr}} = \frac{||\mathbf{D}_{ur}||(T_x)_{ur} + ||\mathbf{D}_{dr}||(T_x)_{dr}}{||\mathbf{D}_{ur}|| + ||\mathbf{D}_{dr}||}. \tag{4.5}$$

We apply one average of the gradient approximation to the whole tensor, for instance the norm-based averaging in equation (4.5). To enforce weighting of the temperature gradient approximation one can apply weighted tensor based averaging, for instance

$$\overline{(T_x)_{ur}, (T_x)_{dr}}\Big|_{D_{11}} = \frac{(D_{11}T_x)_{ur} + (D_{11}T_x)_{dr}}{(D_{11})_{ur} + (D_{11})_{dr}},$$
$$\overline{(T_x)_{ur}, (T_x)_{dr}}\Big|_{D_{21}} = \frac{(|D_{21}|T_x)_{ur} + (|D_{21}|T_x)_{dr}}{|(D_{21})_{ur}| + |(D_{21})_{dr}|},$$

where we take absolute values of the off-diagonal diffusion tensor values to account for the fact that D_{21} can change sign. We are only interested in absolute weighting since the directionality is taken care of by the averaged rotation matrix. This weighted tensor based averaging has as a consequence that we no longer fulfill the form given by equation (4.4). Instead we fulfill the form

$$\overline{(D_{ij}T_x)_{ur}, (D_{ij}T_x)_{dr}} = \overline{(T_x)_{ur}, (T_x)_{dr}}\Big|_{D_{ij}}\ \left[\frac{1}{|\mathbf{b}_{ur} + \mathbf{b}_{dr}|^2}\overline{\mathcal{R}}\ \mathrm{diag}(\overline{D}_\parallel, \overline{D}_\perp)\ \overline{\mathcal{R}}^T\right]_{i,j}.$$

If we remove the gradient approximations as weights all together we get

$$\overline{(D_{11}T_x)_{ur},(D_{11}T_x)_{dr}} = \frac{1}{|\mathbf{b}_{ur}+\mathbf{b}_{dr}|^2}\overline{(T_x)_{ur},(T_x)_{dr}}\left\{\overline{D}_{\parallel}\left[(b_1)_{ur}+(b_1)_{dr}\right]^2 + \overline{D}_{\perp}\left[(b_2)_{ur}+(b_2)_{dr}\right]^2\right\},$$

$$\overline{(D_{22}T_x)_{ur},(D_{22}T_x)_{dr}} = \frac{1}{|\mathbf{b}_{ur}+\mathbf{b}_{dr}|^2}\overline{(T_x)_{ur},(T_x)_{dr}}\left\{\overline{D}_{\perp}\left[(b_1)_{ur}+(b_1)_{dr}\right]^2 + \overline{D}_{\parallel}\left[(b_2)_{ur}+(b_2)_{dr}\right]^2\right\},$$

$$\overline{(D_{21}T_x)_{ur},(D_{21}T_x)_{dr}} = \frac{1}{|\mathbf{b}_{ur}+\mathbf{b}_{dr}|^2}\overline{(T_x)_{ur},(T_x)_{dr}}\left\{(\overline{D}_{\parallel}-\overline{D}_{\perp})\left[(b_1)_{ur}+(b_1)_{dr}\right]\left[(b_2)_{ur}+(b_2)_{dr}\right]\right\}.$$

This involves at least the norm of the averaged vector and does not require an iterative procedure. Recall that the above average can be written in the form given by equation (4.4), specifically

$$\overline{(\mathbf{D}T_x)_{ur},(\mathbf{D}T_x)_{dr}} = \frac{\overline{(T_x)_{ur},(T_x)_{dr}}}{|\mathbf{b}_{ur}+\mathbf{b}_{dr}|^2}\,\overline{\mathcal{R}}\,\mathrm{diag}(\overline{D}_{\parallel},\overline{D}_{\perp})\,\overline{\mathcal{R}}^T,$$

where $\frac{1}{|\mathbf{b}_{ur}+\mathbf{b}_{dr}|}||\overline{\mathcal{R}}|| = 1$. We call this method *unweighted symmetric finite difference* (USFD) as it not weighted with the temperature gradients. We will test two averaging methods of the gradient approximations, arithmetically weighted with the diffusion tensor norms and arithmetically weighted with the specific diffusion tensor components. As a test case we consider the tilted elliptic temperature distribution described in section 2.4.4, equation (3.8). We apply the normalised averaging along the transition line.

From the results for the tilted elliptic distribution in figure 4.6 we see a slight improve-

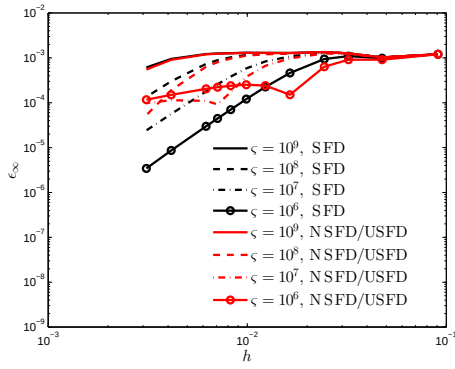

Figure 4.6: Convergence of ϵ_∞ error for tilted elliptic test case with $a = 0.15, b = 0.85, \theta = 1/3\pi$.

ment of the NSFD and USFD methods compared to the SFD scheme for an intermediate resolution range. However, second-order convergence is not achieved and for higher resolutions the convergence stagnates. The separation of the gradient approximation and diffusion coefficients is the limiting factor in terms of accuracy since we are forced

to release the specific tensor weighting of the gradient approximations. Interesting to note is that the results for the USFD method are identical to NSFD.

4.4 Nonnegative tensor values

Instead of applying the normalised averaging from the previous section we aim at resolving an issue underlying the occurrence of the inequality, namely a local change in sign of the off-diagonal diffusion tensor component. Loosely based on the concept of nonnegative finite differencing introduced by Weickert [120] we state a general assertion regarding the differencing of the diffusion tensor. The construction of a nonnegative scheme starts with the following splitting of the diffusion operator

$$\nabla \cdot \mathbf{D} \cdot \nabla T = \partial_{e_{\beta_0}} \left(\alpha_0 \partial_{e_{\beta_0}} T \right) + \partial_{e_{\beta_1}} \left(\alpha_1 \partial_{e_{\beta_1}} T \right) + \partial_{e_{\beta_2}} \left(\alpha_2 \partial_{e_{\beta_2}} T \right),$$

where the α's are weights and the β's are angles with respect to the coordinate axes (see figure 4.7). Here a nonnegative scheme can be obtained *if* for the angles $\beta_0, \beta_k, \beta_{2m}$ we can find positive values for $\alpha_0, \alpha_k, \alpha_{2m}$, where $(2m+1)^2$ is the stencil size, and β_k is an angle for $k = 1 \ldots 2m-1$. This nonnegative splitting for a rectangular grid is possible if (see Weickert [120])

$$\min\left(D_{11} - D_{21}\cot(\beta_k), D_{22} - D_{21}\tan(\beta_k)\right) \geq 0, \quad k = 1, \ldots 2m-1.$$

This does not exclude cases with a combination of $D_{\parallel}/D_{\perp} \gg 1$ and general values of the unit direction vector. However, it does require an increase in stencil size. If the stencil size is increased the maximum and minimum value of β_k is increased and decreased respectively and so the minimum value for $\cot(\beta_k)$ and $\tan(\beta_k)$ is decreased, thus allowing larger anisotropy ratios. Roughly for $D_{\parallel}/D_{\perp} > 10^3$ the required minimum and maximum value is about 9° and 81° respectively. These angles correspond to a stencil size of roughly $(2/\cos\beta - 1)^2 = 12 \times 12$. From this we can derive a quasi-uniform grid with four support nodes within a distance $h/\cos\beta$ of each original node. This way we end up with 45 stencil points instead of 144. Le Potier [79] applied a similar idea to the meshless Generalised Finite Difference Method (GFDM) with a fixed number of 16 stencil nodes. He suggested as angular requirement $\beta = \arctan(\lambda_1/\lambda_2)$. The GFDM approach by Le Potier demonstrated first order accurate monotonous results for moderate levels of anisotropy ($\varsigma \approx 1000$). Weickert's method is second-order accurate, with however a large-stencil requirement on a uniform grid. Le Potier's method is meshless, but it is limited to first-order accuracy. Also, we question the invertability of the Vandermonde matrix for β close to zero or $\pi/2$ as the distance between the points near the local coordinate axes goes to zero, which is the case for extreme levels of anisotropy.

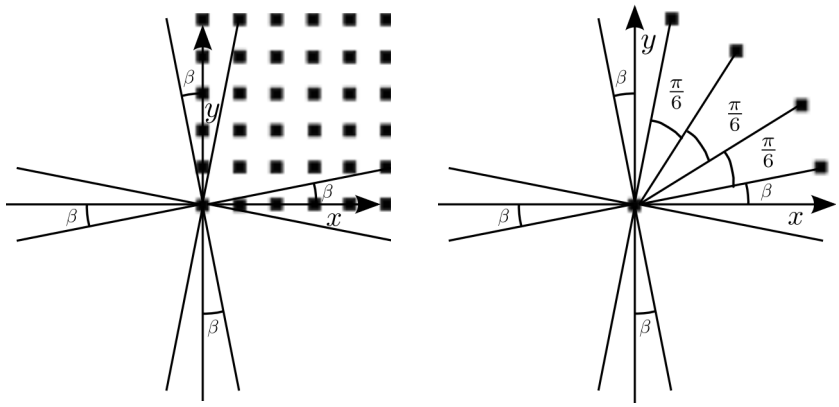

Figure 4.7: Two grid methods to obtain a Discrete Maximum Principle (DMP) satisfying linear operator for high level of anisotropy, (a) uniform grid, FDM, see Weickert [120], (b) meshless, GFDM, see Le Potier [79].

The difference between the two approaches is shown in figure 4.7. We leave this as a suggestion for further research. Although the derivation of the nonnegative method by Weickert is rather involved in a goniometric sense, the resulting change of the linear operator is solely due to the addition of absolute values of the off-diagonal diffusion tensor values. The change in sign of $b_1 b_2$ and subsequently of the off-diagonal coefficients of the linear operator contributions are an artefact of sign-switching of the unit direction vector component between quadrants.

Consider the following: We have two vectors $\mathbf{b}_l$ and $\mathbf{b}_r$, the former vector lies in the first quadrant and the latter vector lies in the fourth quadrant (see figure 4.8). We write

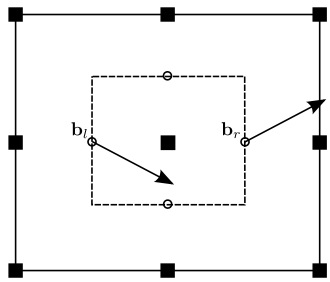

Figure 4.8: Vectors in different quadrants.

the vectors as follows

$$\mathbf{b}_l = \begin{pmatrix} \sqrt{A_l} \\ \sqrt{B_l} \end{pmatrix}, \quad \mathbf{b}_r = \begin{pmatrix} \sqrt{A_r} \\ -\sqrt{B_r} \end{pmatrix},$$

and without loss of generality we assume that $A_l = A_r = A$ and $B_l = B_r = B$. We know that we have a sign change of $b_1 b_2$ going from l to r. This sign change persists for $A \to 1, B \to 0$, we have that

$$(b_1 b_2)_l = -(b_1 b_2)_r.$$

This means that if we write the approximation of $\partial_x(D_{\parallel}b_1b_2T_y)$ with central differences we get

$$\partial_x(D_{\parallel}b_1b_2T_y) \approx \frac{(-b_1b_2((D_{\parallel}T_y)_r + (D_{\parallel}T_y)_l)}{2h}.$$

In general, in the vicinity of quadrant transitions we have

$$\partial_x(D_{\parallel}b_1b_2T_y) \approx \frac{(\pm\overline{b_1b_2}((D_{\parallel}T_y)_+ + (D_{\parallel}T_y)_-)}{2h}.$$

where the subscripts $+$ and $-$ indicate the points with a positive and a negative value for the off-diagonal diffusion tensor components respectively and where $\overline{b_1b_2}$ is a weighted average

$$\overline{b_1b_2} = \frac{(|b_1b_2|D_{\parallel}T_y)_+ + (|b_1b_2|D_{\parallel}T_y)_-}{(D_{\parallel}T_y)_+ + (D_{\parallel}T_y)_-}, \tag{4.6}$$

and so it becomes clear that instead of the differential we approximate some value $\overline{b_1b_2}/\left(h\overline{D_{\parallel}T_y}\right)$, i.e. the sign-switch creates a local inconsistency. Thus, in the differencing of b_1b_2 a sign-change should not be allowed, the sign of b_1b_2 should then only be considered relevant if it serves as a directional weight of a scalar value. Taking this further, we can adapt any discretisation method to fulfill this assertion. The question is how can we do this consistently.

Absolute values

We start by simply getting rid of the mixed signs, i.e. the sign change of the diffusion tensor component D_{21}, D_{12}. For example, for the above approximation we get

$$\partial_x(D_{\parallel}b_1b_2T_y) \approx \sigma\frac{(|b_1b_2|D_{\parallel}T_y)_+ - (|b_1b_2|D_{\parallel}T_y)_-}{2h},$$

where σ is the sign. We base the sign solely on the unit direction vector. The requirement is that the discretisation is unaffected if there is no sign-change and in case there is a sign-change either the largest value of b_1b_2 or the average vector is taken as a reference:

$$\begin{aligned} \text{largest value}: &\quad \sigma = sign[(b_1b_2)_+ + (b_1b_2)_-], \\ \text{average vector}: &\quad \sigma = sign[(b_1)_+ + (b_1)_-]\,[(b_2)_+ + (b_2)_-]. \end{aligned}$$

If we assume that we approximate $\partial_x(D_{21}T_y)$ and $\partial_y(D_{21}T_x)$ with the unknowns exactly on the x- and y-axis respectively we can simplify the divergence requirement to preserving $\partial_x(b_1)$ and $\partial_y(b_2)$. In this case, if we treat the x-derivative and the y-derivative of the divergence separately we must leave the b_1-component and the b_2-component respectively, untouched. Then the value of $\nabla \cdot \mathbf{b}$ is maintained, but now we change the value of $\nabla \cdot \mathbf{b}_\perp$. If we want to maintain the value of $\nabla \cdot \mathbf{b}_\perp$ we have to do exactly the opposite, namely leave the values of $\partial_x(b_2)$ and $\partial_y(b_1)$ untouched. However, we cannot maintain both divergence constraints at the same time.

We will *not* obtain a consistent approximation for the simple reason that we change the sign of $b_1 b_2$ without considering the effect on the angle of the unit direction vector: we change the sign for one of the unit direction vectors. This brings the unit direction vectors in the same quadrant, but at the same time it changes the relative angle of the two unit direction vectors. The result is that $\nabla \cdot \mathbf{b}$ or $\nabla \cdot \mathbf{b}_\perp$ is approximated inconsistently.

Rotation

In the following approach we maintain the relative orientation of the two vectors. Assuming the divergence of the unit direction vectors is zero and provided the two unit direction vectors have a relative angle less than 90° we can rotate both vectors such that they are in the same quadrant. This way the sign of $b_1 b_2$ does not switch. Now, all the unit direction vectors need to be rotated and subsequently the diffusion tensors need to be re-calculated. If $\nabla \cdot \mathbf{b} = 0$ this rotation does not lead to any inconsistency. For simplicity we assume that the relative angle is less than 45°. The angle by which we rotate the unit direction vectors is given by

$$\beta = 2 \max \left[(\arcsin \left(|b_2|_{l,d} \right), \arcsin \left(|b_2|_{r,u} \right)) \right].$$

With the assumption that the relative angle is less than 45° the maximum angle of rotation is 45° and so the angle of rotation is given by

$$\begin{aligned} \beta_{l,d} &= \min \left[\arcsin \left(|b_2|_{l,d} \right), \pi/2 - \arcsin \left(|b_2|_{l,d} \right) \right], \\ \beta_{r,u} &= \min \left[\arcsin \left(|b_2|_{r,u} \right), \pi/2 - \arcsin \left(|b_2|_{r,u} \right) \right], \\ \beta &= 2 \max \left[\beta_{l,d}, \beta_{r,u} \right], \quad \beta = \min \left[(\pi/4, \beta) \right]. \end{aligned}$$

If the relative angle is more than 90° and less than 180° we simply have to take the reverse of one of the unit direction vectors. As a demonstration we apply the above method to the asymmetric finite-difference scheme by Günter et al. We note that for the closed field line cases the number of sign-switches scales with the square root of the number of degrees of freedom, and for open field line cases these sign-switches do not occur. The asymmetric finite-difference scheme is known to perform poorly for closed field line cases and very well for open field lines cases. The symmetric finite-difference scheme is known to perform well in either case. We see from the results in figure 4.9 that preventing a sign switch through rotation significantly increases the accuracy for high levels of anisotropy. In fact for higher resolutions it becomes close to third order accurate, see figure 4.9b. Note that divergence at higher resolutions is most likely caused by the extremely high condition number of the linear operator as the symmetric scheme by Günter et al. also starts to diverge at that point. We show the results also for the singular grid which has grid points lying exactly on the axes of the circular distribution, we see a faster convergence but also a faster divergence. We can conclude for now that rotation of unit direction vectors is a viable method to improve the accuracy of the asymmetric scheme, the application is limited to cases where $\nabla \cdot \mathbf{b} = 0$. This result demonstrates that the sign switch is one of the root causes of the anisotropy dependent error in case of closed field lines.

The rotation method to prevent sign switches is inconsistent when $\nabla \cdot \mathbf{b} \neq 0$ because the

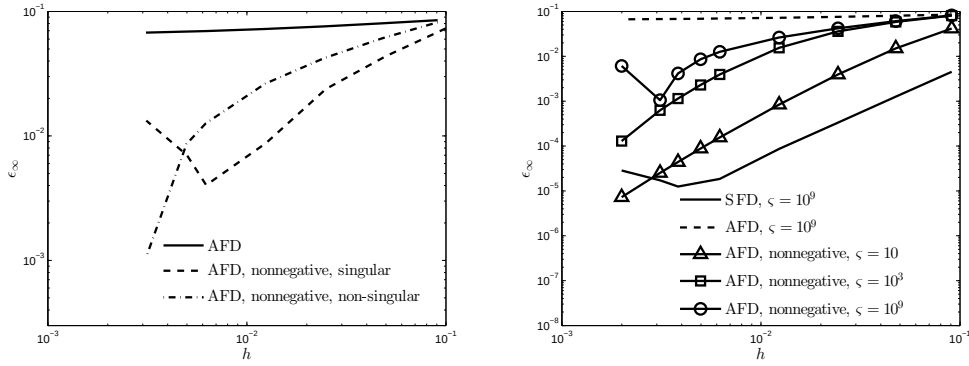

(a) (b)

Figure 4.9: Effect of unit direction rotation on mixed closed/open field lines, shown is the error ϵ_∞ (a) for $\varsigma = 10^9$, (b) for various values of ς.

original values for $\partial_x(b_1)$ and $\partial_y(b_2)$ are not maintained. The rotation method applied to conservative methods does not allow separate treatment of unit direction differencing. So the correction must take place directly in rotating the unit direction vectors. The question is then, is there an angle of rotation for which we remove the sign switch, preserve the relative angle and preserve the relation between $\partial_x(b_1)$, $\partial_y(b_2)$, $\partial_y(b_1)$ and $\partial_x(b_2)$? More generally, can we define a rotation method that preserves the approximation of

$$\nabla \cdot \mathbf{b} = \mathcal{D}_\parallel, \quad \nabla \cdot \mathbf{b}_\perp = \mathcal{D}_\perp,$$

where $|\mathcal{D}_\parallel|$ and $|\mathcal{D}_\perp|$ are non-zero? The rotation is simply given by

$$b_1^* = b_1 \cos\alpha - b_2 \sin\alpha, \quad b_2^* = b_1 \sin\alpha + b_2 \cos\alpha.$$

Assuming we have our unknowns exactly on the coordinate axes, the divergence constraints are

$$\begin{aligned} \partial_x: &\quad \frac{\partial b_1}{\partial x} = \mathcal{D}_\parallel, \quad \nabla_x b_2 = -\mathcal{D}_\perp, \\ \partial_y: &\quad \frac{\partial b_2}{\partial y} = \mathcal{D}_\parallel, \quad \nabla_y b_1 = \mathcal{D}_\perp. \end{aligned}$$

If the divergence constraints are met simultaneously we have

$$\begin{aligned} \partial_x: &\quad \frac{\partial b_1^*}{\partial x} = \mathcal{D}_\parallel, \quad \nabla_x b_2^* = -\mathcal{D}_\perp, \\ \partial_y: &\quad \frac{\partial b_2^*}{\partial y} = \mathcal{D}_\parallel, \quad \nabla_y b_1^* = \mathcal{D}_\perp. \end{aligned}$$

Assuming we use central differencing for the approximation of the derivatives, this means the following must hold:

$$\begin{aligned}
\partial_x: \quad & (b_1^*)_r - (b_1^*)_l = (b_1)_r - (b_1)_l = h\mathcal{D}_\parallel, \\
& (b_2^*)_r - (b_2^*)_l = (b_2)_r - (b_2)_l = -h\mathcal{D}_\perp, \\
\partial_y: \quad & (b_2^*)_u - (b_2^*)_d = (b_2)_u - (b_2)_u = h\mathcal{D}_\parallel, \\
& (b_1^*)_u - (b_1^*)_d = (b_1)_u - (b_1)_d = h\mathcal{D}_\perp.
\end{aligned}$$

If we substitute the expressions for b_1^* and b_2^* we get the trivial result that the constraints only hold simultaneously for $\alpha = 0$, i.e. the rotation method is limited to problems with $\nabla \cdot \mathbf{b} = 0$ which physically relates to a zero parallel gradient of the magnetic field strength.

4.5 Regularisation

4.5.1 *Regularisation of the direction vector*

The situation we try to mimick in this thesis is temperature diffusion in a fusion plasma. The basic physical premisse is that the anisotropy is caused by a primary gyrating motion of the charged particles around the magnetic field lines. We have a simplified representation of these magnetic field lines in the form of a unit direction vector, which is unphysical in the sense that the absolute value is always one, meaning that the equivalent magnetic field is exactly one everywhere. Furthermore we assume a two-dimensional domain, where closed field lines lead to the existence of a singular point in which the unit direction vector is undefined. If a point on which we define a flux value lies on this singular point the unit direction vector may be undetermined.
A physical interpretation of our two-dimensional representation is that we have a non-varying magnetic field line component in z-direction.This interpretation allows us to regularise the diffusion tensor in case we encounter these directional singularities. The regularised diffusion tensor $\mathbf{D}$ is written as

$$\mathbf{D} = (D_\parallel - D_\perp)\frac{\mathbf{BB}}{B_1^2 + B_2^2 + B_z^2} + D_\perp \mathcal{I}, \tag{4.7}$$

where B_z is a very small number. Now, if $B \to 0$, $\mathbf{D} \to D_\perp \mathcal{I}$, i.e. at the singular points we have isotropic diffusion. We can apply this to numerical schemes as follows. For the (a)symmetric scheme we rewrite $\mathbf{D}$ as described above. In figure 4.10 we show the ϵ_∞-error convergence of the symmetric scheme. The regularisation prevents the occurrence of a division by zero and otherwise does not negatively affect the convergence.

Another possible issue is the occurrence of a zero-row in the linear operator. This can occur, depending on the scheme if the temperature node is exactly in the O-point and the field lines are exactly circular. Hence this will not be the case for elliptic field line problems. A simple fix for this problem is a grid displacement relative to the O-point of size $\epsilon \ll L$ where L is a typical length scale of the problem, see figure 4.11. All the following results will have both a displacement of size 10^{-13} as well as the regularisation described by (4.7).

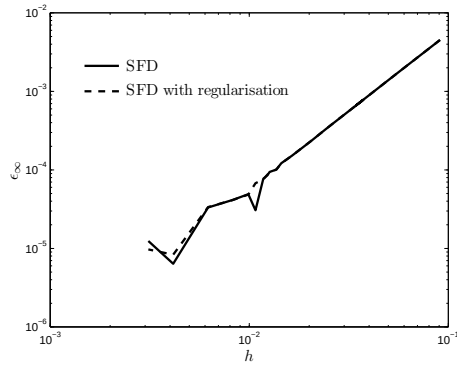

Figure 4.10: Regularisation, $\varsigma = 10^9$, result shown for symmetric scheme with flux point on the O-point, applied to mixed open/closed field line problem.

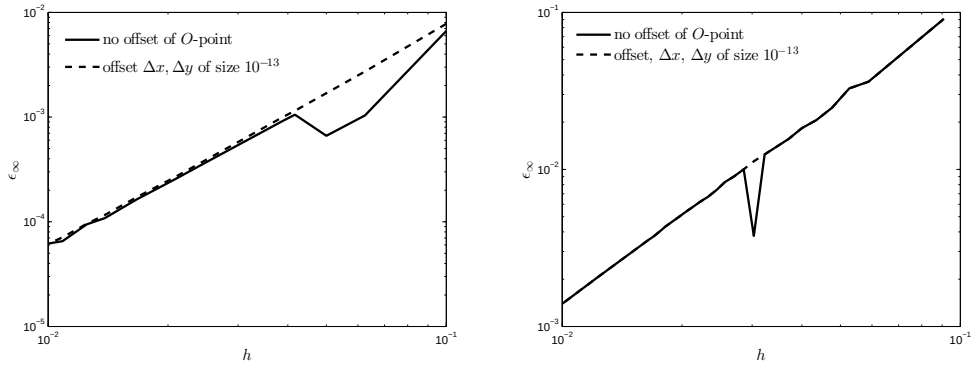

Figure 4.11: Zero-row issue, result shown for symmetric scheme with temperature node on the O-point, (a) mixed open/closed field line problem, $\varsigma = 10^9$, (b) tilted closed field line problem, $a = 1, b = 3, \varsigma = 10^8, \theta = 1/3\pi$.

4.5.2 *Locally avoiding non-regular diffusion tensor differencing*

Normalisation is done implicitly by Droniou and Le Potier [42]. They use local diffusion tensors to construct a vector **Dn** for each element, where **D** is the diffusion tensor and **n** is the cell face normal direction vector. Then they define intersection points between the (extended) cell-faces and these local vectors similar to the work by Agélas et al. [7]. On these intersection points a two-point flux approximation is possible. The method by Droniou and Le Potier is nonlinear as they seek a convex combination of fluxes to obtain a maximum-minimum preserving (MMP) scheme. They further state the following principle that should be satisfied whenever possible: *The points used to obtain the convex combination of fluxes should belong to the same subdomain on which* **D** *is regular.*

Droniou and Le Potier go on to demonstrate that they significantly increase the accuracy if their MMP-scheme satisfies this principle. In fact the order of accuracy increases two-fold compared to the MMP-scheme that does not satisfy this principle.

Instead of displacing the flux points to avoid a local non-regular **D** distribution as do Droniou and Le Potier, we maintain the position of the flux points and merely treat the diffusion tensors to ensure proper normalised averaging. We note that also Droniou and Le Potier take the mean value of diffusion tensors for the heterogenous case, with no reference to normalisation.

Inspired by the principle given by Droniou and Le Potier [42] we now discuss a purely grid based technique to improve the accuracy of existing schemes in case of non-regular, i.e. sign-switching diffusion tensor values. The premiss is that the locations of the unknowns are fixed and that we have a Cartesian uniform grid.

We describe the method for the asymmetric finite difference method.

Asymmetric finite difference method

First we define the problem: For the approximation of the divergence we write for the off-diagonal diffusion tensor components

$$\begin{aligned} \partial_x(D_{12}T_y) &\approx \frac{\left(D_{21}T_y\right)_{i+\frac{1}{2},j} - \left(D_{21}T_y\right)_{i-\frac{1}{2},j}}{2h}, \\ \partial_y(D_{21}T_x) &\approx \frac{\left(D_{21}T_x\right)_{i,j+\frac{1}{2}} - \left(D_{21}T_x\right)_{i,j-\frac{1}{2}}}{2h}, \end{aligned} \tag{4.8}$$

where it may occur that the term b_1b_2 has a different sign for the points $(i \pm \frac{1}{2}, j)$ and $(i, j \pm \frac{1}{2})$, thus creating an inconsistency. Instead of forcing equality of signs or rotating the unit direction vectors we shift the locations of the divergence stencil points horizontally or vertically such that b_1b_2 has no sign difference between the stencil points.

We treat the x-direction and the y-direction separately. In each direction we interpolate the change of the diffusion tensor value b_1b_2 dependent on x or y. The intersection of this interpolation with the x-axis or y-axis determines the new location for the divergence approximation, see figure 4.12. Assuming we have two averaged flux points the

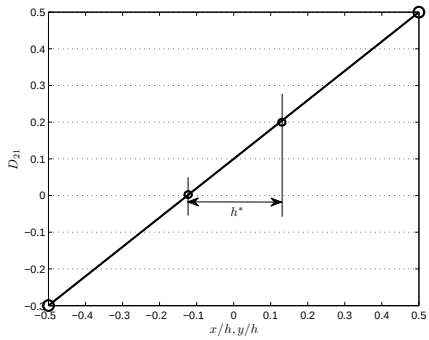

Figure 4.12: Location shift to have same sign for off-diagonal diffusion tensor components.

new locations are given by

$$\begin{aligned}
\partial_x(D_{11}T_x + D_{12}T_y) : x^* &= -\frac{h}{2} + \frac{h(D_{21})_{i-\frac{1}{2},j}}{(D_{21})_{i-\frac{1}{2},j} - (D_{21})_{i+\frac{1}{2},j}}, \quad h_x = 2|x^*|, \\
\partial_y(D_{21}T_x + D_{22}T_y) : y^* &= -\frac{h}{2} + \frac{h(D_{21})_{i,j-\frac{1}{2}}}{(D_{21})_{i,j-\frac{1}{2}} - (D_{21})_{i,j+\frac{1}{2}}}, \quad h_y = 2|y^*|, \\
h^* &= \min\left(h_x, h_y\right)
\end{aligned} \tag{4.9}$$

and to prevent a zero-valued D_{21} we take $h^* = c \min\left(h_x, h_y\right)$ with $|c| < 1$. Since we only apply this displacement method when there is a sign switch the denominators of (4.9) will not go to zero faster than the nominators. Now given the new flux points and the divergence points, we apply the linear interpolation used for the approximation of the new flux points to find the values of the diffusion tensor. Given the new locations for the flux points we have to redefine the approximation for the gradients to maintain the order of accuracy. We consider two basic options: 1) maintain the original approximations for the gradients, this may result in a first order error depending on the displacement $(h/2 - h^*)$, 2) adapt the original approximation to the new non-equidistant local grid. Regarding the first option: The order of accuracy will reduce locally as we introduce an interpolation error. The benefit of maintaining the original approximation for the gradients is ease of implementation. We do expect some improvement compared to the original asymmetric method since we effectively remove a zeroth-order error. We denote this method as *asymmetric reg. 1*.

Regarding the second option: We redefine the approximations for $(T_y)_{i\pm\frac{1}{2},j}$ and $(T_x)_{i,j\pm\frac{1}{2}}$ as follows

$$\begin{aligned}
\left(T_y\right)_{i\pm\frac{1}{2},j} &\approx \frac{h^*}{h}\left(T_y\right)_{i\pm1,j} + \left(1 - \frac{h^*}{h}\right)\left(T_y\right)_{i,j}, \\
\left(T_x\right)_{i,j\pm\frac{1}{2}} &\approx \frac{h^*}{h}\left(T_x\right)_{i,j\pm1} + \left(1 - \frac{h^*}{h}\right)\left(T_x\right)_{i,j},
\end{aligned}$$

where e.g. for (i, j)

$$\left(T_y\right)_{i,j} = \frac{T_{i,j+1} - T_{i,j-1}}{2h}, \quad \left(T_x\right)_{i,j} = \frac{T_{i+1,j} - T_{i-1,j}}{2h},$$

and we keep the approximations for $(T_x)_{i\pm\frac{1}{2},j}$ and $(T_y)_{i,j\pm\frac{1}{2}}$ as is. Note that, if we define these gradient approximations as the average of the bilinear interpolation in each pair of the respective connected quadrants we get the same approximations for $(T_y)_{i\pm\frac{1}{2},j}$, $(T_x)_{i,j\pm\frac{1}{2}}$, $(T_x)_{i\pm\frac{1}{2},j}$ and $(T_y)_{i,j\pm\frac{1}{2}}$. We denote this method as *asymmetric reg. 2*.

There is a singularity when exactly in the point (i, j) the sign difference disappears, i.e. for a closed field line problem where the unknowns lie exactly on the *O*-point axes. If this singularity occurs one can simply place both stencil points on the side of the central point. This obviously introduces a first-order error. If left untreated care should be taken when generating the grid. An easy way to prevent this singularity is shifting the domain center by a small value ϵ.

Further note that our focus in terms of regularity is solely the geometric term $b_1 b_2$. This focus will shift if the application of the diffusion equation shifts, say to the simulation of flow through porous media where the diffusion coefficients change discontinously from one porous layer to the next.

As a test case we consider the mixed closed/open field line case. For higher levels of anisotropy the asymmetric scheme by Günter et al. is zeroth order accurate. We

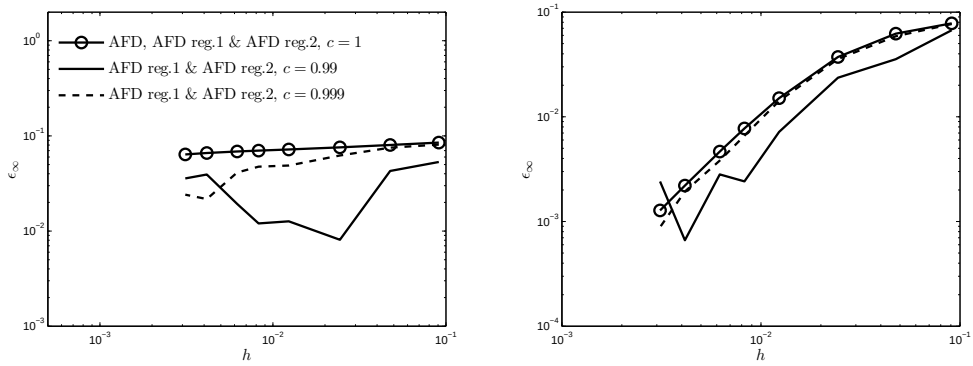

Figure 4.13: Mixed closed/open field lines problem, shown is the error ϵ_∞, for this test case $\nabla \cdot \mathbf{b} = 0$, (a) $\varsigma = 10^6$, (b) for $\varsigma = 10^3$.

see from the results in figure 4.13 that the method *asymmetric reg. 1* is sensitive to the value of c. For the investigated values of c this method is still more accurate than the default asymmetric scheme for this particular case. However, the convergence behavior is erratic. The method *asymmetric reg.2* shows identical results. Method *asymmetric reg.2* differs from method *asymmetric reg.1* only by the way the derivatives belonging to D_{21} and D_{12} are approximated. The fact that the two methods have identical results indicates that the derivative approximations belonging to D_{11} and D_{22} are inappropriate and/or the approximations of the diffusion tensor values are inappropriate.

To test the latter possibility we simply insert the exact values for the diffusion tensor in the new locations. We find identical results as shown in figure 4.13. Therefore we focus on improving the derivatives $(T_x)_{i\pm\frac{1}{2},j}$ and $(T_y)_{i,j\pm\frac{1}{2}}$.
We take the derivative of a biquadratic interpolation through the nine stencil points. For the next results we use the exact diffusion tensor values. Repeating the formulation of the biquadratic interpolation

$$T(x,y) \approx c_1 x^2 y^2 + c_2 x^2 y + c_3 y^2 x + c_4 x^2 + c_5 y^2 + c_6 xy + c_7 x + c_8 y + c_9,$$

the derivatives are given by

$$
\begin{aligned}
(T_x)_{i\pm\frac{1}{2},j} &\approx \pm 2c_4 h^* + c_7, \\
(T_y)_{i\pm\frac{1}{2},j} &\approx c_2 (h^*)^2 \pm c_6 h^* + c_8, \\
(T_x)_{i,j\pm\frac{1}{2}} &\approx c_3 (h^*)^2 \pm c_6 h^* + c_7, \\
(T_y)_{i,j\pm\frac{1}{2}} &\approx \pm 2c_5 h^* + c_8,
\end{aligned}
$$

and the Vandermonde coefficients can be found in section 2.2.5. We denote this method as *asymmetric reg. 3* when we apply the biquadratic interpolation only to $(T_x)_{i\pm\frac{1}{2},j}$ and $(T_y)_{i,j\pm\frac{1}{2}}$ and if we all apply it to all derivatives we denote the method as *asymmetric reg. 3*. We note that method *asymmetric reg. 3* results in locally varying discretisations. This

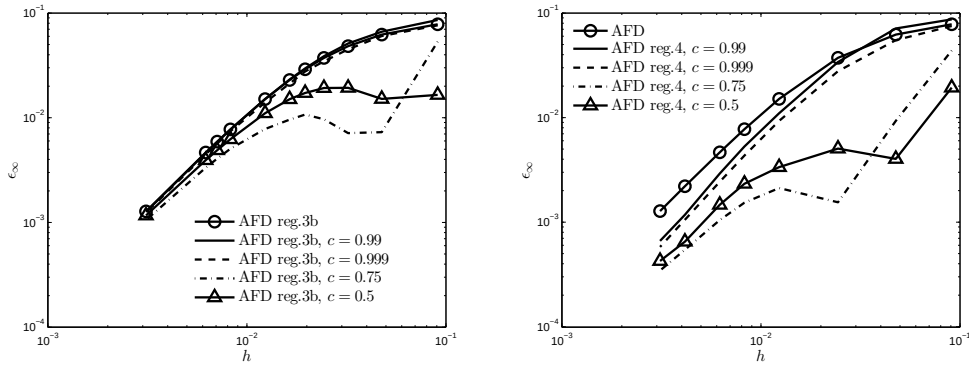

(a) (b)

Figure 4.14: Mixed closed/open field lines problem, shown is the error ϵ_∞. For this test case $\nabla \cdot \mathbf{b} = 0$, $\varsigma = 10^3$, (a) *asymmetric reg. 3*, (b) *asymmetric reg. 4*.

itself may cause inaccuracies. To have a uniform discretisation we apply the same biquadratic interpolation for all nodes with local adaptation of h^* in case of a sign switch. This is denoted as *asymmetric reg. 4*. Note that this is equivalent to the *interp. Vandermonde scheme* discussed in chapter 2 if there is no sign-switch. We see from figure 4.14 that the convergence becomes less irratic and that the uniform discretisation of method *asymmetric reg. 4* is beneficial for the accuracy. We also see that the improvement is most significant for lower resolutions. The same can be said for the results of methods *asymmetric reg. 1* and *asymmetric reg. 2* in figure 4.13.

Focussing on lower resolutions initially second-order convergence is obtained for the methods *asymmetric reg. 3* and *asymmetric reg. 4*, At some point the solution diverges towards the accuracy for the unadapted asymmetric scheme by Günter et al. In figure 4.15 we have plotted the error ϵ_∞ for two values of the anisotropy up to the point of divergence for the method *asymmetric reg. 4*. The convergence up to the divergence point is hardly affected by the level of anisotropy. We see in figure 4.15 that the error ϵ_∞ has a plateau until which the solution converges for different values of c and we also see a clear dependence of the range of improved convergence on the value of c. To

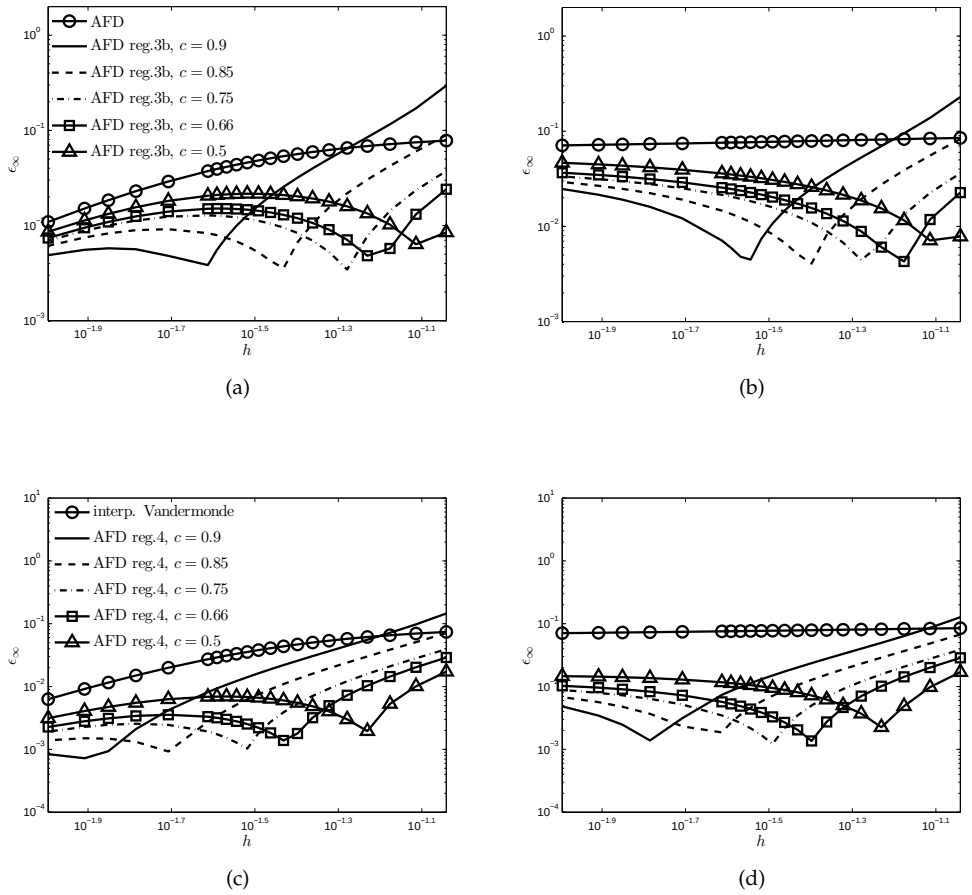

Figure 4.15: Mixed closed/open field lines problem, shown is the error ϵ_∞, specifically the improved convergence, (a) $\varsigma = 10^3$, *asymmetric reg. 3*, (b) $\varsigma = 10^6$, *asymmetric reg. 3*, (c) $\varsigma = 10^3$, *asymmetric reg. 4*, (d) $\varsigma = 10^6$, *asymmetric reg. 4*.

demonstrate that the methods *asymmetric reg. 3* and *asymmetric reg. 4* are applicable also to problems with $\nabla \cdot \mathbf{b} \neq 0$ and $\nabla \cdot \mathbf{b}_\perp \neq 0$, we apply the method to the more general tilted elliptic problem described in section 2.4.4. We see in figure 4.16 that again, for a certain range in resolution, we have second-order convergence. However, as before, we do not get a continuous improvement. The convergence behavior of the methods *asymmetric reg. 1,2,3,4* can perhaps be improved by changing the way that h^* is determined. We leave this open for future research.

We may apply this method to the normal symmetric finite-difference scheme. Note

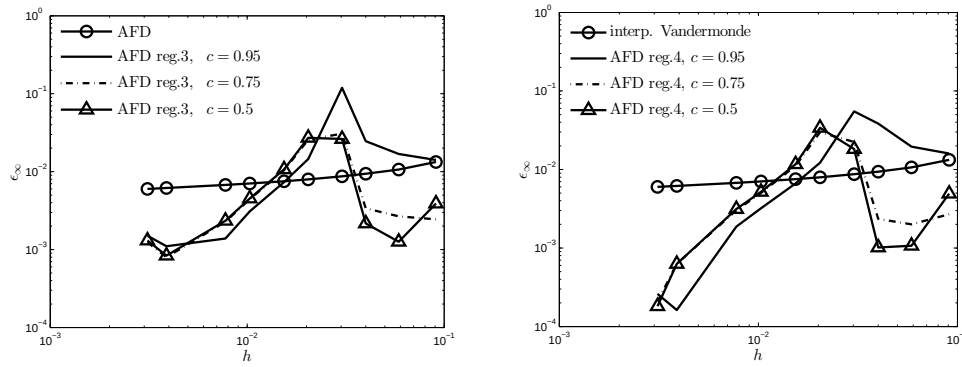

(a) (b)

Figure 4.16: Tilted elliptic problem, shown is the error ϵ_∞, $\varsigma = 10^6$, $\theta = 1/3\pi$, $a = 0.15, b = 0.85$, (a) *asymmetric reg. 3*, (b) *asymmetric reg. 4*.

that for the SFD scheme an iterative procedure is required: Instead of equation (4.8), we have the slightly different

$$\partial_x(D_{12}T_y) \approx \frac{\overline{D_{21}T_y}_{i+\frac{1}{2},j} - \overline{D_{21}T_y}_{i-\frac{1}{2},j}}{2h},$$
$$\partial_y(D_{21}T_x) \approx \frac{\overline{D_{21}T_x}_{i,j+\frac{1}{2}} - \overline{D_{21}T_x}_{i,j-\frac{1}{2}}}{2h},$$

where we have *averaged* values for the diffusion tensor components weighted with the unknown temperature values. That is, to evaluate the location where there is a sign switch we have to involve the temperature values. For the value of h^* one should use equation (4.9) with the off-diagonal diffusion tensor terms replaced by e.g. $\overline{D_{21}T_y}_{i+\frac{1}{2},j}$.

4.6 Conclusion

An important finding from this chapter is that cases with closed field lines are problematic for existing schemes, including the symmetric finite-difference scheme. We conclude that the primary reason for the difficulty of closed field line problems lies in the fact that there are lines along which the off-diagonal diffusion tensor values change sign. This is avoided/mitigated by the symmetric finite-difference scheme in most cases, through weighted averaging of the diffusion tensor values with the unknown temperature values. This mitigation is much less effective for asymmetric test problems with off-axis sign switching of the off-diagonal diffusion tensor. The presence of an *O*-point may offset the accuracy but does not affect the order of accuracy if properly treated, for instance by regularising the unit direction vector. Hence the *O*-point itself is not the main culprit for the reduction in accuracy convergence.

The performance of several numerical approximation techniques for diffusion are made more robust by applying tensor/diffusion-coefficient based adaptations: (1) normalised

averaging of fluxes, (2) directly preventing the sign switch through rotation of the unit direction vector, or (3) avoiding the non-regular diffusion tensor regions. We note that these techniques are problem and/or test case specific. The methods described in sections 4.5.2 and 4.3 can be extended to three dimensions.

5

MODEL ADAPTATION METHODS

Adapting the numerical methods used to approximate the anisotropic diffusion equation is the recipe of the preceding chapters. In the current chapter we take a different route, we adapt the model slightly to enable the numerical method to better approximate the original anisotropic diffusion equation.

5.1 Regions of interest in nuclear fusion plasma

The extreme anisotropy in a tokamak plasma along and perpendicular to the magnetic field lines may allow us to selectively apply different methods dependent on the direction and the location. From our results and from literature it is clear that methods exist that can handle parts of the anisotropic diffusion problem well. Discriminators are for instance: closed versus open field lines and high versus low anisotropy.
With regard to anisotropy important questions are: What is the typical anisotropy ratio in different regions of the fusion plasma? What are typical temperature gradient values and magnetic field strengths? Most likely, in the center of the plasma we can assume that the plasma is aligned with the magnetic field lines and that the parallel temperature gradient is near zero, i.e. going from the edge to the center we reach a point where we can completely ignore the parallel temperature gradient. Near the plasma edge the situation is very different: There are high temperature gradients, high magnetic field (strength and direction) variations, a lower absolute temperature and a smaller value for the average magnetic field strength. Also, towards the plasma edge, transport will play a more important role; small scale turbulence will increase the effective perpendicular diffusion, decreasing the level of anisotropy. Arguably the radii which define the pedestal region can be found roughly by considering the radial gradient of the temperature and the density. If we are in high-confinement mode, this gradient should clearly increase. However, in low-confinement mode this increase of radial gradients is unclear, see figure 5.1. This allows one to roughly divide the plasma into regions where there *is* and where there is no variation of the field aligned temperature. If we can assume for some defined part of the computational domain that the parallel temperature gradient is zero, then we can locally simplify the computation as we showed in section 3.4.3.

We note that for the determination of the infinity error-norm in the test results presented in this chapter we used the original exact temperature distribution, i.e. we only change the approximation by changing the linear operator and/or the source function.

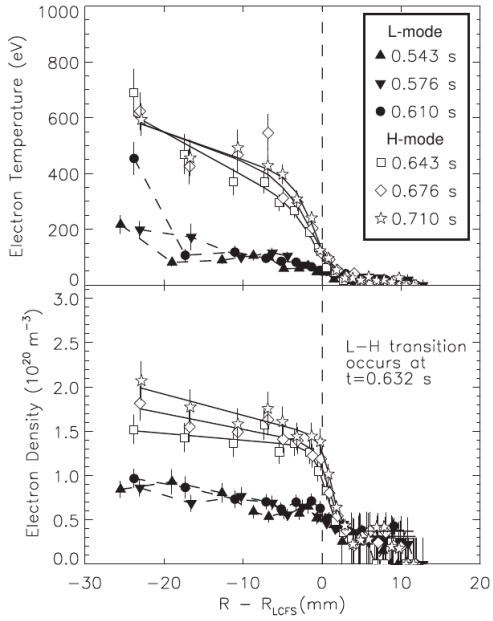

Figure 5.1: Radial distribution of electron density and electron temperature for L and H mode, results from Alcator-C mod (source Hughes et al. [63]).

5.2 Importance of closed field lines

The significance can be visualized by plotting the logarithm of the error for cases with distinct areas of closed and open field lines, see figure 5.2a. Very clearly visible is the

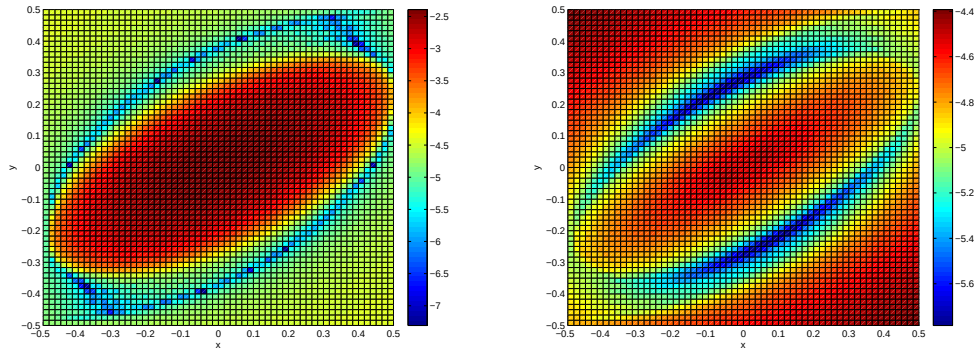

(a) (b)

Figure 5.2: log10 of the solution error using non-symmetric schemes for a test case with elliptic field lines, (a) asymmetric scheme, (b) SFD scheme.

formation of an error plateau exactly overlapping the closed field lines. A direct consequence of this plateau is that there is an overshoot from the areas of the closed field

lines to the areas of the open field lines which in turn may lead to non-monotonicity. The results are better for symmetric schemes but the overshoot will remain, see figure 5.2b.

Given the fact that the numerical issues are so apparently related to the fact that there are areas of closed field lines we can perhaps find a dedicated solution. This requires us to understand what it is that makes these closed field lines problematic for our numerical solvers. For one, closed field lines have no beginning, and no end. If one would follow a curve describing some value along the field line the starting value should match exactly with the end value, it basically behaves as a one-dimensional diffusion problem with periodic boundary conditions. For $\mathbf{b} \cdot \nabla T = 0$ this implies that along the field line quantities should be exactly preserved. Numerically this is very difficult to realise locally, everywhere. As said, the quantities along the closed field line are periodic in nature. Castillo and Chacon [33, 34] use this by integrating the parallel component along the field lines with a Green's function, i.e. they treat the diffusion equation along each field line as a separate integral with periodic boundary conditions.

5.3 Zero parallel diffusion coefficient continued

We saw in chapter 3 that setting $D_{\parallel}$ to zero along a line intersecting all the closed field lines is a means to correct for errors that occur specifically in closed field line problems. We denote this adaptation with *SFD zero* for the symmetric finite difference scheme and apply it along the transition line described in section 4.2.
As test cases we take the tilted elliptic temperature distribution described in section 2.4.4, and the tilted closed field line case described in section 2.4.6. We see from figure

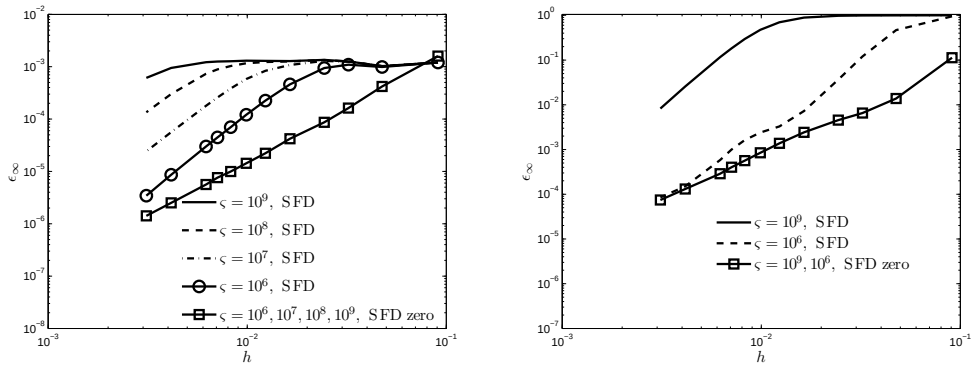

(a) (b)

Figure 5.3: Convergence of ϵ_∞ error using the SFD scheme, (a) for tilted elliptic test case with $a = 0.15, b = 0.85, \theta = 1/3\pi$, (b) tilted closed field line case with $a = 1, b = 3, \theta = 1/3\pi$.

5.3 that this is an effective approach to correct the SFD scheme for non-axis aligned sign-switching of the diffusion tensor. We note that this method is independent of the

grid, and most importantly it does not require information about the topology as we suggested in chapter 3. This approach is however limited to steady cases with $\mathbf{q}_{\|} = 0$. We note that the presence of an intersection of two transition lines indicates the location of an *O*-point and thus of closed field lines.

We also add this correction to the asymmetric scheme described in section 2.2.1. We

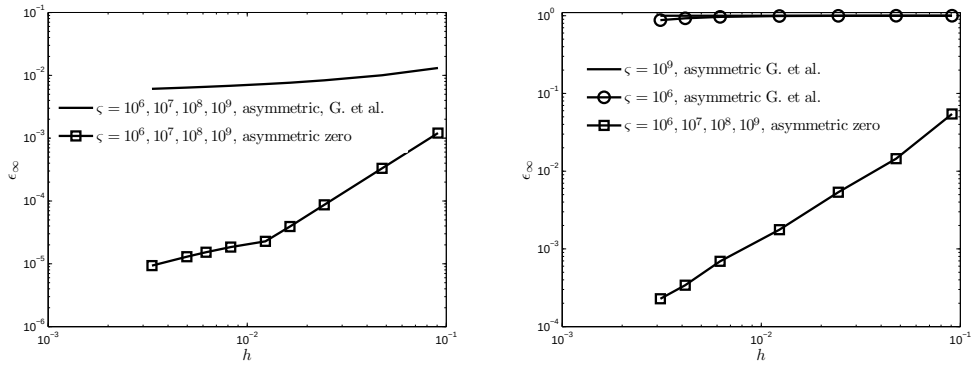

(a) (b)

Figure 5.4: Convergence of ϵ_∞ error using the asymmetric scheme by Günter et al. (a) for the tilted elliptic test case with $a = 0.15, b = 0.85, \theta = 1/3\pi$, (b) tilted closed field line case with $a = 1, b = 3, \theta = 1/3\pi$.

see from figure 5.7 that this correction also works for the asymmetric scheme. With the results from section 3.4.3 we expect this correction to work for any numerical scheme as the adaptation is basically a form of model reduction.

We know from the previous results that $D_{\|} = 0$ enforcement works well for problems with zero parallel temperature gradient. In section 3.4 we demonstrated that the method of setting $D_{\|}$ to zero at selective points can also be applied to unsteady cases with $\mathbf{b} \cdot \nabla T = 0$ in the source function.

5.3.1 *Zero diffusion bands*

To extend the applicability to unsteady cases with non-zero parallel temperature gradient one has to apply the enforcement conditionally, based on the evolution of the parallel temperature gradient. Suppose we have an initial temperature distribution which is diffused along a circular closed field line with zero perpendicular diffusion. Then, along closed field lines the temperature will have evolved completely after some time (see section 2.5 for details). As the arc length along the closed field lines is smaller for smaller radii the temperature will have evolved sooner for those field lines. Now, setting $D_{\|} = 0$ in one point of the closed field line as soon as the temperature has evolved completely, will not prevent numerical perpendicular diffusion along the whole field line. In order to prevent numerical perpendicular diffusion we have to set $D_{\|}$ to zero along the *entire* field line. However this would effectively introduce a discontinuity in the perpendicular direction that may cause numerical instabilities, so care must be

taken.

To demonstrate this idea of a conditional zero parallel diffusion coefficient we apply the Gaussian initial distribution with parallel diffusion along circular field lines. We set the parallel diffusion coefficient to zero for two radius ranges, $(r_0 + m\sigma + n\sqrt{2}h) > r > (r_0 + m\sigma)$ and $(r_0 - m\sigma) > r > (r_0 - m\sigma - n\sqrt{2}h)$. Here σ is the standard deviation of the initial Gaussian distribution and r_0 is the radius of the field line that intersects the center of the Gaussian distribution. I.e. we have defined a circular band of width $2m\sigma$ with central radius r_0 and just outside this non-zero band there are two bands of width $n\sqrt{2}h$ in which $D_\parallel$ is set to zero, see figure 5.5. We use $\sqrt{2}h$ instead of h to account for bands that are locally diagonal with respect to the grid. In order to prevent

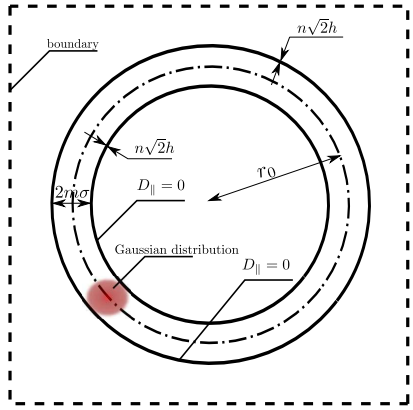

Figure 5.5: $D_\parallel$ is set to zero on bands of $n\sqrt{2}h$ wide enclosing a band of $2m\sigma$ wide that contains the initial Gaussian distribution.

numerical instability we set $D_\perp$ to a non-zero value, $\epsilon \approx 10^{-16}$. The band around the

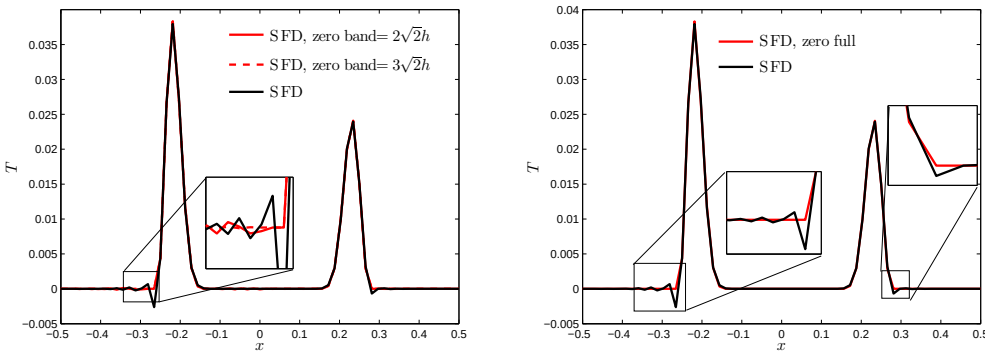

(a) (b)

Figure 5.6: Temperature plot along the line $y = 0$, with $m = 2$, 64×64 grid, $\sigma = 0.025$, $d = 0.15$, $t_{end} = 0.1$, $\Delta t = 1/1000$, (a) $D_\parallel$ set to zero in a band, $n\sigma$ wide, $m\sigma$ away from the Gaussian peak, (b) $D_\parallel$ set to zero at a distance more than $m\sigma$ away from the Gaussian peak, only the non-zero band containing the peak has a non-zero diffusion coefficient.

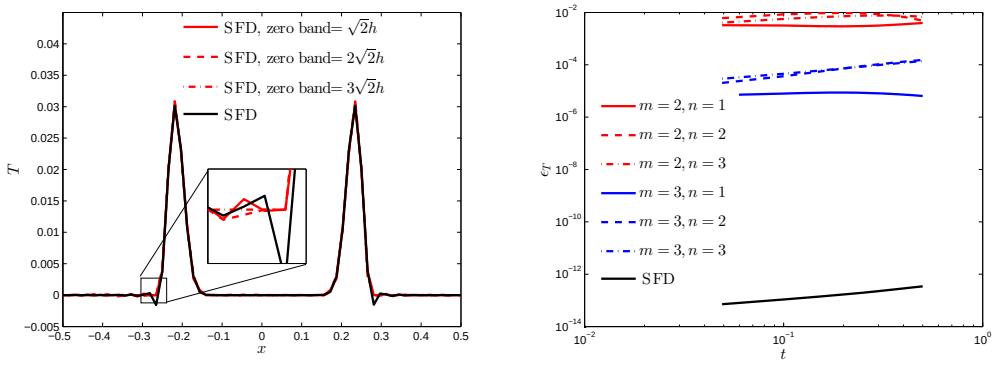

(a) (b)

Figure 5.7: Diffusion of Gaussian initial distribution along magnetic field lines, (a) Temperature plot through the along the line $y = 0$, with $m = 2$, 64×64 grid, $\sigma = 0.025$, $d = 0.15$, $t_{end} = 0.5$, $\Delta t = 1/1000$, $D_{\parallel}$ set to zero in a band, $n\sigma$ wide, $m\sigma$ away from the Gaussian peak, (b) Relative error in total temperature using a 128×128 grid.

initial distribution basically acts as an insulator and prevents the large overshoot near the center of the Gaussian distribution. As can be expected, for increasing zero band size and increasing non-zero band size the wiggles resulting from the discontinuous diffusion coefficients diminish.

The application of the zero band concept can be considered in two ways, (1) either we define finite zero bands in which the parallel diffusion coefficient is zero or (2) we assume that only in the non-zero band the parallel diffusion coefficient is non-zero. Both applications require two field line traces to define the non-zero band. In figure 5.6a we see the result of partial zero bands (option (a)), we notice a reduction in wiggles close to the peak for increasing zero band size. The same holds if we increase the end time of the simulation (see figure 5.7a). In figure 5.7b we show the preservation of the total temperature, increasing the size of the non-zero band brings the result closer to the original SFD scheme. In figure 5.6b we see the result of option (b), we see that the overshoot is not present here for $m = 2$.

The practical application of this zero band concept may lie in the modeling of pellet injections in nuclear fusion plasmas (see e.g. Strauss et al. [111] and Futatani et al. [51]). Periodic injection of neutral particles can be used to mitigate and pace Edge Localized Modes (ELMs), see e.g. Lang et al. [75, 76]. For the modeling of a pellet injection with MHD an instantaneous local density source in the plasma is used by Strauss et al. [111] and Huysmans et al. [64]. In Futatani et al. [51] a time-varying, moving adiabatic density source is used. Both the instantaneous and the moving density source models have a local density peak which can be placed in a non-zero band to prevent nonphysical oscillations.

We leave the extension of this approach to general temperature distributions open for further research.

5.3.2 *Closed field line detection*

For the application of condition insertion methods as described in section 5.3 we have to detect the *O*-point and the edges of the closed field line region (see figure 5.8). Condition insertion assumes that $\mathbf{b} \cdot \nabla T = 0$ and that field line direction data is available, i.e. the closed field line detection procedure is in this case purely geometric in nature. We know specifically that in the *O*-point we have $\nabla \cdot \mathbf{b} = 0$.

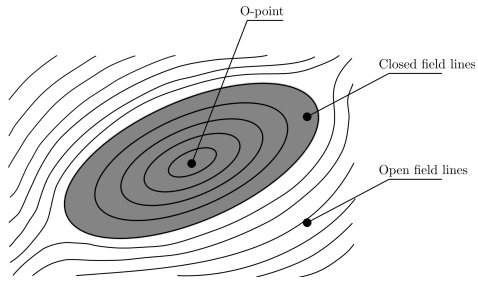

(a)

Figure 5.8: Closed and open field lines.

There are also physical models available for the island width, for instance the Rutherford model. Using the Rutherford model we only need to detect the location of the *O*-point to have a complete method for the closed field line detection.

Fortunately there is a simple geometric method to determine the boundary of the closed field line area; we can simply apply the transition line(s) described in section 4.2. Each intersection of two transition lines indicates the location of an *O*-point and, provided the field lines do no cross the boundary, the ends of the transition lines also indicate the size of the island.

5.4 Adding small perturbations

We note that several of the issues (ill-conditioning, mesh locking, convergence loss) encountered when approximating the anisotropic diffusion equation relate to the limits of the differential equation. What if we loosen the limits? We start by considering the relevant limits of the anisotropic diffusion equation as follows: *In physical reality, there is no such thing as exact, zero or infinity*. Recall, the anisotropic diffusion equation can be written as

$$T_t = \nabla \cdot (D_\parallel \mathbf{b} \cdot \nabla T)\mathbf{b} + \nabla \cdot (D_\perp \mathbf{b}_\perp \cdot \nabla T)\mathbf{b}_\perp + f.$$

If we take this equation in the limit $D_\parallel / D_\perp \to \infty$ with $\mathbf{b} \cdot \nabla T = 0$ we formally get an ill-posed problem. What goes wrong here? Obviously, if we know that $\mathbf{b} \cdot \nabla T = 0$ we can simply remove the parallel conduction term. The problem is that we *do not* know this and so it must naturally drop out of the equation for $D_\parallel / D_\perp \to \infty$. There are two artificial limits here, (1) $D_\parallel / D_\perp \to \infty$, (2) $\mathbf{b} \cdot \nabla T = 0$, both of which are *not* physical. First $D_\parallel / D_\perp$ is a finite number, second the parallel temperature gradient $\mathbf{b} \cdot \nabla T$ is assumed

to be zero based on a timescale argument, relating to the simulation time compared to the time in which the temperature has diffused in the parallel direction. So the parallel diffusion timescale is much smaller than the simulation time. Likewise, if we choose to simulate the parallel diffusion we automatically assume that the perpendicular diffusion is too slow. If we choose to neglect the perpendicular diffusion and we resolve the parallel diffusion on a suitable timescale the problem is well posed and so the linear operator remains well conditioned. The problem is then limited to perpendicular numerical pollution. So we have two separate problems, one dealing with conditioning and one dealing with numerical perpendicular diffusion. We are now dealing with the first problem.

5.4.1 *Alteration of parallel temperature gradient*

We want the parallel conduction to vanish for $D_{\parallel}/D_{\perp}$ larger than some finite value $1/|\epsilon|$ if $\mathbf{b} \cdot \nabla T = 0$. Now assuming that ϵ is a very small number we state that the parallel diffusion is assumed negligible for $D_{\parallel}/D_{\perp} > 1/|\epsilon|$, with $|\mathbf{b} \cdot \nabla T| < |\epsilon|$. We now simply set the following constraints: $D_{\parallel}/D_{\perp} \leq 1/|\epsilon|, \quad |\mathbf{b} \cdot \nabla T| \geq |\epsilon|$. To guarantee the latter constraint we change the linear operator, i.e. we take

$$T_t = \nabla \cdot \left\{ D_{\parallel}(\mathbf{b} \cdot \nabla T + \epsilon)\mathbf{b} + D_{\perp}(\mathbf{b}_{\perp} \cdot \nabla T)\mathbf{b}_{\perp} \right\} + f,$$

which can be written as

$$T_t = \nabla \cdot \left\{ D_{\parallel}(\mathbf{b} \cdot \nabla T)\mathbf{b} \right\} + \nabla \cdot \{ D_{\perp}(\mathbf{b}_{\perp} \cdot \nabla T)\mathbf{b}_{\perp} \} + \nabla \cdot \left(D_{\parallel}\epsilon\mathbf{b} \right) + f.$$

The added term integrated over a volume is given by

$$\oint (D_{\parallel}\epsilon\mathbf{b}) \cdot \mathbf{n} dS. \tag{5.1}$$

The operator for the perpendicular diffusion is not altered. We are not consistent with the original heat diffusion equation unless we make ϵ at least $(p+1)^{th}$ order in h where p is the formal order of accuracy of the approximation method. However, we aim to consistently approximate the altered diffusion equation so we have to make ϵ p^{th} order in h.

Again, the assumption that $\mathbf{b} \cdot \nabla T = 0$ is based on the notion that for $D_{\parallel}/D_{\perp} \to \infty$ the timescale for the parallel diffusion, $\tau_{\parallel}$, compared to the timescale for the perpendicular diffusion, $\tau_{\perp}$, becomes very small. Basically, for $D_{\parallel}/D_{\perp} \to \infty$ we have that $\tau_{\parallel}/\tau_{\perp} \to 0$. This implies that within the parallel diffusion timescale, the perpendicular diffusion does not evolve, and within the perpendicular diffusion timescale the parallel diffusion *has already* evolved. *However*, $D_{\parallel}/D_{\perp} \neq 0$ and within both timescales there *will* be a finite but small ϵ-sized change in temperature. Note that numerical issues with regard to the condition number arise because we imply both $\nabla \cdot \mathbf{q}_{\parallel} = 0$ and $\mathbf{b} \cdot \nabla T = 0$. The former because $D_{\parallel}$ is infinitely large compared to the other terms in the diffusion equation and the latter because we assume that the parallel diffusion has already evolved. None of both is true. As $D_{\parallel} \gg 1$ we simply have that $\mathbf{b} \cdot \nabla T = \epsilon$ where, formally when $D_{\parallel}/D_{\perp} \to \infty$, the parameter ϵ goes to zero. The value ϵ can be considered as an off-set to prevent ill-posedness. As the term $\mathbf{b} \cdot \nabla T$ is an approximation which varies locally there may not be a single optimum value for ϵ. For now we assume that ϵ is

constant for a given grid. The method, that we denote as *SFD-ϵ*, is fully described by adding the source function (5.1), where ϵ is user selected. In figures 5.9 and 5.10 we

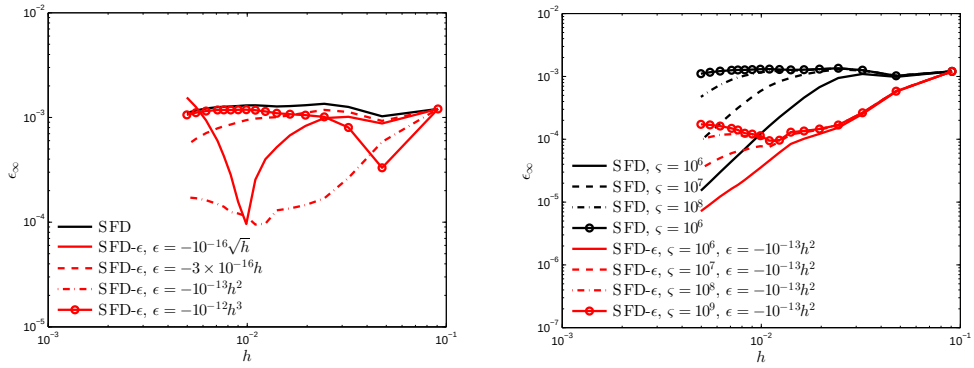

(a) (b)

Figure 5.9: Results of the SFD-ϵ scheme for the tilted elliptic test case with $a = 0.15, b = 0.85, \theta = 1/3\pi$ (a) $\varsigma = 10^9$, (b) $\epsilon = -1 \times 10^{-13} h^2$.

show the results for the tilted elliptic test case. From these results it is clear that adding ϵ can have a positive effect on the accuracy, for a certain range of ϵ. We confirm that the value of ϵ should scale with h^2. We conclude that SFD-ϵ may be a viable improvement

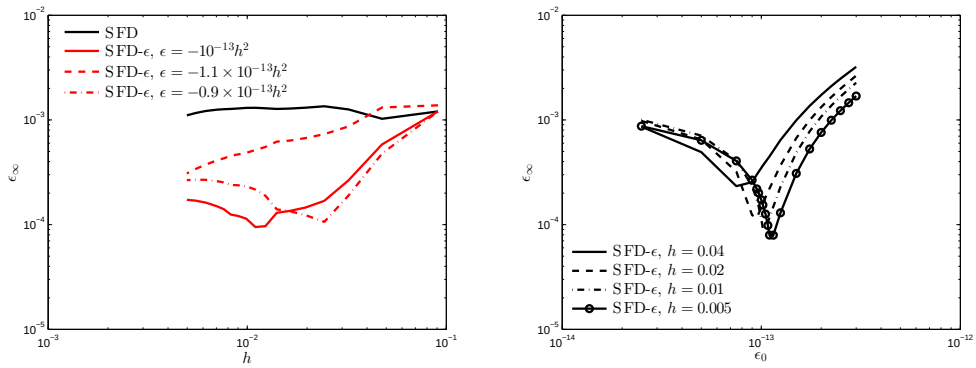

(a) (b)

Figure 5.10: Results of the SFD-ϵ scheme for the tilted elliptic test case with $a = 0.15, b = 0.85, \theta = 1/3\pi$ (a) ϵ_∞ convergence, (b) $\epsilon = -\epsilon_0 h^2$ with various values for ϵ_0.

of the SFD method for extremely anisotropic heterogeneous problems. The caveats are: finding a suitable value for ϵ and the absence of a formal guarantee of convergence.

5.4.2 *Alteration of unit direction vector*

We perform another alteration by adding an ϵ-scaled vector to the unit direction vectors, i.e.

$$T_t = \nabla \cdot \left\{ D_{\parallel}([\mathbf{b} + \mathbf{b}_\epsilon] \cdot \nabla T)\,(\mathbf{b} + \mathbf{b}_\epsilon) + D_{\perp}(\mathbf{b}_\perp \cdot \nabla T)\mathbf{b}_\perp \right\} + f,$$

which is denoted as *SFD-ϵ2*. Here we add a vector scaled with ϵ to the unit direction vector. Note that we now adapt the linear operator whereas for SFD-ϵ we changed the source.

ϵ-sized vector of ones

First we define $\mathbf{b}_\epsilon$ as $\epsilon\,\mathbf{1} = \epsilon[1,1]^T$. We perform this addition in two ways: (1) with random spatial variation of ϵ, (2) with prescribed spatial variation of ϵ. We apply ϵ per row of the linear operator. For the random perturbation, ϵ is defined as $\epsilon = \mathcal{R}\epsilon$ where $\mathcal{R}$ is a random number between zero and one with a uniform probability distribution. We consider the random perturbation because it implies independence of the specific field line distribution. For the tilted closed field line problem we do not see an improvement

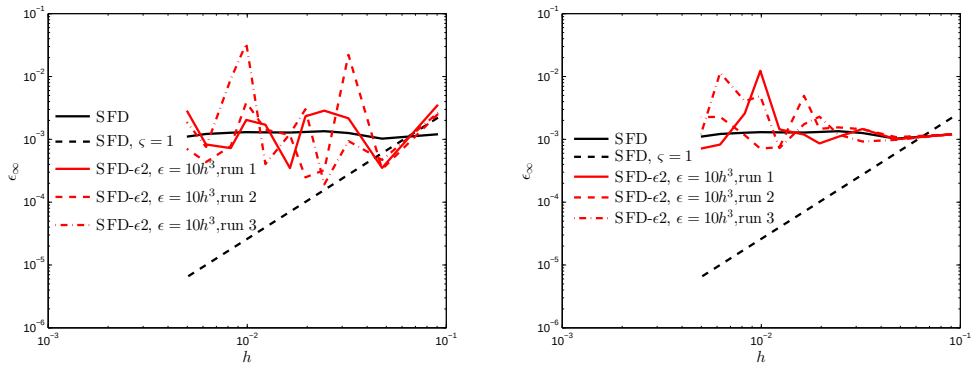

Figure 5.11: Results of the SFD-ϵ2 scheme for the tilted elliptic test case with $a = 0.15, b = 0.85, \theta = 1/3\pi, \varsigma = 10^9$ (a) $\epsilon = 10h^3$, (b) $\epsilon = 2e - 5$.

of the accuracy if we apply a constant value for ϵ. The randomly perturbed ϵ shows improved accuracy for several resolutions but there is no convergence of the accuracy, see figure 5.11. From figures 5.11a and 5.11b it seems that the (relative) size of ϵ is not of significant importance, rather we suspect that the spatial distribution of ϵ determines the effectiveness. We see from figures 5.11a and 5.11b that for some distributions of ϵ the accuracy is close to the formal second-order accuracy. To make the improvement more consistent we replace the random value $\mathcal{R}$ by a periodic value. We apply the MFD-ϵ2 method with the following distribution for ϵ

$$\epsilon = \epsilon_0 \sin(2\pi\omega k/M),$$

where k is the vector index of the unknown, M is the total number of unknowns, ω the frequency of the perturbation and ϵ_0 the maximum perturbation size. The results

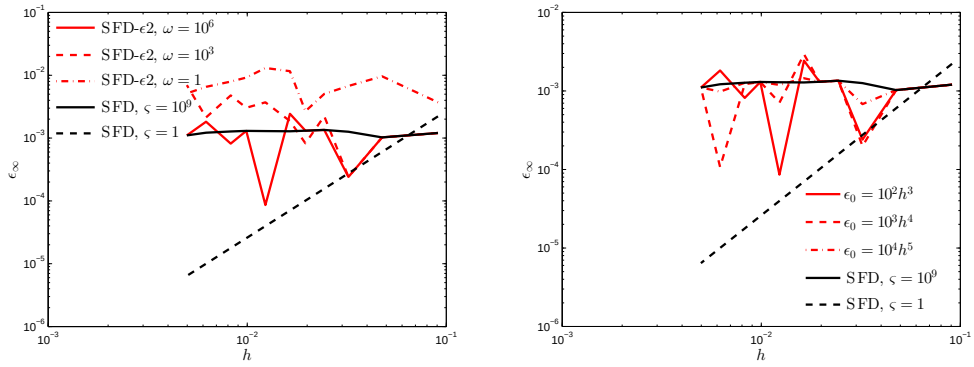

(a) (b)

Figure 5.12: Results of the SFD-ϵ2 scheme for the tilted elliptic test case with $a = 0.15, b = 0.85, \theta = 1/3\pi, \varsigma = 10^9$ with $\epsilon = \epsilon_0 \sin(2\pi\omega k/M)$ where (a) $\epsilon_0 = 10h^3$, (b) $\omega = 10^6$.

shown in figures 5.12a and 5.12b do not indicate a clear improvement or deterioration of the accuracy. We do note that for $\omega = 10^6$ the results are on average better than those of the original SFD scheme. A possible cause for the randomness in the convergence of the SFD-ϵ2 method is the fact that the ϵ-scaled vector always has the same directionality. Also, the idea of a (quasi-)random value for ϵ or k is discarded.

ϵ-sized perpendicular perturbation vector

Consider again the periodic scalar perturbation of the unit direction vector, but now as the multiplier of a perpendicular unit direction vector, i.e.

$$\mathbf{b}_\epsilon = \epsilon_0 \mathbf{b}_\perp \cos(2\pi\omega k/M).$$

This is added to the tangential unit direction vector. Note that setting the frequency ω to zero yields a constant perpendicular perturbation, which transforms closed field lines into spiraling field lines. In figure 5.13a we see the results for a perturbed unit direction vector that is not normalised. For $\omega = 0$ and $\omega = 1$ we see an improvement in convergence initially but the convergence reduces to zeroth order for higher resolutions. In figure 5.13b we see a clearer convergence for $k = \sqrt{x^2 + y^2}$ but second-order accuracy is not attained and the convergence is not smooth. In the same figure we see that setting $k = 1$ significantly improves the accuracy and almost restores second-order accuracy for this test case. We also see that $\omega = 0$ gives the same result as $\omega = 1$, i.e. uniformly offsetting the field lines in a perpendicular direction improves the result for this test case, i.e. $\mathbf{b}_\epsilon = h^2 \mathbf{b}_\perp$. These results suggest the use of a constant normalised perpendicular perturbation of the field lines.
To repeat the results for the tilted elliptic test case with a tilt angle $\theta = 1/3\pi$, ϵ_0 must be negated.

A further improvement may be obtained by also applying the perturbation vector to the perpendicular diffusion component.

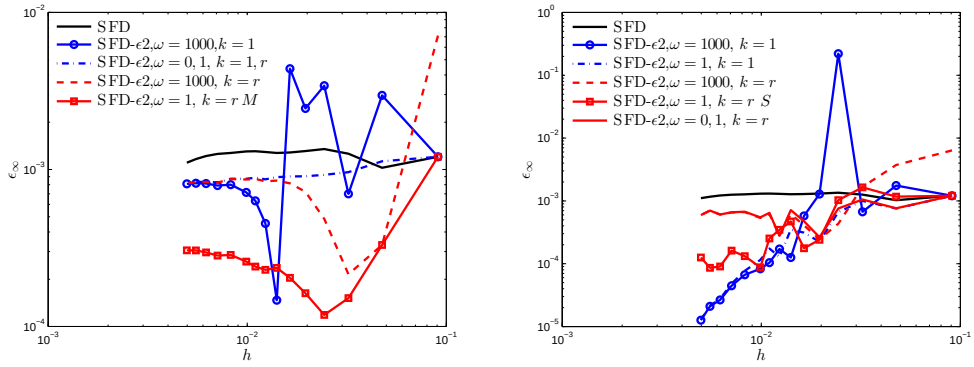

(a) (b)

Figure 5.13: Results of the SFD-ϵ2 scheme for the tilted elliptic test case with $a = 0.15, b = 0.85, \theta = 1/6\pi, \varsigma = 10^9$ with $\mathbf{b}_\epsilon = \epsilon_0 \mathbf{b}_\perp \cos(2\pi\omega k/M)$, $\epsilon_0 = h^2$, (a) non-normalised, (b) normalised.

For further research we suggest to use periodicity of the perpendicular perturbation along the field lines, i.e. k is determined by the distance along a particular field line. This periodicity implies that the field lines have an ϵ-sized wiggle. To impose this wiggle however, we require a field line trace to identify where, and on which field line each degree of freedom is positioned. This tracing requirement is prohibitively expensive. To simplify the idea we suggest to apply: (1) a perpendicular perturbation $\mathbf{b}_\epsilon$ that varies along the tangent of a circle positioned over the O-point of the original field line distribution, i.e.

$$\mathbf{b}_\epsilon = \epsilon_0 \mathbf{b}_\perp \sin(2\pi\omega\, r\theta), \quad \theta = \arctan(y/x), \quad r = \sqrt{x^2 + y^2},$$

(2) perturbations tangent and normal to the contour lines of a double harmonic distribution, i.e.

$$\text{tangent:} \quad \mathbf{b}_\epsilon = \epsilon_0 \frac{1}{\sqrt{\tilde{T}_x^2 + \tilde{T}_y^2}} \left(-\tilde{T}_y, \tilde{T}_x\right)^T,$$

$$\text{normal:} \quad \mathbf{b}_\epsilon = \epsilon_0 \frac{1}{\sqrt{\tilde{T}_x^2 + \tilde{T}_y^2}} \left(\tilde{T}_x, \tilde{T}_y\right)^T,$$

where

$$\tilde{T} = \sin(2\pi\omega x)\sin(2\pi\omega y).$$

5.4.3 *Added ϵ-sized diffusion terms*

Instead of an alteration of the unit direction vector or the parallel temperature gradient we add a parallel diffusion term $\mathcal{D}_\epsilon$:

$$\mathcal{D}_\epsilon = \nabla \cdot (\mathbf{b} \cdot \nabla T)(\epsilon \mathbf{b}).$$

This does not break the assumption that $\mathbf{b} \cdot \nabla T$ is zero and boils down to perturbing the parallel diffusion coefficient with a value ϵ. Basically doing this only changes the maximum eigenvalue slightly. We now assume that in the above equation the term $(\epsilon \mathbf{b})$ is constant, yielding

$$\mathcal{D}_\epsilon = \epsilon \mathbf{b} \cdot \nabla \left(\mathbf{b} \cdot \nabla T \right),$$

and requiring a numerical description of the derivatives. We denote this alteration of the SFD scheme with *SFD-dϵ*. Apparent downside is that it cannot be expressed as a contour integral. From the results shown in figures 5.14a and 5.14b we see that there

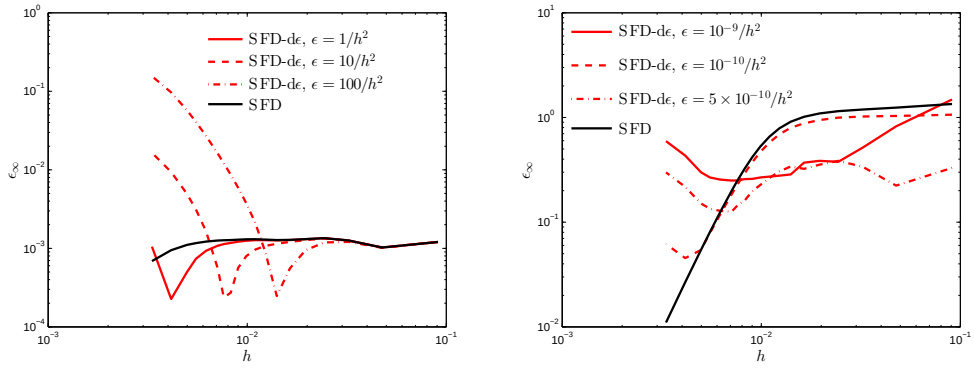

(a) (b)

Figure 5.14: Results of the SFD-dϵ scheme, (a) for the tilted elliptic test case with $a = 0.15, b = 0.85, \theta = 1/3\pi, \varsigma = 10^9$, $\omega = 10^6$, (b) for the tilted closed field line case with $a = 1, b = 3, \theta = 1/3\pi, \varsigma = 10^9$.

is an improved accuracy and convergence as compared to the unchanged SFD scheme, but only for certain values of ϵ and up to a certain resolution.

We try the following ϵ-sized alteration of the parallel diffusion operator

$$\mathcal{D}_\epsilon = \nabla \cdot \left[\epsilon \left(\mathbf{b} \cdot \nabla T \right) \mathbf{b}_\perp \right],$$

where we add perpendicular diffusion based on the parallel gradient. We denote this alteration as *SFD-dϵ 2*. From the results in figure 5.15 we see that the parameter ϵ gives an improvement if it scales as h^p with p larger than approximately 5.25. For the tilted elliptic problem $\epsilon = -0.075 D_\parallel h^{5.5}$ improves the results for all values of the anisotropy.

We conclude that the idea of an ϵ-sized alteration of the model can increase the accuracy with which the unaltered model is approximated. The downsides are that beforehand it is difficult to know the best value of ϵ for which the result is improved, particularly what is the best h-scaling. Further research may be done on this.

5.5 Shifting the unit circle

We have learned that the distribution of the rotation tensor $\mathbf{b}\mathbf{b}^T$ is somehow crucial in determining the performance of the SFD scheme. Also, based on the previous chapter,

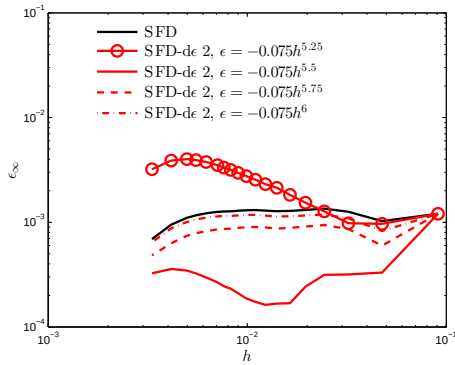

(a)

Figure 5.15: Results of the SFD-dϵ scheme for the tilted elliptic test case with $a = 0.15, b = 0.85, \theta = 1/3\pi, \varsigma = 10^9, \omega = 10^6$.

the sign switch of the off-diagonal diffusion tensor components is the culprit of stagnating convergence and reduced accuracy. A rather simple way to avoid this is to shift the unit circle to the up-right by a value one. I.e. we add one to the components of the unit direction vector. Compare this to section 4.4 where we describe a method that effectively rotates the unit direction vectors in case there is a sign switch and section 5.4.2 where we add a small scalar perturbation.

Here we simply write the new direction vector as $\tilde{\mathbf{b}} = \mathbf{b} + \mathbf{1}$. As all the direction vector components are positive, immediately we have that $\alpha||\mathbf{v}||^2 > \mathbf{v} \cdot \tilde{\mathbf{b}}\tilde{\mathbf{b}}^T > \gamma||\mathbf{v}||^2$ is fullfilled for any $\alpha, \gamma > 0$, and thus the diffusion tensor is strongly elliptic. We identify the following properties of the shifted unit direction vector $\tilde{\mathbf{b}}$ that should be maintained:

- preservation of $\Delta(Ab_1^2)$, $\Delta(Ab_2^2)$, $\Delta(Ab_1b_2)$,
  where A represents $D_\parallel T_x$, $D_\perp T_y$, $D_\parallel T_y$, $D_\perp T_x$, $(D_\parallel - D_\perp)T_x$, or $(D_\parallel - D_\perp)T_y$,
- rotational difference $\Delta\alpha$,

where we do not satisfy the requirement $||\tilde{\mathbf{b}}|| = 1$ since normalising the shifted vector would change the angle of rotation. Shifting the unit direction vectors to the upright will keep Δb_1^2 and Δb_2^2 preserved, as well as the rotational difference. However, the value for $\Delta(b_1b_2)$ is roughly doubled if the unit direction vectors do not lie in the same quadrant and for non-constant A, $\Delta(Ab_1^2)$, $\Delta(Ab_2^2)$ and $\Delta(Ab_1b_2)$ are not preserved as well. For the implementation we shift the unit circle by one and we do not normalise the resulting vector. For the source vector we only apply the shifted vector to the zeroeth order terms. From the results shown in figure 5.16a we see that for extreme anisotropy with $\varsigma > 10^6$, shifting the unit circle improves the accuracy of the SFD scheme. We also see from figure 5.16a that the order of accuracy is not completely restored to second order and that the error is slightly offset upwards. For decreasing anisotropy the order of accuracy is restored similar to the normal SFD scheme.
For the results shown in figure 5.16a we applied the unit shift everywhere in the domain. We can mitigate the negative effect on the accuracy by applying the shift conditionally. In figure 5.16b we see the result of applying the shift only in case there is no sign

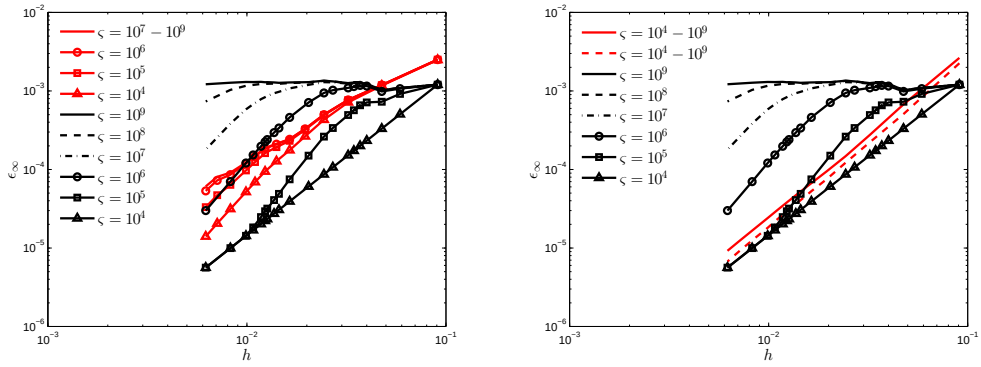

(a) (b)

Figure 5.16: Elliptic field line problem approximated with the SFD scheme, error ϵ_∞ convergence for $\theta = 1/6\pi, a = 0.15, b = 0.85$, SFD scheme with shifted unit circle in red, SFD scheme without shift in black, (a) shift applied everywhere, (b) shift applied with *no sign switch* (solid), *no sign switch including O-point* (dashed).

switch of the off-diagonal diffusion tensor. Locally applying the unit shift restores the convergence the SFD scheme for this test case.
To make this method more robust we should consider the use of a correction factor. Assuming $A_r \approx A_l$ we have

$$\nabla A b_1 b_2 \approx \nabla A \tilde{b}_1 \tilde{b}_2 = \left[(A\tilde{b}_1\tilde{b}_2)_r - (A\tilde{b}_1\tilde{b}_2)_l \right] \frac{(b_1 b_2)_r - (b_1 b_2)_l}{(\tilde{b}_1\tilde{b}_2)_r - (\tilde{b}_1\tilde{b}_2)_l},$$

and for general A

$$\nabla A b_1 b_2 \approx \nabla A \tilde{b}_1 \tilde{b}_2 = \left[(A\tilde{b}_1\tilde{b}_2)_r - (A\tilde{b}_1\tilde{b}_2)_l \right] \frac{(A^* b_1 b_2)_r - (A^* b_1 b_2)_l}{(A^*\tilde{b}_1\tilde{b}_2)_r - (A^*\tilde{b}_1\tilde{b}_2)_l},$$

where A^* is an approximation of A. This result supports one of the conclusions of chapter 4, namely that sign switching of the off-diagonal diffusion tensor values is a main cause for the deterioration of the accuracy, either directly or indirectly.

5.6 Regularisation of the diffusion tensor

In section 4.2 we discussed the relevance of the sign transition and we shortly considered the properties of the diffusion tensor. We noted that the diffusion tensor becomes positive semi-definite for $\varsigma \to \infty$ and that it is not in general strongly elliptic. In section 4.5 we used an ϵ-sized z-component to prevent singular values in O-points. This z-component was merely meant to prevent a division by zero. Here we discuss a similar idea.

Both positive definiteness and strong ellipticity may be ensured by adding a dummy diffusion component D_z. We define the diffusion tensor as

$$\mathbf{D} = \begin{pmatrix} D_{11} & D_{12} & 0 \\ D_{21} & D_{22} & 0 \\ 0 & 0 & D_z \end{pmatrix},$$

i.e. the direction represented by D_z is defined as $\mathbf{z} = \mathbf{b} \times \mathbf{b}_\perp$. The added term is $\frac{\partial D_z T_z}{\partial z}$. Now, to guarantee that the diffusion tensor is SPD we must ensure that the characteristic polynomial only has real and positive eigenvalues. I.e. for the following polynomial

$$\begin{aligned} f(\lambda) = \lambda^3 &- (D_{11} + D_{22} + D_z)\,\lambda^2 \\ &- \left[D_{21}^2 - D_{11}D_{22} - (D_{11} + D_{22})\,D_z\right]\lambda - \left(D_{11}D_{22} - D_{21}^2\right)D_z = 0, \end{aligned}$$

we only want positive real eigenvalues. For this, the local maximum and minimum must lie on the right side of the $f(\lambda)$-axis and the maximum and minimum must be positive and negative valued respectively. To guarantee the latter we take the derivative of the characteristic polynomial and find the roots, which must be distinct and real. We have the following requirements for positive real eigenvalues:

$$\begin{aligned} &(D_{11} + D_{22} + D_z)^2 + 3D_{21}^2 > 3\left[D_{11}D_{22} + (D_{11} + D_{22})D_z\right], \\ &D_{11} + D_{22} + D_z > \sqrt{(D_{11} + D_{22} + D_z)^2 + 3\left(D_{21}^2 - D_{11}D_{22} - (D_{11} + D_{22})D_z\right)}, \end{aligned}$$

which are non-linear and locally variant and so an exact determination is intractable. Note that the latter requirement for positive eigenvalues is sufficient to guarantee that two eigenvalues are real and positive but it is insufficient for all three eigenvalues to be positive and real. It is clear that for D_z large enough we have real distinct positive eigenvalues. Since the minimum value for D_z scales with $D_\parallel$, a safe choice for the value is $\epsilon\varsigma^2$ where ϵ has to be determined by the practitioner.

Since we have a three-dimensional diffusion tensor we now have to solve a three-dimensional diffusion equation. Suppose we take a single stencil only in the z-direction, i.e. three degrees of freedom in the dummy direction are needed. Two of the added degrees of freedom can be discarded if we apply Dirichlet boundary conditions in the z-direction and so the number of unknowns does not increase. The added third dimension should not affect the solution in two dimensions, so $T_{zz} = 0$, but it should also be non-trivial, so $T_z \neq 0$, i.e. T should be linear in the z-direction. The way to go is to set Dirichlet conditions with the constraint that T is linear in z-direction. Suppose we number the points in the x-,y- and z-direction with i, j, k respectively, then the Dirichlet boundary conditions $T_{i,j,1}$ and $T_{i,j,3}$ should be set such that $T_{i,j,1} = T_{i,j,2} - \beta$, $T_{i,j,3} = T_{i,j,2} + \beta$ for all i, j where $k = 2$ indicates the two-dimensional solution. The suggested method described here only works for two-dimensional problems as the added third dimension is only a dummy direction.

Divergence free alteration of flux

Arnold and Falk [10] and Jacq et al. [69] write the diffusion equation in vector form. The vector form allows them to add a divergence free source term (which we denote by $\mathbf{D}^\epsilon$)

to the constitutive part of the equation. This source term does not affect the consistency of the scalar diffusion equation, it is merely meant to regularise the diffusion tensor. Following Arnold and Falk we denote the original term $\mathbf{D}\nabla T$ as the flux and $(\mathbf{D} + \mathbf{D}^\epsilon)\nabla T$ as the pseudo-flux. A divergence free source term is easily found by adding the curl of a vector:

$$\mathbf{D}^\epsilon = \epsilon \nabla \times .$$

This requires three dimensions for a non-trivial application as the curl of a two-dimensional gradient is zero. Note that the addition of $\nabla\times$ does not alter the ellipticity and positive-definiteness of the diffusion tensor but rather affects the positive-definiteness and ellipticity of the linear operator.

5.7 Conclusion

In this chapter we have looked at two model adaptation methods to improve the accuracy and monotonicity for approximating extremely anisotropic diffusion. Firstly, for steady heterogeneous diffusion problems with zero parallel temperature gradient we considered imposing a zero value for the parallel diffusion coefficient on the transition line. This restores the accuracy for both the SFD scheme and the asymmetric finite difference method. We generalised that to unsteady problems with non-zero parallel temperature gradients by dividing the problem in finite-sized bands with zero parallel diffusion coefficients outside the band.
Secondly, we changed the model equations with ϵ-sized differential terms and sources and applied the SFD scheme. We could see improvements for certain values of the small parameter and for certain resolution ranges.

6

CONCLUSION

For magnetic fields not aligned with the computational grid special tools are required to ensure accuracy, convergence and monotonicity. Several of these tools have been developed and/or described in this thesis.

In chapter 2 we have proposed and investigated a new finite-differencing method on a co-located grid that implements the concept of following the field line track within the stencil area to obtain the differencing points that are finally used in the approximation. In terms of accuracy and convergence the aligned methods are similar to exactly differentiating the interpolation schemes. The symmetric variants of our method are more accurate and less anisotropy-dependent than the asymmetric scheme by Günter et al. The symmetric finite difference scheme by Günter et al. works well in maintaining the order of convergence for a wide variety of cases, it exhibits very low numerical pollution of the perpendicular diffusion, but it is also more susceptible to number representation problems. This is apparent because the linear operator becomes ill-conditioned for large anisotropy ratios.
We see that in all cases where the aligned symmetric scheme and the symmetric interpolation scheme do not maintain order of convergence and/or the level of accuracy, the approximation of the perpendicular flux, T_n, determines this behavior.
For almost all the test cases considered, the symmetric finite difference scheme is better able to maintain the order of accuracy. The symmetric finite difference scheme does however show anisotropy-dependent accuracy for tilted (closed) elliptic magnetic field line distributions. This anisotropy dependence is increased if we also make the diffusion-tensor components temperature dependent. This is caused by the interpolation required to get the temperature values in the flux points. For the tilted cases with temperature dependent diffusion coefficients our aligned and interpolated symmetric scheme shows comparable and even superior results.

In chapter 3 we have proposed and investigated a new finite-volume method. The method exploits $\mathcal{C}_1$ continuous connections of each volume with its neighbouring volumes. To have varying connectivity we introduce a parameter e. We conclude that the connectivity as such is not of primary importance for maintaining the convergence and accuracy for the extreme anisotropy.
We further conclude that $D_{\|} = 0$ enforcement is a viable approach to improve numerical methods in case of extremely anisotropic problems with closed field lines and zero parallel diffusion. Inserting $D_{\|} = 0$ on a line connecting the O-point with the last closed field line recovers the formal accuracy in all the test problems described in this paper,

including the Sovinec test case and the tilted elliptic test case. We also conclude that having a temperature unknown exactly in the *O*-point can improve the anisotropy independence significantly in case of closed field lines.

An important finding from chapter 4 is that cases with closed field lines are problematic for the symmetric finite difference scheme. The cause of this is the occurrence of sign switching around the axes that go through the *O*-point. We conclude that the primary reason for the difficulty of closed field line problems is the fact that in these problems there are lines along which the off-diagonal diffusion tensor values change sign.
The performance of the symmetric finite difference scheme and the performance of the asymmetric finite difference/finite volume scheme are made more robust for specific test cases by applying tensor/diffusion-coefficient based adaptations: (1) normalised averaging of fluxes, (2) directly preventing the sign switch through rotation of the unit direction vector, (3) avoiding the non-regular diffusion tensor regions.

In chapter 5 we have looked at two model adaptation methods to improve the accuracy for approximating extremely anisotropic diffusion. Firstly, for steady heterogeneous diffusion problems with zero parallel temperature gradient we reconsidered imposing a zero value for the parallel diffusion coefficient on the transition line. This restores the accuracy for both the symmetric finite difference scheme and the asymmetric finite difference method. We apply this idea to unsteady problems with non-zero parallel temperature gradients by dividing the initial temperature distribution in finite-sized bands with zero parallel diffusion coefficients outside the band.
Secondly, we change the model equations with very small-sized differential terms and sources and apply the symmetric finite difference scheme. We see improvements in accuracy and convergence, for certain values of the small parameter and for certain resolution ranges.
The most promising result is obtained by shifting the unit circle of the unit direction vector as a means to guarantee strong ellipticity for extremely anisotropic diffusion operators.

We recommend that field-aligned discretisation schemes are further investigated to create monotonicity preserving methods for extremely anisotropic diffusion as they do not rely on post-processing of the results or on iterative procedures. We further recommend that the methods presented in this thesis are applied to anisotropic diffusion with a partially aligned coordinate system to investigate the mitigation of numerical errors caused by misalignment. The methods described in this thesis are developed with a two-dimensional application in mind: specifically the approximation of nuclear fusion plasma through the poloidal plane of a torus, where the toroidal direction is approximated by a Fourier series. The field aligned finite difference scheme, the eight point finite volume scheme, normalisation and regularisation of the diffusion tensor, and the model adaptation methods *do* allow for an extension to three dimensions, we recommend this as a topic for further research. Further, we note that, specifically for a uniform rectangular Cartesian grid, the symmetric finite difference scheme is akin to mimetic difference methods in preserving the self-adjointness of the divergence and the flux operator. A topic for future research could be to rigorously test mimetic finite dif-

ference methods with the extremely anisotropic diffusion test cases that are presented in this thesis.

A

IMPORTANCE OF SYMMETRY FOR ENERGY CONSERVATION

The symmetric scheme of Günter et al. preserves the self-adjointness of the differential operator

$$\nabla \cdot (\mathbf{D} \cdot \nabla T) = \nabla \cdot \Big(D_{\parallel} (\mathbf{b} \cdot \nabla T) \mathbf{b} \Big) + \nabla \cdot (D_{\perp} (\mathbf{b}_{\perp} \cdot \nabla T) \mathbf{b}_{\perp}) \,.$$

Both parts in the right hand side are self-adjoint and thus have a complete set of real orthogonal eigenvectors. This basically means that the linear operator is symmetric and so we have a full set of real eigenvalues. Consider the following description of the diffusion equation

$$\begin{aligned} \nabla \cdot (\mathbf{D} \cdot \nabla T) &= \nabla \cdot \mathbf{q}_{\parallel} + \nabla \cdot \mathbf{q}_{\perp} \\ &= \nabla \cdot \Big(D_{\parallel} (\mathbf{b} \cdot \nabla T) \mathbf{b} \Big) + \nabla \cdot (D_{\perp} (\mathbf{b}_{\perp} \cdot \nabla T) \mathbf{b}_{\perp}) \,. \end{aligned}$$

Analytically the two flux vectors $\mathbf{q}_{\parallel}$ and $\mathbf{q}_{\perp}$ cannot be written in terms of each other because they are perpendicular through the vector $\mathbf{b}_{\perp}$. This is made clear by writing the diffusion operator as follows

$$\nabla \cdot (\mathbf{D} \cdot \nabla T) = \nabla \cdot \left[\mathcal{R} \begin{pmatrix} D_{\parallel} & 0 \\ 0 & 0 \end{pmatrix} \mathcal{R}^T \right] \cdot \nabla T + \nabla \cdot \left[\mathcal{R} \begin{pmatrix} 0 & 0 \\ 0 & D_{\perp} \end{pmatrix} \mathcal{R}^T \right] \cdot \nabla T, \quad \text{(A.1)}$$

where $\mathcal{R}$ is the local rotation matrix; rotating from the global coordinates to the local field aligned coordinates. Suppose that for a node inside the computational domain we have the following description of the linear operator

$$\begin{aligned} -\nabla \cdot (\mathbf{D} \cdot \nabla T) \approx \mathbf{L}T, \quad \mathbf{L}T = (\mathcal{D}\mathbf{D}\mathcal{G})T, \\ \mathbf{w} = \mathbf{D} \cdot \nabla T, \quad \mathcal{G}T = -\nabla T, \quad \mathcal{D}\mathbf{w} = \nabla \cdot \mathbf{w}, \end{aligned}$$

where $\mathbf{L}$, $\mathcal{D}$ and $\mathcal{G}$ are linear operators. Now we write equation A.1 as

$$\mathbf{L}T = (\mathcal{D}\mathbf{D}_{\parallel}\mathcal{G})T + (\mathcal{D}\mathbf{D}_{\perp}\mathcal{G})T, \quad \text{(A.2)}$$

where clearly only the diffusion tensors matter in separating the parallel diffusion from the perpendicular diffusion. This means that preserving the self-adjointness does not guarantee that parallel and perpendicular diffusion components are separated since that refers only to the relation between the divergence and the gradient operators.
This can also be demonstrated by considering the properties of the discrete operators. If the linear operators are symmetric they can be written as

$$\mathbf{R}\Lambda\mathbf{R}^T = \mathbf{R}_{\parallel}\Lambda_{\parallel}\mathbf{R}_{\parallel}^T + \mathbf{R}_{\perp}\Lambda_{\perp}\mathbf{R}_{\perp}^T,$$

and inversely, since $\mathbf{R}^T = \mathbf{R}^{-1}$,

$$\mathbf{R}_{\parallel}^T \mathbf{L}_{\parallel} \mathbf{R}_{\parallel} = \Lambda_{\parallel}, \quad \mathbf{R}_{\perp}^T \mathbf{L}_{\perp} \mathbf{R}_{\perp} = \Lambda_{\perp}.$$

We know from the fact that the matrices are self-adjoint that $\mathbf{R}_{\parallel}$ and $\mathbf{R}_{\perp}$ are complete sets of orthogonal eigenvectors. Basically we know that $\mathbf{R}$ spans some N-dimensional space, so do $\mathbf{R}_{\parallel}$ and $\mathbf{R}_{\perp}$. Hence,

$$\mathbf{R}(i) = \mathbf{R}_{\parallel}(i) + \mathbf{R}_{\perp}(i), \quad \mathbf{R}_{\parallel}(i) \cdot \mathbf{R}_{\perp}(i) = 0, \quad \forall i,$$

is extremely unlikely. We do have that the product $\mathcal{L}_{\parallel}\mathcal{L}_{\perp}$, where $\mathcal{L}_{\parallel}$ and $\mathcal{L}_{\perp}$ are the linear operators for the parallel and the perpendicular diffusion respectively, is also symmetric, i.e. $(\mathbf{R}_{\parallel}\Lambda_{\parallel}\mathbf{R}_{\parallel}^T)(\mathbf{R}_{\perp}\Lambda_{\perp}\mathbf{R}_{\perp}^T)$ is itself symmetric.

The symmetry of the operators helps in preserving global energy. Because of the symmetry of the linear operator we can write

$$T\frac{\partial T}{\partial t} = T^T \mathbf{L} T = \sum_{i=1}^{N} \lambda_i T_i^2,$$

$$T^T \left(\mathbf{R}_{\parallel}\Lambda_{\parallel}\mathbf{R}_{\parallel}^T + \mathbf{R}_{\perp}\Lambda_{\perp}\mathbf{R}_{\perp}^T \right) T = \sum_{i=1}^{N} \lambda_i^{\parallel} T_i^2 + \sum_{i=1}^{N} \lambda_i^{\perp} T_i^2,$$

where N is the number of unknowns, $\mathbf{L}$ the linear operator, and $\mathbf{R}, \Lambda$ the eigenvectors and eigenvalues respectively. This tells us that quadratic forms of the linear operator can be separated in a parallel and perpendicular component.
We can directly observe that if $\lambda_i^{\perp}/\lambda_i^{\parallel} \to 0$ the contribution to the energy goes to zero as well, not affecting the energy of the parallel part. Reversely there is no added value to the perpendicular part for $\lambda_i^{\parallel} \to \infty$ since the quadratic forms are strictly separated.

B

INTERPOLATION COEFFICIENTS

Given an interpolation for T

$$T(x,y) = c_1x^2y^2 + c_2x^2y + c_3y^2x + c_4x^2 + c_5y^2 + c_6xy + c_7x + c_8y + c_9, \quad x,y \in [-h,h], \tag{B.1}$$

the coefficients $c_1, \dots c_9$ follow from

$$\begin{pmatrix} c_1 \\ c_2 \\ c_3 \\ c_4 \\ c_5 \\ c_6 \\ c_7 \\ c_8 \\ c_9 \end{pmatrix} = \mathbf{V}^{-1}\mathbf{T}, \quad \mathbf{V} = \begin{pmatrix} h^4 & h^3 & -h^3 & h^2 & h^2 & -h^2 & -h & h & 1 \\ h^4 & h^3 & h^3 & h^2 & h^2 & h^2 & h & h & 1 \\ h^4 & -h^3 & -h^3 & h^2 & h^2 & h^2 & -h & -h & 1 \\ h^4 & -h^3 & h^3 & h^2 & h^2 & -h^2 & h & -h & 1 \\ 0 & 0 & 0 & h^2 & 0 & 0 & -h & 0 & 1 \\ 0 & 0 & 0 & h^2 & 0 & 0 & h & 0 & 1 \\ 0 & 0 & 0 & 0 & h^2 & 0 & 0 & h & 1 \\ 0 & 0 & 0 & 0 & h^2 & 0 & 0 & -h & 1 \\ 0 & 0 & 0 & 0 & 0 & 0 & 0 & 0 & 1 \end{pmatrix},$$

$$\mathbf{T} = \begin{pmatrix} T_{i-1,j+1} \\ T_{i+1,j+1} \\ T_{i-1,j-1} \\ T_{i+1,j-1} \\ T_{i-1,j} \\ T_{i+1,j} \\ T_{i,j+1} \\ T_{i,j-1} \\ T_{i,j} \end{pmatrix},$$

and are given by 2.8 in section (2.2.5). Note that using the interpolation scheme with the symmetric coefficients c_4^S, c_5^S, c_7^S, c_8^S, given by (2.10), does not give a fully symmetric

approximation for the derivatives in $\mathbf{x} = \left(\pm\frac{h}{2}, \pm\frac{h}{2}\right), \mathbf{x} = \left(\mp\frac{h}{2}, \pm\frac{h}{2}\right)$. We can obtain a suitable description of the local derivatives by defining c_7 and c_8 as

$$\begin{aligned} c_7 =& \alpha_{ru}\frac{T_{i+1,j+1} + T_{i+1,j} - T_{i,j+1} - T_{i,j}}{2h} + \alpha_{lu}\frac{T_{i,j} + T_{i,j+1} - T_{i-1,j+1} - T_{i-1,j}}{2h} \\ &+ \alpha_{ld}\frac{T_{i,j} + T_{i,j-1} - T_{i-1,j} - T_{i-1,j-1}}{2h} + \alpha_{rd}\frac{T_{i+1,j} + T_{i+1,j-1} - T_{i,j} - T_{i,j-1}}{2h}, \\ c_8 =& \alpha_{ru}\frac{T_{i+1,j+1} + T_{i,j+1} - T_{i,j} - T_{i+1,j}}{2h} + \alpha_{lu}\frac{T_{i,j+1} + T_{i-1,j+1} - T_{i-1,j} - T_{i,j}}{2h} \\ &+ \alpha_{ld}\frac{T_{i,j} + T_{i-1,j} - T_{i-1,j-1} - T_{i,j-1}}{2h} + \alpha_{rd}\frac{T_{i+1,j} + T_{i,j} - T_{i,j-1} - T_{i+1,j-1}}{2h}. \end{aligned}$$

With a bilinear description for each coefficient α, the α's are given in equation (2.27).

C

LINEAR OPERATOR

For the determination of the linear operator it is convenient to collect the factors for each temperature value

$$\begin{aligned} T(x,y) = {} & a_{i,j}T_{i,j} + a_{i+1,j}T_{i+1,j} + a_{i-1,j}T_{i-1,j} + a_{i,j+1}T_{i,j+1} \\ & + a_{i,j-1}T_{i,j-1} + a_{i+1,j+1}T_{i+1,j+1} + a_{i-1,j+1}T_{i-1,j+1} \\ & + a_{i+1,j-1}T_{i+1,j-1} + a_{i-1,j-1}T_{i-1,j-1}, \end{aligned}$$

where for the Vandermonde coefficients we have

$$\begin{aligned} a_{i,j} &= \frac{x^2y^2}{h^4} - \frac{x^2}{h^2} - \frac{y^2}{h^2} + 1, \\ a_{i\pm1,j} &= \frac{1}{2}\left(-\frac{x^2y^2}{h^4} \mp \frac{y^2x}{h^3} + \frac{x^2}{h^2} \pm \frac{x}{h}\right), \\ a_{i,j\pm1} &= \frac{1}{2}\left(-\frac{x^2y^2}{h^4} \mp \frac{x^2y}{h^3} + \frac{y^2}{h^2} \pm \frac{y}{h}\right), \\ a_{i\pm1,j+1} &= \frac{1}{4}\left(\frac{x^2y^2}{h^4} + \frac{x^2y}{h^3} \pm \frac{y^2x}{h^3} \pm \frac{xy}{h^2}\right), \\ a_{i\pm1,j-1} &= \frac{1}{4}\left(\frac{x^2y^2}{h^4} - \frac{x^2y}{h^3} \pm \frac{y^2x}{h^3} \mp \frac{xy}{h^2}\right), \end{aligned} \tag{C.1}$$

and for the symmetric coefficients

$$\begin{aligned} a_{i,j} &= \frac{x^2y^2}{h^4} - \frac{1}{2}\frac{x^2}{h^2} - \frac{1}{2}\frac{y^2}{h^2} + 1, \\ a_{i\pm1,j} &= \frac{1}{2}\left(-\frac{x^2y^2}{h^4} \mp \frac{y^2x}{h^3} + \frac{1}{2}\frac{x^2}{h^2} - \frac{1}{2}\frac{y^2}{h^2} \pm \frac{1}{2}\frac{x}{h}\right), \\ a_{i,j\pm1} &= \frac{1}{2}\left(-\frac{x^2y^2}{h^4} \mp \frac{x^2y}{h^3} - \frac{1}{2}\frac{x^2}{h^2} + \frac{1}{2}\frac{y^2}{h^2} \pm \frac{1}{2}\frac{y}{h}\right), \\ a_{i\pm1,j+1} &= \frac{1}{4}\left(\frac{x^2y^2}{h^4} + \frac{x^2y}{h^3} \pm \frac{y^2x}{h^3} + \frac{1}{2}\frac{x^2}{h^2} + \frac{1}{2}\frac{y^2}{h^2} \pm \frac{xy}{h^2} \pm \frac{1}{2}\frac{x}{h} + \frac{1}{2}\frac{y}{h}\right), \\ a_{i\pm1,j-1} &= \frac{1}{4}\left(\frac{x^2y^2}{h^4} - \frac{x^2y}{h^3} \pm \frac{y^2x}{h^3} + \frac{1}{2}\frac{x^2}{h^2} + \frac{1}{2}\frac{y^2}{h^2} \mp \frac{xy}{h^2} \pm \frac{1}{2}\frac{x}{h} - \frac{1}{2}\frac{y}{h}\right). \end{aligned} \tag{C.2}$$

The local symmetric coefficients are applied to the derivatives, so:

$$\begin{aligned}
T_x(x,y) &= a^x_{i,j}T_{i,j} + a^x_{i+1,j}T_{i+1,j} + a^x_{i-1,j}T_{i-1,j} + a^x_{i,j+1}T_{i,j+1} \\
&\quad + a^x_{i,j-1}T_{i,j-1} + a^x_{i+1,j+1}T_{i+1,j+1} + a^x_{i-1,j+1}T_{i-1,j+1} \\
&\quad + a^x_{i+1,j-1}T_{i+1,j-1} + a^x_{i-1,j-1}T_{i-1,j-1}, \\
T_y(x,y) &= a^y_{i,j}T_{i,j} + a^y_{i+1,j}T_{i+1,j} + a^y_{i-1,j}T_{i-1,j} + a^y_{i,j+1}T_{i,j+1} \\
&\quad + a^y_{i,j-1}T_{i,j-1} + a^y_{i+1,j+1}T_{i+1,j+1} + a^y_{i-1,j+1}T_{i-1,j+1} \\
&\quad + a^y_{i+1,j-1}T_{i+1,j-1} + a^y_{i-1,j-1}T_{i-1,j-1},
\end{aligned}$$

where

$$\begin{aligned}
a^{x,y}_{i,j} &= \frac{1}{2h}\left(-\alpha_{ru} \mp \alpha_{rd} \pm \alpha_{lu} + \alpha_{ld}\right), \\
a^{x,y}_{i+1,j} &= \frac{1}{2h}\left(\pm\alpha_{ru} + \alpha_{rd}\right), \quad a^{x,y}_{i-1,j} = \frac{1}{2h}\left(\alpha_{lu} \mp \alpha_{ld}\right), \\
a^{x,y}_{i,j+1} &= \frac{1}{2h}\left(\mp\alpha_{ru} + \alpha_{lu}\right), \quad a^{x,y}_{i,j-1} = \frac{1}{2h}\left(-\alpha_{rd} \pm \alpha_{ld}\right), \\
a^{x,y}_{i+1,j+1} &= \frac{1}{2h}\alpha_{ru}, \quad a^{x,y}_{i-1,j+1} = \mp\frac{1}{2h}\alpha_{lu}, \\
a^{x,y}_{i+1,j-1} &= \pm\frac{1}{2h}\alpha_{rd}, \quad a^{x,y}_{i-1,j-1} = -\frac{1}{2h}\alpha_{ld},
\end{aligned} \tag{C.3}$$

where the α's are defined by (2.27), and where the upper sign in $\pm$ and $\mp$ refers to superscript x and vice versa the lower sign to superscript y. The terms in equation (2.4) can be approximated by the following schemes

$$\begin{aligned}
\mathcal{A}_1 &= -(D_\parallel - D_\perp)N\frac{T_u - T_d}{2\Delta n}, \\
\mathcal{A}_2 &= (D_\parallel - D_\perp)S\frac{T_r - T_l}{2\Delta s}, \\
\mathcal{A}_3 &= D_\parallel\frac{T_r - 2T_c + T_l}{\Delta s^2} + D_\perp\frac{T_u - 2T_c + T_d}{\Delta n^2}, \\
\mathcal{A}_4 &= \frac{D_{\parallel_r} - D_{\parallel_l}}{2\Delta s}\frac{T_r - T_l}{2\Delta s} + \frac{D_{\perp_u} - D_{\perp_d}}{2\Delta n}\frac{T_u - T_d}{2\Delta n}.
\end{aligned}$$

Using the above descriptions for $a_{i\pm1,j+1}$, $a_{i\pm1,j-1}$, $a_{i,j\pm1}$, $a_{i\pm1,j}$ and $a_{i,j}$ the linear operator can be written as

$$\begin{aligned}
\tilde{f}_{i,j} \approx T_{i,j}d_c + \sum_{n=-1}^{1}\sum_{m=-1}^{1} &\left[a_{i+m,j+n}(x_r,y_r)d_r + a_{i+m,j+n}(x_l,y_l)d_l\right. \\
&\left. + a_{i+m,j+n}(x_u,y_u)d_u + a_{i+m,j+n}(x_d,y_d)d_d\right] T_{i+m,j+n},
\end{aligned}$$

where $\tilde{f}_{i,j}$ is the local source value, including boundary terms. The terms $d_{l,r,u,d,c}$ are described by

$$
\begin{aligned}
d_r &= (D_\parallel - D_\perp)\frac{S}{2\Delta s} + \frac{D_\parallel}{\Delta s^2} + \frac{D_{\parallel_r} - D_{\parallel_l}}{4\Delta s^2}, \\
d_l &= -(D_\parallel - D_\perp)\frac{S}{2\Delta s} + \frac{D_\parallel}{\Delta s^2} - \frac{D_{\parallel_r} - D_{\parallel_l}}{4\Delta s^2}, \\
d_u &= -(D_\parallel - D_\perp)\frac{N}{2\Delta n} + \frac{D_\perp}{\Delta n^2} + \frac{D_{\perp_u} - D_{\perp_d}}{4\Delta n^2}, \\
d_d &= (D_\parallel - D_\perp)\frac{N}{2\Delta n} + \frac{D_\perp}{\Delta n^2} - \frac{D_{\perp_u} - D_{\perp_d}}{4\Delta n^2}, \\
d_c &= -2\frac{D_\parallel}{\Delta s^2} - 2\frac{D_\perp}{\Delta n^2}.
\end{aligned}
$$

D

TAYLOR EXPANSIONS

For the **Asymmetric scheme** described in section 2.2.1 the local truncation errors of the different terms are found by writing out the Taylor expansions

$$(D_{11}T_x)_x : T_x D_{11_x} + T_{xx} D_{11} + h^2 \left[\frac{1}{24} T_x D_{11_{xxx}} + \frac{1}{8} T_{xx} D_{11_{xx}} + \frac{1}{6} T_{xxx} D_{11_x} + \frac{1}{24} T_{xxxx} D_{11} \right] + \mathcal{O}(h^4),$$

$$(D_{21}T_y)_x : T_y D_{21_x} + T_{xy} D_{21} + h^2 \left[\frac{1}{24} T_y D_{21_{xxx}} + \frac{1}{144} T_{yyy} D_{21_x} + \frac{1}{8} T_{xy} D_{21_{xx}} + \frac{1}{6} T_{xyyy} D_{21} + \frac{1}{6} T_{xxxy} D_{21} + \frac{1}{4} T_{xxy} D_{21_x} \right] + \mathcal{O}(h^4),$$

and similarly for $(D_{22}T_y)_y$ and $(D_{21}T_x)_y$ respectively. Likewise for the **Symmetric scheme** in section 2.2.2 the approximations are given by

$$(D_{11}T_x)_x : T_x D_{11_x} + T_{xx} D_{11} + h^2 \left[T_x \left(\frac{1}{8} D_{11_{xyy}} + \frac{1}{24} D_{11_{xxx}} \right) + T_{xx} \left(\frac{1}{8} D_{11_{yy}} + \frac{1}{8} D_{11_{xx}} \right) + \frac{1}{4} T_{xy} D_{11_{xy}} + \frac{1}{4} T_{xyy} D_{11_x} + \frac{1}{4} T_{yyx} D_{11_y} + \frac{1}{6} T_{xxx} D_{11_x} + \frac{1}{4} T_{xxyy} D_{11} + \frac{1}{12} T_{xxxx} D_{11} \right] + \mathcal{O}(h^4),$$

$$(D_{21}T_y)_x : T_y D_{21_x} + T_{xy} D_{21} + h^2 \left[T_y \left(\frac{1}{8} D_{21_{xyy}} + \frac{1}{24} D_{21_{xxx}} \right) + T_{xy} \left(\frac{1}{8} D_{21_{yy}} + \frac{1}{8} D_{21_{xx}} \right) + \frac{1}{4} T_{yy} D_{21_{xy}} + \frac{1}{24} T_{yyy} D_{21_x} + \frac{1}{16} T_{xyy} D_{21_y} + \frac{1}{16} T_{yxx} D_{21_x} + \frac{1}{6} T_{xyyy} D_{21} + \frac{1}{6} T_{yxxx} D_{21} \right] + \mathcal{O}(h^4),$$

and similarly for $(D_{22}T_y)_y$ and $(D_{21}T_x)_y$ respectively. Similar to section 2.2.5, the approximations for the **aligned finite-difference scheme** are given by

$$
\begin{aligned}
\mathcal{A}_1 &= (D_{\parallel} - D_{\perp})\,(c_8 b_1 - c_7 b_2)\left(b_1^2 c_7^{b_2} - b_2^2 c_8^{b_1} - b_1 b_2 c_7^{b_1} + b_1 b_2 c_8^{b_2}\right) \\
&\quad + h_*^2\left(D_{\parallel} - D_{\perp}\right)\Big[\left(-c_3 b_1^2 b_2 + c_2 b_1 b_2^2\right)\left(b_1^2 c_7^{b_2} - b_2^2 c_8^{b_1} - b_1 b_2 c_7^{b_1} + b_1 b_2 c_8^{b_2}\right) \\
&\quad + (c_8 b_1 - c_7 b_2)\left(-b_1^2 b_2^2 c_2^{b_1} + b_1^2 b_2^2 c_3^{b_2} + b_1^3 b_2 c_2^{b_2} - b_1 b_2^3 c_3^{b_1}\right)\Big] + \mathcal{O}(h_*^4), \\
\mathcal{A}_2 &= (D_{\parallel} - D_{\perp})\,(c_7 b_1 + c_8 b_2)\left(b_2^2 c_7^{b_1} + b_1^2 c_8^{b_2} - b_1 b_2 c_7^{b_2} - b_1 b_2 c_8^{b_1}\right) \\
&\quad + h_*^2\left(D_{\parallel} - D_{\perp}\right)\Big[\left(c_2 b_1^2 b_2 + c_3 b_1 b_2^2\right)\left(b_2^2 c_7^{b_1} + b_1^2 c_8^{b_2} - b_1 b_2 c_7^{b_2} - b_1 b_2 c_8^{b_1}\right) \\
&\quad + (c_7 b_1 + c_8 b_2)\left(b_1^2 b_2^2 c_2^{b_2} + b_1^2 b_2^2 c_3^{b_1} - b_1 b_2^3 c_2^{b_1} - b_1^3 b_2 c_3^{b_2}\right)\Big] + \mathcal{O}(h_*^4), \\
\mathcal{A}_3 &= 2D_{\parallel}\left(b_1^2 c_4 + b_2^2 c_5 + b_1 b_2 c_6\right) + 2D_{\perp}\left(b_2^2 c_4 + b_1^2 c_5 - b_1 b_2 c_6\right) \\
&\quad + 2h_*^2\left(D_{\parallel} + D_{\perp}\right) b_1^2 b_2^2 c_1 + \mathcal{O}(h_*^4), \\
\mathcal{A}_4 &= (c_7 b_1 + c_8 b_2)\left(c_7^{D_{\parallel}} b_1 + c_8^{D_{\parallel}} b_2\right) + (-c_7 b_2 + c_8 b_1)\left(-c_7^{D_{\perp}} b_2 + c_8^{D_{\perp}} b_1\right) \\
&\quad + h_*^2\Big[b_1^3 b_2\left(c_2 c_7^{D_{\parallel}} + c_7 c_2^{D_{\parallel}}\right) + b_2^3 b_1\left(c_3 c_8^{D_{\parallel}} + c_8 c_3^{D_{\parallel}}\right) \\
&\quad + b_1^2 b_2^2\left(c_2 c_8^{D_{\parallel}} + c_8 c_2^{D_{\parallel}} + c_3 c_7^{D_{\parallel}} + c_7 c_3^{D_{\parallel}}\right)\Big] \\
&\quad + h_*^2\Big[-b_1^3 b_2\left(c_3 c_8^{D_{\perp}} + c_8 c_3^{D_{\perp}}\right) - b_2^3 b_1\left(c_2 c_7^{D_{\perp}} + c_7 c_2^{D_{\perp}}\right) \\
&\quad + b_1^2 b_2^2\left(c_3 c_7^{D_{\perp}} + c_7 c_3^{D_{\perp}} + c_2 c_8^{D_{\perp}} + c_8 c_2^{D_{\perp}}\right)\Big] + \mathcal{O}(h_*^4),
\end{aligned}
$$

where it should be noted that here $h_* = \Delta s = \Delta n$ represents the step size in the aligned stencil. If h_* goes to zero we get

$$
\begin{aligned}
\mathcal{A}_1 &= (D_{\parallel} - D_{\perp})\,(c_8 b_1 - c_7 b_2)\left(b_1^2 c_7^{b_2} - b_2^2 c_8^{b_1} - b_1 b_2 c_7^{b_1} + b_1 b_2 c_8^{b_2}\right), \\
\mathcal{A}_2 &= (D_{\parallel} - D_{\perp})\,(c_7 b_1 + c_8 b_2)\left(b_2^2 c_7^{b_1} + b_1^2 c_8^{b_2} - b_1 b_2 c_7^{b_2} - b_1 b_2 c_8^{b_1}\right), \\
\mathcal{A}_3 &= 2D_{\parallel}\left(b_1^2 c_4 + b_2^2 c_5 + b_1 b_2 c_6\right) + 2D_{\perp}\left(b_2^2 c_4 + b_1^2 c_5 - b_1 b_2 c_6\right), \\
\mathcal{A}_4 &= (c_7 b_1 + c_8 b_2)\left(c_7^{D_{\parallel}} b_1 + c_8^{D_{\parallel}} b_2\right) + (-c_7 b_2 + c_8 b_1)\left(-c_7^{D_{\perp}} b_2 + c_8^{D_{\perp}} b_1\right),
\end{aligned}
$$

which is equal to the exact differentation scheme from section 2.2.7.

E

VON NEUMANN STABILITY ANALYIS

Continuing the analysis of section 2.3 we give a more precise description of the stability dependency on the angle, using the Von Neumann stability analysis. Von Neumann stability analysis relies on the substitution of harmonic solutions in the discretized system of equations, assuming constant coefficients, equidistant grids and periodic boundary conditions. If the assumptions for the Von Neumann stability analysis apply it is equivalent to the Lax-Richtmeyer stability analysis.

For the stability analysis the time integration is assumed to be the θ-method; by change of θ a range of time integration schemes can be considered. The spatial discretisation is set to the asymmetric scheme by Günter et al. The θ-method is described in general as

$$T_{i,j,n} \approx T_{i,j,n-1} + (1-\theta)\Delta t \mathcal{L}(\Delta x, \Delta y, \alpha) T_{i,j,n-1} + \theta \Delta t \mathcal{L}(\Delta x, \Delta y, \alpha) T_{i,j,n},$$

where the linear operator $\mathcal{L}$ is made up of three components

$$\mathcal{L} = A\mathcal{L}_{xx} + B\mathcal{L}_{yy} + C\mathcal{L}_{xy},$$

with A, B and C given by

$$A = D_{\parallel} b_1^2 + D_{\perp} b_2^2, \quad B = D_{\parallel} b_2^2 + D_{\perp} b_1^2, \quad C = 2(D_{\parallel} - D_{\perp}) b_1 b_2.$$

First the Von Neumann stability analysis is performed using the asymmetric stencil, described in section 2.2.1. Writing out the stencil completely with the time integration scheme and collecting terms gives

$$\begin{aligned}
&T_{i,j}^{n+1} + \left(2\frac{A}{\Delta x^2} + 2\frac{B}{\Delta y^2}\right)\theta T_{i,j}^{n+1}\Delta t = T_{i,j}^{n} + \\
&\quad \frac{A\theta\Delta t}{\Delta x^2}\left(T_{i+1,j}^{n+1} + T_{i-1,j}^{n+1}\right) + \frac{B\theta\Delta t}{\Delta y^2}\left(T_{i,j+1}^{n+1} + T_{i,j-1}^{n+1}\right) + \\
&\quad \frac{C\theta\Delta t}{4\Delta x\Delta y}\left(T_{i+1,j+1}^{n+1} + T_{i-1,j-1}^{n+1} - T_{i+1,j-1}^{n+1} - T_{i-1,j+1}^{n+1}\right) + \\
&\quad \frac{A(1-\theta)\Delta t}{\Delta x^2}\left(T_{i+1,j}^{n} - 2T_{i,j}^{n} + T_{i-1,j}^{n}\right) + \frac{B(1-\theta)\Delta t}{\Delta y^2}\left(T_{i,j+1}^{n} - 2T_{i,j}^{n} + T_{i,j-1}^{n}\right) + \\
&\quad \frac{C(1-\theta)\Delta t}{4\Delta x\Delta y}\left(T_{i+1,j+1}^{n} + T_{i-1,j-1}^{n} - T_{i+1,j-1}^{n} - T_{i-1,j+1}^{n}\right).
\end{aligned}$$

Assuming a harmonic solution and taking a single Fourier component the solution in point i, j is written as

$$T_{i,j}^{n} = E_{i,j}^{n} e^{\hat{i}(i\psi_x + j\psi_y)}, \quad \psi_x = k\Delta x,\ \psi_y = k\Delta y. \tag{E.1}$$

This solution is substituted in above stencil and the subsequent result is divided by the solution for n, i, j, yielding

$$\left(\frac{1}{\theta\Delta t}+2\frac{A}{\Delta x^2}+2\frac{B}{\Delta y^2}\right)\theta\Delta t\frac{E^{n+1}}{E^n}=1+$$
$$A\frac{\theta\Delta t}{\Delta x^2}\frac{E^{n+1}}{E^n}\left(e^{\hat{i}\psi_x}+e^{-\hat{i}\psi_x}\right)+B\frac{\theta\Delta t}{\Delta y^2}\frac{E^{n+1}}{E^n}\left(e^{\hat{i}\psi_y}+e^{-\hat{i}\psi_y}\right)+$$
$$C\frac{\theta\Delta t}{4\Delta x\Delta y}\frac{E^{n+1}}{E^n}\left(e^{\hat{i}\psi_x}e^{\hat{i}\psi_y}+e^{-\hat{i}\psi_x}e^{-\hat{i}\psi_y}-e^{-\hat{i}\psi_x}e^{\hat{i}\psi_y}-e^{\hat{i}\psi_x}e^{-\hat{i}\psi_y}\right)\quad,$$
$$A\frac{(1-\theta)\Delta t}{\Delta x^2}\left(e^{\hat{i}\psi_x}-2+e^{-\hat{i}\psi_x}\right)+B\frac{(1-\theta)\Delta t}{\Delta y^2}\left(e^{\hat{i}\psi_y}-2+e^{-\hat{i}\psi_y}\right)+$$
$$C\frac{(1-\theta)\Delta t}{4\Delta x\Delta y}\left(e^{\hat{i}\psi_x}e^{\hat{i}\psi_y}+e^{-\hat{i}\psi_x}e^{-\hat{i}\psi_y}-e^{-\hat{i}\psi_x}e^{\hat{i}\psi_y}-e^{\hat{i}\psi_x}e^{-\hat{i}\psi_y}\right).$$

Using the Euler formula for complex numbers and some trigonometric identities we can write

$$\frac{E^{n+1}}{E^n}=\frac{1+(1-\theta)\left[2A\alpha(\cos\psi_x-1)+2B\beta(\cos\psi_y-1)+C\gamma\sin\psi_x\sin\psi_y\right]}{1-\theta\left[2A\alpha(\cos\psi_x-1)+2B\beta(\cos\psi_y-1)+C\gamma\sin\psi_x\sin\psi_y\right]},$$

with $\alpha=\frac{\Delta t}{\Delta x^2}$, $\beta=\frac{\Delta t}{\Delta y^2}$, $\gamma=\frac{\Delta t}{\Delta x\Delta y}$. The amplification factor is now defined as $G=\left|\frac{E^{n+1}}{E^n}\right|$ and for stability this should be smaller than or equal to one. We write the goniometric terms as

$$A=D_\perp A^{'},\quad B=D_\perp B^{'},\quad C=D_\perp C^{'},$$
$$A^{'}=(\varsigma b_1^2+b_2^2),\quad B^{'}=(\varsigma b_2^2+b_1^2),\quad C^{'}=2(\varsigma-1)b_1b_2,\quad \varsigma=\frac{D_\parallel}{D_\perp},$$

where the misalignment of the parallel diffusion with respect to the $x-$axis is represented by b_1 and b_2, the horizontal and vertical component respectively. For a grid with $\Delta x=\Delta y=h$ and $\tau=\Delta t/h^2$ it holds:

$$\frac{E^{n+1}}{E^n}=\frac{1+(1-\theta)D_\perp\tau\left[2A^{'}(\cos\psi_x-1)+2B^{'}(\cos\psi_y-1)+C^{'}\sin\psi_x\sin\psi_y\right]}{1-\theta D_\perp\tau\left[2A^{'}(\cos\psi_x-1)+2B^{'}(\cos\psi_y-1)+C^{'}\sin\psi_x\sin\psi_y\right]}.\quad\text{(E.2)}$$

The unconditional stability for $\theta\geq 0.5$ remains unaffected. Now the values for τ should be sought which give $G\leq 1$ for $0\leq\theta<0.5$. For the special case $\psi_x=\psi_y=2\psi$, writing out the geometric terms, it follows

$$\left|\frac{E^{n+1}}{E^n}\right|=\left|1-\frac{D_\perp\tau\left[4(1+\varsigma)+2(1-\varsigma)b_1b_2\right]\sin^2\psi}{1+\theta D_\perp\tau\left[4(1+\varsigma)+2(1-\varsigma)b_1b_2\right]\sin^2\psi}\right|,$$
$$2>\frac{D_\perp\tau\left[4(1+\varsigma)+2(1-\varsigma)b_1b_2\right]\sin^2\psi}{1+\theta D_\perp\tau\left[4(1+\varsigma)+2(1-\varsigma)b_1b_2\right]\sin^2\psi}>0.$$

For $\theta<0.5$ the stability requirement according to Von Neumann stability analysis for the asymmetric finite difference scheme is then given by

$$\tau<\frac{1}{D_\perp\frac{1}{2}(1-2\theta)\left[4(1+\varsigma)+2(1-\varsigma)b_1b_2\right]}.\quad\text{(E.3)}$$

If we set $\cos\psi_x = \cos\psi_y = -1$ in equation E.2 we find

$$\tau < \frac{1}{D_\perp \frac{1}{2}(1-2\theta)\left[4(1+\varsigma)\right]}. \tag{E.4}$$

As can be expected, the stability requirements given by equations (E.3), (E.4) are less stringent than the stability criterion resulting from the Gershgorin circle theorem used in section 2.3. Surprisingly the most conservative value following from the Von Neumann stability analysis is not dependent on the angle of misalignment.

F

REGARDING CONSISTENCY OF THE NORMALISED AVERAGING

Continuing the discussion of section 4.3.2 we locally enforce the following form of the averaged flux values

$$\overline{q_x} = \overline{D_{11}}\ \overline{T_x} + \overline{D_{21}}\ \overline{T_y}, \quad \overline{q_y} = \overline{D_{21}}\ \overline{T_x} + \overline{D_{22}}\ \overline{T_y}. \tag{F.1}$$

This enables us to preserve the identity of the resulting averaged diffusion tensor. By performing this splitting of the average we might break the conservation since for general real valued a and b we have that $\overline{a}\ \overline{b} \neq \overline{a\,b}$, and therefore we have to apply the normalised averaging with care. As normalisation is only relevant in specific parts of the computational domain we selectively apply the normalised averaging; specifically at the locations where arithmetic averaging of the diffusion tensor is inappropriate, i.e. where $|\sum_i \mathbf{b}_i| < \sum_i |\mathbf{b}_i|$. This is the case along the transition line discussed in section 4.2, i.e. where

$$\frac{(D_{21})_{i+\frac{1}{2},j+\frac{1}{2}}}{|\,(D_{21})_{i+\frac{1}{2},j+\frac{1}{2}}\,|}\,\frac{(D_{21})_{i-\frac{1}{2},j-\frac{1}{2}}}{|\,(D_{21})_{i-\frac{1}{2},j-\frac{1}{2}}\,|}\,\frac{(D_{21})_{i+\frac{1}{2},j-\frac{1}{2}}}{|\,(D_{21})_{i+\frac{1}{2},j-\frac{1}{2}}\,|}\,\frac{(D_{21})_{i-\frac{1}{2},j+\frac{1}{2}}}{|\,(D_{21})_{i-\frac{1}{2},j+\frac{1}{2}}\,|} < 1.$$

Consider the averaging of DT_x over the points u and d,

$$\begin{aligned} \text{arithmetic:} \quad & \overline{DT_x} = \frac{1}{2}\left[(DT_x)_u + (DT_x)_d\right], \\ \text{normalised:} \quad & \overline{D}\ \overline{T_x} = \overline{\mathcal{R}}\ \mathrm{diag}(\overline{D}_{\|}, \overline{D}_{\perp})\overline{\mathcal{R}}\ \overline{T_x}, \end{aligned}$$

where the averaging of the derivatives T_x is left open. For $h \to 0$ it is certain that

$$\overline{D}\ \overline{T_x} \to \overline{DT_x} + \mathcal{O}(h^{\kappa}),$$

where the order of convergence κ depends on the smoothness of the diffusion tensor distribution.
In order to make a statement about the consistency we assume the coarsest possible averaging namely unweighted arithmetic averaging for both the temperature and the

diffusion tensor value. Using Taylor series we get the following approximations of the two averages and the difference:

$$\begin{aligned}
\text{arithmetic:}\quad & \frac{1}{2}T_x(D_d+D_u)+\frac{1}{2}T_{xy}(D_u-D_d)h+\frac{1}{4}T_{xyy}(D_d+D_u)h^2 \\
& +\frac{1}{12}T_{xyyy}(D_u-D_d)h^3+\frac{1}{48}T_{xyyyy}(D_d+D_u)h^4, \\
\text{unweighted normalised:}\quad & \frac{1}{2}T_x(D_d+D_u)+\frac{1}{4}T_{xyy}(D_d+D_u)h^2 \\
& +\frac{1}{48}T_{xyyyy}(D_d+D_u)h^4, \\
\text{arithmetic - normalised:}\quad & =\frac{1}{2}(D_u-D_d)T_{xy}h+\frac{1}{12}(D_u-D_d)T_{xyyy}h^3+\mathcal{O}(h^5).
\end{aligned}$$

The above indicates that (1) for smooth diffusion tensor distributions the difference between the two averages is determined by the order with which D_u approaches D_d and that (2) in case of sign switching of D, the difference is first order in h and $|D_u - D_d|$. It also indicates that unweighted normalised averaging leads to a zeroeth order accurate approximation of the divergence due to the absence of T_{xy}.

To get more insight in how the value of the first order term $(D_u - D_d)$ changes we plot the value of $\Delta b_1 b_2 = (b_1 b_2)_{i+\frac{1}{2},j+\frac{1}{2}} - (b_1 b_2)_{i+\frac{1}{2},j-\frac{1}{2}}$ for different values of h along the line $x = 0.25$, for the circular and the elliptic field line case. Striking from the results shown in figure F.1 is the large relative variation of $\Delta b_1 b_2$ with change in step size h. We note that there is hardly any difference between the plots of $b_1 b_2$ and $1/2\left[(b_1 b_2)_{i+\frac{1}{2},j+\frac{1}{2}} + (b_1 b_2)_{i+\frac{1}{2},j-\frac{1}{2}}\right]$ for the different values of h, hence they are not shown.

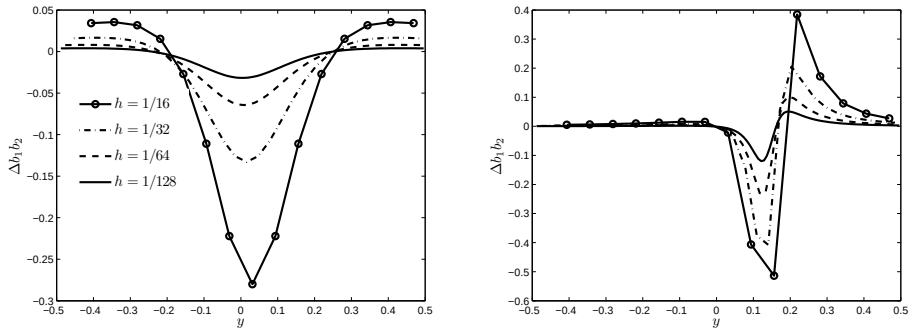

(a) (b)

Figure F.1: Value of first-order term in arithmetic average, plotted along the line $x = 0.25$ for (a) mixed open/closed field line problem, (b) tilted elliptic test case with $a = 0.15, b = 0.85, \theta = 1/6\pi$.

The results shown in figure F.1, indicate that unweighted normalised differencing is not appropriate due to the large absolute value of $\Delta b_1 b_2$.

Weighted normalised averaging is obtained by applying the following weighted average for the temperature derivatives

$$\overline{(T_x)_u, (T_x)_d} = \frac{(|D|T_x)_u + (|D|T_x)_d}{|D_u| + |D_d|}.$$

Using Taylor series expansions we get for the weighted normalised average:

$$\begin{aligned}\frac{(|D|T_x)_u) + (|D|T_x)_d}{|D_u| + |D_d|} \approx & \frac{T_x}{2|D_d| + 2|D_u|}(D_d + D_u)(|D_d| + |D_u|) \\ & + \frac{T_{xy}}{2|D_d| + 2|D_u|}(D_d - D_u)(|D_d| - |D_u|)h \\ & + \frac{1}{2}\frac{T_{xyy}}{2|D_d| + 2|D_u|}(D_d + D_u)(|D_d| + |D_u|)h^2 \\ & + \frac{1}{6}\frac{T_{xyyy}}{2|D_d| + 2|D_u|}(D_d - D_u)(|D_d| - |D_u|)h^3 \\ & + \frac{1}{24}\frac{T_{xyyyy}}{2|D_d| + 2|D_u|}(D_d + D_u)(|D_d| + |D_u|)h^4 + \mathcal{O}(h^5),\end{aligned}$$

which is also first order accurate in h for general D_u and D_d. If we assume that we only apply this averaging when $D_u\, D_d < 0$ we get the following

$$\begin{aligned}&D_d < 0,\, D_u > 0 \rightarrow \\ &\frac{D_u^2 - D_d^2}{|D_d| + |D_u|}\left[\frac{1}{2}T_x + \frac{1}{2}T_{xy}h + \frac{1}{4}T_{xyy}h^2 + \frac{1}{12}T_{xyyy}h^3 + \frac{1}{48}T_{xyyyy}h^4\right], \\ &D_d > 0,\, D_u < 0 \rightarrow \\ &\frac{D_d^2 - D_u^2}{|D_d| + |D_u|}\left[\frac{1}{2}T_x + \frac{1}{2}T_{xy}h + \frac{1}{4}T_{xyy}h^2 + \frac{1}{12}T_{xyyy}h^3 + \frac{1}{48}T_{xyyyy}h^4\right].\end{aligned}$$

Hence, if $|D_u| = |D_d|$ the average is zero. Shown in figure F.2 is the value of the

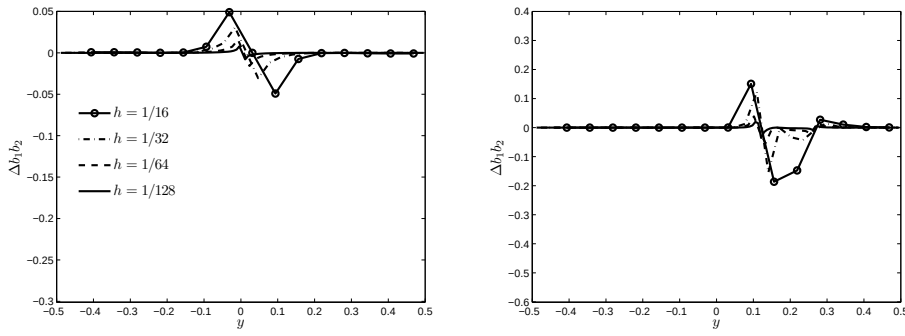

(a) (b)

Figure F.2: Value of first-order term in weighted normalised average value of (DT_x), plotted along the line $x = 0.25$ for (a) mixed open/closed field line problem, (b) tilted elliptic test case with $a = 0.15, b = 0.85, \theta = 1/6\pi$.

first order term of the weighted normalised average, called $\Delta b_1 b_2$ in the figure. The above analysis indicates that normalised averaging will deteriorate the local accuracy. This analysis also indicates that an asymmetric distribution of $\Delta b_1 b_2$ can be a factor in determining the global inaccuracy and lack of convergence of the mimetic finite difference scheme for elliptic closed field line problems.

BIBLIOGRAPHY

[1] I. Aavatsmark. Multipoint flux approximation methods for quadrilateral grids. 9^{th} *International Forum on Reservoir Simulation*, 2007.

[2] I. Aavatsmark, T. Barkve, Ø. Bøe, and T. Mannseth. Discretization on non-orthogonal, curvilinear grids for multi-phase flow. *Proc. of the 4th European Conf. on the Mathematics of Oil Recovery, Røros*, 6, 1994.

[3] I. Aavatsmark, T. Barkve, Ø. Bøe, and T. Mannseth. Discretization on non-orthogonal, quadrilateral grids for inhomogeneous, anisotropic media. *J. Comput. Phys.*, 127:2–14, 1996.

[4] I. Aavatsmark, T. Barkve, Ø. Bøe, and T. Mannseth. Discretization on unstructured grids for inhomogeneous, anisotropic media. part I: Derivation of the methods. *SIAM J. Sci. Comput.*, 19(5):1700–1716, 1998.

[5] I. Aavatsmark, T. Barkve, Ø. Bøe, and T. Mannseth. Discretization on unstructured grids for inhomogeneous, anisotropic media. part II: Discussion and numerical results. *SIAM J. Sci. Comput.*, 19(5):1717–1736, 1998.

[6] L. Agélas, A. Di Pietro, and J. Droniou. The G method for heterogeneous anisotropic diffusion on general meshes. *Math. Model. Numer. Anal.*, 4(44):597–625, 2010.

[7] L. Agélas, R. Eymard, and R. Herbin. A nine-point finite volume scheme for the simulation of diffusion in heterogeneous media. *C.R. Acad. Sci. Paris*, 347(11-12):673–676, 2009.

[8] P.F. Antonietti, M. Verani, and L. Zikatanov. A two-level method for mimetic finite difference discretizations of elliptic problems. *ArXiv e-prints*, (1310.2828v2), Nov. 2013.

[9] C. Aricò and T. Tucciarelli. Monotonic solution of heterogeneous anisotropic diffusion problems. *J. Comput. Phys.*, 252:219–249, 2013.

[10] D.N. Arnold and R.S. Falk. A new mixed formulation for elasticity. *Numer. Math.*, 53:13–30, 1988.

[11] I. Babuška and M. Suri. On locking and robustness in the finite element method. *SIAM J. Numer. Anal.*, 220:751–771, 1992.

[12] F. Bassi and S. Rebay. A high-order accurate discontinuous finite element method for the numerical solution of the compressible Navier-Stokes equations. *J. Comput. Phys.*, 131(2):267–279, 1997.

[13] P. Bochev and M. Gerritsma. A spectral mimetic least-squares method. *Comput. Math. Appl.*, 68, 2014.

[14] J. Bonelle and A. Ern. Analysis of compatible discrete operator schemes for elliptic problems on polyhedral meshes. *ESAIM Math. Model. Numer. Anal.*, 48(2):553–581, 2014.

[15] J. Breil and P.-H. Maire. A cell-centered diffusion scheme on two-dimensional unstructured meshes. *J. Comput. Phys.*, 224:785–823, 2007.

[16] F. Brezzi, K. Lipnikov, and M. Shashkov. Convergence of the mimetic finite difference method for diffusion problems on polyhedral meshes. *SIAM J. Numer. Anal.*, 43(5):1872–1896, 2005.

[17] F. Brezzi, K. Lipnikov, and V. Simoncini. A family of mimetic finite difference methods on polygonal and polyhedral meshes. *Math. Models Methods Appl. Sci.*, 15:1533–1551, 2005.

[18] A. Cangiani and G. Manzini. Flux reconstruction and solution post-processing in mimetic finite difference methods. *Comput. Methods Appl. Mech. Engrg.*, 197:933–945, 2008.

[19] L. Chacón, D. del Castillo-Negrete, and C.D. Hauck. An asymptotic-preserving semi-Lagrangian algorithm for the time-dependent anisotropic heat transport equation. *J. Comput. Phys.*, 272:719–746, 2014.

[20] J. Chen, S.C. Jardin, and H.R. Strauss. Solving anisotropic transport equation on misaligned grids. In *Computational Science – ICCS 2005*, Lecture Notes in Computer Science, pages 1076–1079. Springer Berlin Heidelberg, 2005.

[21] B. Cockburn, J. Gopalakrishnan, and R. Lazarov. Unified hybridization of discontinuous Galerkin, mixed, and continuous Galerkin methods for second order elliptic problems. *SIAM J. Numer. Anal.*, 47(2):1319–1365, 2009.

[22] B. Cockburn and C.-W. Shu. The local discontinuous Galerkin method for time-dependent convection-diffusion systems. *SIAM J. Numer. Anal.*, 35:2440–2463, 1998.

[23] R.W. Conn. The engineering of magnetic fusion reactors. *Scientific American*, 249(4), October.

[24] Ricardo Costa, Stéphane Clain, and GasparJosé Machado. Finite volume scheme based on cell-vertex reconstructions for anisotropic diffusion problems with discontinuous coefficients. In *Computational Science and Its Applications – ICCSA 2014*, Lecture Notes in Computer Science, pages 87–102. Springer, 2014.

[25] Y. Coudière, J.-P. Vila, and P. Villedieu. Convergence rate of a finite volume scheme for a two dimensional convection-diffusion problem. *ESAIM Math. Model. Numer. Anal.*, 33(3):493–516, 1999.

[26] L.B. Da Veiga, F. Brezzi, A. Cangiani, G. Manzini, L.D. Marini, and A. Russo. Basic principles of virtual element methods. *M3AS Math. Models Methods Appl. Sci.*, 199(23):199–214, 2013.

[27] L.B. da Veiga, F. Brezzi, L.D. Marini, and A. Russo. Virtual element methods for general second order elliptic problems on polygonal meshes. *ArXiv e-prints*, (1412.2646), December 2014.

[28] L.B. Da Veiga, G. Manzini, and K. Lipnikov. Arbitrary-order nodal mimetic discretizations of elliptic problems on general meshes. *SIAM J. Numer. Anal.*, 5(49):1737–1760, 2011.

[29] L.B. da Veiga, G. Manzini, and M. Putti. Post processing of solution and flux for the nodal mimetic finite difference method. *Numer. Methods Partial Differential Eq.*, 31:336–363, 2014.

[30] P. Degond, F. Deluzet, A. Lozinski, J. Narski, and C. Negulescu. Duality-based asymptotic-preserving method for highly anisotropic diffusion equations. *Commun. Math. Sci.*, 10:1–31, 2012.

[31] P. Degond, F. Deluzet, and C. Negulescu. An asymptotic preserving scheme for strongly anisotropic elliptic problems. *Multiscale Model. Simul.*, 8(2):645–666, 2009.

[32] P. Degond, A. Lozinksi, J. Narski, and C. Negulescu. An Asymptotic-Preserving method for highly anisotropic elliptic equations based on a micro-macro decomposition. *J. Comput. Phys.*, 231(7):2724–2740, 2012.

[33] D. del Castillo-Negrete and L. Chacón. Local and nonlocal parallel heat transport in general magnetic fields. *Phys. Rev. Lett.*, 106(19), 2011.

[34] D. del Castillo-Negrete and L. Chacón. Parallel heat transport in integrable and chaotic magnetic fields. *Phys. Plasmas*, 19(5):1–5, 2012.

[35] M. Desbrun, A. Hirani, M. Leok, and J. Marsden. Discrete exterior calculus. *ArXiv e-prints*, (0508341v2), 2005.

[36] D.A. Di Pietro and A. Ern. *Mathematical Aspects of Discontinuous Galerkin Methods*. Springer, 2012.

[37] J. Douglas Jr. and T. Dupont. Interior penalty procedures for elliptic and parabolic Galerkin methods. In *Computing Methods in Applied Sciences*, volume 58 of *Lecture Notes in Phys.*, page 207–216. 1976.

[38] J. Droniou. Finite volume schemes for diffusion equations: introduction to and review of modern methods. *HAL report hal-00813613*, 2013.

[39] J. Droniou and R. Eymard. A mixed finite volume scheme for anisotropic diffusion problems on any grid. *Numer. Math.*, 105(1):35–71, 2006.

[40] J. Droniou, R. Eymard, T. Gallouët, and R. Herbin. A unified approach to mimetic finite difference, hybrid finite volume and mixed finite volume methods. *Math. Models Methods Appl. Sci.*, 20(2):265–295, 2008.

[41] J. Droniou, R. Eymard, T. Gallouët, and R. Herbin. Gradient schemes: a generic framework for the discretisation of linear, nonlinear and nonlocal elliptic and parabolic equations. *HAL report hal-00757155v2*, 2012.

[42] J. Droniou and C. Le Potier. Construction and convergence study of schemes preserving the elliptic local maximum principle. *SIAM J. Numer. Anal.*, 49(2):459–490, 2011.

[43] M.G. Edwards and C.F. Rogers. Finite volume discretization with imposed flux continuity for the general tensor pressure equation. *Comput. Geosci.*, 2:259–290, 1998.

[44] R. Eymard, T. Gallouët, and R. Herbin. A cell-centred finite-volume approximation for anisotropic diffusion operators on unstructured meshes in any space dimension. *IMA J. Numer. Anal.*, 26:326–353, 2006.

[45] R. Eymard, T. Gallouët, and R. Herbin. A new finite volume scheme for anisotropic diffusion problems on general grids: convergence analysis. *C. R., Math., Acad. Sci. Paris*, 344(1-2):403–406, 2007.

[46] R. Eymard, T. Gallouët, and R. Herbin. Discretization of heterogeneous and anisotropic diffusion problems on general nonconforming meshes, SUSHI: a scheme using stabilization and hybrid interfaces. *IMA J. Numer. Anal.*, 30(4):1009–1043, 2010.

[47] R. Eymard, C. Guichard, R. Herbin, and R. Masson. Vertex-centered discretization of multiphase compositional Darcy flows on general meshes. *Comput. Geosci.*, 16(4):987–1005, 2012.

[48] R. Eymard, G. Henry, R. Herbin, F. Hubert, R. Klöfkorn, and G. Manzini. 3D benchmark on discretization schemes for anisotropic diffusion problems on general grids. In *Finite Volumes for Complex Applications VI, Problems and Perspectives*, volume 4 of *Springer Proceeding in Mathematics*, pages 895–930. ISTE, 2011.

[49] R. Eymard, R. Herbin, and C. Guichard. Small-stencil 3D schemes for diffusive flows in porous media. *ESAIM Math. Model. Numer. Anal.*, 2(46):265–290, 2012.

[50] J.H. Ferziger and M. Perić. *Computational Methods for Fluid Dynamics*. Springer, 2002.

[51] S. Futatani, G. Huijsmans, A. Loarte, L.R. Baylor, N. Commaux, T.C. Jernigan, M.E. Fenstermacher, C. Lasnier, T.H. Osborne, and B. Pegourié. Non-linear MHD modelling of ELM triggering by pellet injection in DIII-D and implications for ITER. *Nuclear Fusion*, 54(7), 2014.

[52] G. Gassner, F. Lörcher, and C.-D. Munz. A contribution to the construction of diffusion fluxes for finite volume and discontinuous Galerkin schemes. *J. Comput. Phys.*, 224(2):1049–1063, 2007.

[53] S. Günter, K. Lackner, and C. Tichmann. Finite element and higher order difference formulations for modelling heat transport in magnetised plasmas. *J. Comput. Phys.*, 226:2306–2316, 2007.

[54] S. Günter, Q. Yu, J. Krüger, and K. Lackner. Modelling of heat transport in magnetised plasmas using non-aligned coordinates. *J. Comput. Phys.*, 209:354–370, 2005.

[55] R. Haberman. *Applied Partial Differential Equations: With Fourier Series and Boundary Value Problems*. Pearson Prentice Hall, Pearson Education, Incorporated, 2004.

[56] R. Herbin and F. Hubert. Benchmark on discretization schemes for anisotropic diffusion problems on general grids. In *Finite Volumes for Complex Applications V*, pages 659–692. ISTE, 2008.

[57] F. Hermeline. A finite volume method for the approximation of diffusion operators on distorted meshes. *J. Comput. Phys.*, (160):481–499, 2000.

[58] F. Hermeline. A finite volume method for approximating 3D diffusion operators on general meshes. *J. Comput. Phys.*, (228):5763–5786, 2009.

[59] R.R. Hiemstra, D. Toshniwal, R.H.M. Huijsmans, and M.I. Gerritsma. High order geometric methods with exact conservation properties. *J. Comp. Phys.*, 257, Part B:1444 – 1471, 2014. Special issue: Physics-Compatible Numerical Methods.

[60] A.N. Hirani. *Discrete Exterior Calculus*. PhD thesis, California Institute of Technology, 2003.

[61] A.N. Hirani, K.B. Nakshatrala, and J.H. Chaudhry. Numerical method for Darcy flow derived using Discrete Exterior Calculus. *ArXiv e-prints*, (0810.3434v4), 2008.

[62] M. Hölzl. *Diffusive Heat Transport across Magnetic Islands and Stochastic Layers in Tokamaks*. PhD thesis, Technische Universität München, Max-Planck-Institut für Plasmaphysik, 2010.

[63] J.W. Hughes, A.E. Hubbard, D.A. Mossessian, B. LaBombard, T.M. Biewer, R.S. Granetz, M. Greenwald, I.H. Hutchinson, J.H. Irby, Y. Lin, E.S. Marmar, M. Porkolab, J.E. Rice, J.A. Snipes, J.L. Terry, S. Wolfe, and K. Zhurovich. H-mode pedestal and L-H transition studies on Alcator C-Mod. *Fusion Science and Technology*, 51(3):317–341, 2007.

[64] G.T.A. Huysmans, S.J.P. Pamela, E. van der Plas, and P. Ramet. Non-linear MHD simulations of edge localized modes (ELMs). *Plasma Phys. Control. Fusion*, 51(12), 2009.

[65] J. Hyman, J. Morel, M. Shashkov, and S. Steinberg. Mimetic finite difference methods for diffusion equations. *Comput. Geosci.*, 6:333–352, 2002.

[66] J. Hyman and M. Shashkov. The approximation of boundary conditions for mimetic finite-difference methods. *Comput. Math. Appl.*, 36:79–99, 1998.

[67] J. Hyman, M. Shashkov, and S. Steinberg. The numerical solution of diffusion problems in strongly heterogeneous non-isotropic materials. *J. Comput. Phys.*, 132:130–148, 1997.

[68] J. Hyman, M. Shashkov, and S. Steinberg. The effect of inner products for discrete vector fields on the accuracy of mimetic finite difference methods. *Comput. Math. Appl.*, 42(12):1527–1547, 2001.

[69] P. Jacq, P-H Maire, and R. Abgrall. A cell centered finite volume scheme for solving a vectorial diffusion equation on unstructured grids. Application to the compressible Navier-Stokes equations. In *11th World Congress on Computational Mechanics*, 2014.

[70] P. Jacq, P-H Maire, and R. Abgrall. A nominally second-order cell-centered finite volume scheme for simulating three-dimensional anisotropic diffusion equations on unstructured grids. *Commun. Comput. Phys.*, 16:841–891, 2014.

[71] P. Jacq, P.H. Maire, and R. Abgrall. A high-order cell-centered finite volume scheme for simulating three dimensional anisotropic diffusion equations on unstructured grids. *HAL report hal-00835537*, 2013.

[72] S.C. Jardin. A triangular finite element with first-derivative continuity applied to fusion MHD applications. *J. Comput. Phys.*, 200(1):133 – 152, 2004.

[73] R.A. Klausen and T.F. Russell. Relationships among some locally conservative discretization methods which handle discontinuous coefficients. *Comput. Geosci.*, 8:341–377, 2004.

[74] J. Kreeft, A. Palha, and M. Gerritsma. Mimetic framework on curvilinear quadrilaterals of arbitrary order. *ArXiv e-prints*, (1111.4304).

[75] P.T. Lang, A. Burckhart, M. Bernert, L. Casali, R. Fischer, O. Kardaun, G. Kocsis, M. Maraschek, A. Mlynek, B. Plöckl, M. Reich, F. Ryter, J. Schweinzer, B. Sieglin, W. Suttrop, T. Szepesi, G. Tardini, E. Wolfrum, D. Zasche, H. Zohm, and The ASDEX Upgrade Team. ELM pacing and high-density operation using pellet injection in the ASDEX upgrade all-metal-wall tokamak. *Nuclear Fusion*, 54(8), 2014.

[76] P.T. Lang, G.D. Conway, T. Eich, L. Fattorini, O. Gruber, S. Günter, L.D. Horton, S. Kalvin, A. Kallenbach, M. Kaufmann, G. Kocsis, A. Lorenz, M.E. Manso, M. Maraschek, V. Mertens, J. Neuhauser, I. Nunes, W. Schneider, W. Suttrop, H. Urano, and the ASDEX Upgrade Team. ELM pace making and mitigation by pellet injection in ASDEX upgrade. *Nuclear Fusion*, 44(5), 2004.

[77] C. Le Potier. A finite volume method for the approximation of highly anisotropic diffusion operators on unstructured meshes. *Finite Volumes for Complex Applications IV*, 2005.

[78] C. Le Potier. Schéma volumes finis monotone pour des opérateurs de diffusion fortement anisotropes sur des maillages de triangles nonstructurés. *C.R. Math.*, 341(12):787–792, 2005.

[79] C. Le Potier. Un schéma linéaire vérifiant le principe du maximum pour des opérateurs de diffusion très anisotropes sur des maillages déformés. *C. R., Math., Acad. Sci. Paris*, 347(1-2):105–110, 2009.

[80] C. Le Potier and T.H. Ong. A cell-centered scheme for heterogeneous anisotropic diffusion problems on general meshes. *Int. J. Finite Vol.*, 8:1–40, 2012.

[81] A.W. Leonard, A. Herrmann, K. Itami, J. Lingertat, A. Loarte, T.H. Osborne, and W. Suttrop et al. The impact of ELMs on the ITER divertor. *J. of Nucl. Mat.*, 266-269:109–117, 1999.

[82] X. Li and W. Huang. An anisotropic mesh adaptation method for the finite element solution of heterogeneous anisotropic diffusion problems. *J. Comput. Phys.*, 229:8072–8094, 2010.

[83] K. Lipnikov and G. Manzini. A high-order mimetic method on unstructured polyhedral meshes for the diffusion equation. *J. Comput. Phys.*, 272:360–385, 2014.

[84] K. Lipnikov, G. Manzini, and M. Shashkov. Mimetic finite difference method. *J. Comput. Phys.*, 257:1163–1227, 2014.

[85] K. Lipnikov, G. Manzini, and D. Svyatskiy. Analysis of the monotonicity conditions in the mimetic finite difference method for elliptic problems. *J. Comput. Phys.*, 230:2620–2642, 2011.

[86] K. Lipnikov and M. Shashkov. Local flux mimetic finite difference methods. *Numer. Math.*, 112:115–152, 2009.

[87] K. Lipnikov, M. Shashkov, D. Svyatskiy, and Y. Vassilevski. Monotone finite volume schemes for diffusion equations on unstructured triangular and shape-regular polygonal meshes. *J. Comput. Phys.*, 227:492–512, 2007.

[88] K. Lipnikov, M. Shashkov, and I. Yotov. Local flux mimetic finite difference methods. Technical Report LA-UR-05-8364, Los Alamos National Laboratory, 2005.

[89] K. Lipnikov, D. Svyatskiy, and Y. Vassilevski. Interpolation-free monotone finite volume method for diffusion equations on polygonal meshes. *J. Comput. Phys.*, 228:703–716, 2009.

[90] R. Liska, M. Shashkov, and V. Ganzha. Analysis and optimization of inner products for mimetic finite difference methods on triangular grid, 2003.

[91] P.-H. Maire and J. Breil. A high-order finite volume cell-centered scheme for anisotropic diffusion on two-dimensional unstructured grids. *J. Comput. Phys.*, 224(2):785–823, 2011.

[92] P.-H. Maire and J. Breil. A nominally second-order accurate finite volume cell-centered scheme for anisotropic diffusion on two-dimensional unstructured grids. *J. Comput. Phys.*, 231:2259–2299, 2012.

[93] W. McLean. *Strongly Elliptic Systems and Boundary Integral Equations*. Cambridge University Press, 2000.

[94] E.T. Meier, V.S. Lukin, and U. Shumlak. Spectral element spatial discretization error in solving highly anisotropic heat conduction equation. *Comput. Phys. Commun.*, 181:837–841, 2010.

[95] A. Mentrelli and C. Negulescu. Asymptotic preserving scheme for highly anisotropic, nonlinear diffusion equations. *J. Comput. Phys.*, 231(24):8229–8245, 2012.

[96] J.E. Morel, R.M. Roberts, and M. Shashkov. A local support-operators diffusion discretization scheme for quadrilateral $r-z$ meshes. *J. Comput. Phys.*, 144:17–51, 1998.

[97] J. Narski and M. Ottaviani. Asymptotic Preserving scheme for strongly anisotropic parabolic equations for arbitrary anisotropy direction. *Comput. Phys. Commun.*, 185:3189–3203, 2014.

[98] J.T. Oden, I. Babuška, and C.E. Baumann. A discontinuous hp finite element method for diffusion problems. *J. Comput. Phys.*, 146(2):491–519, 1998.

[99] T.H Ong. *Schémas volumes finis pour des opérateurs de diffusion anisotropes hétérogènes sur des maillages non-conformes*. PhD thesis, Université Paris-Est, 2012.

[100] A. Palha, P.P. Rebelo, R. Hiemstra, J. Kreeft, and M. Gerritsma. Physics-compatible discretization techniques on single and dual grids, with application to the Poisson equation of volume forms. *J. Comput. Phys.*, 257, Part B:1394 – 1422, 2014.

[101] S.J.P. Pamela and G.T.A. Huysmans. Equilibrium flows in non-linear MHD simulations of X-point plasmas. In *AIP Conference Proceedings*, volume 1069 of *Theory of fusion plasmas*, pages 318–324.

[102] S.J.P. Pamela, G.T.A. Huysmans, M.N.A. Beurskens, S. Devaux, T. Eich, and S. Benkadda et al. Nonlinear MHD simulations of edge-localized-modes in JET. *Plasma Phys. Control. Fusion*, 53, 2011.

[103] A.J. Pasdunkorale and I.W. Turner. A second order control-volume finite element least-squares strategy for simulating diffusion in strongly anisotropic media. *J. Comput. Math.*, 23(1):1–16, 2005.

[104] J. Peraire and P.-O. Persson. The compact discontinuous Galerkin (CDG) method for elliptic problems. *SIAM J. Sci. Comput.*, 30(4):1806–1824, 2008.

[105] D.A. Di Pietro, A. Ern, and S. Lemaire. A high-order cell-centered finite volume scheme for simulating three dimensional anisotropic diffusion equations on unstructured grids. *HAL report hal-00978198*, 2014.

[106] P.P. Rebelo, A. Palha, and M. Gerritsma. Mixed mimetic spectral element method applied to Darcy's problem. *ArXiv e-prints*, (1304.7147).

[107] P. Sharma and G.W. Hammett. Preserving monotonicity in anisotropic diffusion. *J. Comput. Phys.*, 227:123–142, 2007.

[108] M. Shashkov and S. Steinberg. Support-operator finite-difference algorithms for general elliptic problems. *J. Comput. Phys.*, 118:131–151, 1995.

[109] C.R. Sovinec, A.H. Glasser, T.A. Gianakon, D.C. Barnes, R.A. Nebel, S.E. Kruger, D.D. Schnack, S.J. Plimpton, A. Tarditi, and M.S. Chu. Nonlinear magnetohydrodynamics simulation using high-order finite elements. *J. Comput. Phys.*, 195:355–386, 2004.

[110] A. Stegmeir, D. Coster, O. Maj, and K. Lackner. Numerical methods for 3D tokamak simulations using a flux-surface independent grid. *Contrib. Plasm. Phys.*, 54(4-6), 2014.

[111] H.R. Strauss, W. Park, E. Belova, G.Y. Fu, and L.E. Sugiyama. 3-D MHD simulations of pellet injection and disruptions in tokamak plasmas. *Nuclear Fusion*, 39(11Y):2069, 1999.

[112] V. Subramanian and J.B. Perot. Higher-order mimetic methods for unstructured meshes. *J. Comput. Phys.*, 219(2):68–85, 2006.

[113] M.V. Umansky, M.S. Day, and T.D. Rognlien. On numerical solution of strongly anisotropic diffusion equation on misaligned grids. *Numer. Heat Transf., Part B.*, 47:533–554, 2005.

[114] B. van Es, B. Koren, and H.J. de Blank. Finite-difference schemes for anisotropic diffusion. *J. Comput. Phys.*, 272:1–24, 2014.

[115] J. van Kan, A. Segal, and F. Vermolen. *Numerical Methods in Scientific Computing*. VSSD, 2005.

[116] B. van Leer, M. Lo, and M. van Raalte. A discontinuous Galerkin method for diffusion based on recovery. *AIAA-paper 4083*, 2007.

[117] B. van Leer and S. Nomura. Discontinuous Galerkin for diffusion. *AIAA-paper 5108*, 2005.

[118] P.E. Vincent, P. Castonguay, and A. Jameson. A new class of high-order energy stable flux reconstruction schemes. *J. Sci. Comput.*, 47(1):50–72, 2011.

[119] F. Wagner, G. Becker, K. Behringer, D. Campbell, and et al. A. Eberhagen. Regime of improved confinement and high beta in neutral-beam-heated divertor discharges of the ASDEX tokamak. *Phys. Rev. Lett.*, 49(19):1408–1412, 1982.

[120] J. Weickert. *Anisotropic Diffusion in Image Processing*. Teubner, Stuttgart, 1998.

[121] D.M. Williams, P. Castonguay, P.E. Vincent, and A. Jameson. Energy stable flux reconstruction schemes for advection–diffusion problems on triangles. *J. Comput. Phys.*, 250:53 – 76, 2013.

ACKNOWLEDGEMENTS

Before starting with this PhD I have heard several abbreviations for the sought-for title, permanent head damage was one of them, coined by the same person who said CFD stands for continuous Fortran debugging. There is a level of cynism in there that I lost in an unpredictable manner. I found out that science is riddled with rituals and quirks like all human social endeavours, and although no sane scientist would claim science is perfect one has to do PhD research to experience and appreciate this imperfectness. The road was long, curvy and somewhere down the road I thought of becoming a full time fast-food restaurant worker and/or a circus acrobat but in the end my curiosity and stubbornness prevailed, and I believe it will in the future.

Of course, doing a PhD is not just a matter of rituals and traditions, in fact it is mostly a matter of persistence, self-motivation *and* social interaction. Plotting a graph of my level of motivation would surely give the impression that somewhere along the line I lost my mind, found it, lost it and refound it finally for the last stretch. Many important things happened in that period, many not so nice, some a lot nicer. I had a relationship, then I didn't, then I did, then I didn't, ad infinitum, with exponentionally shorter timespans , i.e. it was a fastly convergent series and it turned out to be a positive number although perhaps not the value we at first hoped for, Laura, thank you for your support, patience and your lessons, I love you.

Many times my 'outside' friends and my family thought I was still graduating, a basic attempt of a conversation starter would be to ask if I finished studying already, or even whether my (4-year!) internship had ended. The downslope of my aforementioned motivation curve could be in part attributed to an increase in the number of these occurrences. Nevertheless I thank you for accepting my strange working hours and inexplicable mood swings. A big shout-out goes to the my former roommates in Haarlem, Linda, Sjoerd, Bas, Monique, Jeroen and later Mathijs and Maarten. That first year of my PhD was one of the best years of my life so far.

I learned how incredible my mother is in her endless support, and how not even in a thousand lifes I could balance her dedication, patience and kindness on the same scale, I love you, unconditionally. I also owe gratitude to my grandmother 'Jopie' and my late grandfather Gerard, who supported me throughout my studies, not only financially but also by showing genuine interest in my work. I cannot leave out my brother now that I have reached the proverbial end-of-the-line in terms of higher education. You should know that I have always looked up to you, and these last years I saw exactly why I did that. Ruud, you are a kind and loving person, and you are part of my mother's happiness, for that and much more, thank you.

After many years in the academia I learned I had attention deficit disorder, one year before the end of my contract period. This perhaps explains why I sometimes poured yoghurt in my coffee cup, brushed my teeth with handcreme for a week, found my hair

brush in the refrigerator, why reading a book cost me ages, why my graduation thesis ended up being more than 270 pages long, why this current work could have been more than 300 pages, why this list is rather long and not to mention why my heart clouded my intellect with inspirational romantic fantasies or idealistic visions for many months on end.

Now I can say that I have finally learned to focus after three decades of life, perhaps mostly due to the continuous requirement imposed on me by the expected end-result of my work; a consistent thesis with one theme. It would be highly misplaced to claim it was just me and the situation that caused this, there were several individuals that assisted in life's training. Willem Haverkort and Benjamin Sanderse, you were relentless in your critique, and I wouldn't expect anything less from TUDelft alumni. Most of all you remained friends during the PhD and after. There is a crucial difference between someone who is harsh and someone who is honest, even if both have an intent to make you a better person, the latter avoids psychological trauma.. Ben I truly admire your rigor and sharpness. I will never forget the darkness of that empty room in the city hall of Vienna, darkness that you expelled with piano chords that were not supposed to be heard. Sometimes beauty lies still in darkness, waiting to be moved, and so it is.
Willem, the ease and almost nonchalance with which you produced complex new ideas with little assistance was as admirable as it was humbling, academia is waiting for your return.

There is much to be said about my work place, my colleagues in Amsterdam and Nieuwegein. Linda Plantagie, I do not think there is better example of persistence, hope and character. You never lost your spirit, whatever life threw at you, you kept looking at the horizon. I respect you for that, you know what I mean.
My office was close to the Multiscale Dynamics group, which seemed like a different world to me. As I mostly worked alone, it was refreshing to hear the heated debates over what schemes to use or what open source libraries to simulate their plasma leaders with. Fitting for their main research topic, sparks were sometimes flying. In terms of energy, the feeling of urgency and importance, this was very motivational. Ute, Willem, Anna & Anna, Aram, Anbang, Christoph, Jannis, Gideon, Enrico, Delyan, Ashu, Margreet, thanks for being inspiring neighbors.
Initially I shared the office with Yunus Hassen, one of the funniest people I have ever met, and also the most sarcastic. Your analogies of events with Ethiopian rural life put things in perspective, if I am depressed I will adopt a goat, let it demolish my apartment, and sell it a few weeks later to be happier than I started. In my memory you are an Islamic Bob Marley mixed with Noam Chomsky. I hope you have found life and love in Canada, we meet again.
Aram Markosyan, your pro-deo (blunt force) psychoanalysis helped me in my decision making, especially regarding relationships, and if not it was interesting to listen to you. I am sure that there were moments our colleagues thought we had secretly married, so intense would our squarrels be and so loudly would we talk. Someday, when you will not expect it, I will be standing outside your house in Michigan, ready to sucker punch you on the shoulder, and give you a hug of course.
Christoph Köhn, you were not only the driving force of the activity committee and the weekly football list, you have also been a good friend. You are a scientist pur sang and

I wish you all the best chasing lightning bolts and anti-matter.
Having mentioned the activity committee I cannot leave out the initiator Léon Ouwerkerk who continuously put in effort to support us, thank you for your positiveness and your vision.
Wagner, we had good times in Amsterdam, thank you for letting me in on your life in Amsterdam. I helped you with finding a job here, not just out of courtesy but also because I would have liked you to stay. Now that I am officially allowed to file your tax-reports in the Netherlands, I trust it that you save a room for me in Rio de Janeiro, preferably with a bubble bath. Otherwise I feel you are obliged to come back to Europe..
Shashi Jain, we were often in the pantry drawing out ideas for startup companies. Perhaps life's wisdom will bring us the necessary equipment to actually *start* up a company one day!
Ashutosh Agnihotri, by now you are married to a very lucky woman. It is a pity that I just met you in the last year of my PhD, no more surprise chanting, push-up contests or everlasting ping-pong matches. Good luck with the forest of hyperbolic solvers, mysterious source terms and the intricacies of plasma physics. I hope someday we may be partners in work or business.

"Dancing white bunny rabbits doing the flip flop with flip flops on" was the aspired name of the CWI football team since 2012, perhaps the character length of the name was a hint of our final ranking. Thankfully CWI did better in the Amsterdam Marathon, coming in second place three years in a row on the eight km run, which is quite a performance given there are more than a hundred teams running each year. It speaks for CWI that these sort of events were arranged and sponsored, keep it up.

Nada Mitrovic, without you several groups would come to a grinding halt. Not only in an organisational sense, you were also the person that added a human touch, and of course plants, candy, home grown fruits and other foodstuffs. Thank you so much for your kindness.

Minnie, Ruud, Tilly, Bikkie, Duda, Rob&Rob and others that made sure the PhD students can think and work freely and without worry, thank you. You are a crucial part of everyday CWI life, more then people realise perhaps.

I want to thank the HR department of CWI for allowing me to be a member of the works council, and subsequently I thank the HR department of FOM DIFFER for granting me the two extra months that I really needed to finish writing my thesis.
Thank you Chris Wesseling and Maarten Dijkema for your support in setting up a knowledge sharing platform, it certainly was a long stretch, and I do hope you finish it.

There are many people that I am glad to have met, Gebrekirstos Gebreselassie, Tom Sterkenburg, Eleni Petraki, Sonja Boas, Yağhiz Kargin, Simon Gunkel, Debarati Bhaumik, Hannes Mühlhausen, Emmanuelle Beauxis-Aussalet, Janis Bajars, Wander Wadman, Keith Myerscough, Wybe Rozema, Jesse Dorrestijn, Joost Bosman, Michael Kaisers, Nela Lekić and others.

I want to give some words of appreciation to my Monday and Thursday evening football mates. Gunnar, you are probably the coolest group leader I never had. Alex, Thomas, Andreas, Greg, Hany, Rafa, Victor, Cyrille, Akshay, Ronald, Stephan, Steven, Ruben, Sergio, Tibert, Jose, Bart and many more, you guys were always one of the highlights of the week.

Barry, thank you for believing in me and letting my mind wander freely through the realms of endless possibilities. Hugo, thank you for the well-needed explanations of plasma physics and both of you, thank you for taking the time to correct my work. I also want to thank the committee for correcting my final thesis concept, and especially Marc Gerritsma for his thoroughness.

Hüseyin Özdemir thank you for supporting me in pursuing a PhD, I will not tell anyone that you were the abbreviation guy mentioned in the beginning.

Just when I was having second doubts about the usefulness of poster sessions at conferences, I received a very insightful hint that created the make-it-or-break-it test case presented in this thesis. Thank you Dr. Klaus Hallatschek for giving me an important clue on the importance of symmetry in test cases from literature.

After my contract at CWI ended I had a job interview where it was made clear that the job was about applying hammers (numerical tools) and other equipment for research, and that I was primarily focussed on making these hammers. A disappointing result of the interview but finally I have a short and powerful answer when someone asks me what I did during my PhD research; I was in the construction business.

I think that the most common and most dreaded question asked to PhD students is; "what can you do with it?". I say this: science is not research & development of new products, it is research & development of something far more valuable, **new knowledge**.

SUMMARY

Magnetically confined nuclear fusion plasma is characterised by strong magnetic fields and high temperatures. This combination leads to extreme differences in the mobility of charged particles along the magnetic field lines and perpendicular to the field lines. When simulating diffusion processes this extreme anisotropy needs to be taken into account and this poses challenges to the accuracy and convergence of the numerical methods used.

In this thesis we approach the numerical approximation of the anisotropic diffusion problem in several novel ways, taking into account the directionality of diffusion, the connectivity of finite volumes and local values of the diffusion tensor.

We develop approaches that make use of the strong magnetic field alignment of the charged particles. We develop and apply a new differencing method on a co-located grid that implements the concept of following the field line within the stencil area to obtain the differencing points that are finally used in the approximation. We find that the interpolation used to determine the stencil is important for the accuracy, specifically our symmetric interpolation coefficients lead to better results than the conventional Vandermonde coefficients.
To investigate the effect of element connectivity we develop a finite volume method with varying connectivity, using both octogonal and square finite volumes. For this hybrid finite volume method we apply several flux approximations. The results indicate that connectivity plays a role in the accuracy, but it also appears that there is no clear optimal value for the connectivity parameter.

We also consider some local adaptations to the steady case based on the local characteristics of the diffusion tensor. An important finding is that cases with closed field lines are problematic for existing schemes due to the occurrence of sign switching around the axes that go through the *O*-point. The performance of numerical approximation techniques for diffusion are made more robust by applying normalised averaging or by directly preventing the sign switch, either through local rotation of the unit direction vectors or by locally adapting the grid size.

The accuracy for steady problems with the parallel temperature gradient tending to zero, with closed field lines present, can be restored completely by imposing a zero value for the parallel diffusion coefficient in points lying on a cross-section line of the closed field line region.

Finally, we propose small-sized model adaptations to increase the accuracy of the finite-difference methods. The results indicate that a form of model reduction can be used to improve the accuracy of current methods.

SAMENVATTING

Magnetisch ingesloten kernfusieplasma wordt gekenmerkt door sterke magnetische velden en hoge temperaturen. Deze combinatie leidt tot extreme verschillen in de mobiliteit van geladen deeltjes langs de magnetische veldlijnen en in richtingen loodrecht op de veldlijnen. Bij het simuleren van diffusieprocessen dient rekening te worden gehouden met deze extreme anisotropie. De anisotropie vormt een uitdaging voor de nauwkeurigheid en convergentie van numerieke methoden die worden gebruikt.

In dit proefschrift voeren we de numerieke benadering van het anisotrope diffusieprobleem op meerdere manieren uit, waarbij we de diffusierichtingen, de connectiviteit van eindige volumes en de lokale waarden van de diffusietensor in acht nemen.

We ontwikkelen een nieuwe eindige differentiediscretisatie op een gecoloceerd rekenrooster, een discretisatie die voor het verkrijgen van de punten van het differentiemolecuul lokaal de magnetische veldlijnen volgt. De interpolatie die gebruikt wordt voor de bepaling van de punten is belangrijk voor de nauwkeurigheid. Het gebruik van symmetrische interpolatiecoëfficiënten leidt tot een beter resultaat dan de conventionele Vandermonde coëfficiënten.

Om het effect van element-connectiviteit te onderzoeken ontwikkelen we een eindige-volume methode met variërende connectiviteit, gebruikmakend van zowel achthoekige als vierkante eindige volumes. Voor deze hybride eindige-volume methode passen we lokaal symmetrische coëfficiënten en Vandermonde coëfficiënten toe. De resultaten geven aan dat connectiviteit een rol speelt in de nauwkeurigheid, maar er is geen duidelijke optimale waarde voor de connectiviteitsparameter in het algemene geval.

We beschouwen ook enkele lokale aanpassingen voor het tijdsonafhankelijke geval, gebaseerd op lokale eigenschappen van de diffusietensor. Een belangrijk resultaat is dat algemene testgevallen met gesloten veldlijnen voor bestaande numerieke methoden problematisch zijn vanwege het optreden van een tekenwisseling in de diffusietensor rond de assen die door het O-punt gaan. De prestaties van de numerieke benaderingsmethoden voor diffusie kunnen waarschijnlijk meer robuust worden gemaakt door genormaliseerd te middelen daar waar mogelijk, of door het voorkomen van de tekenwisseling, door of lokale rotatie van de eenheidsrichtingsvectoren of door lokaal het differentiemolecuul aan te passen.

De nauwkeurigheid voor tijdsonafhankelijke problemen met de parallelle temperatuurgradiënt neigend naar nul en met gesloten veldlijnen, kan volledig hersteld worden door op te leggen dat de parallelle diffusiecoëfficiënt nul is op een lijn die de gesloten veldlijnoppervlakte doorsnijdt.

Uiteindelijk gebruikten we kleine modeladaptaties om de nauwkeurigheid van de eindige differentiemethodes te verbeteren. Voor selectieve waarden van de adaptatieparam-

eter merkten we een verbetering op voor een bepaald bereik van de roosterfijnheid. Hieruit concluderen we dat een vorm van modelreductie gebruikt kan worden om de nauwkeurigheid te verbeteren.

CURRICULUM VITAE

Bram van Es was born on August the fifth 1981, in IJmuiden, the Netherlands. He attended the Noordzee College from 1993 until 2000 where he completed an atheneum education. From 2000 until 2002 he studied aeronautical engineering at Haarlem University of Applied Sciences. From 2002 until 2009 he studied aerospace engineering at Delft University of Technology, where he obtained his Master of Science on a thesis titled 'Comparison and application of unsteady integral boundary layer equations' under the supervision of Dr. B. van Oudheusden and Dr. H. Özdemir. From 2007 until 2009 he studied law, obtaining a pre-master certificate for information law in 2009. From 2010 to 2014 he conducted PhD research on the numerical approximation of anisotropic diffusion. During this period he was employed by the Dutch Institute For Fundamental Energy Research (FOM-DIFFER) and seconded at the Centrum Wiskunde & Informatica (CWI), where he was a member of the works council for two years.